

# **Novel Molecular Probes for Non-invasive Optical Imaging of Fatty Acid and Triglyceride Uptake in Living Animals**

**Thèse N° 8437**

Présentée le 28 janvier 2019

à la Faculté des sciences de base

Laboratoire de protéines et peptides thérapeutiques

Programme doctoral en chimie et génie chimique

pour l'obtention du grade de Docteur ès Sciences

par

**GRIGORY KARATEEV**

Acceptée sur proposition du jury

Prof. V. Hatzimanikatis, président du jury

Prof. C. Heinis, directeur de thèse

Prof. H. Riezman, rapporteur

Dr H. Watzke, rapporteur

Dr R. Hovius, rapporteur

2019



# Acknowledgements

I would like to thank the members of my thesis jury Dr. Ruud Hovius, Professor Howard Riezman and Dr. Heribert Watzke for evaluating my work. My deepest gratitude to Professor Vassily Hatzimanikatis for all his kind support and advice and for being a president of the jury committee.

I thank Professor Elena Goun for the introduction in the field of chemical biology.

I would like to express my sincere gratitude to Professor Christian Heinis for his support, guidance, encouragement and advice. I would like to thank Professor Jan S Hesthaven, Dr. Jeroen van Hunen, Professor Sandrine Gerber and Mrs. Anne Lene Odegaard for all their help and support.

I would also like to warmly thank Dr. Arkadiy Bazhin for the precious scientific discussions, for his help and assistance during my work and for many nice moments, we shared during these years. I am very grateful to Manuel Drefahl for the enthusiastic conversations about Science, his fruitful ideas and for the nice time we had during our PhD studies. I also wish to thank Gennady Nikitin for his advice and opinion.

I express my gratitude to Professor Andreas Stahl and his team for our collaboration on various projects related to fatty acids. I wish to thank Professor Clemens Lowik, Dr. Arno Roos and Dr. Ksenya Shchors for the collaboration on the fluorescence tumor imaging. I would like to thank Dr. Anzhelika Vorobyeva for the fruitful collaboration on the nitroreductase imaging and for her help with the nanoluc project. I am grateful to Dr. James Collins for teaching me with the bacterial work. I wish to express my gratitude to Dr. Jason Chou for his encouragement, scientific advice and feedback on my projects.

I would like to warmly thank Dr. Riccardo Sinisi, Dr. Aleksandra Konovalova, Dr. Ghyslain Budin, Dr. Aurélien Godinat, Dr. Sergey Malashikhin, Dr. Jens Frigell and Dr. Alma Morales as well as the former and the current members of LPPT for the good moments and for the nice and positive atmosphere.

I would like to express my special gratitude to my family for the constant support and encouragement despite the long distance between us.





# Remark

Grigory Karateev performed this PhD thesis in the Laboratory of Bioorganic Chemistry and Molecular Imaging (LCBIM) headed by Prof. Dr. Elena Goun from September 10, 2012 to January 16, 2018. All the results presented belong to the laboratory of Prof. Goun.



# Abstract

Molecular imaging allows non-invasive visualization of biological processes in their native environment within living systems. It can give a better understanding of fundamental biology, help in identifying disease mechanisms and visualizing pathological tissues, and enable monitoring disease progression and studying the drug efficacy in intact living organisms. Among various imaging modalities, bioluminescence and fluorescence imaging are powerful techniques that have become essential methods for non-invasive real-time studies of biological processes *in vivo*.

The aim of my thesis was the development of novel fluorescent and bioluminescent probes for *in vivo* imaging of fatty acid and triglyceride uptake. The goal of my first project was the development of a near-infrared fluorescent fatty acid probe for glioma imaging. Some tumors such as glioma may rely on the uptake of extracellular fatty acids. Fatty acids can therefore be considered as targeting molecules for these tumors and could be used to develop tumor-imaging probes. The probe design is based on a near-infrared fluorophore indocyanine green (ICG) that is conjugated to a long-chain fatty acid palmitic acid. The conjugation of ICG to a fatty acid (ICG-FA) was envisioned to improve cell permeability of the fluorophore and its accumulation in glioma. The ICG-FA probe was first evaluated for its ability to mimic the uptake of natural fatty acids in cells and was then applied for glioma imaging studies *in vivo*, where it showed significant tumor accumulation. As a proof-of-concept, the probe was tested for intraoperative image-guided surgery in a canine patient with mastocytoma, where it allowed intraoperative fluorescence tumor imaging and provided optical guidance for a surgeon during tumor resection.

The aim of my second project was the development of bioluminescent triglyceride probes for real-time non-invasive imaging of triglyceride uptake *in vivo*. Applying an optimized strategy for generating conjugates with luciferin, I developed several bioluminescent triglyceride probes. These imaging tools were validated in cells and mice and were shown to mimic the absorption of natural triglycerides. The developed probes enabled sensitive non-invasive real-time imaging and quantification of triglyceride absorption in living mice. Furthermore, these probes were successfully used to demonstrate the effects of the anti-obesity drug orlistat and the influence of the gut microbiota on the intestinal absorption of triglycerides *in vivo*. Considering the high importance of triglycerides for human health and nutrition and their implication in several pathologies such as

obesity, metabolic syndrome, type 2 diabetes and cancer, the bioluminescent triglyceride probes could offer valuable imaging tools for preclinical research.

## Keywords

*In vivo* molecular imaging; bioluminescence imaging; near-infrared fluorescence imaging; molecular imaging probes; tumor imaging; indocyanine green; glioma; mastocytoma; image-guided surgery; fatty acids; triglycerides; lipid absorption; gut microbiota.

# Résumé

L'imagerie moléculaire permet une visualisation non-invasive des processus biologiques dans leur environnement natif au sein des systèmes vivants. Elle peut permettre une meilleure compréhension de la biologie fondamentale, aider à identifier les mécanismes de la maladie et à visualiser les tissus pathologiques, et permettre de suivre la progression de la maladie et étudier l'efficacité du médicament dans les organismes vivants intacts. Parmi les diverses modalités d'imagerie, la bioluminescence et l'imagerie par fluorescence sont des techniques puissantes qui sont devenues des méthodes essentielles pour des études en temps réel non invasives de processus biologiques *in vivo*.

Le but de ma thèse était le développement de nouvelles sondes fluorescentes et bioluminescentes pour l'imagerie *in vivo* de l'absorption des acides gras et des triglycérides. Le but de mon premier projet était le développement d'une sonde d'acide gras fluorescente proche infrarouge pour l'imagerie du gliome. Certaines tumeurs telles que les gliomes peuvent dépendre de l'absorption d'acides gras extracellulaires. Les acides gras peuvent donc être considérés comme des molécules de ciblage pour ces tumeurs et pourraient être utilisés pour développer des sondes d'imagerie tumorale. La conception de la sonde était basée sur un fluorophore Indocyanine green dans le proche infrarouge (ICG) qui est conjugué à un acide palmitique d'acide gras à longue chaîne. La conjugaison de l'ICG à un acide gras (ICG-FA) a été envisagée pour améliorer la perméabilité cellulaire et l'accumulation dans le gliome. La sonde ICG-FA a d'abord été évaluée pour sa capacité à imiter l'absorption des acides gras naturels dans les cellules et a ensuite été appliquée pour des études d'imagerie du gliome *in vivo* où il a montré une accumulation tumorale significative. Comme preuve de concept, la sonde a été testée pour une chirurgie intra-opératoire guidée par imagerie dans un brevet canin avec mastocytome, où elle permettait l'imagerie tumorale peropératoire par fluorescence et fournissait un guidage optique pour un chirurgien lors de la résection tumorale.

Le but de mon deuxième projet était le développement de sondes bioluminescentes à base de triglycérides pour l'imagerie non invasive en temps réel de l'absorption des triglycérides *in vivo*. En appliquant une stratégie optimisée pour générer des conjugués avec la luciférine, j'ai développé plusieurs sondes de triglycérides bioluminescentes. Ces outils d'imagerie ont été validés dans des cellules et des souris et ont montré qu'ils imitent l'absorption des triglycérides naturels. Les sondes développées ont permis l'imagerie sensible non-invasive en temps réel et la quantification de

l'absorption des triglycérides chez les souris vivantes. De plus, ces sondes ont été utilisées avec succès pour démontrer les effets de l'Orlistat, médicament contre l'obésité, et l'influence du microbiote intestinal sur l'absorption intestinale des triglycérides *in vivo*. Compte tenu de la grande importance des triglycérides pour la santé et la nutrition humaine et de leur implication dans plusieurs pathologies telles que l'obésité, le syndrome métabolique, le diabète de type 2 et le cancer, les sondes bioluminescentes à triglycérides pourraient offrir des outils d'imagerie précieux pour la recherche préclinique.

## Mots-clés

Imagerie moléculaire *in vivo*; imagerie de bioluminescence; imagerie de fluorescence proche infrarouge; sondes d'imagerie moléculaire; imagerie tumorale; vert d'indocyanine; gliome; mastocytome; chirurgie guidée par l'image; acides gras; triglycérides; absorption des lipides; microbiote intestinal.

# Contents

Acknowledgements.....	iii
Remark.....	v
Abstract.....	vii
Keywords .....	viii
Résumé .....	ix
Mots-clés.....	x
Contents.....	xi
List of Figures.....	xiii
List of Tables.....	xv
List of Schemes .....	xvii
Abbreviation.....	xix
<b>Chapter 1 Introduction.....</b>	<b>1</b>
1.1 Molecular imaging.....	1
1.2 Optical imaging.....	1
1.3 Bioluminescence imaging.....	2
1.4 Firefly luciferase/D-luciferin system .....	4
1.5 Caged luciferin probes for <i>in vivo</i> molecular imaging.....	7
1.6 Fluorescence imaging.....	14
1.7 Near-infrared fluorescence .....	16
<b>Chapter 2 Fluorescent Fatty Acid Probe for Non-Invasive <i>in Vivo</i> Imaging of Glioma.....</b>	<b>19</b>
2.1 Fluorescent probes for glioma imaging .....	19
2.2 Results .....	22
2.2.1 Probe design .....	22
2.2.2 Probe synthesis.....	23
2.2.3 Optical properties of ICG-FA probe .....	26
2.2.4 ICG-FA uptake studies in 3T3-L1 cells.....	26
2.2.5 ICG-FA uptake studies in U87MG-luc cells .....	32
2.2.6 Biodistribution studies in mice .....	35
2.2.7 <i>In vivo</i> fluorescence imaging of glioma in living mice using ICG-FA.....	39
2.2.8 Intraoperative tumor fluorescence imaging and image-guided surgery using ICG-FA.....	45
2.3 Experimental Section .....	49
2.3.1 Materials and methods. Chemical part .....	49

2.3.2	Materials and methods. Biological part .....	51
2.4	Supplementary figures .....	55
<b>Chapter 3</b>	<b>Bioluminescence Imaging of Triglyceride Uptake.....</b>	<b>57</b>
3.1	Triglyceride structure .....	57
3.2	Intestinal absorption of triglycerides .....	59
3.2.1	Gastric lipid digestion .....	59
3.2.2	Intestinal lipid digestion .....	60
3.3	Methods for <i>in vivo</i> measurement of intestinal triglyceride absorption .....	62
3.4	Results .....	65
3.4.1	Probe design .....	65
3.4.2	Mechanism of the probe activation .....	66
3.4.3	Synthesis of probes.....	68
3.4.4	Validation of triglyceride probes in luciferase expressing cells. ....	74
3.4.5	Validation of triglyceride probes in luciferase expressing mice.....	81
3.4.6	Influence of the gut microbiota on triglyceride absorption <i>in vivo</i> .....	87
3.5	Experimental Section .....	91
3.5.1	Materials and methods. Chemical part .....	91
3.5.2	Materials and methods. Biological part .....	99
<b>Chapter 4</b>	<b>Conclusion .....</b>	<b>105</b>
<b>Chapter 5</b>	<b>References .....</b>	<b>109</b>
<b>Chapter 6</b>	<b>Annexes.....</b>	<b>127</b>
6.1	Curriculum Vitae .....	127



## List of Figures

<b>Figure 1.1</b> Chemical structure of D-aminoluciferin .....	7
<b>Figure 1.2</b> Concept of bioluminogenic (caged luciferin) probes.....	8
<b>Figure 1.3</b> Bioluminescent approach for monitoring cellular uptake of biomolecules using caged luciferin strategy .....	13
<b>Figure 1.4</b> Simplified Jablonski diagram representing the energy transitions for fluorophores following light absorption.....	15
<b>Figure 2.1</b> Chemical structures of ICG and Fluorescein (disodium salt) that enable passive tumor imaging via EPR effect. ....	20
<b>Figure 2.2</b> 5-Aminolevulinic acid (5-ALA) is a metabolic precursor of fluorescent protoporphyrin IX (PpIX) for glioma imaging. ....	21
<b>Figure 2.3</b> Design of ICG-FA probe .....	22
<b>Figure 2.4</b> Optical properties of ICG-FA .....	26
<b>Figure 2.5</b> Comparison of ICG-FA and BODIPY-FA uptake in 3T3-L1 fibroblasts and adipocytes by fluorescence microscopy .....	28
<b>Figure 2.6</b> Concentration-dependent ICG-FA uptake by 3T3-L1 fibroblasts and adipocytes .....	30
<b>Figure 2.7</b> Kinetics of ICG-FA uptake by 3T3-L1 fibroblasts and adipocytes .....	31
<b>Figure 2.8</b> Effect of oleate on the uptake of ICG-FA by 3T3-L1 adipocytes .....	32
<b>Figure 2.9</b> Imaging of ICG-FA uptake in U87MG-luc by fluorescence microscopy .....	33
<b>Figure 2.10</b> Comparison of ICG-FA and ICG uptake by U87MG-luc cells.....	34
<b>Figure 2.11</b> <i>In vivo</i> dorsal fluorescence imaging of Swiss nu/nu mice after intravenous administration of ICG-FA (left mouse) or ICG (right mouse) .....	36
<b>Figure 2.12</b> <i>In vivo</i> ventral fluorescence imaging of Swiss nu/nu mice after intravenous administration of ICG-FA (left mouse) or ICG (right mouse) .....	37
<b>Figure 2.13</b> Comparison of whole-body fluorescent signals from ICG-FA and ICG in Swiss nu/nu mice .....	38
<b>Figure 2.14</b> <i>In vivo</i> imaging of glioma xenografts in a mouse model .....	40
<b>Figure 2.15</b> Comparison of fluorescent signals <i>in vivo</i> after administration of ICG-FA or ICG in Swiss nu/nu mice bearing subcutaneous glioma (U87MG-luc) xenografts .....	41
<b>Figure 2.16</b> Representative <i>in vivo</i> and <i>ex vivo</i> images showing fluorescent signals from ICG-FA or ICG and corresponding bioluminescent signals in the subcutaneous glioma (U87MG-luc) xenograft mouse model .....	42
<b>Figure 2.17</b> <i>Ex vivo</i> comparison of fluorescent signals from ICG-FA and ICG in subcutaneous U87MG-luc tumor xenografts and in the corresponding brains after their excision from Swiss nu/nu mice bearing the xenografts .....	43
<b>Figure 2.18</b> <i>Ex vivo</i> fluorescence imaging of brain tumors using ICG-FA and ICG in <i>GRLp53fko</i> transgenic mouse model that develops spontaneous high-grade glioma and comparison with fluorescence imaging of normal brains .....	44
<b>Figure 2.19</b> <i>Ex vivo</i> comparison of fluorescent signals from ICG-FA and ICG in the whole brains of <i>GRLp53fko</i> transgenic mice that develop spontaneous high-grade glioma (indicated as Tumor) versus fluorescent signals in whole brains of wild-type <i>FVB/NJ</i> mice (indicated as Normal) .....	44
<b>Figure 2.20</b> Intraoperative <i>in vivo</i> fluorescence imaging of mastocytoma in a dog using ICG-FA probe .....	46

<b>Figure 2.21</b> <i>Ex vivo</i> fluorescence imaging of excised mastocytoma from a canine patient injected i.v. with ICG-FA (0.32 mg/kg) 10 h prior to surgery .....	47
<b>Figure 3.1</b> The general stereochemical structure of a triglyceride.....	58
<b>Figure 3.2</b> Triglycerides which are present in some natural fats and oils .....	58
<b>Figure 3.3</b> Mechanism of pancreatic lipase catalysis.....	61
<b>Figure 3.4</b> The mechanism of the BL signal generation by LCTG-Luc1 in luciferase expressing cells. ..	68
<b>Figure 3.5</b> Bioluminescence imaging of LCTG-Luc1 and LCTG-Luc2 uptake by Caco2-luc cells.....	75
<b>Figure 3.6</b> Bioluminescence imaging of MCTG-Luc1 uptake by Caco2-luc cells .....	76
<b>Figure 3.7</b> Comparison of the bioluminescent signals produced from MCTG-Luc1, LCTG-Luc1 and LCTG-Luc2 (15 $\mu$ M for each probe in emulsion in 1 mM NaTDC in PBS) in Caco2-luc cells in the presence of pancreatic lipase (200 ng/mL) supplemented with colipase (40 ng/mL) .....	76
<b>Figure 3.8</b> Bioluminescence imaging of LCTG-Luc1 and LCTG-Luc2 uptake by Caco2-luc cells in the presence of orlistat .....	78
<b>Figure 3.9</b> Comparison of the bioluminescent signal produced from LCTG-Luc1 and LCGE-Luc1 in Caco2-luc cells .....	79
<b>Figure 3.10</b> Extracellular release of luciferin MPr-AL from the control probe LCGE-Luc1 induced by added GSH, which resulted in bioluminescent signal production in Caco2-luc cells.....	80
<b>Figure 3.11</b> Real-time bioluminescence imaging of intestinal triglyceride absorption in living mice using LCTG-Luc1.....	81
<b>Figure 3.12</b> Bioluminescence imaging of intestinal absorption of LCTG-Luc1 in FVB-luc+ mice.....	82
<b>Figure 3.13</b> Comparison of bioluminescent responses from LCTG-Luc1 and control probe LCGE-Luc1 administered by oral gavage in FVB-luc+ mice.....	83
<b>Figure 3.14</b> Influence of orlistat on the bioluminescent response from LCTG-Luc1 administered by oral gavage in FVB-luc+ mice .....	85
<b>Figure 3.15</b> Comparison of bioluminescent responses from LCTG-Luc1 and LCTG-Luc2 administered by oral gavage in FVB-luc+ mice .....	86
<b>Figure 3.16</b> Representative luminescent image of the excised gastro-intestinal tract from FVB-luc+ mouse 10 min after oral gavage of LCTG-Luc-1 (40 nmol in 150 $\mu$ L corn oil) .....	87
<b>Figure 3.17</b> Influence of antibiotics treatment on the intestinal absorption of LCTG-Luc1 in FVB-luc+ mice .....	88
<b>Figure 3.18</b> Influence of antibiotics treatment on the intestinal absorption of LCTG-Luc2 in FVB-luc+ mice .....	89
<b>Figure 3.19</b> Influence of <i>Lactobacillus plantarum</i> treatment with or without bile salt hydrolase activity on the bioluminescence from LCTG-Luc1 (40 nmol in 150 $\mu$ L corn oil by oral gavage) in FVB-luc+ mice.....	90

## List of Tables

<b>Table 1.1</b> Luciferase-luciferin pairs commonly used for BLI .....	3
<b>Table 1.2</b> Examples of caged luciferin probes used for molecular imaging of enzymatic activity, small molecules and metabolic events <i>in vitro</i> and <i>in vivo</i> .....	10
<b>Table 1.3</b> Examples of caged luciferin probes used to monitor cellular uptake of biomolecules.....	14
<b>Table 1.4</b> Selected examples of near-infrared organic fluorescent dyes for <i>in vivo</i> imaging applications .....	17
<b>Table 3.1</b> Structures of triglyceride-luciferin and fatty acid-luciferin probes .....	66



## List of Schemes

<b>Scheme 1.1</b> Mechanism of D-luciferin oxidation catalysed by firefly luciferase that results in bioluminescence .....	5
<b>Scheme 1.2</b> Dark reaction pathway of luciferin-adenylate oxidation catalysed by firefly luciferase .....	6
<b>Scheme 2.1</b> Synthesis of 16-aminopalmitic acid ( <b>4</b> ) .....	24
<b>Scheme 2.2</b> Synthesis of ICG-COOH ( <b>9</b> ) .....	24
<b>Scheme 2.3</b> Synthesis of ICG-FA ( <b>11</b> ) .....	25
<b>Scheme 3.1</b> Lipolysis of TG probes by pancreatic lipase .....	67
<b>Scheme 3.2</b> General approach for the synthesis of lipid-luciferin conjugates.....	68
<b>Scheme 3.3</b> Synthesis of PyS-MPr-AL ( <b>6</b> ) .....	69
<b>Scheme 3.4</b> Synthesis of LCTG-Luc1 ( <b>14</b> ) .....	70
<b>Scheme 3.5</b> Synthesis of LCTG-Luc2 ( <b>19</b> ) .....	71
<b>Scheme 3.6</b> Synthesis of LCGE-Luc ( <b>29</b> ) .....	72
<b>Scheme 3.7</b> Synthesis of FA-Luc ( <b>31</b> ) .....	73
<b>Scheme 3.8</b> Synthesis of MCTG-Luc ( <b>38</b> ) .....	73



# Abbreviation

AcOEt	Ethyl acetate
AcOH	Acetic acid
AL	D-aminoluciferin
5-ALA	5-Aminolevulinic acid
AMP	Adenosine monophosphate
ATP	Adenosine triphosphate
AVNM	Ampicillin, vancomycin, neomycin, metronidazole
BAT	Brown adipose tissue
BBB	Blood-brain barrier
BH <sub>3</sub> *THF	Borane-tetrahydrofuran
BL	Bioluminescence
BLI	Bioluminescence imaging
BODIPY	4,4-Difluoro-4-bora-3a,4a-diaza-s-indacene
BODIPY-FA	4,4-Difluoro-5,7-dimethyl-4-bora-3a,4a-diaza-s-indacene-3-hexadecanoic acid
bp.	Boiling point
BSA	Bovine serum albumin
BSH	Bile salt hydrolase
CCD	Charge-coupled device
CD8	Cluster of differentiation 8
CD36/FAT	Cluster of differentiation 36 / fatty acid translocase
CHCl <sub>3</sub>	Chlorophorm
CT	Computed tomography
DCM	Dichloromethane
DIPEA	<i>N,N</i> -Diisopropylethylamine
DMAP	4-Dimethylaminopyridine
DMF	Dimethyl formamide
DMSO	Dimethyl sulfoxide
EDCI	<i>N</i> -(3-Dimethylaminopropyl)- <i>N</i> '-ethylcarbodiimide hydrochloride
EGFR	Epidermal growth factor receptor

EPR	Enhanced permeability and retention
Et <sub>2</sub> O	Diethyl ether
Et <sub>3</sub> SiH	Triethylsilane
FA	Fatty acid
FAAH	Fatty acid amide hydrolase
FABP	Fatty acid binding protein
FABP <sub>pm</sub>	Plasma membrane fatty acid binding protein
FATP	Fatty acid transport protein
FLI	Fluorescence imaging
FLuc	Firefly luciferase
GBM	Glioblastoma multiforme
GSH	Glutathione
HBSS	Hank's balanced salt solution
H&E	Hematoxylin and eosin
HEPES	(4-(2-hydroxyethyl)-1-piperazineethanesulfonic acid)
HPLC	High-performance liquid chromatography
IC	Internal conversion
ICG	Indocyanine green
IL	Interleukin
i.p.	Intraperitoneal
ISC	Intersystem crossing
i.v.	Intravenous
LCFA	Long-chain fatty acid
LCGE	Long-chain glycerol triether
LCMG	Long-chain monoglyceride
LCTG	Long-chain triglyceride
Luc	Luciferin
MCTG	Medium-chain triglyceride
Me <sub>3</sub> N·HCl	Trimethylamine hydrochloride
MeOH	Methanol
MPr-AL	6-N-(3-mercaptopropyl)-aminoluciferin
MRI	Magnetic resonance imaging
MsCl	Methanesulfonyl chloride
NaH	Sodium hydride



NaTDC	Sodium taurodeoxycholate
NBD	Nitrobenzoxadiazole
NHS	N-Hydroxysuccinimide
NIR	Near-infrared
NTR	Nitroreductase
PBS	Phosphate-buffered saline
PET	Positron emission tomography
PL	Pancreatic lipase
PLRP	Pancreatic lipase-related protein
PpIX	Protoporphyrin IX
PPTS	Pyridinium p-toluenesulfonate
Py	Pyridine
RT	Room temperature
SBR	Signal-to-background ratio
S <sub>N</sub> 2	Bimolecular nucleophilic substitution
SPECT	Single-photon emission computed tomography
T/B	Tumor-to-background ratio
TFA	Trifluoroacetic acid
TG	Triglyceride
THF	Tetrahydrofuran
THP	Tetrahydropyran
Trt	Trityl
TSTU	N,N,N',N'-Tetramethyl-O-(N-succinimidyl)uronium tetrafluoroborate



# Chapter 1 Introduction

## 1.1 Molecular imaging

Molecular imaging is an interdisciplinary research field with the aim to visualize, characterize and quantify specific biological processes at the molecular and cellular levels in living systems in a non-invasive manner (1-3). Molecular imaging technologies are based on the interaction of different forms of energy with biological tissues and commonly utilize molecular probes to produce the imaging signal. They employ energies within a wide range of spectrum, where electromagnetic or acoustic signals are collected and transformed into images in order to provide spatio-temporal information about certain molecular and cellular processes in living subjects (4-6). Molecular imaging modalities include computed tomography (CT) measuring the absorption of X-rays by biological tissues, single-photon emission computed tomography (SPECT) and positron emission tomography (PET) that detect gamma ray and positron annihilation photons, respectively, magnetic resonance imaging (MRI) that detects radiofrequency radiation, optical imaging techniques such as bioluminescence imaging (BLI) and fluorescence imaging (FLI) that exploit photons in the visible through near-infrared (NIR) part of the electromagnetic spectrum (4), and ultrasound imaging that uses high-frequency acoustic waves. FLI and MRI require excitation process in order to trigger the signal production, while SPECT and PET are based on nuclear radioactive decay to generate the signal. BLI relies on light emission that is produced as a result of special chemical reactions inside living organisms catalyzed by enzymes known as luciferases. In order to interrogate a biochemical process of interest most of the molecular imaging modalities require specific molecular imaging probes (2, 5), therefore the development of novel imaging agents is important for the field of molecular imaging and biomedical research (3, 5).

## 1.2 Optical imaging

Among various molecular imaging techniques used in biomedical research, optical imaging modalities such as fluorescence imaging (FLI) and bioluminescence imaging (BLI) are the most commonly applied for live animal studies due to their high sensitivity, relatively low cost and versatility (4, 6). Both BLI and FLI utilize low energy photons as compared to high-energy imaging modalities such as PET and SPECT, therefore optical imaging is relatively safe (7). Ease of operation, short acquisition times and the possibility of simultaneous imaging of several animals make both BLI and FLI suitable for high-throughput imaging and useful for preclinical research (5). Optical imaging modalities rely on light

detection using highly sensitive systems such as charge-coupled device (CCD) cameras that provide registration of very low levels of photons from ultraviolet (UV) to near-infrared (NIR) range of optical spectrum (5, 8).

### 1.3 Bioluminescence imaging

Bioluminescence (BL) is a natural phenomenon and a form of chemiluminescence, in which the light is produced inside living organisms from an enzymatic oxidation reaction of luciferase enzymes with their substrates, luciferins. The vast majority of bioluminescent organisms is of marine origin and includes luminescent fishes, crustaceans and microorganisms. Click beetles, fireflies, glowworms and some types of fungi represent terrestrial luminescent organisms. These species use BL for various purposes such as locating food, attracting a mate or defending against predators (9-11). BLI is based on this biological phenomenon and represents a valuable tool for non-invasive real-time quantitative analysis of various molecular and cellular processes in cell culture and *in vivo*. Unlike FLI, BLI does not require an external excitation light. In addition, biological tissues do not have endogenous bioluminescence. These factors make BLI highly sensitive and result in higher signal to background ratios as compared to fluorescence (7). Although many different types of luciferase enzymes have been found in nature, only a few of them are utilized for imaging applications. Luciferase-luciferin pairs commonly applied for molecular imaging can be divided into several categories, based on a substrate used for luminescence (**Table 1.1**):

1. Luciferases utilizing D-luciferin. These enzymes isolated from click beetles, North American and Italian fireflies and their engineered analogs oxidize the substrate in the presence of molecular oxygen, ATP and  $Mg^{2+}$  to form oxyluciferin in the excited electronic state that undergoes relaxation to the ground state with light emission at around 600 nm (**Table 1.1**, entries **1-5**). The exact emission wavelength depends on the tertiary structure of the enzyme that determines the internal microenvironment of the luciferase-luciferin complex (12, 13).

2. Luciferases utilizing coelenterazine. These enzymes found in marine species such as *Renilla* or *Gaussia* oxidize the substrate to coelenteramide using molecular oxygen and produce blue-green light (**Table 1.1**, entries **6-8**). These luciferases do not require co-factors such as ATP and therefore can operate extracellularly. *Gaussia* luciferase is a naturally secreted enzyme (14).

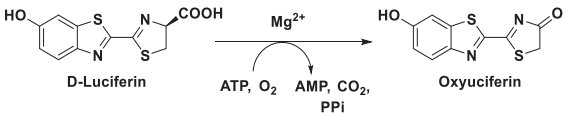
3. Nanoluc luciferase utilizing furimazin. This luciferase was engineered from a native enzyme isolated from the deep sea shrimp, *Oplophorus gracilirostris*. Nanoluc was found to have optimal performance with a synthetic analog of coelenterazine, furimazine that produces blue light upon enzymatic oxidation with molecular oxygen (**Table 1.1**, entry **9**). This engineered luciferase-substrate

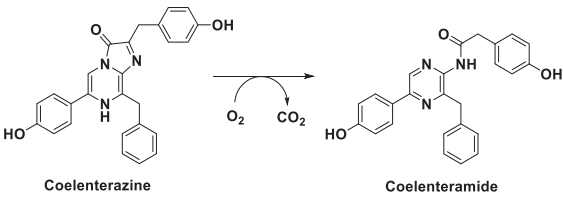
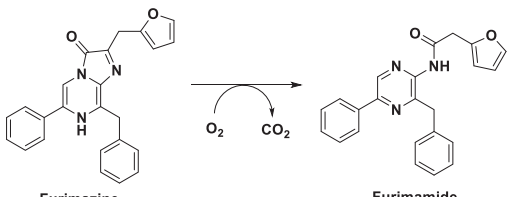
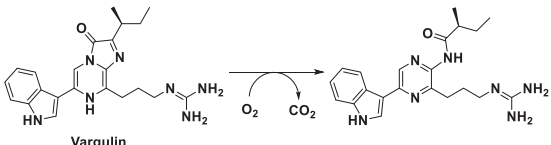
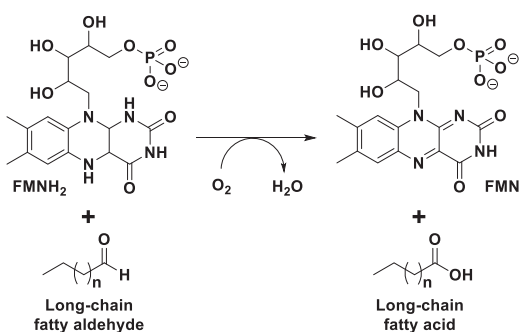
pair generates glow-type luminescence with high intensity, possesses high physical stability and has been applied for *in vivo* imaging (15, 16).

4. *Vargula* luciferase utilizing vargulin. Naturally secreted from cells, the enzyme was found in a small marine organism, *Vargula hilgendorfii*. This luciferase catalyzes oxidation of vargulin by molecular oxygen with emission of blue light (Table 1.1, entry 10) (17). In combination with *Gaussia* and firefly luciferases a codon-optimized variant of *Vargula* luciferase has been applied for trimodal BL *in vivo* imaging (18).

5. Bacterial luciferases LuxAB utilizing reduced flavin mononucleotide (FMNH<sub>2</sub>) and a long-chain aldehyde as substrates. These enzymes are mainly present in marine bacteria (*Vibrio harveyi*), but can also be found in bacteria in terrestrial environment (*Photorhabdus luminescens*). LuxAB luciferases generate light in a two-step mechanism and utilize two substrates. First, reduced flavin mononucleotide (as FMNH<sup>-</sup>) binds to LuxAB followed by oxidation with molecular oxygen and generates a peroxy-intermediate that then reacts with a long-chain aldehyde to produce a second intermediate (peroxyhemiacetal adduct). The latter decays into a carboxylic acid and enzyme bound hydroxyflavin in the excited state that undergoes transition to the ground state with emission of a photon (Table 1.1, entry 11). Bacterial *lux* operon (*luxCDABE*) contains luciferase genes *luxA* and *luxB* as well as the genes that are required for the substrate expression. Hence, *lux* operon encodes all necessary components for luminescence and provides a system that is not dependent on addition of an external luciferase substrate (19, 20).

**Table 1.1** Luciferase-luciferin pairs commonly used for BLI (adapted from (13) and (21)).

	Luciferase	Luciferin	Enzymatic reaction	Emission peak <i>in vivo</i> λ, nm	Ref.
1	North American firefly; <i>Photinus pyralis</i> (FLuc)	D-luciferin	 <p>D-Luciferin + ATP, O<sub>2</sub>, Mg<sup>2+</sup> → Oxyluciferin + AMP, CO<sub>2</sub>, PPi</p>	612	(22)
2	North American firefly; <i>Photinus pyralis</i> red (PpyRE8/9)			618	(23)
3	Click beetle green; <i>Pyrophorus plagiophthalmus</i>			544	(22, 24)
4	Click beetle red; <i>Pyrophorus plagiophthalmus</i>			611	(22, 24)
5	Italian firefly; <i>Luciola italica</i>			610	(25)

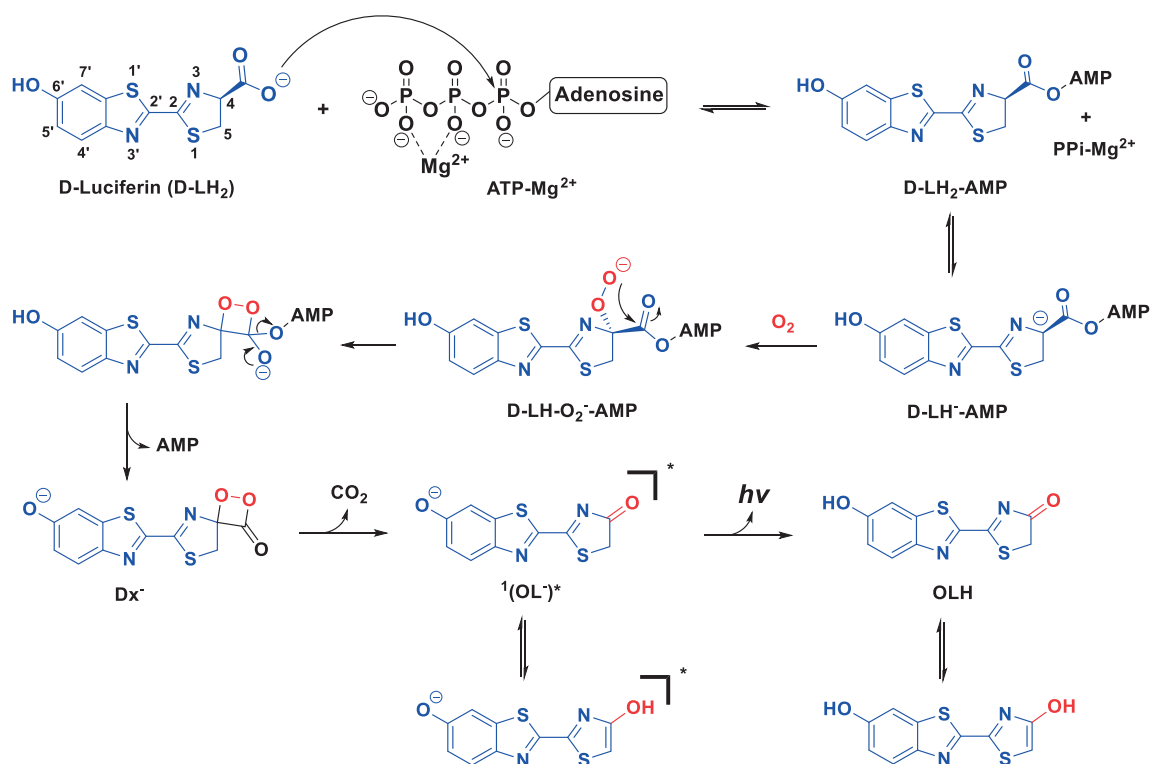
6	<i>Gaussia</i> ; <i>Gaussia princeps</i> (GLuc)	Coelentera -zine		480	(26, 27)
7	Sea pancy; <i>Renilla reniformis</i> (RLuc8)			480	(28)
8	Sea pancy; <i>Renilla reniformis</i> (RLuc8.6-535)			535	(29)
9	<i>Oplophorus gracilirostris</i> (NanoLuc)	Furimazine		460	(15)
10	<i>Vargula hilgendorffii</i> (VLuc)	Vargulin (Cypridinid luciferin)		460	(17, 18)
11	<i>Photorhabdus luminescens</i> (LuxAB)	FMNH <sub>2</sub> + long-chain fatty aldehyde		490	(30)

## 1.4 Firefly luciferase/D-luciferin system

FLuc/D-luciferin pair is the most intensively studied and commonly used BL system for molecular imaging. FLuc is the intracellular enzyme (62 kDa) that catalyzes oxidation of D-luciferin (D-LH<sub>2</sub>) by molecular oxygen with production of light and requires cofactors such as ATP and Mg<sup>2+</sup>.

The enzymatic process starts with the reaction of D-LH<sub>2</sub> with ATP to produce enzyme-bound D-luciferyl-adenylate (D-LH<sub>2</sub>-AMP) due to S<sub>N</sub>2 nucleophilic attack of an oxygen atom of the carboxylate group of D-LH<sub>2</sub> on the electrophilic phosphorous atom of the α-phosphoryl group of ATP with the release of pyrophosphate (PPi) as a leaving group (**Scheme 1.1**). This adenylation reaction proceeds with an involvement of Mg<sup>2+</sup> cations that act as a Lewis acid and form ATP-Mg<sup>2+</sup> complexes, facilitating the S<sub>N</sub>2 nucleophilic attack of the carboxylate due to the influence of Mg<sup>2+</sup> cations on the phosphate groups conformation and partial shielding of the negative phosphate charges. The attachment of AMP to D-LH<sub>2</sub> increases the acidity of C4 carbon in D-LH<sub>2</sub>-AMP and leads to the formation of a carbanion

intermediate (enolate) D-LH-AMP that acts as a nucleophile and attacks molecular oxygen to produce a peroxide anion D-LH-O<sub>2</sub><sup>-</sup>-AMP. Since AMP is a good leaving group, intramolecular nucleophilic substitution of AMP by generated peroxide anion forms a strained four-membered cyclic intermediate, an energy-rich luciferin dioxetanone anion (Dx<sup>-</sup>). This intermediate undergoes spontaneous decarboxylation with the production of oxyluciferin <sup>1</sup>(OL<sup>-</sup>)\* in a singlet excited state, since the energy of decomposition of Dx<sup>-</sup> is sufficient for chemiexcitation of the decomposition product (OL<sup>-</sup>) (31). Relaxation of <sup>1</sup>(OL<sup>-</sup>)\* to the ground state results in the light emission with a broad spectrum (530-640 nm) and maximum intensity *in vitro* around 562 nm at pH 7.5 (**Scheme 1.1**) (32-34). FLuc is a temperature- and pH-sensitive enzyme. Acidic conditions (pH 5-6) shift the emission to the red region of the spectrum (peak maximum shift to 620 nm) as well as diminish the quantum yield (maximal quantum yield 41.0 ± 7.4% was determined at pH 8.5) (35). Higher temperatures and heavy metal cations also shift the BL spectrum to longer wavelengths (32).

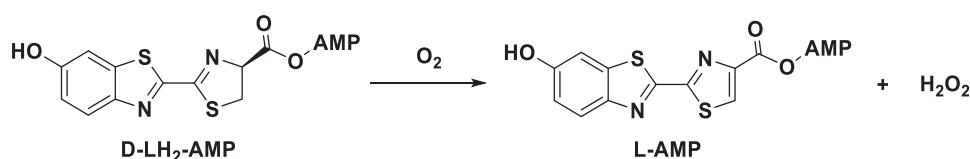


**Scheme 1.1** Mechanism of D-luciferin oxidation catalysed by firefly luciferase that results in bioluminescence (adapted from (33)).

The colour of bioluminescence is determined by conformational changes of FLuc during the reaction, influencing the microenvironment of the active site. The wild-type enzyme undergoes conformational switch of its active site from the open to the closed form during the formation of D-luciferyl-adenylate, resulting in tight binding of the oxyluciferin in the excited state that becomes

surrounded by non-polar microenvironment created by the hydrophobic residue of Ile288 (36). Upon the conformational change Ile288 moves towards the benzothiazole ring of oxyluciferin, consequently minimizing energy dissipation of the excited molecule  $^1(OL^-)^*$  that finally emits yellow-green light. This hypothesis was supported by the fact that the S286N mutant of FLuc was found to keep an open conformation during the catalysis, producing red luminescence. Additionally, analysis of the BL spectra from I288V and I288A mutants demonstrated that the spectral changes correlated with the size and hydrophobicity of the introduced amino acid residues at the position 288 with the shift towards orange and red light respectively. Since less hydrophobic and less rigid microenvironment of the active site allows some energy dissipation from the excited state of oxyluciferin, this results in the spectral changes with emission of lower-energy light (36).

F-Luc also catalyzes a side-reaction, in which D-LH<sub>2</sub>-AMP reacts with molecular oxygen via a dark reaction pathway that produces dehydroluciferyl-AMP (L-AMP) and hydrogen peroxide (**Scheme 1.2**).



**Scheme 1.2** Dark reaction pathway of luciferin-adenylate oxidation catalysed by firefly luciferase.

Both L-AMP and the product of a luminescent oxidation pathway, oxyluciferin, have an inhibitory effect on FLuc with  $K_i$  3.8  $\mu$ M and 0.5  $\mu$ M respectively. These products are responsible for the flash pattern of bioluminescence produced by FLuc/D-luciferin pair *in vitro*, where a fast initial increase in light production is followed by suppression of BL signal to low level within a few seconds (33).

BL produced by FLuc is a stereospecific process, in which only the D-enantiomer of luciferin can be oxidized with light emission, whereas the L-isomer acts as a competitive inhibitor of FLuc ( $K_i$  between 3 and 4  $\mu$ M) (37). However, FLuc is able to adenylate L-luciferin that can further be converted to a CoA derivative by the enzyme. The enolization of the L-luciferyl-CoA derivative leads to racemization and formation of D-LH<sub>2</sub>-CoA that upon hydrolysis yields D-luciferin. This process explains weak luminescence with slow kinetics produced by L-luciferin upon interaction with FLuc and suggests that L-luciferin can be a biosynthetic intermediate in the synthesis of D-luciferin *in vivo*, since cysteine, the presumed precursor of D-luciferin biosynthesis, exists *in vivo* as L-enantiomer (33, 37, 38).



A synthetic luminescent D-luciferin analogue that is widely used for BLI was obtained by replacing the 6'-OH group of D-luciferin by NH<sub>2</sub>-group to generate D-aminoluciferin (AL) (**Figure 1.1**) (39).

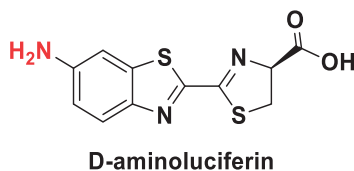


**Figure 1.1** Chemical structure of D-aminoluciferin.

AL emits more red-shifted light with the maximum at 578 nm. Compared to D-luciferin, AL possesses higher affinity for FLuc ( $K_m$  16 and 0.62  $\mu$ M respectively), whereas D-luciferin demonstrates about 10-times higher rate of photon emission ( $V_{max}$ ) *in vitro*, meaning that FLuc has a higher catalytic efficiency for AL (higher value  $V_{max}/K_m$  for AL than for D-luciferin) (40).

## 1.5 Caged luciferin probes for *in vivo* molecular imaging

The presence of the electron-donating 6'-hydroxy or 6'-amino group in the luciferin molecule is crucial for the light generation (39, 41, 42). Modifications at these groups may prohibit the substrate interaction with FLuc resulting in bioluminescence turn off. Specifically, alkylation or acylation of the 6'-hydroxy group of D-luciferin or acylation of the 6'-amino group of D-aminoluciferin abolishes bioluminescence. Analogously, modifications of the carboxylic group of luciferins, such as esterification or amidation, prevent the first step of the BL reaction, the substrate adenylation, and turn off bioluminescence. Therefore, structural transformations of luciferin with installation of appropriate protecting groups (cages) that undergo deprotection with the release of free luciferin only in the presence of a specific enzyme or a small bioactive molecule allow the development of caged-luciferin probes for imaging applications. Such probes can produce BL only upon removal of protecting groups, where the amount of deprotected (uncaged) luciferin, and consequently the light intensity, is proportional to the activity of an enzyme or a small molecule of interest (**Figure 1.2**).

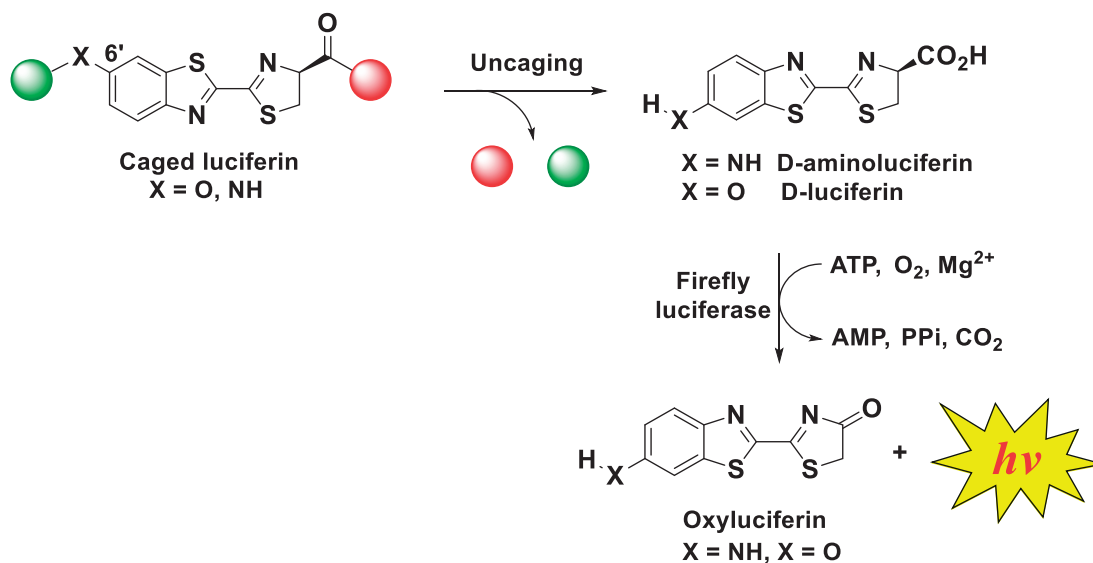


**Figure 1.2** Concept of bioluminogenic (caged luciferin) probes. Chemically modified luciferin with protecting groups (cages) at 6'-hydroxy or 6'-amino position or with a masked carboxylic group does not produce light in the presence of firefly luciferase. A specific enzyme or a small molecule triggers uncaging, which results in generating free luciferin that interacts with luciferase with light emission.

Interestingly, 6'-N-alkylated aminoluciferins still act as substrates for FLuc, which was demonstrated for a series of aminoluciferin derivatives with increasing 6'-N-alkyl chain length, where some analogs emitted stronger luminescence than D-aminoluciferin (43). This N-alkyl aminoluciferin scaffold was shown to be a useful alternative to luciferin for generating bioluminogenic probes (44).

Caged luciferin probes have been developed for *in vitro* and *in vivo* imaging of various enzymes and small molecules either via functionalization of luciferin at the 6'-hydroxy or 6'-amino group or by masking the carboxyl group of luciferin (Table 1.2). First bioluminogenic assays based on caging D-luciferin were reported by Miska et al. for *in vitro* sensing the activity of various enzymes such as alkaline phosphatase, carboxylic esterase, carboxypeptidases A and B and aryl sulfatase. The probes contain corresponding cages at 6'-hydroxy group of luciferin and act as enzyme substrates exhibiting high sensitivity with the detection limit for enzymes between 10 and 500 fg per assay (41, 45). Caging 6'-amino group of D-aminoluciferin with N-acetyl-L-phenylalanine afforded a bioluminogenic probe for  $\alpha$ -chymotrypsin with a detection limit for the enzyme 0.3 ng per assay (Table 1.2, entry 2) (42).

Upon development of luciferase expressing cells and animals the caged luciferin approach was translated from *in vitro* assays to *in vivo* studies, where various bioluminogenic probes have been applied for imaging of enzymatic activity in living mice (Table 1.2, entries 4-11). Caged luciferin probes have been utilized to visualize protease activity *in vivo*, such as activation of caspases, which play important role in the mechanism of apoptosis or programmed cell death and are involved in a number

of pathologies such as cancer and neurodegenerative diseases (46). A bioluminogenic substrate DEVD-aminoluciferin (**Table 1.2**, entry **7**) that is caged at 6'-amino group with amino acid sequence DEVD (Asp-Glu-Val-Asp) via an amide bond is recognized by caspases 3 and 7 and cleaved to produce free D-aminoluciferin. The probe was applied for *in vivo* monitoring of tumor xenografts apoptosis following the chemotherapeutic treatment (46). A conjugate of D-luciferin with a nitrofuryl cage via the 6'-hydroxy group of the former was developed for imaging of nitroreductase (NTR) activity (**Table 1.2**, entry **9**) (47). The reduction of the nitro group of the probe by nitroreductases produces the amino group that leads to cage removal due to 1,6-elimination of D-luciferin acting as a leaving group. The probe was applied for NTR imaging in bacteria, cells and mouse models and it should be useful for preclinical development of enzyme-activatable prodrugs for cancer treatment.

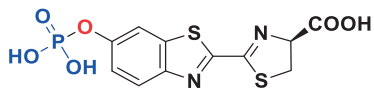
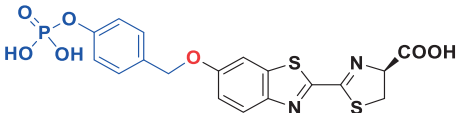
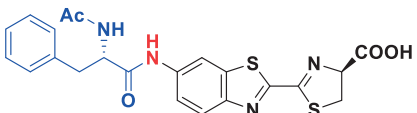
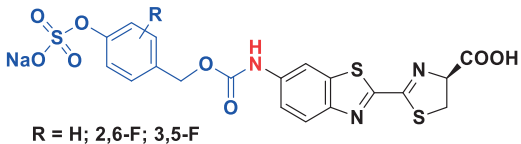
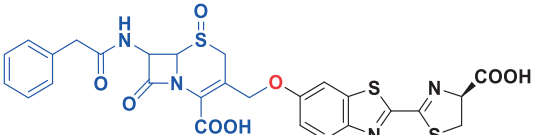
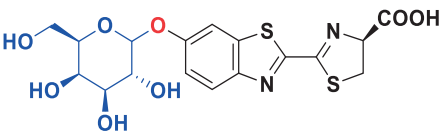
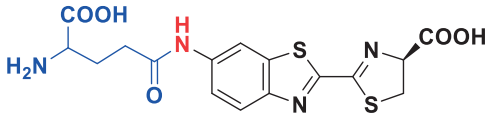
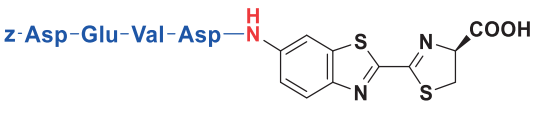
An alternative way for generating caged luciferin probes employs modifications of the carboxylic group of luciferin. This approach was used to create molecular probes for imaging such enzymes as fatty acid amide hydrolase (FAAH), which metabolizes a neurotransmitter anandamide, an agonist of the cannabinoid receptor CB1. FAAH is an appealing drug target for the treatment of certain neurological diseases including pain and anxiety. Nonluminescent luciferin amides (**Table 1.2**, entry **10**) are hydrolyzed to corresponding luciferins by FAAH and allow imaging the enzyme activity in cells and mice (48), which makes the probes useful for *in vivo* screening of FAAH inhibitors.

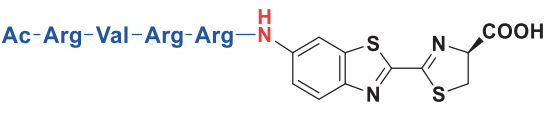
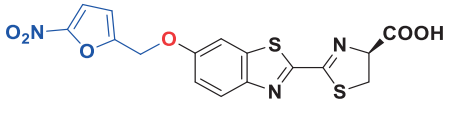
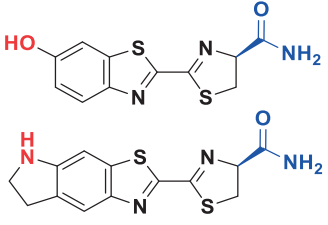
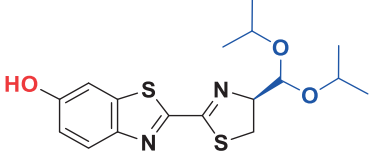
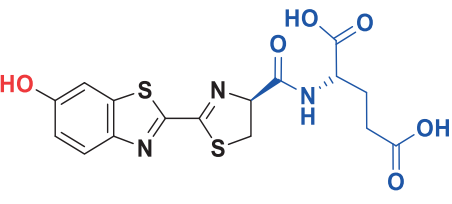
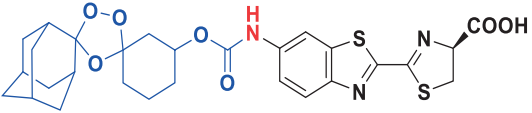
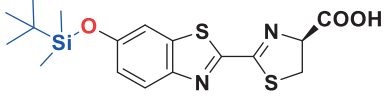
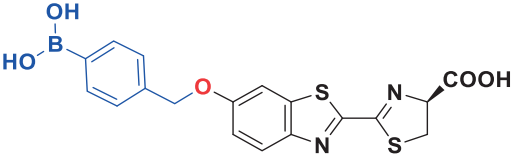
The caged luciferin approach is also used for imaging of bioactive small molecules in living systems (**Table 1.2**, entries **13-21**). Van de Bittner et al. developed a caged luciferin probe via protecting the 6'-hydroxy group of D-luciferin with H<sub>2</sub>O<sub>2</sub>-sensitive aryl boronic acid (**Table 1.2**, entry **15**) that is sensitive to hydrogen peroxide (H<sub>2</sub>O<sub>2</sub>). The probe was applied for *in vivo* imaging of H<sub>2</sub>O<sub>2</sub> production in a tumor xenograft mouse model (49). Caged luciferin probes were also developed for *in vivo* imaging of metal ions. A bioluminogenic probe for iron(II) detection contains endoperoxide cage attached to D-aminoluciferin via a carbamate linker that undergoes metal- and redox-specific Fe<sup>2+</sup>-triggered uncaging with the production of free D-aminoluciferin (**Table 1.2**, entry **13**). The probe was shown to detect physiological changes of labile iron(II) as well as iron accumulation in a mouse model of systemic bacterial infection (50).

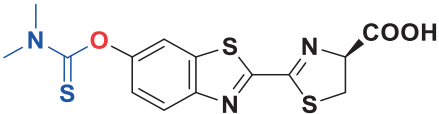
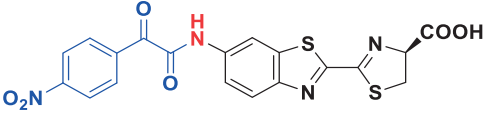
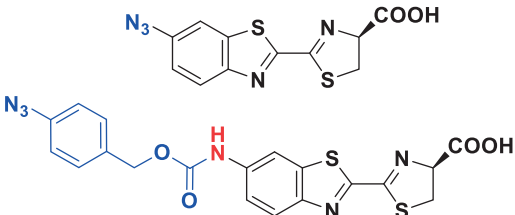
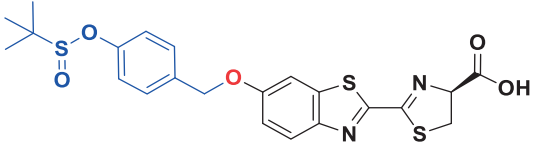
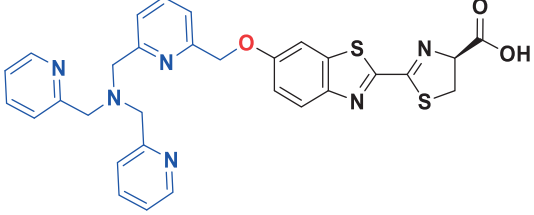
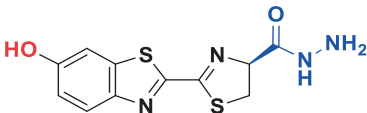
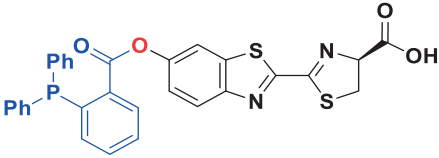
Another application of the luciferin caging strategy is imaging of metabolic processes using the Staudinger ligation. The approach was developed by Bertozzi et al. and relies on utilizing azido-labeled molecules that can react with caged luciferin-phosphine (**Table 1.2**, entry **22**) producing free D-luciferin upon the Staudinger ligation. This strategy was used to image cell-surface glycosylation in live cells following metabolic incorporation of azido sugars in the cellular glycans (51). This approach could

potentially be expanded for imaging of other molecules of interest, provided that a molecule allows incorporation of the azido group.

**Table 1.2** Examples of caged luciferin probes used for molecular imaging of enzymatic activity, small molecules and metabolic events *in vitro* and *in vivo*.

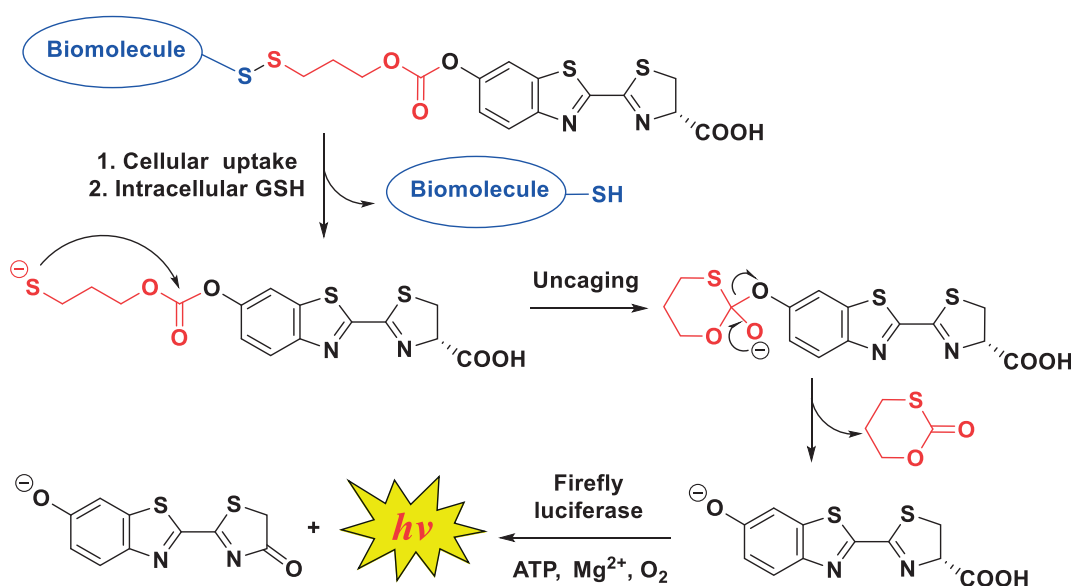
	Caged luciferin	Imaging target	Application	Ref.
<b>I. Imaging of enzymatic activity</b>				
	<b>Caging at 6'-position of luciferin</b>			
1		Alkaline phosphatase	<i>In vitro</i>	(41, 45)
				(52)
2		$\alpha$ -Chymotrypsin	<i>In vitro</i>	(42)
3	 R = H; 2,6-F; 3,5-F	Sulfatase	<i>In vitro</i>	(53)
4		$\beta$ -Lactamase	<i>In vitro, in vivo</i>	(54)
5		$\beta$ -Galactosidase	<i>In vitro, in vivo</i>	(55, 56)
6		$\gamma$ -Glutamyl transpeptidase	<i>In vitro, in vivo</i>	(57)
7		Caspase-3/7	<i>In vitro, in vivo</i>	(46, 58)

8		Furin	<i>In vitro, in vivo</i>	(59)
9		Nitroreductase	<i>In vitro, in vivo</i>	(47)
<b>Caging via masking the carboxyl group of luciferin</b>				
10		Fatty acid Amide hydrolase	<i>In vitro, in vivo</i>	(48)
11		Cytochrome P450	<i>In vitro, in vivo</i>	(60, 61)
12		Carboxy- peptidase G	<i>In vitro</i>	(62)
<b>II. Imaging of small molecules</b>				
<b>Caging at 6'-position of luciferin</b>				
13		Fe <sup>2+</sup> (Iron(II))	<i>In vitro, in vivo</i>	(50)
14		F <sup>-</sup> (Fluoride)	<i>In vitro, in vivo</i>	(63)
15		H <sub>2</sub> O <sub>2</sub> (Hydrogen peroxide)	<i>In vitro, in vivo</i>	(49)

16		$\text{ClO}^-$ (Hypochlorite)	<i>In vitro,</i> <i>in vivo</i>	(64)
17		$\text{ONOO}^-$ (Peroxynitrite)	<i>In vitro,</i> <i>in vivo</i>	(65)
18		$\text{H}_2\text{S}$ (Hydrogen sulfide)	<i>In vitro,</i> <i>in vivo</i>	(66, 67)
19		RSH (Intracellular thiols)	<i>In vitro</i> (cellular assays)	(68)
20		$\text{Cu}^+$ (Copper(I))	<i>In vitro,</i> <i>in vivo</i>	(69)
<b>Caging via masking the carboxyl group of luciferin</b>				
21		$\text{Cu}^{2+}$ (Copper(II))	<i>In vitro,</i> <i>in vivo</i>	(70)
<b>III. Imaging of metabolic processes using the Staudinger ligation</b>				
<b>Caging at 6'-position of luciferin</b>				
22		Cell surface glycosylation (azido glycans)	<i>In vitro</i> (cellular assays)	(51)

The caged luciferin strategy has also been applied to monitor cellular uptake of biomolecules in cells and animals. An uptake probe consists of a biomolecule of interest that is conjugated to a caged

D-luciferin via a disulfide-carbonate linker. Once such a conjugate is taken up by cells, it encounters a high intracellular concentration of glutathione (GSH) that triggers the reduction of the disulfide bond (**Figure 1.3**). Generated thiolate intramolecularly attacks the carbonate group with the intracellular release of free D-luciferin, followed by its oxidation catalyzed by luciferase and light emission (71). This approach allows for measurement of real-time cellular uptake kinetics of biomolecules, provided that the conjugation with D-luciferin does not drastically change their biological properties and the uptake by cells.

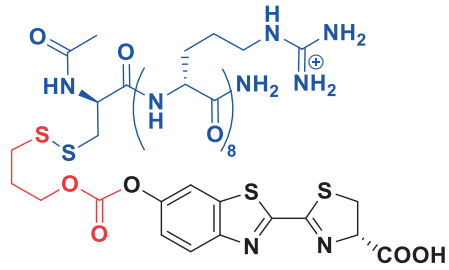
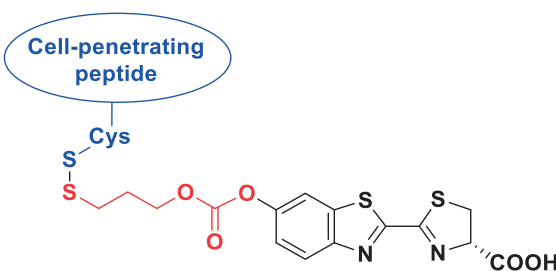
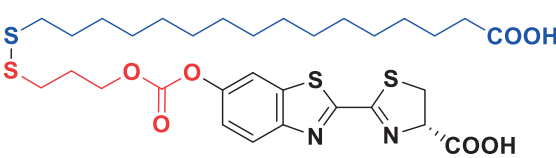


**Figure 1.3** Bioluminescent approach for monitoring cellular uptake of biomolecules using caged luciferin strategy.

The reported examples of the application of this strategy include the uptake studies of cell-penetrating peptides and long-chain fatty acids (**Table 1.3**, entries 1-2). Henkin et al. developed the conjugate of caged luciferin with palmitic acid (**Table 1.3**, entry 2) for real-time imaging of fatty acid uptake in luciferase expressing cells and mice (72). The probe was first validated in luciferase expressing cells, where it showed the competition with oleic acid for cellular uptake in 3T3-L1 adipocytes as well as it exhibited increased uptake in HEK293 cells following the transient expression of the fatty acid transporter FATP5, demonstrating the cellular uptake behavior similar to that of natural long-chain fatty acids. The probe was further orally gavaged in luciferase expressing mice to determine the intestinal site of fatty acid absorption. Additionally, the fatty acid-luciferin probe was administered to mice to image the metabolic activation of brown adipose tissue (BAT), since long-chain fatty acids act as a main energetic substrate for BAT (72). Lynes et al. successfully employed the fatty acid-luciferin probe to prove the metabolic effects of a novel BAT activator 12,13-dihydroxy-9Z-

octadecenoic acid (12,13-diHOME) in a transgenic mouse model that expresses luciferase specifically in BAT (73).

**Table 1.3** Examples of caged luciferin probes used to monitor cellular uptake of biomolecules.

	Caged luciferin	Imaging target	Application	Ref.
1	 <p>Octaarginine-luciferin</p>	Peptide uptake	<i>In vivo</i>	(71, 74, 75)
			<i>In vitro</i> (cellular assays)	(76-78)
2	 <p>Fatty acid-luciferin</p>	Long-chain fatty acid uptake	<i>In vivo</i>	(72, 73)

## 1.6 Fluorescence imaging

Another optical imaging modality that allows for obtaining relevant biological information from living organisms is fluorescence imaging (FLI). FLI employs molecules called fluorophores that can absorb photons with a specific energy to reach the excited electronic state followed by returning to the ground state with fluorescence emission. Fluorescence imaging is a very sensitive modality, as it requires as low as  $10^{-9}$  –  $10^{-12}$  M concentrations of fluorescent probes to obtain detectable signal (5). The process of energetic transitions of molecules that result in fluorescence is described by Jablonski diagram (Figure 1.4).



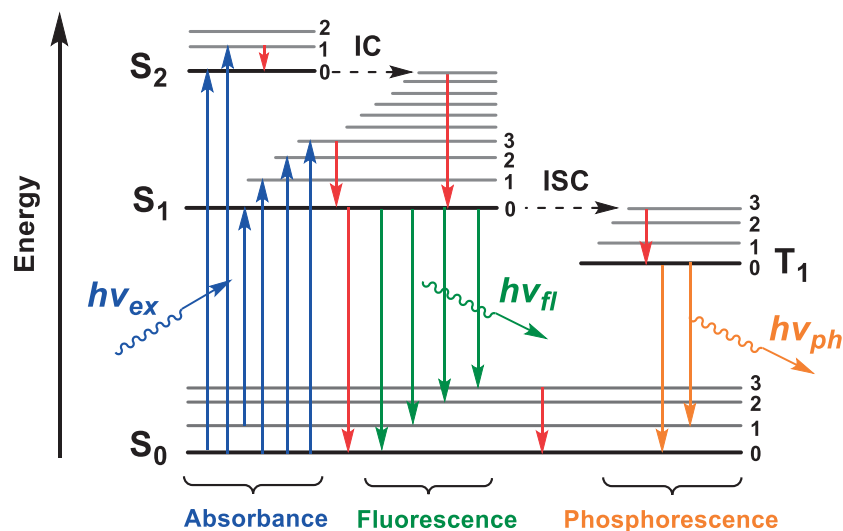


**Figure 1.4** Simplified Jablonski diagram representing the energy transitions for fluorophores following light absorption.  $S_0$  – the ground electronic singlet state,  $S_1$  and  $S_2$  – the first and the second electronic singlet states respectively,  $T_1$  – the lowest excited triplet state. IC – internal conversion, ISC – intersystem crossing.  $h\nu_{ex}$  – excitation light,  $h\nu_{fl}$  – fluorescence emission,  $h\nu_{ph}$  – phosphorescence emission. Blue, green, orange and red arrows represent energy transitions leading to excitation, fluorescence emission, phosphorescence emission and non-radiative (vibrational) relaxation respectively. Numbered levels represent vibrational states for each electronic energy level (adapted from (79) and (80)).

When a fluorescent molecule absorbs a photon, the photon's energy ( $E = h \times c/\lambda$ , where  $c$  and  $\lambda$  are speed of light in vacuum and the wavelength of a photon absorbed respectively and  $h$  is Planck's constant) is transmitted to the fluorophore, which results in its transition from the ground electronic singlet state  $S_0$  to one of the excited singlet states  $S_1$  or  $S_2$ . If the energy provided by a photon is higher than the minimal energy required for the transition from  $S_0$  to  $S_1$  or  $S_2$ , the molecule will occupy one of the vibrational levels of  $S_1$  or  $S_2$ . Such a transition occurs in femtoseconds ( $10^{-15}$  s) (79). The absorption spectrum of a fluorophore represents the energy transitions that happen during the excitation process, where the molar extinction coefficient of a molecule  $\epsilon$  shows the probability of light absorption, when it passes through a solution of a fluorophore. Organic molecules used for fluorescence imaging have  $\epsilon$  values in the range between 100000 and 200000  $M^{-1} \times cm^{-1}$  (81).

Following a photon absorption an excited molecule will release the absorbed energy and return to the ground state  $S_0$  via several distinct pathways. The first mechanism to take place after excitation is the internal conversion (IC) that allows isoenergetic transition from low vibrational levels of one electronic state to higher vibrational levels of a lower electronic state (e.g. transition from  $S_2$  to  $S_1$ ) (Figure 1.4). After this, the energy excess is dissipated to the environment through vibrational relaxation resulting in the energy transition to the lowest vibrational level of  $S_1$ . Internal conversion may continue further to bring the molecule back to the ground state  $S_0$ . Internal conversion and

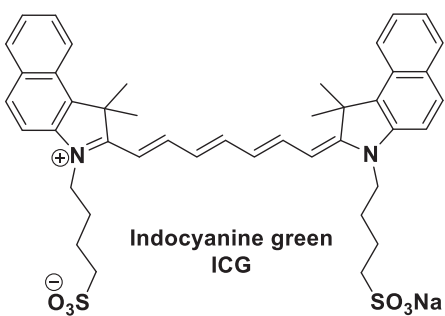
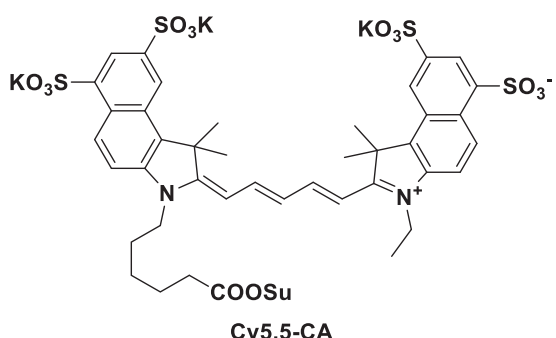
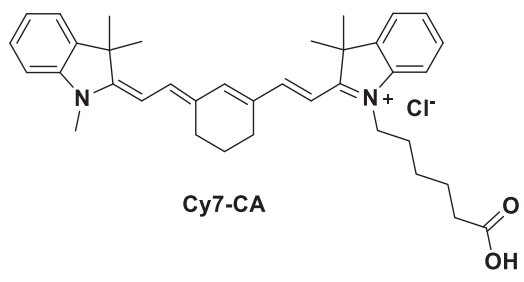
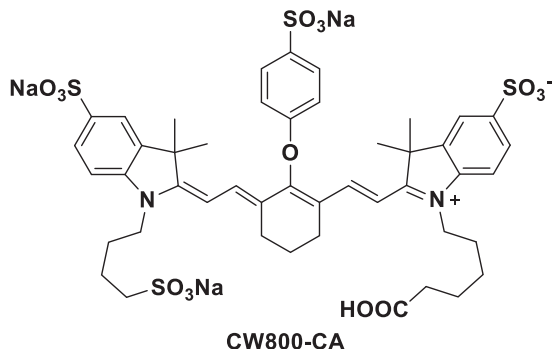
vibrational relaxation are nonradiative transitions that occur in picoseconds ( $10^{-12}$  s). Once the molecule reaches the lowest vibrational level of  $S_1$ , it can also undergo the transition to  $S_0$  through radiative process. There are two possible pathways of radiative relaxation: fluorescence and phosphorescence. Fluorescence results from energy transitions to one of the vibrational levels of the ground state  $S_0$  and takes place in nanoseconds ( $10^{-9}$  s). Phosphorescence requires first intersystem crossing (ISC) via forbidden isoenergetic transition to a vibrational level of the lowest excited triplet state  $T_1$  ( $S_1 \rightarrow T_1$ ), where an electron has to change its spin, and consequently has a low probability. Following vibrational relaxation to the lowest vibrational level of  $T_1$  the molecule can undergo radiative transition to one of vibrational levels of the ground singlet state  $S_0$  ( $T_1 \rightarrow S_0$ ) that is called phosphorescence (**Figure 1.4**). This transition is forbidden and has low probability. Phosphorescence lifetimes can vary from microseconds ( $10^{-6}$  s) to seconds (79, 80). As a molecule emits fluorescence from the lowest vibrational level of  $S_1$ , the emitted photons have longer wavelengths than the absorbed photons (Stokes shift), since the excess of energy is released through vibrational relaxation during de-excitation to the lowest vibrational mode of  $S_1$ . Fluorophores in the triplet state can be subjected to photochemical reactions leading to phototoxicity and irreversible bleaching.

## 1.7 Near-infrared fluorescence

Since fluorescence imaging requires both excitation and emission photons to travel through biological tissues, one has to take into account optical properties of tissues in order to choose suitable fluorophores with optimal spectral parameters. Biological systems interact with light leading to light absorption and scattering by endogenous molecules such as water, haemoglobin and lipids, which limits the penetration depth of photons. Additionally, native tissues produce strong autofluorescence within ultraviolet ( $< 400$  nm) and visible (400-650 nm) regions of the spectrum, which significantly complicates utilization of fluorophores that absorb and emit light within these regions. However, fluorescent dyes with excitation and emission wavelengths within the near-infrared (NIR) region that spans the part of the optical spectrum between 650 nm and 900 nm are suitable for *in vivo* imaging. For NIR photons the tissue absorption coefficient is much lower, since hemoglobin and water have the minimal absorbance in the NIR region. As a result, NIR light penetrates deeper into biological tissues. In addition, NIR light has lower scattering, because the scattering intensity is a function of the inverse fourth power of the wavelength ( $1/\lambda^4$ ). Moreover, tissue autofluorescence also achieves its minimum within the NIR window (5, 81-83). Altogether, these properties of NIR fluorescence allow for deeper tissue imaging and improve signal to background ratio (SBR).

The most commonly used NIR fluorophores are small organic molecules (**Table 1.4**). They are used as free dyes (indocyanine green) or as conjugates to targeting moieties such as proteins, peptides, antibodies, antibody fragments or small molecules.

**Table 1.4** Selected examples of near-infrared organic fluorescent dyes for *in vivo* imaging applications (adapted from (84)).

	Fluorophore	$\lambda_{\text{abs}}$ , nm	$\lambda_{\text{em}}$ , nm	$\epsilon$ , $\text{M}^{-1}\cdot\text{cm}^{-1}$	Quantum yield, %
1	 <p>Indocyanine green ICG</p>	807	822	121000	9.3
2	 <p>Cy5.5-CA</p>	680	697	166000	21.0
3	 <p>Cy7-CA</p>	743	767	196000	16.8
4	 <p>CW800-CA</p>	786	800	237000	14.2

Besides organic fluorescent molecules, there is another type of near-infrared fluorescent imaging agents such as inorganic semiconductor nanocrystals or quantum dots. These agents consist of such elements as Cd, Zn, S, Se and Te. Quantum dots have a core-shell structure surrounded by organic coating and emit fluorescence with a high quantum yield and a narrow fluorescence bandwidth (25-35 nm) being resistant to photobleaching (85, 86). However, these fluorescent agents have limitations for *in vivo* applications due to their large size (hydrodynamic diameter 3-20 nm), which hampers their clearance by renal filtration resulting in high background. Moreover, they consist of toxic inorganic materials, which may lead to systemic toxicity. Quantum dots may also form aggregates in the bloodstream and compromise microcirculation. All these drawbacks significantly limit the potential of quantum dot-based imaging agents for clinical translation (85, 87).

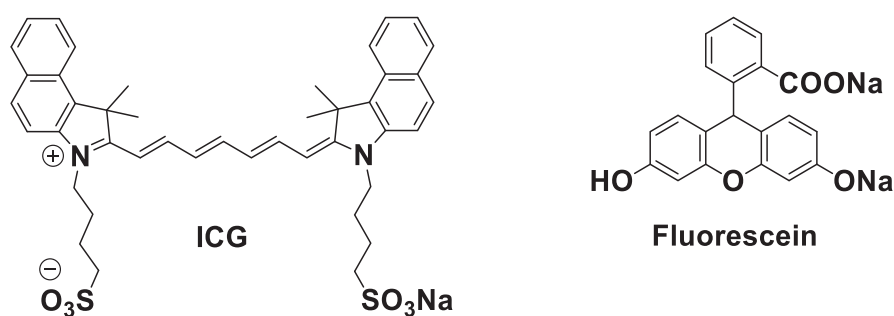
## Chapter 2    Fluorescent Fatty Acid Probe for Non-Invasive *in Vivo* Imaging of Glioma

Malignant glioma is a highly invasive primary brain cancer with poor prognosis despite active treatment, which accounts for up to 80% of primary brain tumors (88). This type of tumor is characterized by high aggressiveness and invasiveness. Glioblastoma multiform (GBM), a grade IV glioma, is the most common and most aggressive manifestation of glioma with a median survival time from 9 to 12 months (89). GBM is characterized by rapid malignant progression with very high resistance to therapy. Glioblastoma extensively invades into surrounding healthy brain tissues and tends to recur adjacent to resection margins. Maximal surgical resection of glioma is associated with a longer remission period and increased survival of patients with both low-grade and high-grade gliomas (90, 91). Intraoperative fluorescence imaging based on employing specific imaging agents for tumor targeting can provide real-time precise visualization of tumor tissues during surgical treatment and has a potential to become a state-of-the-art technology that enables maximal efficiency of brain tumor resection (91, 92).

### 2.1    Fluorescent probes for glioma imaging

Several types of fluorescent imaging agents have been developed for glioma imaging in preclinical settings. However, a very limited number of imaging probes have been applied in clinical studies in humans. Fluorescent probes for potential image-guided glioma surgery can be classified into three groups based on the mechanism of action: 1) passive probes, 2) activity-based or metabolic probes, and 3) affinity-based molecular probes (90, 91, 93). Probe accumulation in tumors can often result from a combination of these mechanisms.

Passive probes accumulate in tumor tissues due to a diffusive mechanism, which is also called enhanced permeability and retention (EPR) effect (94, 95). Solid tumors are characterized by extensive angiogenesis, defective and leaky vasculature and impaired lymphatic drainage that lead to the EPR effect for lipid molecules and macromolecules (96). Indocyanine green (ICG) and fluorescein are examples of passive fluorescent probes for glioma imaging (**Figure 2.1**) (97, 98). ICG is a small fluorescent dye with absorption around 800 nm and emission around 820-830 nm in tissue (99, 100). Since ICG absorbs and emits near-infrared light, it has favourable optical properties for deeper tissue



The second group of probes includes metabolic or activity-based probes that provide fluorescent signal in tumors due to their transformation from a non-fluorescent state into a fluorescent state as a result of upregulation of a certain metabolic process in the tumor tissue. The most widely studied metabolic agent for image-guided surgery of glioma is 5-aminolevulinic acid (5-ALA) (103), which was approved for visualization of malignant tissue during glioma surgery by the U.S. Food and Drug administration in 2017. This agent is a natural metabolic intermediate in the heme biosynthesis. In the tissues, 5-ALA is metabolised into the red fluorescent molecule protoporphyrin IX (PpIX) with the excitation peak at 405 nm and two emission peaks at 635 nm and 710 nm (**Figure 2.2**) (91). Following oral administration of 5-ALA malignant brain tumors exhibit increased accumulation of the endogenous fluorophore PpIX, however, the detailed mechanism of enhanced PpIX synthesis in tumor cells is not completely understood (99, 104). Compromised blood-brain barrier was suggested as one of key factors for selective accumulation of 5-ALA in gliomas (105). 5-ALA-induced PpIX formation was more prominent in higher-grade gliomas compared to low-grade gliomas (99). Glioma surgery guided by fluorescence from 5-ALA derived PpIX allows more complete removal of malignant tissues and results in increased progression-free survival of patients (103). The PpIX fluorophore has drawbacks such as photobleaching and the requirement of blue light for excitation that limits tissue depth penetration (99). Additionally, 5-ALA may not provide sufficient fluorescence for detecting low-grade gliomas (91).

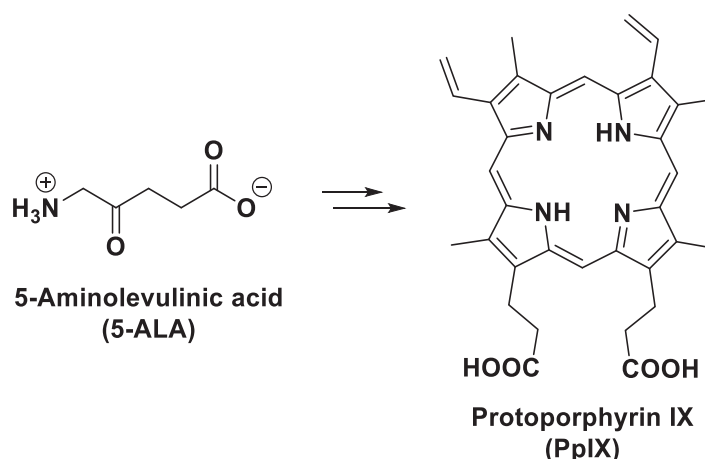


**Figure 2.2** 5-Aminolevulinic acid (5-ALA) is a metabolic precursor of fluorescent protoporphyrin IX (PpIX) for glioma imaging.

Another example of an activity-based agent for glioma imaging is a fluorogenic probe, named GB119, which was investigated in a mouse model. The probe activation is triggered by cysteine protease cathepsin-L, which is upregulated in glioma cells. GB119 contains a Cy5 fluorophore linked to a quencher QSY 21 via a peptide substrate that specifically targets cathepsin-L. Interaction of the probe with the enzyme results in a bond rearrangement and release of the quencher, followed by fluorescence turn on and covalent binding of the fluorophore to the enzyme (106). Topical application of the probe in a mouse model allowed glioma visualization and identification of residual malignant cells after tumor resection (107).

The third group of probes for glioma imaging includes affinity-based molecular agents. These probes selectively bind to tumor tissues via recognizing specific molecular targets on a cell surface or inside the tumor cells (91, 102). Such probes consist of a recognition part (small molecule, peptide, antibody or antibody fragment) that is responsible for selective binding to a molecular target and a fluorescent dye conjugated to the recognition element via a linker. An example of affinity-based agents utilizing a small molecule as a targeting moiety for glioma imaging is a near-infrared fluorescent probe named CLR1502 (108, 109). This probe is an alkylphosphocholine derivative containing a near-infrared cyanine dye that has an increased uptake into various cancer cells including glioma. CLR1502 probe was tested in a glioblastoma xenograft mouse model and demonstrated higher tumor-to-normal brain ratio in comparison to 5-ALA. However, the probe requires administration *in vivo* four days before imaging (109).

Another example of an affinity-based imaging probe for glioma is an antibody-fluorophore conjugate cetuximab-IRDye 800 CW that binds to the epidermal growth factor receptor (EGFR) (110).

## 2.2 Results

### 2.2.1 Probe design

Tumors are known to have an increased *de novo* synthesis of fatty acids due to expression of high levels of fatty acid synthase (111). Some tumors may have upregulated uptake of extracellular fatty acids. It has been demonstrated that hypoxia, which is a predominant feature of glioblastoma (112), leads to upregulation of fatty acid binding proteins 3 and 7 (FABP3, FABP7) in tumor cells and suppression of *de novo* fatty acid synthesis, which results in glioblastoma dependency on fatty acid uptake from the circulation (113). In addition, Lin et al. have recently demonstrated that proliferation of malignant glioma cells requires fatty acid oxidation, whereas the majority of acetyl-CoA in these cells is not produced from glucose sources, suggesting that fatty acids may act as metabolic substrates for glioma *in vivo* (114). Thus, fatty acids may be envisioned as potential targeting molecules for the development of probes for glioma imaging.

The strategy for design of a molecular probe that can represent cellular uptake of natural fatty acids and be applied for *in vivo* fluorescence imaging was based on the conjugation of a near-infrared (NIR) fluorophore indocyanine green (ICG) to a long-chain fatty acid palmitic acid (Figure 2.3).

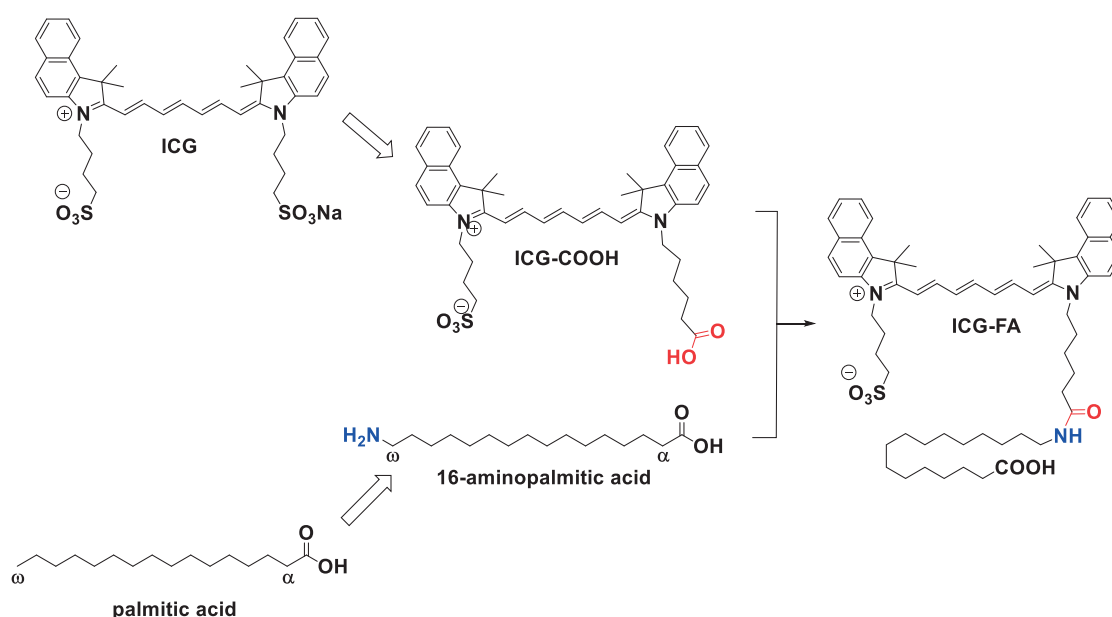


**Figure 2.3** Design of ICG-FA probe.

Since ICG lacks functional groups that enable its conjugation to other molecules, a monocarboxylic ICG analog (ICG-COOH) was synthesized and utilized as a building block for the probe synthesis. For the fatty acid part, an amino analog of palmitic acid was synthesized and conjugated to ICG-COOH via the amide bond to give the final probe ICG-FA (Figure 2.3).



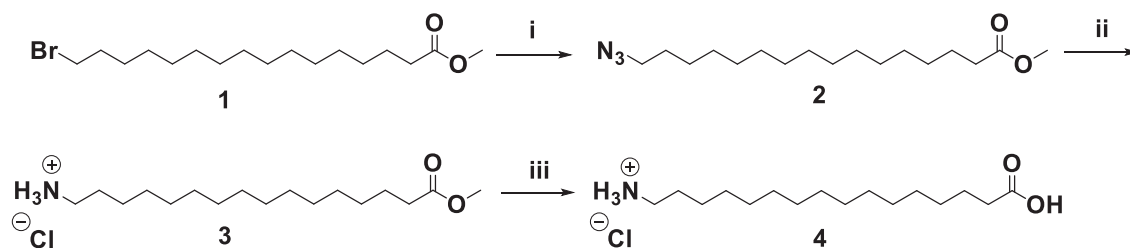
The choice of the  $\omega$ -carbon atom of palmitic acid for the attachment of the ICG fluorophore was based on the structural requirements for substrates of fatty acid transport proteins, since they tolerate chemical modifications of long-chain fatty acids at the end of the aliphatic chain (72, 115). Fluorescent analogs of long-chain fatty acids containing fluorophores such as BODIPY or NBD at the  $\omega$ -carbon atom are taken up by cells similarly to natural fatty acids and utilized as fatty acid probes for cellular studies (115-120). However, BODIPY- and NBD-based fatty acid probes cannot be applied for *in vivo* imaging because of their unsuitable spectral properties, since they absorb and emit light in the visible range of the electromagnetic spectrum.

ICG has been chosen as a fluorescent dye for the probe development due to its optical properties, as it absorbs and emits light within the near-infrared region of 650-900 nm (the absorption and emission maxima of ICG in plasma are 805 or 807 nm and 822 nm respectively) (100, 121). Since NIR light has minimal absorption by biological tissues and tissue autofluorescence is low within the NIR region, fluorophores such as ICG enable deeper tissue imaging and provide much better signal-to-noise ratio compared to fluorophores that absorb and emit light in the visible range of the spectrum. These optical properties make ICG suitable for *in vivo* imaging (83, 100, 122, 123). In addition, ICG is the only 800 nm NIR fluorophore, which was approved by the Food and Drug Administration and European Medicines Agency (EMA) for clinical applications (100, 124-126). Moreover, ICG is a suitable contrast agent for optoacoustic imaging due to the partial conversion of its excitation energy into optoacoustic waves (ICG quantum yield in plasma 9.3% (100)) that could be detected and processed into high-resolution images (127-129). Therefore, ICG-based molecular probes including ICG-FA can be applied for both optical and optoacoustic imaging.

### 2.2.2 Probe synthesis

Convergent synthesis of **ICG-FA** proceeded in 9 steps, which included the synthesis of 16-aminopalmitic acid (**4**) and an ICG derivative (**9**) containing a carboxylic group. The conjugation of (**4**) and (**9**) via amide bond formation led to the final probe **ICG-FA** (**11**).

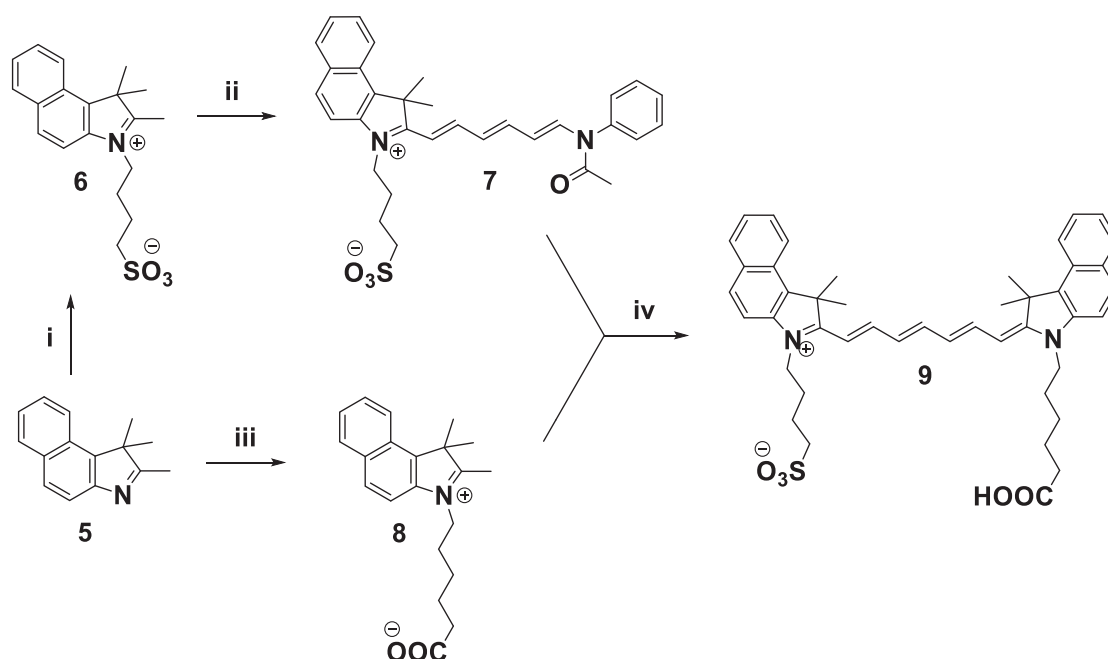
16-Aminopalmitic acid (**4**) was synthesized in three steps (96% overall yield) as a hydrochloride salt (**Scheme 2.1**).



**Scheme 2.1** Synthesis of 16-aminopalmitic acid (4). (i)  $\text{NaN}_3$ , DMF,  $90^\circ\text{C}$ , 14 h; (ii)  $\text{H}_2$  (1 atm), 5% Pd/C, MeOH, 6 M HCl (aq.), 4 h; (iii) 1. NaOH,  $\text{H}_2\text{O-MeOH}$ , 12 h; 2. HCl (aq.).

First, methyl 16-bromohexadecanoate (**1**) was reacted with  $\text{NaN}_3$  in DMF to produce azido ester (**2**) in 99% yield, which was subsequently reduced by Pd-catalyzed hydrogenation in the presence of HCl (aq.) to afford amino ester (**3**). Addition of HCl was found to be essential to obtain the product (**3**), since in the absence of HCl the catalytic reduction of azido ester (**2**) led to the formation of a significant amount of a secondary amine as a result of a reductive dimerization (130, 131). Hydrolysis of amino ester (**3**) by aqueous NaOH followed by acidification afforded the final amino fatty acid (**4**) as hydrochloride salt (97% yield over two last steps).

A monocarboxylic analog of ICG (**9**) was synthesized in four steps (Scheme 2.2).

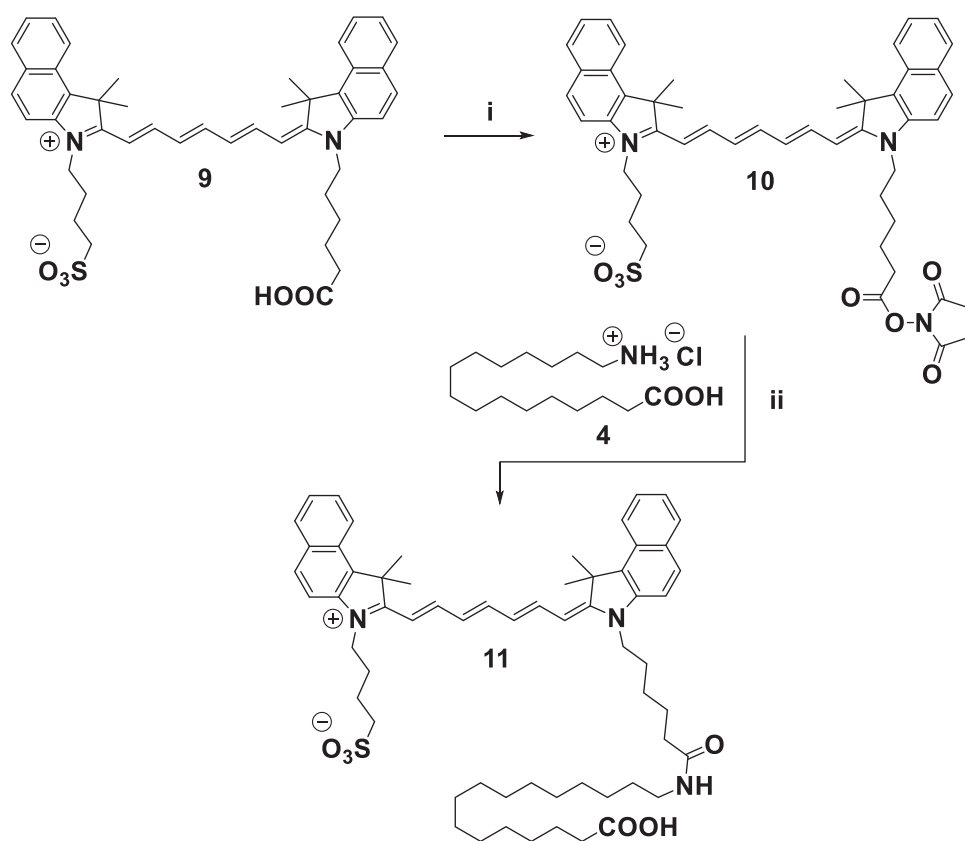


**Scheme 2.2** Synthesis of ICG-COOH (**9**). (i) 1,4-butane sultone,  $130^\circ\text{C}$ , 3 h; (ii) *N*-[5-(phenylamino)-2,4-pentadienylidene]aniline monohydrochloride,  $\text{Ac}_2\text{O}$ ,  $100^\circ\text{C}$ , 1.5 h; (iii) 6-bromohexanoic acid,  $\text{CH}_3\text{NO}_2$ , MW,  $150^\circ\text{C}$ , 2 h; (iv) pyridine,  $40^\circ\text{C}$ , 30 min.

First, 1,1,2-trimethyl-1H-benzo[e]indole (**5**) was alkylated with 1,4-butane sultone to produce sulfonate (**6**) in 67% yield. Sulfonate (**6**) underwent a condensation reaction with *N*-[5-(Phenylamino)-

2,4-pentadienylidene]aniline monohydrochloride in acetic anhydride to give hemicyanine (**7**) in 76% yield. It has been reported that the synthesis of quaternary heterocyclic *N*-alkyl ammonium salts can be facilitated by the microwave irradiation, which allows reducing reaction times and also promotes reactions when *N*-halogenalkylcarboxylic acids are utilized as alkylating agents [3, 4]. This approach was employed to synthesize the second fragment of the ICG moiety containing *N*-alkylcarboxylic group (**8**). Specifically, 1,1,2-trimethyl-1H-benzo[*e*]indole (**5**) was alkylated by 6-bromohexadecanoic acid in nitromethane in a sealed tube under microwave irradiation to afford the product (**8**) after 2 h in 62% yield. Condensation of compound (**8**) with hemicyanine (**7**) in pyridine under mild heating resulted in the monocarboxylic analog of ICG (**9**) in 62% yield.

For the conjugation of aminopalmitic acid (**4**) to the monocarboxylic ICG analog (**9**), the latter was first converted into *N*-hydroxysuccinimide derivative (**10**) upon treatment with *N,N,N',N'*-tetramethyl-*O*-(*N*-succinimidyl)uronium tetrafluoroborate (TSTU) (Scheme 2.3).



**Scheme 2.3** Synthesis of ICG-FA (**11**). (i) TSTU, DIPEA, DMF, 30 min; (ii) 16-aminopalmitic acid **4**, DIPEA, DMSO, 24 h.

Then, the resultant NHS-ester (**10**) was reacted in the same flask with aminopalmitic acid hydrochloride (**4**) in the presence of DIPEA to give ICG-FA probe (**11**) in 74% yield after reverse-phase chromatographic purification.

### 2.2.3 Optical properties of ICG-FA probe

Free ICG is known to bind to plasma proteins, which shifts the absorption spectrum about 25 nm towards longer wavelengths from 780 nm to 805 nm (100, 121, 132) and leads to chemical stabilization of the dye (133). Similarly, ICG binding to plasma proteins shifts the emission peak (126). For absorption and emission spectra measurements, ICG-FA probe was dissolved in PBS in the presence of bovine serum albumin (BSA). ICG-FA demonstrated two absorption peaks, the lower at 730 nm and the higher at 800 nm (**Figure 2.4a**) being similar to the absorption spectrum of ICG in plasma that has two absorption maxima at 730 nm and 805 nm (121). Free fatty acids are known to bind to serum albumin, which acts as a transport vehicle for them in the bloodstream (134-136). This suggests that ICG-FA also binds to albumin, which leads to decrease of the probe aggregation in aqueous solutions. Irradiation of ICG-FA solution by NIR light at 731 nm resulted in fluorescence with the peak maximum at 818 nm (**Figure 2.4b**) that is similar to the observed emission maximum of ICG in serum at 822 nm (100).

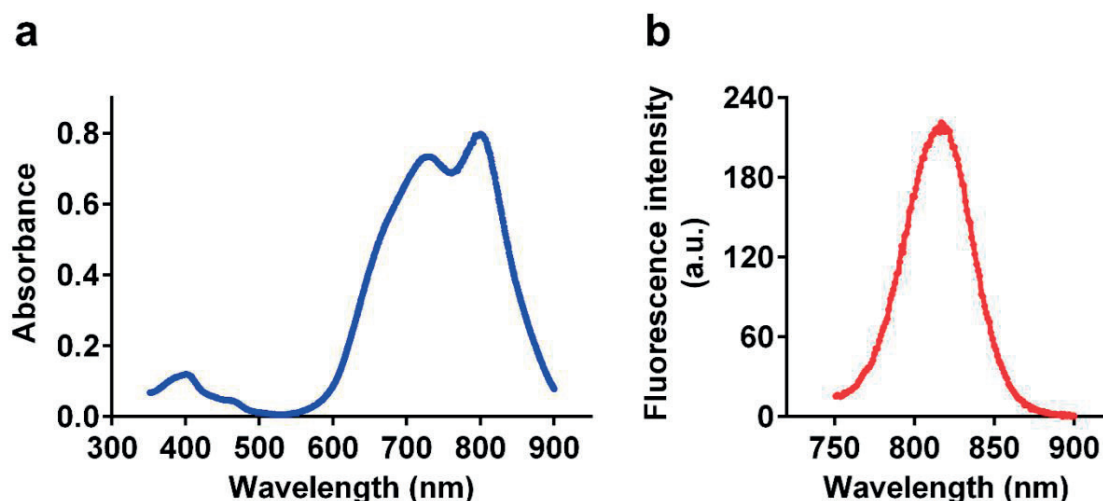


**Figure 2.4** Optical properties of ICG-FA. Absorption (a) and emission (b) spectra of 10  $\mu$ M ICG-FA dissolved in PBS containing 0.1% fatty acid free BSA. The emission spectrum was obtained by excitation at 731 nm. a.u., arbitrary units.

### 2.2.4 ICG-FA uptake studies in 3T3-L1 cells

To evaluate the ability of ICG-FA probe to mimic the cellular uptake of long-chain fatty acids, the probe uptake in 3T3-L1 cells was investigated. 3T3-L1 cell line originally derived from mice is a

widely used cellular model to study the fatty acid uptake, since 3T3-L1 fibroblasts can be differentiated to adipocytes following specific culturing conditions (116, 119, 137, 138). Cell differentiation into adipocytes induces expression of fatty acid transport proteins such as FATP1, FATP4, CD36, caveolin-1 and FABPpm, which results in significant enhancement of long-chain fatty acid uptake and accumulation of lipid droplets in the cytosol (116, 117, 119, 120, 139-142). For ICG-FA uptake experiment, 3T3-L1 fibroblasts and adipocytes were incubated with a solution of ICG-FA bound to bovine serum albumin, which was supplemented with a fluorescent BODIPY-labeled analog of palmitic acid BODIPY™ FL C<sub>16</sub> (BODIPY-FA) as a positive control, and after washing and nuclear staining the cells were examined with a fluorescent microscope (**Figure 2.5**).

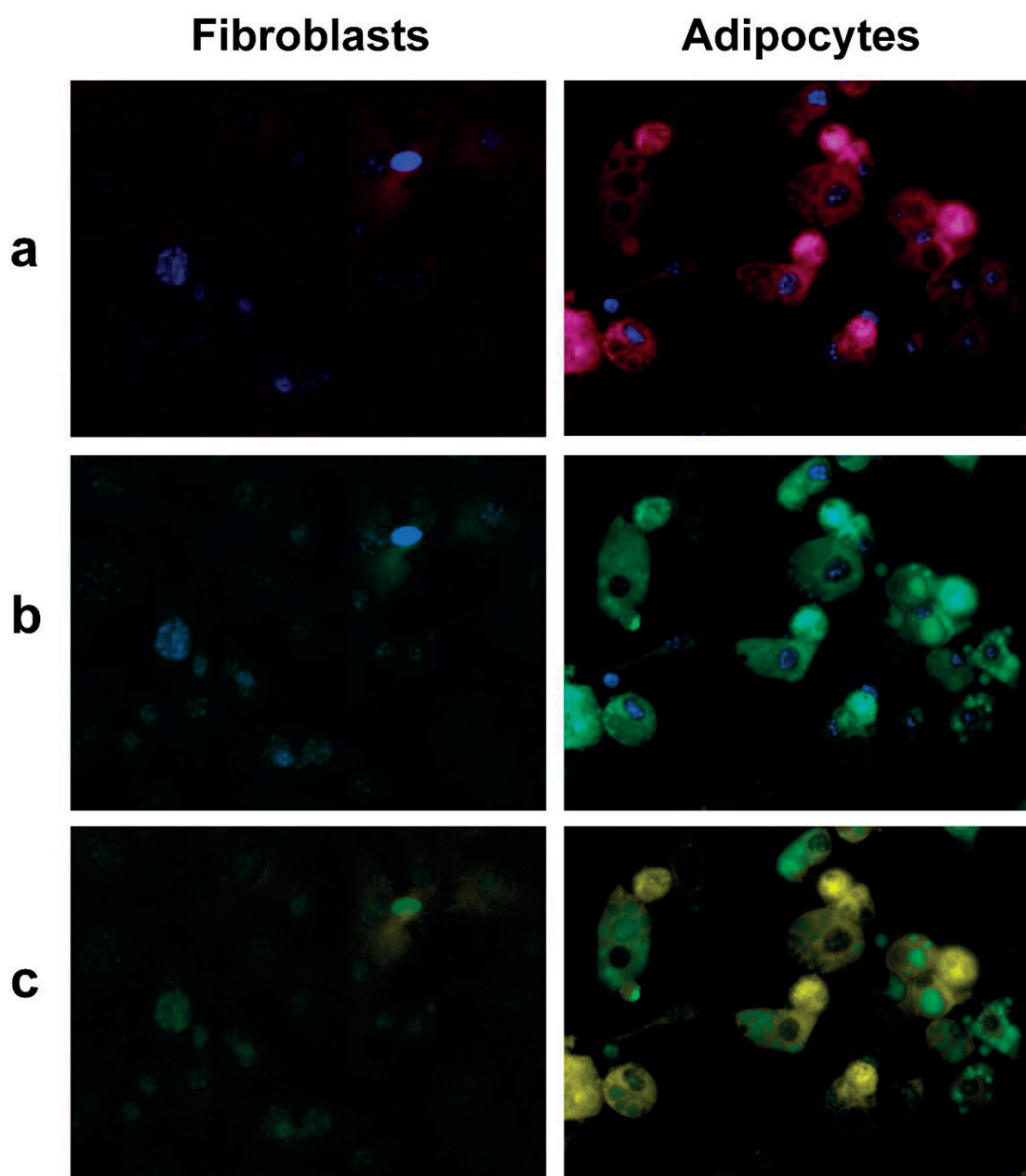


**Figure 2.5** Comparison of ICG-FA and BODIPY-FA uptake in 3T3-L1 fibroblasts and adipocytes by fluorescence microscopy. The cells were incubated with a mixture of BODIPY-FA (1  $\mu$ M) and ICG-FA (5  $\mu$ M) in HBSS containing 0.1% fatty acid free BSA for 30 min at 37°C and washed, and then the nuclei were stained with Hoescht 33342 (1  $\mu$ g/mL) followed by live-cell fluorescence microscopy at 40 $\times$  magnification. (a) Merged images for red (ICG-FA) and blue (Hoescht) channels. (b) Merged images for green (BODIPY-FA) and blue (Hoescht 33342) channels. (c) Merged images for red (ICG-FA) and green (BODIPY-FA) channels, which show colocalization of ICG-FA and BODIPY-FA signals resulting in yellow color. Fluorescent images were acquired using the same imaging settings for fibroblasts and adipocytes.

This experiment clearly demonstrated that ICG-FA produces fluorescence inside adipocytes, confirming that ICG-FA is a cell permeable probe. Comparison of fluorescent signals from fibroblasts and adipocytes revealed much higher ICG-FA uptake by the differentiated cells (**Figure 2.5a**). A similar

difference in cellular uptake by 3T3-L1 fibroblasts and adipocytes was obtained for BODIPY-FA, which was used as a positive control (**Figure 2.5b**). These results are in agreement with the previous studies based on radiolabeled, fluorescent and bioluminescent fatty acids (72, 116, 117, 120). In addition, ICG-FA and BODIPY-FA demonstrated similar localization patterns in the intracellular space of adipocytes except the lipid droplets (**Figure 2.5c**), where ICG-FA did not give significant fluorescence. A possible reason for lack of fluorescence from ICG-FA in the lipid droplets may be due to the dependence of a molar absorptivity of the ICG fluorophore as well as its quantum yield and therefore overall fluorescence intensity on the polarity of the environment, where non-polar solvents suppress fluorescence intensity of ICG (143, 144). Since lipid droplets consist of triglycerides and sterol esters (145), they provide non-polar environment, which may inhibit ICG-FA fluorescence. In contrast, BODIPY fluorescence is almost insensitive to environmental polarity (146). In addition, ICG-FA fluorescence can be quenched because of the dye aggregation (132, 147, 148), which can be expected in non-polar lipid droplets.

The uptake of ICG-FA in 3T3-L1 fibroblasts and adipocytes was also analyzed and quantified using a fluorescence microplate reader. The cells were treated with increasing concentrations of ICG-FA and after washing and lysing cells in MeOH the fluorescence of lysates was measured with a microplate reader. Cell lysis and dilution in MeOH decreases probe aggregation as ICG fluorophore has high affinity to MeOH (149). Both fibroblasts and adipocytes demonstrated a dose-dependent increase in ICG-FA fluorescence from cell lysates with an increase of the probe concentration (**Figure 2.6**). However, adipocytes showed much more robust probe uptake compared to fibroblasts, which is consistent with the results for ICG-FA uptake in 3T3-L1 cells obtained with fluorescence microscopy (**Figure 2.5**).

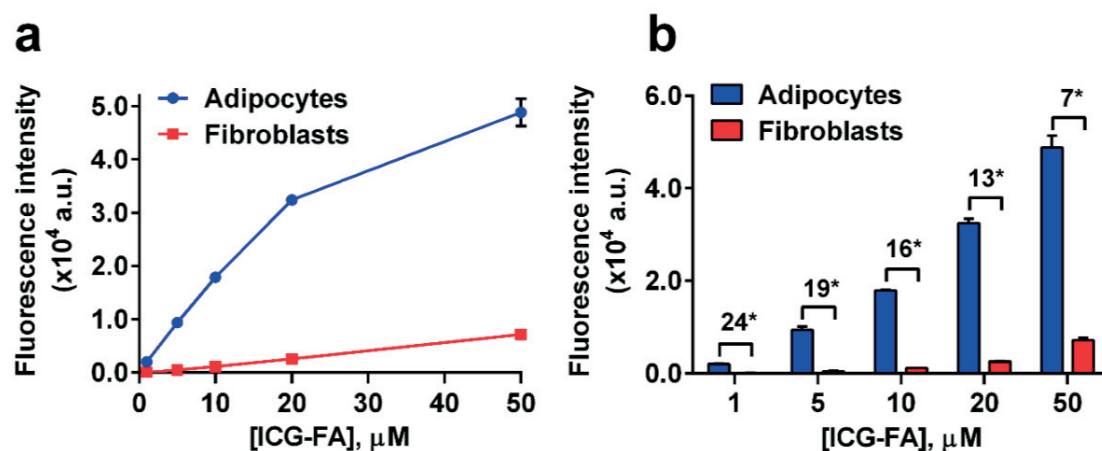


**Figure 2.6** Concentration-dependent ICG-FA uptake by 3T3-L1 fibroblasts and adipocytes. (a) Measured fluorescent signals from lysates of adipocytes and fibroblasts in MeOH following incubation with indicated concentrations of ICG-FA in HBSS containing 0.1% fatty acid free BSA for 30 min at 37°C. (b) Bar-graph representation of data shown in (a). Fluorescence measurements were performed with Tecan Infinite M1000 plate reader with excitation at 785 nm and emission 815 nm. Error bars are  $\pm$ SD,  $n = 3$ . Statistical analyses were performed with a two-tailed t-test (\* $P < 0.0001$ ). a.u., arbitrary units.

Moreover, adipocytes revealed a non-linear increase in fluorescence for higher probe concentrations, whereas fibroblasts demonstrated a linear fluorescent response ( $R^2 = 0.9984$ ) for all range of used concentrations of ICG-FA (0-50  $\mu$ M) (Figure 2.6a). These results suggest that ICG-FA uptake by adipocytes exhibits saturation effects at higher probe concentrations due to the presence of a known saturable protein-mediated component of fatty acid uptake in differentiated cells (116, 120, 141). A decrease in the ratios of fluorescent signals from adipocytes and fibroblasts for higher ICG-FA concentrations is also indicative of saturable probe uptake by adipocytes (Figure 2.6b). In contrast to adipocytes, the same concentrations of ICG-FA did not exhibit saturation effects in undifferentiated 3T3-L1 cells, being consistent with the fact that undifferentiated fibroblasts take up fatty acids by passive diffusion (120).

Next, ICG-FA uptake kinetics in 3T3-L1 adipocytes was compared to that in fibroblasts. The cells were incubated with the same concentration of ICG-FA for various time intervals (5, 10, 20, 40, 60, 90 min), followed by measurements of fluorescence from cell lysates. While fibroblasts showed slow increase of fluorescent signal over 90 min, adipocytes demonstrated much faster ICG-FA uptake kinetics (Figure 2.7).



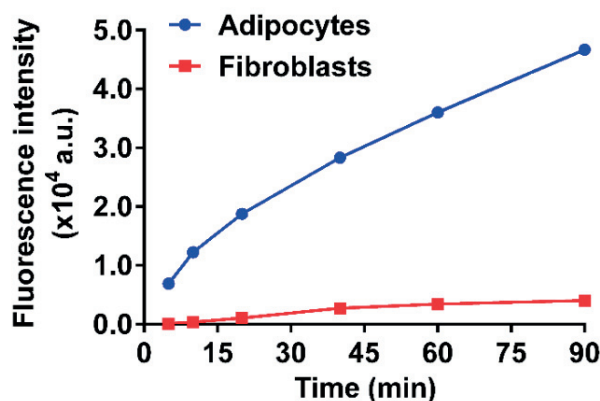


**Figure 2.7** Kinetics of ICG-FA uptake by 3T3-L1 fibroblasts and adipocytes. Fluorescent signals from cell lysates in MeOH were measured after cell incubations with ICG-FA (20  $\mu$ M) in HBSS containing 0.1% fatty acid free BSA for indicated periods of time at 37°C. Fluorescence measurements were performed with Tecan Infinite M1000 plate reader with excitation at 785 nm and emission 815 nm. The difference between adipocytes and fibroblasts for each time point is significant ( $P < 0.0001$ ). Error bars are  $\pm$ SD,  $n = 3$ . a.u., arbitrary units.

The analysis of the kinetic curves represented in **Figure 2.7** between two first time points (from 5 to 10 min) provided slope values 1062 a.u./min and 49 a.u./min for adipocytes and fibroblasts respectively, indicating about 22-fold higher ICG-FA uptake rate in differentiated cells compared to fibroblasts within this time interval. This kinetics pattern for ICG-FA uptake is consistent with the previous kinetics data for fatty acid uptake in 3T3-L1 cells obtained using fluorescent BODIPY-FA probe (117).

To further test the hypothesis that ICG-FA uptake by cells is similar to the uptake of natural fatty acids, 3T3-L1 adipocytes were incubated with ICG-FA in the presence of increasing concentrations of a natural fatty acid oleic acid (used in the form of sodium oleate). Addition of oleate resulted in a dose-dependent decrease of ICG-FA fluorescence from differentiated 3T3-L1 cells (**Figure 2.8**), demonstrating a competition between ICG-FA and oleic acid for cellular uptake in adipocytes. This result suggests that the probe uptake by adipocytes overlaps with that of natural fatty acids. As can be seen in **Figure 2.8** excess of oleate did not fully suppress ICG-FA uptake. This may result from the fact that oleate influences only the protein-mediated component of cellular fatty acid uptake (150-153), suggesting that the observed residual fluorescence from the probe in the presence of high concentrations of oleate represents passive uptake of ICG-FA into adipocytes.

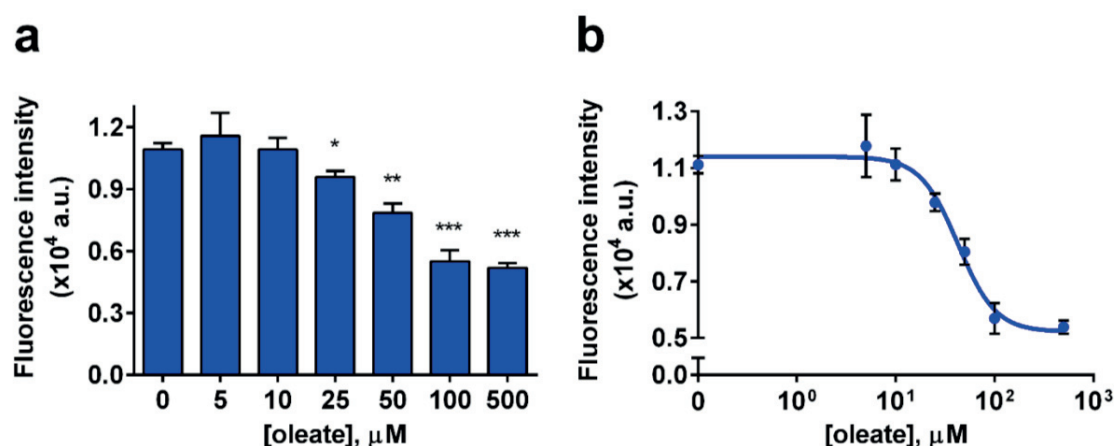


**Figure 2.8** Effect of oleate on the uptake of ICG-FA by 3T3-L1 adipocytes. (a) Measured fluorescent signals from lysates of cells in MeOH after incubation with ICG-FA (1 μM) in HBSS in the presence of indicated concentrations of sodium oleate for 30 min at 37°C. (b) Sigmoidal graph representation of data shown in (a), which gives IC<sub>50</sub> value of 43 μM for oleate. Error bars are ±SEM, n = 3. Statistical analyses were performed with a two-tailed t-test (\*P < 0.05, \*\*P < 0.01, \*\*\*P < 0.001 relative to signal in the absence of oleate). a.u., arbitrary units.

Taken together, the results of ICG-FA uptake experiments in 3T3-L1 cells are consistent with the previous studies of differentiation-induced changes in long-chain fatty acid uptake by 3T3-L1 cells based on utilizing radiolabeled and fluorescent fatty acids (116, 117, 120), which supports the hypothesis that ICG-FA mimics the uptake of natural long-chain fatty acids.

### 2.2.5 ICG-FA uptake studies in U87MG-luc cells

ICG-FA probe uptake was investigated in a U87MG human glioblastoma cell line (154, 155) that was expressing luciferase enzyme (U87MG-luc), as U87MG is one of the most commonly used cell lines for studies on human glioma. U87MG-luc were subsequently used in this work for generating tumor xenograft models for *in vivo* studies of ICG-FA, since the expression of luciferase in xenografts provides the ability for non-invasive monitoring of tumor growth using D-luciferin substrate and bioluminescence imaging (156).

For ICG-FA uptake studies, U87MG-luc were incubated with a solution of the probe bound to BSA and after washing and nuclear staining the cells were examined by fluorescence microscopy. As can be seen in **Figure 2.9** the fluorescent signal from ICG-FA was detected inside the cells, verifying that the probe is cell permeable and accumulates in U87MG-luc cells.

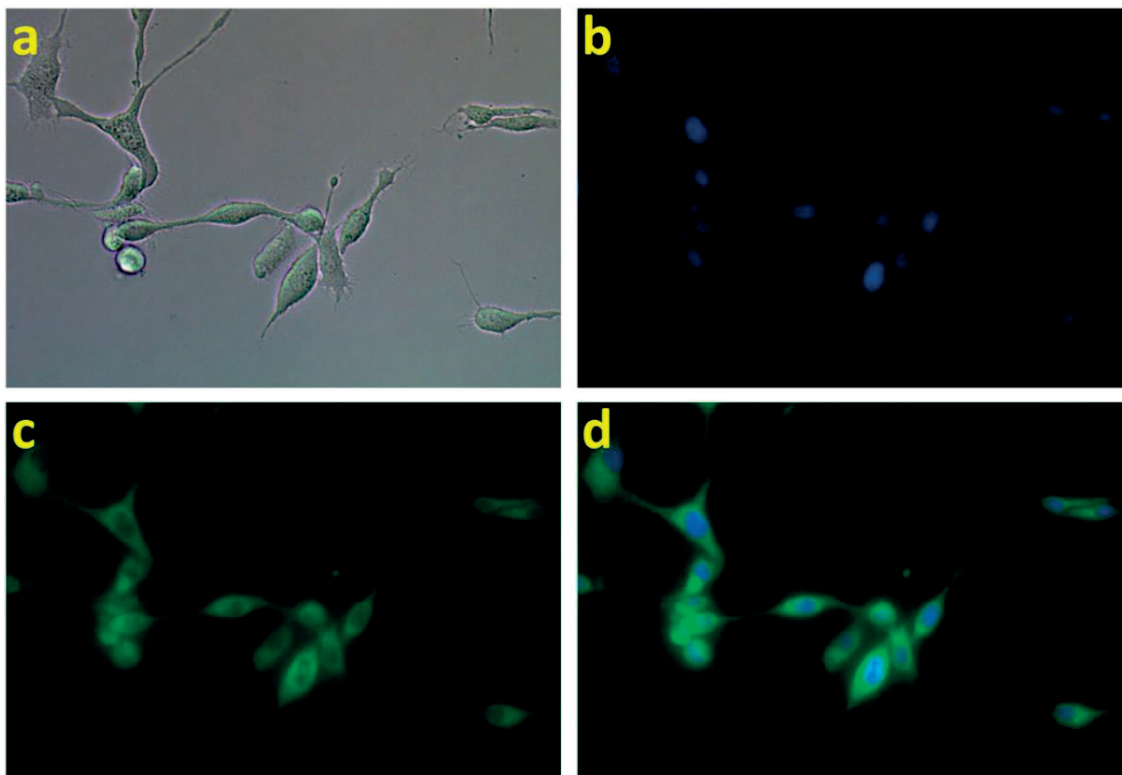


**Figure 2.9** Imaging of ICG-FA uptake in U87MG-luc by fluorescence microscopy. The cells were incubated with ICG-FA (20  $\mu$ M) in HBSS containing 0.1% fatty acid free BSA for 3 h at 37°C and washed, and then the nuclei were stained with Hoescht 33342 (1  $\mu$ g/mL) followed by live-cell fluorescence microscopy at 40 $\times$  magnification. (a) Bright-field image. (b) Fluorescent image representing blue channel (Hoescht 33342). (c) Fluorescent image representing green channel (ICG-FA). (d) Merged fluorescent image for green (ICG-FA) and blue (Hoescht 33342) channels.

Next, the uptake of ICG-FA by U87MG-luc cells was compared with the uptake of ICG. Cells were incubated with increasing concentrations of the probes in a BSA solution followed by washing and cell lysis in MeOH and then measuring fluorescence using a microplate reader. Both ICG-FA and ICG showed an increase of a fluorescent signal from cell lysates in a concentration-dependent manner (**Figure 2.10**). ICG-FA demonstrated robust dose-dependent uptake by U87MG-luc cells, whereas the cellular uptake of ICG was significantly lower (**Figure 2.10b**). As a negatively charged molecule, free ICG dye cannot passively cross a cellular membrane. Uptake of ICG by tumor cells is not well studied, however some reports showed involvement of organic anion transporting polypeptide (OATP) in squamous cell carcinoma (157), organic anion transporting polypeptide 1B3 (OATP1B3) and sodium-taurocholate co-transporting polypeptide (NTCP) in hepatic tumor cells in the ICG uptake (158). In a recent study, Onda et al. investigated ICG uptake in colon cancer cells and suggested that membrane transporters such as OATP1B3 facilitate ICG incorporation in tumor cells only partially, and it was proposed that endocytosis plays a major role in ICG uptake by tumor cells (124).

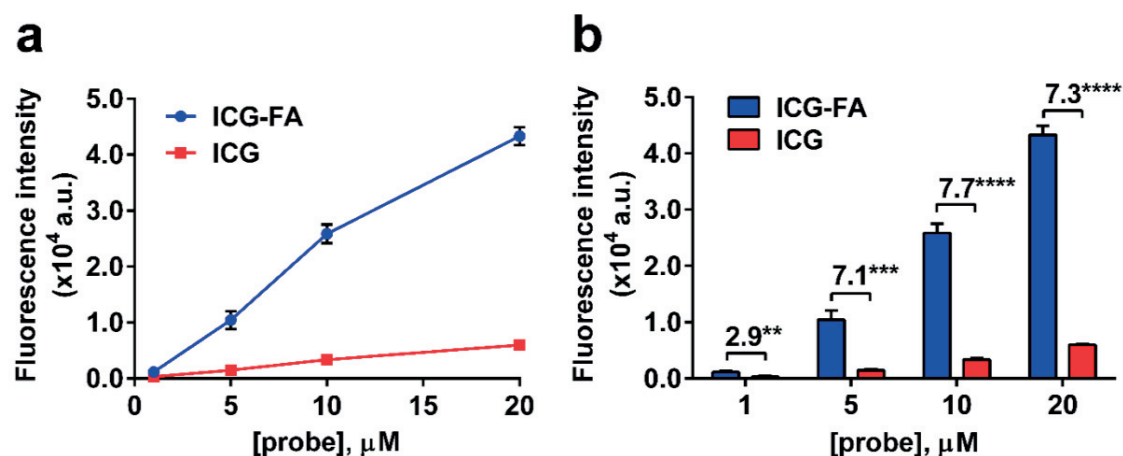


**Figure 2.10** Comparison of ICG-FA and ICG uptake by U87MG-luc cells. (a) Measured fluorescent signals from lysates of cells in MeOH after incubation with indicated concentrations of ICG-FA or ICG in HBSS containing 0.1% fatty acid free BSA for 3 h at 37°C. (b) Bar-graph representation of data shown in (a). Error bars are  $\pm$ SD,  $n = 3$ . Statistical analyses were performed with a two-tailed t-test (\*\* $P < 0.01$ , \*\*\* $P < 0.001$ , \*\*\*\* $P < 0.0001$ ). a.u., arbitrary units.

The results of the uptake studies in U87MG-luc cells demonstrate that conjugation of ICG to a long-chain fatty acid to form ICG-FA results in increased cellular uptake of the conjugate compared to the uptake of free ICG and provides enhanced fluorophore accumulation inside the cells (**Figure 2.10**). U87MG cells were shown to express high levels of the fatty acid transporter FATP3, which is also called acyl-CoA synthase ACSVL3 that was shown to be important for growth and maintenance of the malignant phenotype of the cells and glioma xenografts in mice (159). The expression of another member of fatty acid transport proteins family, FATP4, was also found in U87MG cells (159). FATPs are known to be implicated in the uptake of long-chain fatty acids by cells (160). In addition, fatty acid binding proteins 3 and 7 (FABP3 and FABP7) as well as adipophilin (ADRP), which are involved in the cellular uptake of long-chain fatty acids (161-163), are upregulated in U87MG cells under hypoxia that occurs during the increase of the tumor mass, and they become essential for cellular fatty acid uptake as well as for the maintenance of *in vivo* growth of U87MG xenografts (113). This suggests that enhanced uptake of ICG-FA by U87MG-luc may result from the involvement of the cellular proteins mediating the transport of long-chain fatty acids in glioma cells, which leads to stronger fluorescent signal from ICG-FA in the cells as compared to ICG.

### 2.2.6 Biodistribution studies in mice

The biodistribution of ICG-FA in mice was evaluated and compared with the biodistribution of free ICG by whole body *in vivo* fluorescence imaging and *ex vivo* imaging of the excised organs. Two groups of Swiss nu/nu mice were intravenously injected with equal doses of ICG-FA and ICG respectively, and the whole body dorsal and ventral fluorescent signals were monitored *in vivo* over 50 hours (**Figure 2.11** and **Figure 2.12**). Imaging 30 min post injection detected non-significant difference between whole-body fluorescence from ICG-FA and ICG (**Figure 2.13**) that produced respectively 31 ( $P < 0.01$ ) and 22-fold ( $P < 0.0001$ ) higher dorsal signals than the background fluorescence and 34 ( $P < 0.001$ ) and 49-fold ( $P < 0.001$ ) higher ventral signals than the background signal. However, ventral imaging 30 min post injection revealed stronger fluorescence from ICG in the upper abdominal area (**Figure 2.12**). ICG is known to have rapid elimination from the bloodstream (plasma half-life 3-4 min) via fast and exclusive uptake by hepatocytes with subsequent excretion with the bile into the intestine (132). ICG demonstrated fast decrease of *in vivo* dorsal fluorescence and slower decrease of ventral fluorescent signal due to the intestinal excretion of the fluorophore that in turn determines the rate of ICG elimination from the body. However, for ICG-FA the dorsal fluorescent signal was stable up to 8 h post injection followed by gradual decrease. Analysis of ventral images revealed that ICG-FA also accumulated in the liver and during later time points post injection produced strong fluorescence from the abdominal region (**Figure 2.12**), which suggests that the probe or its metabolite undergoes hepatobiliary excretion into the intestine. Dorsal and ventral whole-body fluorescent signals from ICG-FA 50 h post injection were respectively 4 and 5-fold ( $P < 0.0001$ ) stronger than the background level. *In vivo* fluorescence from ICG 50 h post injection was not different in comparison to the background signal.

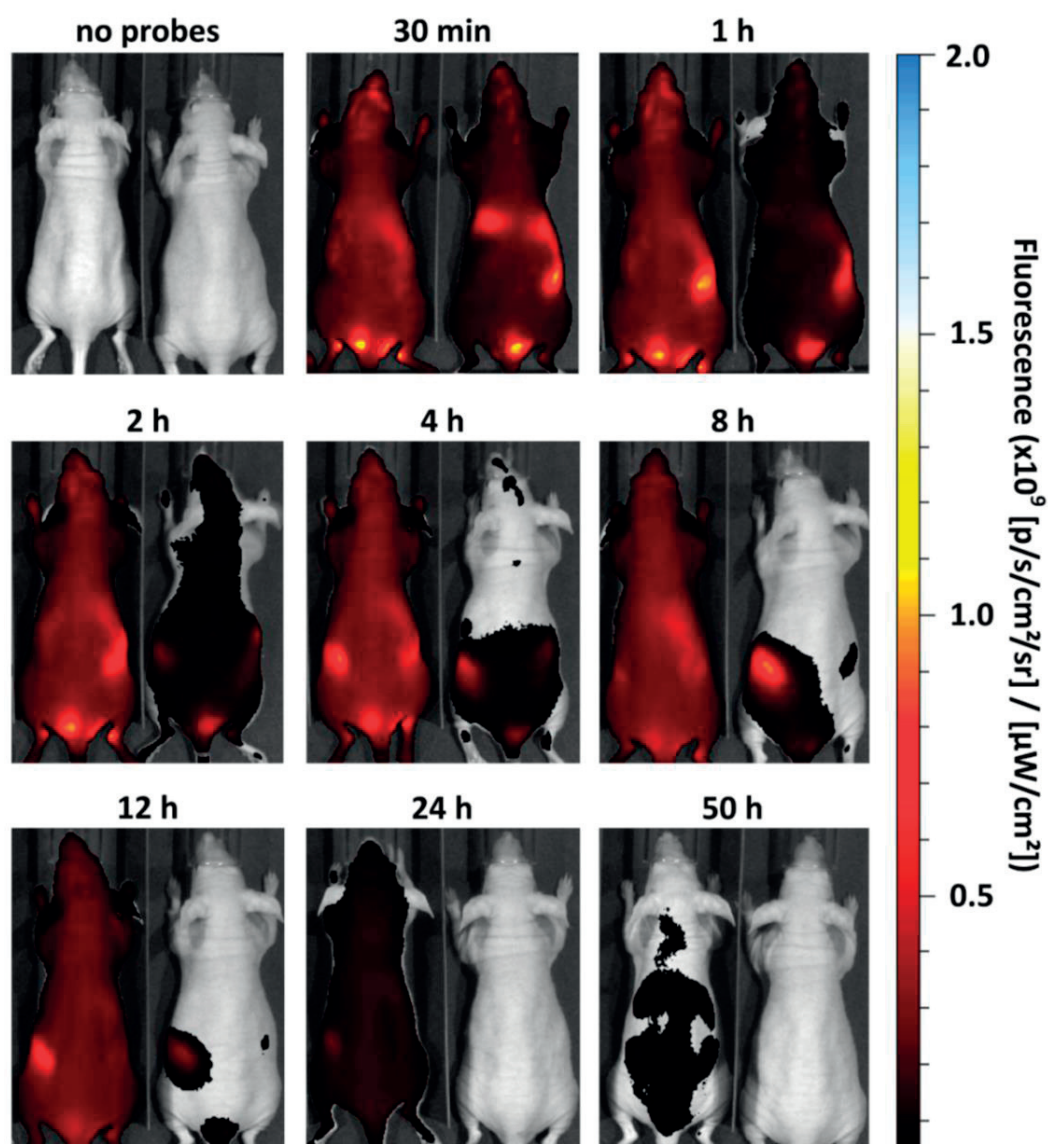


**Figure 2.11** *In vivo* dorsal fluorescence imaging of Swiss nu/nu mice after intravenous administration of ICG-FA (left mouse) or ICG (right mouse). Equal dose of ICG-FA or ICG (20 nmol/25 g, 100  $\mu\text{M}$  probe solution in PBS containing 0.1% (w/v) fatty acid free BSA) was injected via tail vein and imaging was performed at indicated time points post injection. Representative images ( $n = 3$  per group).



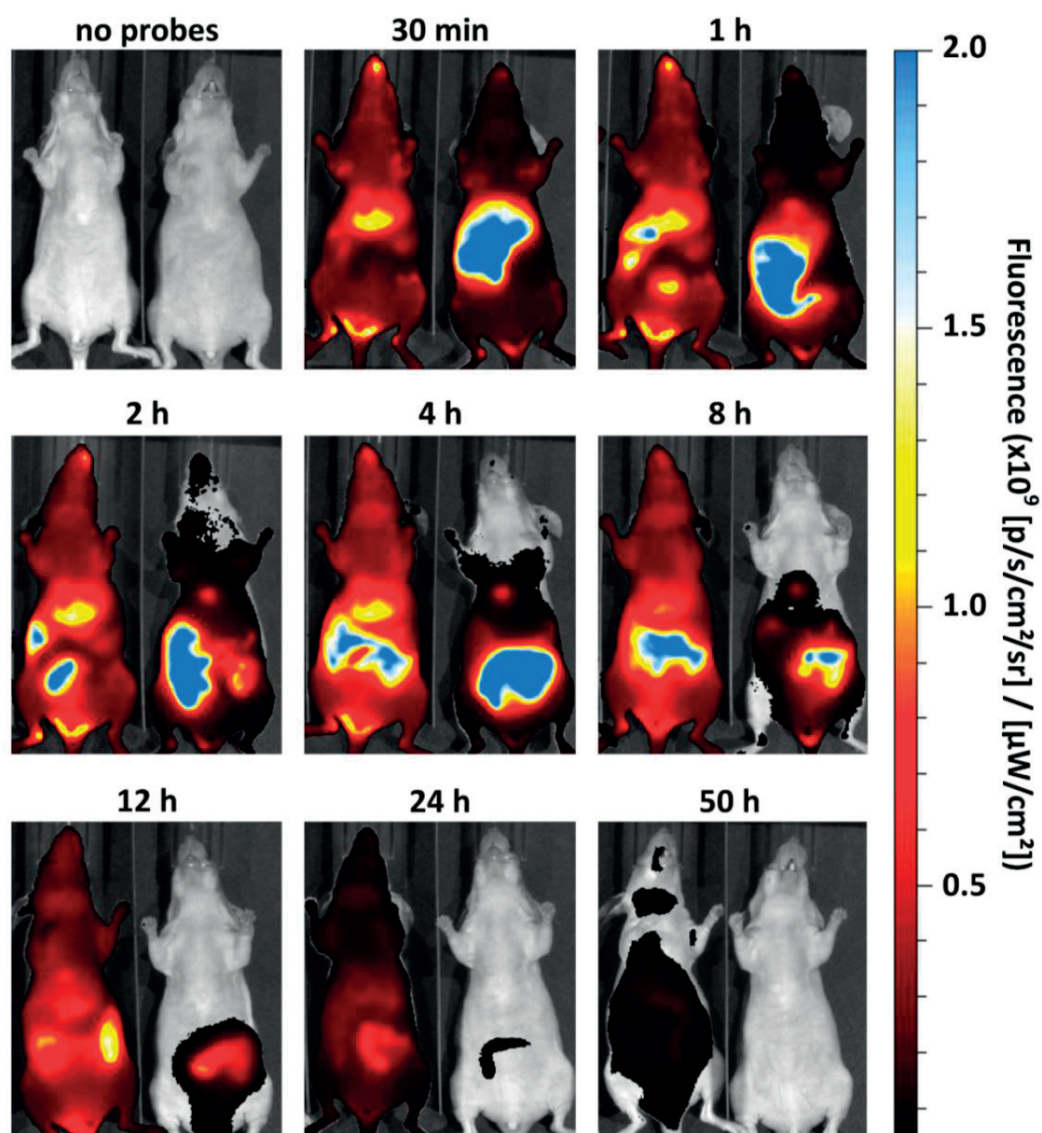


**Figure 2.12** *In vivo* ventral fluorescence imaging of Swiss nu/nu mice after intravenous administration of ICG-FA (left mouse) or ICG (right mouse). ICG-FA and ICG (20 nmol/25 g, 100  $\mu$ M probe solution in PBS containing 0.1% (w/v) fatty acid free BSA) were injected via tail vein and imaging was performed at indicated time points post injection. Representative images (n = 3 per group).

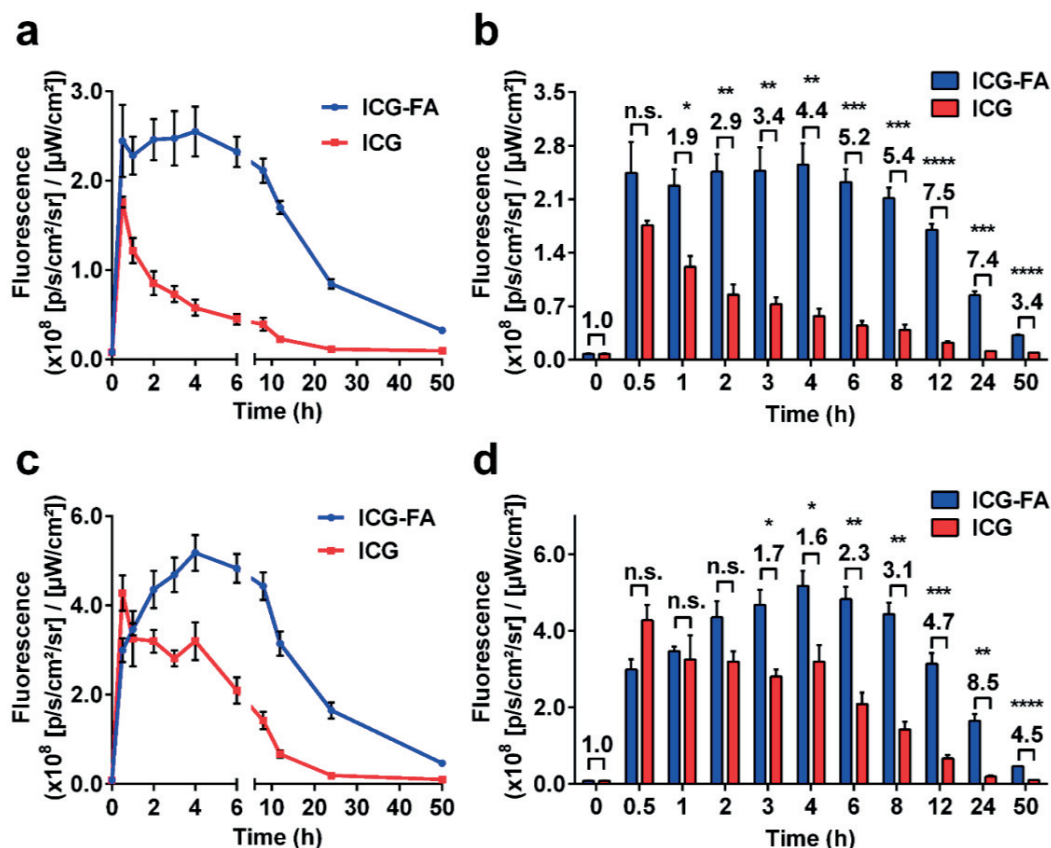


**Figure 2.13** Comparison of whole-body fluorescent signals from ICG-FA and ICG in Swiss nu/nu mice. Mice were injected with equal doses of ICG-FA or ICG (20 nmol/25 g, 100 μM probe solution in PBS containing 0.1% (w/v) fatty acid free BSA) via tail vein and were imaged at indicated time points post injection. (a) Kinetics of dorsal fluorescence from mice injected with ICG-FA or ICG. (b) Bar-graph representation of data shown in (a). (c) Kinetics of ventral fluorescence from mice injected with ICG-FA or ICG. (d) Bar-graph representation of data shown in (c). The signals for  $t = 0$  correspond to background fluorescence from mice before administration of the probes. Error bars are  $\pm$ SEM,  $n = 3$  ( $n = 2$  for  $t = 0.5$  h). Statistical analyses were performed with a two-tailed t-test (\* $P < 0.05$ , \*\* $P < 0.01$ , \*\*\* $P < 0.001$ , \*\*\*\* $P < 0.0001$ ).

*Ex vivo* imaging of excised organs (liver, kidney, lung, brown adipose tissue and white adipose tissue, spleen, skeletal muscles, heart, brain) 2 h after intravenous injection of ICG-FA revealed about an order of magnitude stronger tissue fluorescence compared to the signal from the organs following equimolar ICG injection (Figure S2.1).

Intravenous administration of the probe with the doses up to 50 nmol per mouse (2 mg/kg) did not lead to any behavioral or physiological alterations during the observation period over 6 months, suggesting that the probe does not exhibit toxic effects *in vivo* for the used range of doses.

Taken together, the biodistribution studies *in vivo* and *ex vivo* demonstrate that the conjugation of ICG to the long-chain fatty acid palmitic acid results in much higher accumulation and



longer retention of ICG-FA in various tissues. These results are consistent with the cellular experiments, which demonstrated that ICG-FA is a cell-permeable probe that mimics the uptake of long-chain fatty acids. Since various organs require fatty acid uptake from the circulation for their metabolic needs (164), it can be suggested that the fatty acid uptake mechanism contributes to the increased organ accumulation and retention of ICG-FA *in vivo*.

### 2.2.7 *In vivo* fluorescence imaging of glioma in living mice using ICG-FA

The cellular studies demonstrated high ICG-FA accumulation in U87MG-luc glioma cells. To determine whether ICG-FA can be utilized for glioma imaging *in vivo*, the probe accumulation was studied in a subcutaneous murine U87MG-luc tumor xenograft model. To establish tumor xenografts, U87MG-luc cells were subcutaneously implanted in Swiss nu/nu mice. Expression of the luciferase enzyme in the implanted cells allowed non-invasive *in vivo* monitoring of the tumor location and size, which was achieved by intraperitoneal D-luciferin injection (**Figure 2.14a**). When the tumors had reached 4-7 mm in diameter, two groups of xenograft-bearing mice were injected with equal doses of ICG-FA and ICG (20 nmol/25 g) respectively followed by *in vivo* fluorescence imaging over 24 h in order to determine the signal kinetics from the injected probes in the tumors. ICG-FA produced fluorescent signal in the tumor that was distinguishable from the signal in surrounding tissues as early as 30 min post injection (**Figure 2.14b**). The fluorescence from ICG-FA in the tumor was increasing over time and reached the maximum around 8 h post injection. However, the same dose of free ICG dye did not produce comparable fluorescence in the tumor (**Figure 2.14b**). The quantification of detected signals from ICG-FA and ICG in the xenografts demonstrated completely different kinetics of fluorescence from the probes (**Figure 2.15a,b**). Whereas tumoral fluorescence from ICG-FA was increasing during 8 h post injection with a slow decrease during later time points, the tumoral signal from ICG was continuously decreasing over 24 h after injection. When 2.5 times higher dose of probes (50 nmol/25 g) was injected in the xenograft bearing mice the kinetics pattern for the tumoral fluorescence from each probe was similar to the corresponding kinetic curves observed for the lower dose (**Figure 2.15c, Figure S2.2**). ICG-FA signal in the tumor increased 1.9 times ( $P = 0.019$ ) during 8 hours after injection (dose 50 nmol/25 g) and then until the last imaging time point (49 h) decreased 3.3 times ( $P < 0.005$ ) from the maximal level. The tumor-to-background ratio (T/B) for ICG-FA was in the range 1.9-2.5 ( $P < 0.05$  for all time points) over 49 h. The same dose of ICG gave the maximal tumoral signal during the first hour post injection that was comparable to the fluorescence from ICG-FA, however the ICG signal rapidly decreased with 32-fold reduction over 48 h. The highest *in vivo* T/B value for ICG was 2.0 that was only observed 1 h post injection, and after that the tumor signal was close to the background level during the later imaging period.

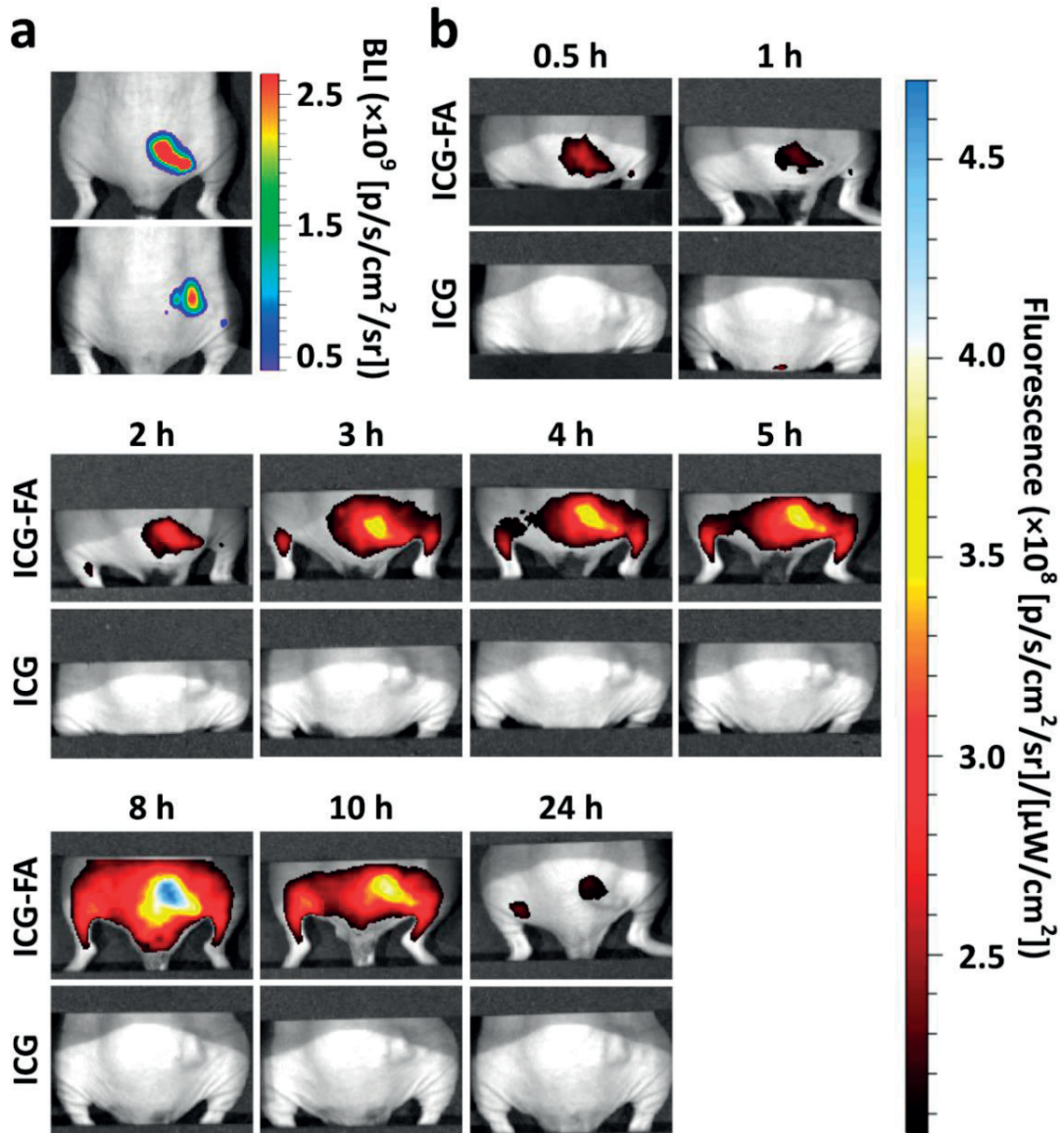


**Figure 2.14** *In vivo* imaging of glioma xenografts in a mouse model. Swiss nu/nu mice bearing subcutaneous tumors (U87MG-luc) were injected with D-luciferin potassium salt (3 mg/kg in PBS i.p.) followed by bioluminescence imaging 10 min post injection. After 24 h the mice ( $n = 2$  per group) were injected with ICG-FA or ICG (20 nmol/25 g for both probes i.v.) and fluorescence was monitored over 24 h. (a) Representative bioluminescence images of tumor xenografts following D-luciferin injection. (b) Representative fluorescence images of tumor xenografts at indicated time points post injection over 0-24 h following ICG-FA or ICG administration. The images correspond to the same mice, which are shown in (a).

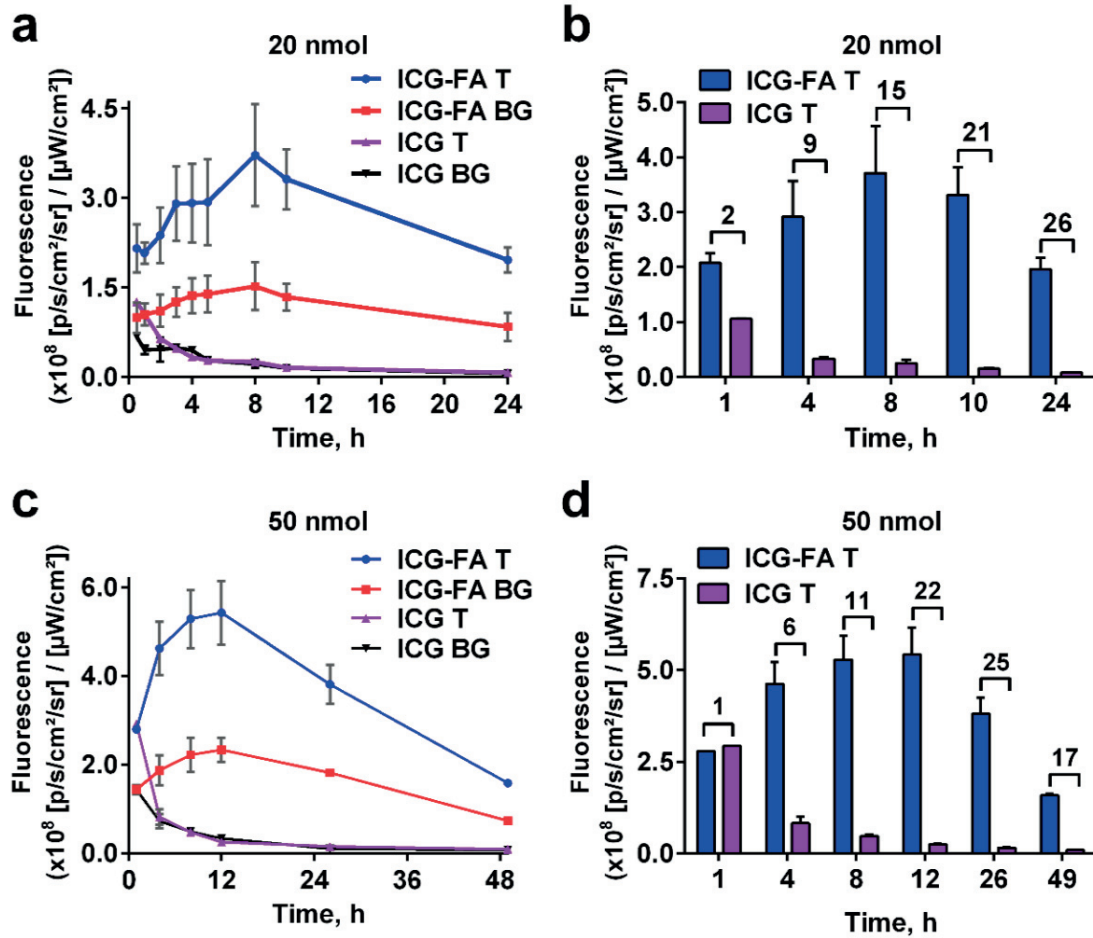


**Figure 2.15** Comparison of fluorescent signals *in vivo* after administration of ICG-FA or ICG in Swiss nu/nu mice bearing subcutaneous glioma (U87MG-luc) xenografts. (a) Kinetics of fluorescent signals from ICG-FA or ICG (20 nmol/25 g for each probe i.v.) in tumor (T) and skin above healthy region (BG) of mice measured over 24 h post injection. (b) Comparison of fluorescent signals in tumors from ICG-FA and ICG (20 nmol/25 g for each probe i.v.) at indicated time points post injection. (c) Kinetics of fluorescent signals from an increased dose of ICG-FA or ICG (50 nmol/25 g for each probe i.v.) in tumor (T) and skin above healthy region (BG) of mice monitored over 48 h post injection. (d) Comparison of fluorescent signals in tumors after injecting a higher dose of ICG-FA or ICG (50 nmol/25 g for each probe i.v.) at indicated time points post injection. In (a,b)  $n = 2$  for each group. In (c,d)  $n = 3$  for ICG-FA,  $n = 2$  for ICG. Error bars are  $\pm$ SEM.

To confirm *in vivo* results, ICG-FA accumulation in the subcutaneous U87MG-luc tumor xenografts was also analyzed by *ex vivo* imaging of excised tumors. In addition, tumor-to-background ratio (T/B) for the resected glioma xenografts was calculated, where the fluorescence from the healthy brains of mice was used as a background level. In this experiment first the tumor fluorescence was measured *in vivo* 15 h post injection of ICG-FA and ICG followed by registration of *in vivo* bioluminescent tumoral signals, which was initiated by D-luciferin administration. Immediately after that, the mice were euthanized and the excised tumors and brains were imaged *ex vivo* (Figure 2.16).

Similar to *in vivo* results, robust fluorescent signals from ICG-FA were detected in the excised tumor xenografts.

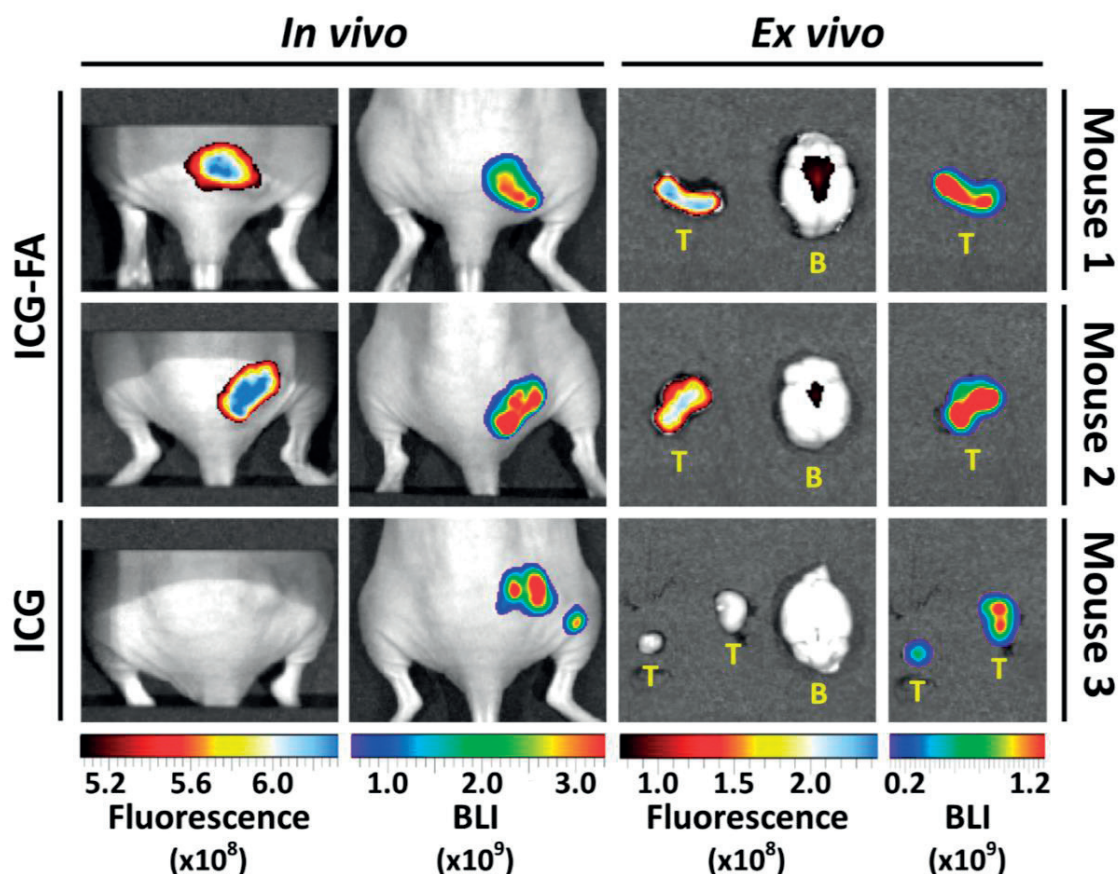


**Figure 2.16** Representative *in vivo* and *ex vivo* images showing fluorescent signals from ICG-FA or ICG and corresponding bioluminescent signals in the subcutaneous glioma (U87MG-luc) xenograft mouse model. Swiss nu/nu mice bearing the tumor xenografts were injected with ICG-FA or ICG (50 nmol/25 g for each probe i.v.) followed by *in vivo* fluorescence imaging 15 h post injection. Then, the mice received injection of D-luciferin potassium salt (3 mg/kg in PBS i.p.) and *in vivo* bioluminescence imaging (BLI) was performed 10 min post injection. Immediately after that, the mice were euthanized, the tumor (T) and the brain (B) from each animal were harvested and their *ex vivo* fluorescence was measured. Next, bioluminescence imaging for excised tumors was performed. For ICG-FA n = 4, for ICG n = 1. Fluorescence units are [p/s/cm<sup>2</sup>/sr] / [μW/cm<sup>2</sup>]. Bioluminescence units are [p/s/cm<sup>2</sup>/sr].

The tumor that was excised from the mouse after ICG injection did not produce significant fluorescence. ICG-FA generated 26-fold stronger signal in the glioma xenograft compared to the tumor signal from ICG (**Figure 2.17**). The calculated T/B ratio (tumor signal/brain signal) for the mice injected with ICG-FA was 4.5 ( $P < 0.01$ ), whereas for the mouse that received ICG injection there was no difference between *ex vivo* fluorescent signals from the tumor and the brain. According to the literature, accumulation of a fluorescent probe in a tumor is considered substantial if the tumoral fluorescence is  $> 2.5$ -fold stronger as compared to the fluorescence from the healthy tissue (165).

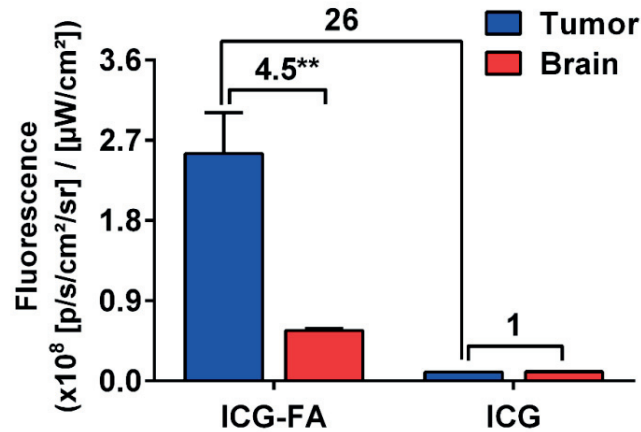


**Figure 2.17** *Ex vivo* comparison of fluorescent signals from ICG-FA and ICG in subcutaneous U87MG-luc tumor xenografts and in the corresponding brains after their excision from Swiss nu/nu mice bearing the xenografts. The mice were injected with ICG-FA or ICG (50 nmol/25 g for each probe i.v.) and were sacrificed 15 h post injection followed by fluorescence imaging of excised tumors and brains. Error bars are  $\pm$ SEM; n = 4 for ICG-FA, n = 1 for ICG. Statistical analysis was performed with a two-tailed t-test (\*\*P < 0.01).

ICG-FA was also tested in a transgenic mouse model *GRLp53fko* that spontaneously develops glioma (166). This experiment was performed in collaboration with Dr. Ksenya Shchors (Prof. Douglas Hanahan lab, EPFL). Symptomatic *GRLp53fko* mice and wild-type *FVB/NJ* mice were intravenously injected with equal doses of ICG-FA or ICG followed by *ex vivo* fluorescence imaging and histopathological analysis of excised brains. As shown in **Figure 2.18**, ICG-FA produced strong fluorescence in the brain with tumor, with the brightest fluorescent signal coming from the middle part of the brain, which corresponded to the tumor location determined using histopathological analysis. In contrast, ICG generated 7.1-fold weaker fluorescence in the brain that contained bigger tumor (**Figure 2.18**, **Figure 2.19**). Importantly, ICG-FA revealed 2.8-fold stronger signal from the brain with glioma than in the normal brain.



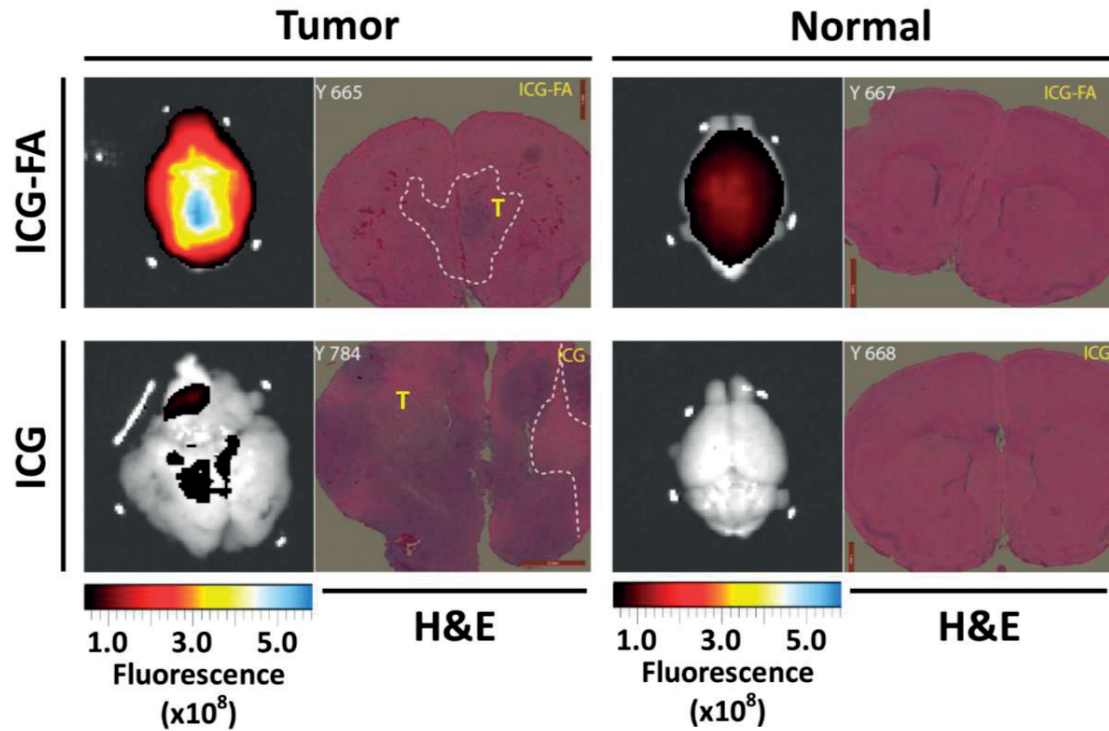


**Figure 2.18** Ex vivo fluorescence imaging of brain tumors using ICG-FA and ICG in *GRLp53fko* transgenic mouse model that develops spontaneous high-grade glioma and comparison with fluorescence imaging of normal brains. Symptomatic mice that developed spontaneous brain tumor and wild-type *FVB/NJ* mice were injected with ICG-FA or ICG (20 nmol/25 g for each probe). After 2 h the mice were euthanized and the brains were excised followed by fluorescence imaging. For each fluorescence image the corresponding hematoxylin and eosin (H&E) staining is shown on the right. Dashed line in H&E images indicates the border between the tumor (T) and healthy tissue. Fluorescence units are  $[p/s/cm^2/sr] / [\mu W/cm^2]$ . The experiment was performed in collaboration with Dr. Ksenya Shchors (Prof. Douglas Hanahan lab, EPFL). H&E staining was performed by Dr. Ksenya Shchors.

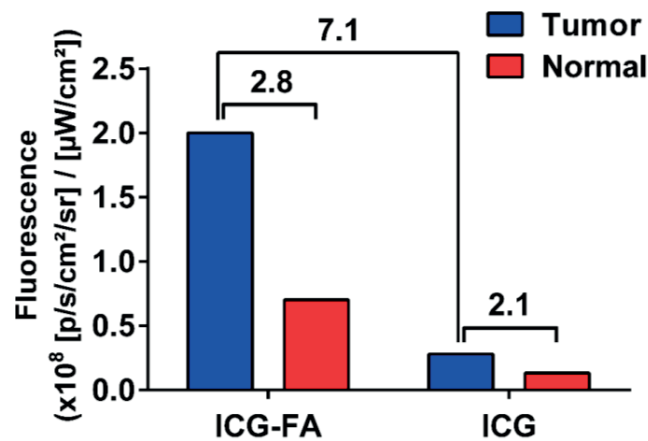


**Figure 2.19** Ex vivo comparison of fluorescent signals from ICG-FA and ICG in the whole brains of *GRLp53fko* transgenic mice that develop spontaneous high-grade glioma (indicated as Tumor) versus fluorescent signals in whole brains of wild-type *FVB/NJ* mice (indicated as Normal). The data correspond to Figure 2.18. Each group represents one mouse. The experiment was performed in collaboration with Dr. Ksenya Shchors (Prof. Douglas Hanahan lab, EPFL).

Although a small sample size restricts statistical value of the studies in the spontaneous tumor model, the obtained experimental results are consistent with the data for the ICG-FA and ICG studies in the subcutaneous glioma xenographt model.

Altogether, these results demonstrate the ability of ICG-FA to target glioma in mice in U87MG-luc xenographt model and in *GRLp53fko* transgenic model.

### 2.2.8 Intraoperative tumor fluorescence imaging and image-guided surgery using ICG-FA

The ability to detect tumor margins is necessary for complete removal of malignant tissues, which in turn determines the effectiveness of surgical treatment and patient prognosis. Visual inspection and palpation are standard ways for a surgeon to discriminate between malignant and healthy tissues during surgery; however, they are not always sufficient. Near-infrared fluorescent probes that target cancer cells can aid a surgeon to achieve complete tumor resection (167). ICG-FA probe was assessed as an imaging agent for intraoperative tumor imaging in a canine patient with mastocytoma. Mastocytoma is the most common skin cancer in dogs accounting for up to 21% of all canine skin cancers and represents a malignant transformation of mast cells that are normally involved in immune responses and inflammatory processes (168, 169). A canine patient with mastocytoma was intravenously injected with a solution of ICG-FA prior to surgery to assess the ability of the probe to target the tumor. The canine imaging experiment was performed by veterinarian Dr. Arno Roos (Veterinair Verwijscentrum Gouda, Netherlands) according to the provided experimental protocol. An open-air intraoperative fluorescence imaging system was used for detecting near-infrared fluorescence from ICG-FA in the canine patient in real time (170). Intraoperative imaging 10 h post-injection detected a strong fluorescent signal from ICG-FA in the tumor (**Figure 2.20**). Following mastocytoma resection the tumor bed showed minimal background fluorescence (**Figure 2.20d**).

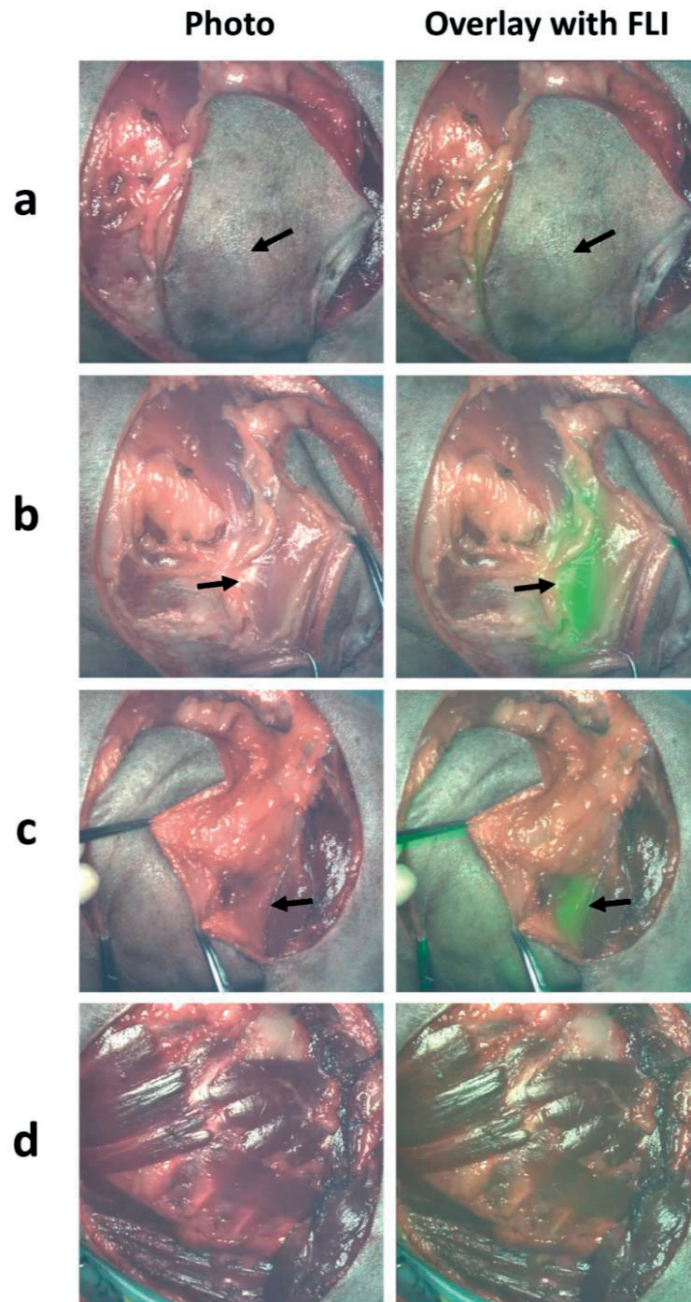


**Figure 2.20** Intraoperative *in vivo* fluorescence imaging of mastocytoma in a dog using ICG-FA probe. A canine patient with mastocytoma was injected intravenously with ICG-FA (0.32 mg/kg, 200  $\mu$ M solution in PBS containing 0.1% (w/v) fatty acid free BSA). 10 h post injection *in vivo* fluorescence imaging and fluorescence-guided tumor surgery were performed. The images demonstrate a photograph (left) and an overlay of a photograph with a fluorescence image (FLI) (right). Fluorescence is represented by green pseudocolor. (a) Tumoral area with skin dissected around the tumor. (b) Left tumor margin is exposed. (c) Right tumor margin is exposed. (d) Wound bed after tumor excision. Arrows indicate the tumor. Imaging was performed using Solaris open-air fluorescence imaging system (PerkinElmer) with a fluorescent channel 800 nm. The imaging experiment was performed by Dr. Arno Roos (Veterinair Verwijscentrum Gouda, Netherlands).



The excised tumor tissue was imaged *ex vivo* and showed strong fluorescence that was detectable through the intact skin above the tumor (Figure 2.21).

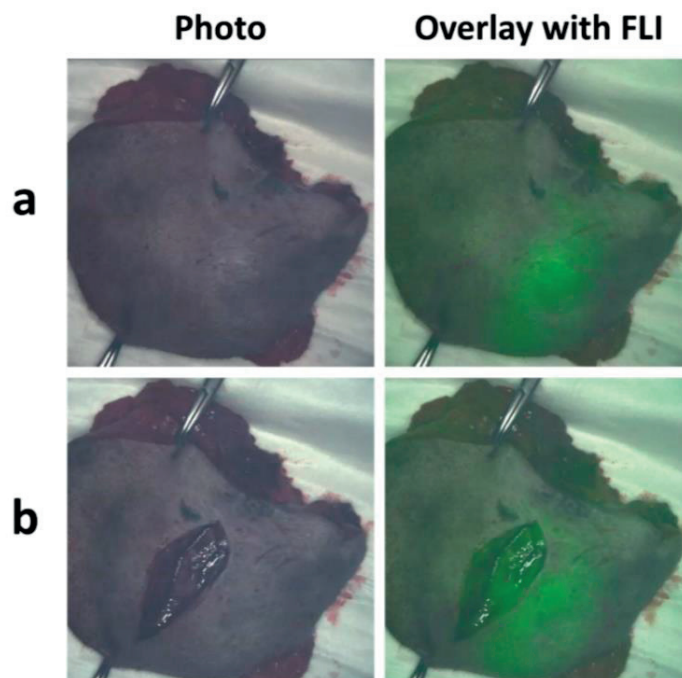


**Figure 2.21** *Ex vivo* fluorescence imaging of excised mastocytoma from a canine patient injected i.v. with ICG-FA (0.32 mg/kg) 10 h prior to surgery. The images demonstrate a photograph (left) and an overlay of a photograph with a fluorescence image (FLI) (right). Fluorescence is represented by green pseudocolor. (a) Images of excised tissue with the intact skin above the tumor. (b) Images of excised tissue with dissected skin above the tumor. Imaging was performed using Solaris open-air fluorescence imaging system (PerkinElmer) with a fluorescent channel 800 nm. The imaging experiment was performed by Dr. Arno Roos (Veterinair Verwijscentrum Gouda, Netherlands).

Although, the exact mechanism of the probe accumulation in this type of tumor is not clear, this result demonstrates the ability of ICG-FA to target mastocytoma *in vivo*. Enhanced permeability and retention (EPR) effect that is known to be present in various tumors may play role in ICG-FA targeting mastocytoma. Another possible mechanism could be the upregulation of long-chain fatty acid uptake in mastocytoma cells. One study found that the uptake rate of a polyunsaturated long-chain fatty acid arachidonic acid was very fast in murine mastocytoma cells (171), which suggests the involvement and possible upregulation of the protein-mediated fatty acid uptake mechanism in these cells that can be shared for the uptake of other types of long-chain fatty acids (116).

This proof-of-concept experiment demonstrates the applicability of the ICG-FA probe for image-guided tumor surgery that provides valuable optical guidance for a surgeon during the tumor resection allowing maximal cancer excision with preservation of healthy surrounding tissues. The

established ability of ICG-FA to target glioma in murine tumor models suggests that the probe may also be applicable for image-guided surgery of glioma.

## 2.3 Experimental Section

### 2.3.1 Materials and methods. Chemical part

**General information.** All reactions were performed under inert atmosphere of nitrogen unless otherwise noted. The solvents and reagents were ordered from Acros, Sigma-Aldrich, TCI, Fluorochem and were used as received. Analytical thin-layer chromatography was carried out using SiO<sub>2</sub>-coated glass plates (DC Kieselgel 60G F<sub>254</sub>, Merck). The compounds on TLC plates were visualized by UV-light at 254 nm or by immersing the plates in cerium molybdate solution followed by heating. LCMS analysis was carried out with Waters Acquity UPLC system with Acquity UPLC® BEH C8 or C18 column (2.1 × 50 mm, 1.7 μm) connected to Waters Acquity LC/MS system or with Agilent Infinity 1260 HPLC system (Agilent, Santa Clara, CA) using SunFire® C18 column (2.1 × 20 mm, 3.5 μm) connected to Quadrupole LC/MS system (Agilent). Degassed HPLC grade solvents from Fisher Chemicals and Millipore water were used for LCMS analysis. Preparative HPLC purification was performed with Waters preparative HPLC system connected to XTerra® Prep MS C18 OBD™ column (5 μm, 19 × 50 mm) using HPLC grade solvents from Fisher Chemicals and Millipore water. Nuclear magnetic resonance spectra were acquired on Bruker AV-400 MHz spectrometer. NMR chemical shifts are reported in parts per million δ (ppm) using the central line of the solvent residual proton and carbon signal as an internal reference. Splitting patterns are defined as s (singlet), d (doublet), dd (doublet of doublets), t (triplet), q (quartet), m (multiplet), br (broad). HRMS measurements (ESI-HRMS) were performed at the EPFL Mass Spectrometry Service using Micro Mass QTOF Ultima (Waters).

**Methyl 16-azidohexadecanoate (2)** was synthesized following a modified procedure described in (189). Sodium azide (746 mg, 11.5 mmol) was added to a solution of methyl 16-bromohexadecanoate (2.0 g, 5.74 mmol) in DMF (20 mL) at RT and then the mixture was stirred at 90°C for 14 h under N<sub>2</sub>. Next, the reaction mixture was cooled to RT and then diluted with AcOEt (80 mL) and then mixed with water (100 mL). A separated water phase was extracted with AcOEt (2 × 40 mL). Combined organic fractions were washed with brine (2 × 50 mL), then dried with Na<sub>2</sub>SO<sub>4</sub> and then concentrated in vacuo to give almost colourless oil, which upon drying in high vacuum yielded a white solid of **2** (1.71 g, 99% yield), which was directly used in the next step without purification. <sup>1</sup>H NMR (400 MHz, CDCl<sub>3</sub>) δ 3.66 (s, 3H), 3.25 (t, *J* = 7.0 Hz, 2H), 2.30 (t, *J* = 7.6 Hz, 2H), 1.68-1.53 (m, 4H), 1.41-1.19 (m, 22H).

**Methyl 16-aminohexadecanoate hydrochloride (3)** was synthesized following a modified procedure described in (189). Methyl 16-azidohexadecanoate **2** (860 mg, 2.76 mmol) was dissolved in MeOH (35 mL) followed by three vacuum-N<sub>2</sub> cycles. Then, 5% Pd/C (175 mg) and aqueous 6 M HCl (2.3 mL, 13.8 mmol) were added to the reaction mixture under N<sub>2</sub>. The reaction flask was filled with

H<sub>2</sub>, and the compound **2** was hydrogenated under normal pressure for 4 h. The catalyst was removed by filtration through a pad of Celite and the filtrate was concentrated *in vacuo* to provide the product **3**, which was directly used in the next step without purification. **MS** (ESI): calculated for C<sub>17</sub>H<sub>36</sub>NO<sub>2</sub> [M+H]<sup>+</sup> 286.3, found 286.3.

**16-Aminohexadecanoic acid hydrochloride (4).** The whole amount of ester **3** obtained in the previous step was dissolved in MeOH (25 mL) followed by dropwise addition of 4.5 M NaOH (6 mL, 27.3 mmol) under stirring at RT. The resultant suspension was sonicated for 5 min and then was stirred overnight at RT. Next, the reaction mixture was evaporated *in vacuo* to dryness and then was redispersed in aqueous 1.2 M HCl (35 mL) followed by filtration. A separated white precipitate was washed on a filter with aqueous 1.2 M HCl (2 × 20 mL) followed by drying in vacuum to give the product **4** as a white solid (816 mg, 96% yield), which was used in the following synthesis without purification. **MS** (ESI): calculated for C<sub>16</sub>H<sub>34</sub>NO<sub>2</sub> [M+H]<sup>+</sup> 272.3, found 272.3.

**4-(1,1,2-trimethyl-1H-benzo[e]indol-3-ium-3-yl)butane-1-sulfonate (6)** was prepared following the procedure described in (190). 1,1,2-trimethyl-1H-benzo[e]indole **5** (5.00 g, 23.9 mmol) was mixed with 1,4-Butanesultone (3.25 g, 23.9 mmol) and the reaction mixture was refluxed for 3 h at 130°C. The black solid was filtered and washed with acetone (3 × 30 mL) and then dried *in vacuo* to afford the product **6** as a grey powder (5.50 g, 67%). **MS** (ESI): calculated for C<sub>19</sub>H<sub>24</sub>NO<sub>3</sub>S [M+H]<sup>+</sup> 346.2, found 346.2.

**4-(1,1-dimethyl-2-((1E,3E,5E)-6-(N-phenylacetamido)hexa-1,3,5-trien-1-yl)-1H-benzo[e]indol-3-ium-3-yl)butane-1-sulfonate (7)** was prepared following a modified procedure described in (191). Sulfonate **6** (1.21 g, 3.51 mmol) was mixed with acetic anhydride (50 mL) followed by addition of *N*-[5-(phenylamino)-2,4-pentadienylidene]aniline monohydrochloride (1.0 g, 3.51 mmol), and the resultant mixture was stirred at 100°C for 1.5 h. After cooling down, the mixture was mixed with water (30 mL) and the formed precipitate was isolated and washed with water (1 × 30 mL) and then with Et<sub>2</sub>O (3 × 20 mL) followed by drying *in vacuo* to give the product **7** as a violet solid (1.45 g, 76% yield). **MS** (ESI): calculated for C<sub>32</sub>H<sub>35</sub>N<sub>2</sub>O<sub>4</sub>S [M+H]<sup>+</sup> 543.2, found 543.2.

**6-(1,1,2-trimethyl-1H-benzo[e]indol-3-ium-3-yl)hexanoate (8).** 1,1,2-trimethyl-1H-benzo[e]indole **5** (969 g, 4.63 mmol) was dissolved in nitromethane (1 mL) in a tube for microwave synthesis, followed by addition of 6-bromohexanoic acid (903 mg, 4.63 mmol). The resultant suspension was sonicated for 5 min and then was heated in a microwave reactor at 150°C for 2 h. After cooling down, the reaction mixture was mixed with Et<sub>2</sub>O (30 mL) to form a sticky solid, which was filtered and mixed again with Et<sub>2</sub>O (30 mL) followed by sonication. Dark-brown powder was separated and mixed with DCM (10 mL) followed by sonication. The solid was filtered and washed with DCM

(1 × 5 mL), then with Et<sub>2</sub>O (3 × 20 mL) and then was dried *in vacuo* to provide the product **8** as a purple powder (1.17 g, 78% yield). **MS** (ESI): calculated for C<sub>21</sub>H<sub>26</sub>NO<sub>2</sub> [M+H]<sup>+</sup> 324.2, found 324.2.

**4-(2-((1*E*,3*E*,5*E*,7*E*)-7-(3-(5-carboxypentyl)-1,1-dimethyl-1,3-dihydro-2*H*-benzo[*e*]indol-2-ylidene)hepta-1,3,5-trien-1-yl)-1,1-dimethyl-1*H*-benzo[*e*]indol-3-ium-3-yl)butane-1-sulfonate (9).** Compound **7** (336 mg, 0.62 mmol) was dissolved in pyridine (9.5 mL), followed by addition of the intermediate **8** (250 mg, 0.77 mmol), and the resultant mixture was stirred at 40°C for 30 min under N<sub>2</sub>. Then, the mixture was concentrated *in vacuo* and the solid obtained was dissolved in DCM with subsequent addition of toluene (15 mL), and then the solvents were evaporated *in vacuo*. The green residue was purified by SiO<sub>2</sub> column chromatography using a gradient elution with a mixture of DCM-MeOH (from 0% to 12% (v/v) of methanol) to give a dark green powder of the product **9** (222 mg, 49%). **MS** (ESI): calculated for C<sub>45</sub>H<sub>51</sub>N<sub>2</sub>O<sub>5</sub>S [M+H]<sup>+</sup> 731.35, found 731.30.

**4-(2-((1*E*,3*E*,5*E*,7*E*)-7-(3-(6-((15-carboxypentadecyl)amino)-6-oxohexyl)-1,1-dimethyl-1,3-dihydro-2*H*-benzo[*e*]indol-2-ylidene)hepta-1,3,5-trien-1-yl)-1,1-dimethyl-1*H*-benzo[*e*]indol-3-ium-3-yl)butane-1-sulfonate (11).** Monocarboxylic analog of ICG **9** (6 mg, 8.2 μmol) was dissolved in DMF (0.5 mL) followed by addition of *O*-(*N*-Succinimidyl)-*N,N,N',N'*-tetramethyluronium tetrafluoroborate (TSTU) (3.2 mg, 10.6 μmol) and DIPEA (1.7 μl, 9.8 μmol). The mixture was stirred for 1 h at RT with protection from light to produce *N*-hydroxysuccinimide derivative **10**, the formation of which was monitored by LCMS analysis. Then, a suspension of compound **4** (7.6 mg, 24.6 μmol) in DMSO (1 mL) was added directly to the reaction mixture containing NHS-ester **10** followed by addition of DIPEA (4.3 μl, 24.8 μmol) and stirring for 20 h at RT under N<sub>2</sub> with protection from light. Next, the mixture was concentrated *in vacuo* and the residue was purified by preparative HPLC (C18 column, solvent A: H<sub>2</sub>O + 0.1% formic acid, solvent B: acetonitrile + MeOH 1:1 (v/v), gradient: from 20% to 100% of solvent B over 10 min) to afford pure ICG-FA (**11**) as a dark-green solid (6 mg, 74% yield). **HRMS** (ESI): calculated for C<sub>61</sub>H<sub>81</sub>N<sub>3</sub>NaO<sub>6</sub>S [M+Na]<sup>+</sup> 1006.5744, found 1006.5704.

### 2.3.2 Materials and methods. Biological part.

**Cell lines.** 3T3-L1 cells were obtained from ATCC. U87MG-luc cells were obtained from Dr. Aleksey Yevtodiyenko.

**3T3-L1 differentiation into adipocytes.** 3T3-L1 fibroblasts were grown in Dulbecco's Modified Eagle Medium (DMEM) containing 4.5 g/L glucose, 10% fetal calf serum and 1% penicillin/streptomycin. Differentiated cells were generated by treating fibroblasts 48 hours post-confluency with DMEM containing 10% fetal bovine serum (FBS) and 1% penicillin/streptomycin, 1 μg/ml insulin, 0.25 μM dexamethasone, 0.5 mM IBMX and 2 μM rosiglitazone (DM1-R medium) for

48 h. Then DM1-R medium was replaced by DMEM containing 10% FBS and 1% penicillin/streptomycin, supplemented with 1  $\mu\text{g}/\text{ml}$  insulin (DM2) for 48 h, followed by maintenance in DMEM containing 10% FBS and 1% penicillin/streptomycin (DMS). Differentiated adipocytes were used between day 8 and day 12 after initiating the differentiation with DM1-R.

**ICG-FA uptake experiments in 3T3-L1 cells.** 3T3-L1 fibroblasts were seeded in 6 well plates (Corning® CellBIND® 6 Well Clear Multiple Well Plates, Flat Bottom, with lid, Sterile, Product #3335) at density 3000 cells/cm<sup>2</sup> in DMEM (4.5 g/L glucose) containing 10% fetal calf serum and 1% penicillin/streptomycin. Differentiation into adipocytes was performed as described above. ICG-FA and BODIPY-FA (BODIPY™ FL C16, ThermoFisher Scientific, Cat. # D3821) were dissolved in DMSO to get 10 mM or 50 mM stock solutions and were stored under nitrogen in darkness at -20°C. Prior to the experiments the stock solutions were diluted in 0.1% fatty acid-free BSA in HBSS (with Ca<sup>2+</sup> and Mg<sup>2+</sup>) to get the final uptake solutions, unless otherwise noted. Sodium oleate was dissolved in Millipore water to get 100 mM stock solution and aliquots were stored under nitrogen in darkness at -20°C.

For the fluorescence microscopy study, fibroblasts and adipocytes were seeded in a 8-well chamber slide 24 h before the experiment. After starvation in FBS-free DMEM for 1 h the cells were incubated with an uptake solution containing a mixture of BODIPY-FA (1  $\mu\text{M}$ ) and ICG-FA (5  $\mu\text{M}$ ) in HBSS containing 0.1% fatty acid free BSA for 30 min at 37°C and then were washed three times with 0.5% fatty acid-free BSA-HBSS for 10 min on ice. Next, the nuclei were stained with Hoechst 33342 (1  $\mu\text{g}/\text{mL}$ ) for 5 min followed by washing with PBS. Live-cell fluorescence microscopy was performed using EVOS FL Auto Cell Imaging System at 40× magnification applying the same imaging settings for both fibroblasts and adipocytes for each fluorescent channel.

For the dose-response experiment, 3T3-L1 fibroblasts and adipocytes grown in 6 well plates were serum starved in FBS-free DMEM (4.5 g/L glucose) for 1 h before the assay and then were incubated with ICG-FA solutions (1-50  $\mu\text{M}$ ) in 0.1% fatty acid-free BSA-HBSS for 30 min. Following the incubation the cells were rinsed with HBSS containing 0.1% fatty acid free BSA and then were washed three times with 0.5% fatty acid-free BSA-HBSS for 10 min while keeping the cells on ice. After washing the cells were rinsed with PBS and trypsinized, and then the cell suspension was diluted with 0.1% fatty acid free BSA-HBSS followed by centrifugation at 1300 rpm for 5 min. The cell pellet was resuspended in 1 ml of absolute MeOH followed by sonication to give a fine dispersion. The cell dispersions were loaded in Corning® clear bottom black wall 96 well plates (200  $\mu\text{l}$  per well) in triplicates and fluorescence measurements were performed using Tecan Safire2 plate reader at  $\lambda_{\text{ex/em}}$  785/815 nm.

Kinetics of ICG-FA uptake in 3T3-L1 cells was measured by incubating the cells with a solution of ICG-FA (20  $\mu\text{M}$  in HBSS containing 0.1% fatty acid free BSA) for the indicated time periods (0-90 min)

followed by processing the cells using the protocol as described above for the dose-response experiment.

For the competition experiment with oleate, an uptake solution of ICG-FA (1  $\mu$ M) was prepared in HBSS supplemented with 2% of HEPES followed by the addition of sodium oleate (100 mM stock solution) to obtain the indicated final concentrations of oleate. Cell incubations and all the following steps were performed according to the protocol described above for the dose-response assay.

**ICG-FA uptake experiments in U87MG-luc cells.** U87MG-luc cells were grown in Eagle's Minimum Essential Medium (EMEM) containing 10% FBS and 1% penicillin/streptomycin.

For the fluorescence microscopy study, U87MG-luc cells were seeded in a 8-well chamber slide ( $10^4$  cells per well) 24 h before the experiment. After starvation in FBS-free DMEM for 1 h the cells were incubated with ICG-FA (20  $\mu$ M) in HBSS containing 0.1% fatty acid free BSA for 3 h at 37°C and then were washed three times with 0.5% fatty acid-free BSA-HBSS for 10 min on ice. Next, the nuclei were stained with Hoescht 33342 (1  $\mu$ g/mL) for 5 min followed by washing with PBS. Live-cell fluorescence microscopy was performed with EVOS FL Auto Cell Imaging System applying 40 $\times$  magnification using the near-infrared EVOS light cube.

For the comparison of ICG-FA and ICG uptake, U87MG-luc cells were seeded in Corning® CellBIND® 6 Well Clear Multiple Well Plates 24 h before the experiment. After starvation in FBS-free EMEM for 1 h the cells were incubated with ICG-FA or ICG (1-20  $\mu$ M for each probe) in HBSS containing 0.1% fatty acid free BSA for 3 h at 37°C and then the cells were processed using the protocol as described above for the dose-response experiment in 3T3-L1 cells.

**Animal experiments.** Animals were housed and treated in accordance with the animal protocols approved by the Swiss Federal Food Safety and Veterinary Office. The canine experiment was performed in accordance with the regulations at Veterinair Verwijscentrum Gouda, Netherlands.

**Imaging Equipment and Software.** Mice imaging was performed using the IVIS Spectrum imaging system (PerkinElmer). Photon fluxes of regions of interest were calculated with the IVIS Living Image software.

**Biodistribution studies of ICG-FA.** Two groups of Swiss nu/nu mice were injected intravenously with ICG-FA (group 1) and ICG (group 2) (20 nmol/25 g, 100  $\mu$ M solution in 0.1% fatty acid free BSA in PBS) followed by fluorescence imaging under anesthesia with 2% isoflurane in oxygen.

**Glioma imaging in a subcutaneous xenograft mouse model.** Swiss nu/nu female mice (6-7 weeks old) were injected with U87MG-luc cells ( $2 \times 10^6$  cells/mouse in 100  $\mu$ L PBS) subcutaneously into

the lower dorsal side. For bioluminescence imaging of xenografts the mice were injected intraperitoneally with D-luciferin potassium salt (3 mg/kg in PBS) 10 min before imaging. Fluorescence imaging was performed when the tumors reached 4-7 mm in diameter. Xenograft bearing mice were administered intravenously with ICG-FA or ICG (20 or 50 nmol/25 g, 100  $\mu$ M solution in 0.1% fatty acid free BSA in PBS) followed by *in vivo* fluorescence imaging under anesthesia with 2% isoflurane in oxygen.

For *ex vivo* imaging experiment, the mice were first injected with ICG-FA or ICG (50 nmol/25 g) and imaged 15 h post injection. Then the animals received injection of D-luciferin potassium salt (3 mg/kg in PBS) followed by bioluminescence imaging 10 min post injection. Immediately after that the mice were euthanized and the xenografts and the brains were excised and imaged *ex vivo*.

**Glioma imaging in a transgenic mouse model.** The experiment was performed in collaboration with Dr. Ksenya Shchors (Prof. Douglas Hanahan lab, EPFL) who provided the animals. Symptomatic *GRLp53<sup>ko</sup>* mice and wild-type FVB/NJ mice were intravenously injected with ICG-FA or ICG (20 nmol/25 g, 100  $\mu$ M solution in 0.1% fatty acid free BSA in PBS). After 2 h the mice were sacrificed followed by harvesting the brains and *ex vivo* imaging. Then, the brains were fixed by zinc formalin fixative followed by histopathological analysis using hematoxylin and eosin staining (performed by Dr. Ksenya Shchors).

**Intraoperative mastocytoma imaging using ICG-FA in a canine patient.** The experiment was executed by veterinarian Dr. Arno Roos (Veterinair Verwijscentrum Gouda, Netherlands) who selected the dog with mastocytoma, carried out the probe administration according to the provided experimental protocol, performed surgery and *in vivo* and *ex vivo* tumor imaging. The dog with mastocytoma was intravenously injected with ICG-FA solution (0.32 mg/kg, 200  $\mu$ M in PBS containing 0.1% fatty acid free BSA) 10 h before the surgery. Intraoperative *in vivo* and *ex vivo* tumor imaging was performed using Solaris open-air fluorescence imaging system (PerkinElmer) with a fluorescent channel 800 nm.



## 2.4 Supplementary figures

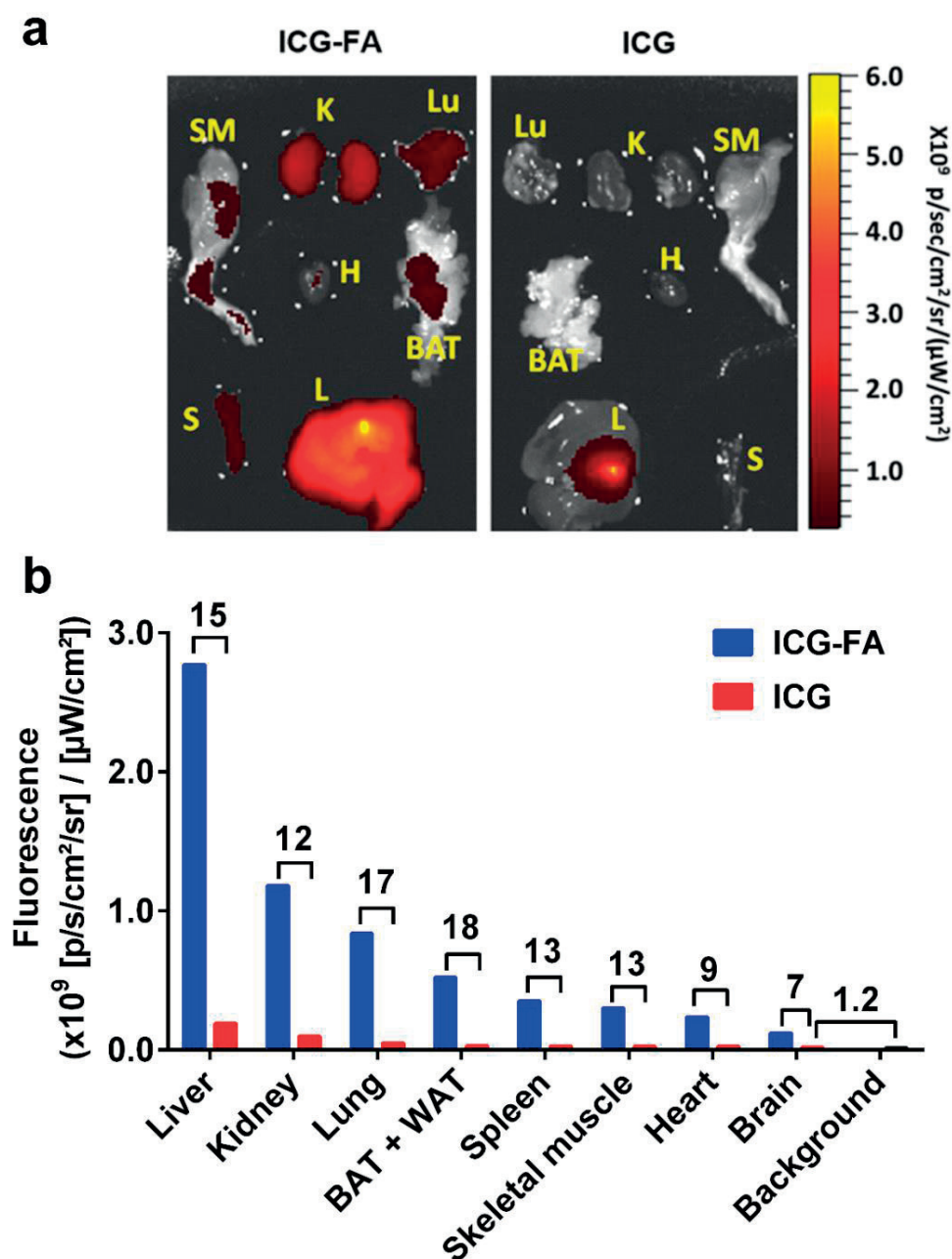


**Figure S2.1** Comparison of ICG-FA and ICG biodistribution in healthy FVB/NJ mice. Mice were injected with ICG-FA or ICG (20 nmol/25 g) and sacrificed 2 h postinjection. Organs were harvested and imaged using IVIS Spectrum imaging system. (a) Fluorescence images of harvested organs. SM - skeletal muscles, K - kidney, Lu - lung, H - heart, BAT - brown adipose tissue with surrounding white adipose tissue, S - spleen, L - liver. (b) Measured fluorescence from harvested organs. The measurement was performed using the same size region of interest (ROI) for all organs.

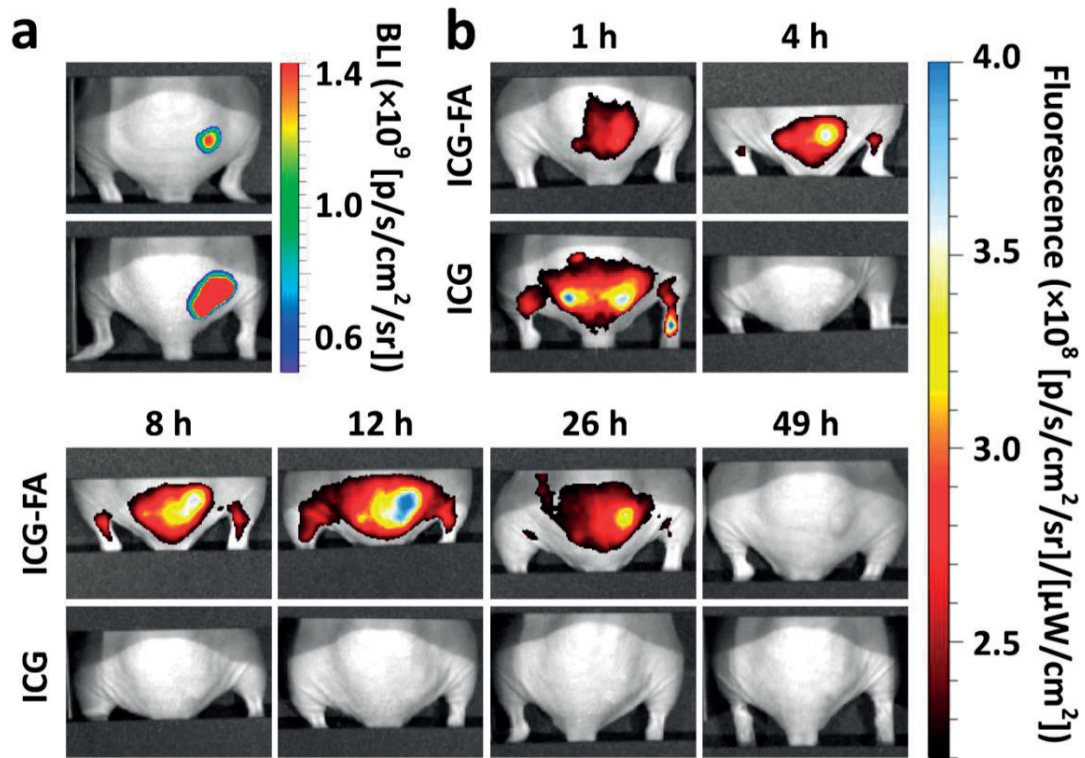


**Figure S2.2** *In vivo* imaging of glioma xenografts in a mouse model. Swiss nu/nu mice bearing subcutaneous tumors (U87MG-luc) were injected with D-luciferin potassium salt (3 mg/kg in PBS i.p.) followed by bioluminescence imaging 10 min post injection. After 24 h the mice were injected with ICG-FA or ICG (50 nmol/25 g for both probes i.v.) and fluorescence was monitored over 24 h. (a) Representative bioluminescence images of tumor xenografts following D-luciferin injection. (b) Representative fluorescence images of tumor xenografts at indicated time points post injection over 0-24 h following ICG-FA or ICG administration. The images correspond to the same mice, which are shown in (a). For ICG-FA n = 3, for ICG n = 2.

## Chapter 3 Bioluminescence Imaging of Triglyceride Uptake

Triglycerides (TGs) are a major lipid component in the diet comprising 95% of consumed lipids (192). They are one of the most important energy sources providing about 40% of daily calories in the Western diet (192, 193). TGs deposited in the adipose tissue and in the liver constitute the main form of energy storage in the human body (194). Dietary TGs act as a source of fatty acids including essential fatty acids that cannot be synthesized by humans and must be taken up with food. Dietary TGs also act as a vehicle for fat-soluble vitamins. Intact triglycerides cannot pass through the gastrointestinal barrier, as they should be hydrolysed first by gastrointestinal lipases in order to be absorbed (195-200). The stomach and the small intestine are the major organs of triglyceride digestion and absorption, where important physico-chemical and enzymatic processes take place that enable efficient uptake of the lipolysis products of TGs by enterocytes (192, 193, 195, 201). The efficiency of TG absorption by the digestive system under normal conditions is more than 95% (193, 202). Although TGs play important nutritional role, their increased consumption may lead to the development of obesity, the metabolic syndrome, cardiovascular disease, non-alcoholic fatty liver disease, diabetes, and cancer (203-207). Considering the high significance of TGs for human health and nutrition, studies of TG absorption *in vivo* and monitoring its changes in various physiological and pathological conditions as well as a result of pharmacotherapy and certain approaches for modulating lipid digestion are of great importance (208-212).

### 3.1 Triglyceride structure

Triglyceride molecules consist of a glycerol backbone and three acyl groups attached to it via ester bonds (Figure 3.1). Since TGs may contain different fatty acids, their positions are designated by the stereochemical numbering system (*sn*). If the acyl group of a TG, which is connected to the middle carbon of glycerol, is drawn to the left in the Fischer projection, then the top, the middle and the bottom carbons of glycerol become designated as *sn*-1, *sn*-2 and *sn*-3 respectively (Figure 3.1) (213, 214). In most TGs the acyl groups at *sn*-1 and *sn*-3 positions are different, which makes the *sn*-2 carbon asymmetric, and therefore two enantiomers for such TGs exist.

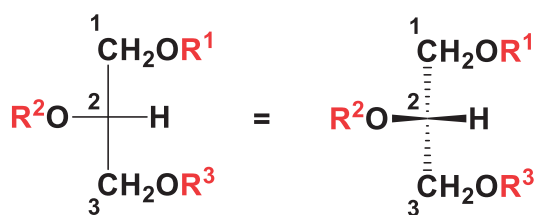


**Figure 3.1** The general stereochemical structure of a triglyceride. Fischer (left) and wedge-and-dash (right) projections.  $R^1$ ,  $R^2$  and  $R^3$  represent different acyl groups. For the  $R^2O$ -group drawn to the left in the Fisher projection, the top carbon of the glycerol backbone is designated as *sn*-1, the middle carbon is designated as *sn*-2, and the bottom carbon is designated as *sn*-3 (214).

Each type of fat (vegetable oil, animal fat) consists of hundreds of different complex triglycerides due to the presence of various types of fatty acyl chains in TG molecules (213). The aliphatic chain length of fatty acids can vary from 4 to 28 carbons, which determines their classification: short chain (< 6 carbons), medium chain (6 to 12 carbons), long chain (13 to 21 carbons), and very long chain ( $\geq 22$  carbons) (215). In turn, the length of the fatty acyl chains in TG molecules defines the nomenclature of short-chain TGs (SCTGs), medium-chain TGs (MCTGs) and long-chain TGs (LCTGs) (215). The majority of dietary triglycerides are LCTGs, which may contain both saturated and unsaturated fatty acids (192, 213, 216). MCTGs provide less calories than LCTGs, 8.3 kcal/g and 9.2 kcal/g respectively (215, 217). Examples of TGs, which are present in some dietary fats and oils, are shown in **Figure 3.2**.

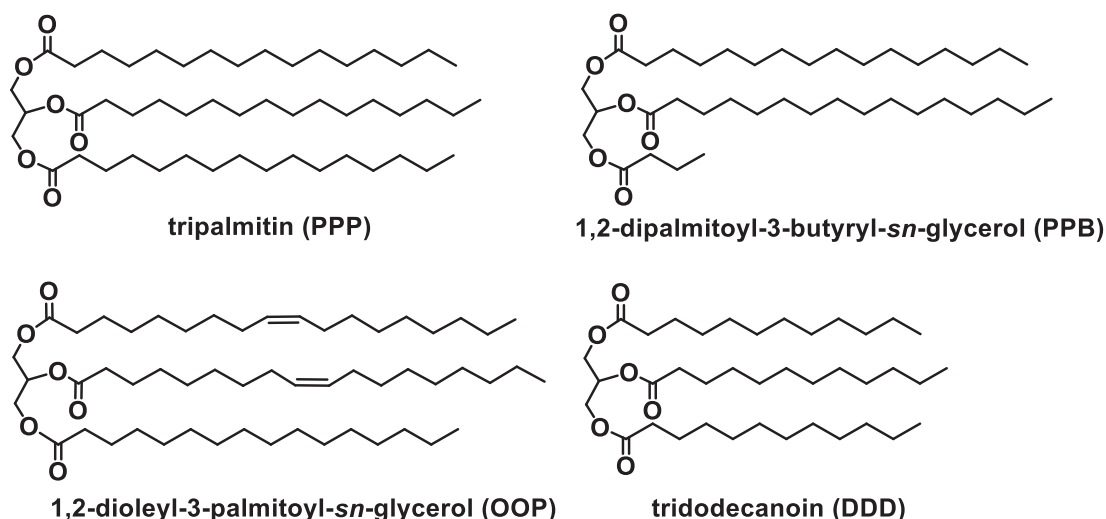


**Figure 3.2** Triglycerides which are present in some natural fats and oils.

LCTG tripalmitin (PPP) is present in palm oil (218). 1,2-dipalmitoyl-3-butyryl-*sn*-glycerol (PPB) and 1,2-dioleoyl-3-palmitoyl-*sn*-glycerol (OOP) are major components in butter fat and olive oil respectively (213). MCTG tridodecanoin (DDD) is a major constituent of the coconut oil (213).

## 3.2 Intestinal absorption of triglycerides

Intact triglycerides cannot be absorbed in the gastrointestinal tract. The digestion of dietary TGs requires several sequential physicochemical and enzymatic processes that convert TGs into more water-soluble products, which can be absorbed by enterocytes (195-200). The first step results in emulsification of dietary fat in the stomach. During the second step, the emulsion undergoes enzymatic hydrolysis in the stomach and small intestine by the action of gastrointestinal lipases. Then, the products of TG hydrolysis are solubilized in mixed micelles with bile salts and phospholipids and are transported to the surface of enterocytes. During the last step, the lipolytic products (fatty acids and *sn*-2-monoacylglycerol) are taken up by enterocytes, reassembled into TGs and secreted as chylomicrons from the basolateral side of the cells into the lymphatic system (derived from LCTG) or predominantly into the portal vein as free fatty acids (derived from MCTG) (192, 196, 201, 215, 216, 219).

### 3.2.1 Gastric lipid digestion

The digestion of dietary lipids starts in the stomach, where they first undergo emulsification to form lipid droplets due to mechanical processing (propulsion, grinding, retroplulsion) by stomach peristalsis. Emulsification leads to an increase of the surface area of the lipid-water interface, which is necessary for the efficient TG digestion by lipases, since lipases are water-soluble enzymes that exhibit their activity only on the surface of water-insoluble substrates (192, 195, 220). Potential emulsifying agents that act in the acidic environment of the stomach are digestion products of dietary proteins, complex polysaccharides and phospholipids (220). The generated lipid droplets consist of a hydrophobic core, which includes the majority of TG molecules mixed with esterified cholesterol and fat soluble vitamins, and a surface monolayer containing phospholipids, free cholesterol and small amount of TGs (2-5 mol%) available for cleavage by lipases (221).

Gastric lipolysis of TGs takes place by the action of acid-stable preduodenal lingual and gastric lipases. Humans produce predominantly gastric lipase, whereas rodents produce predominantly lingual lipase (201). One study reported that lingual lipase activity in humans has only 0.015% of the total gastric lipase activity (222). Human gastric lipase consists of 379 amino acid residues with a molecular weight of about 50 kDa and has close homology with rat lingual lipase, which is composed of 377 amino acid residues (223). Both lingual and gastric lipases show lack of homology with porcine pancreatic lipase and do not require any cofactors such as colipase (223). Lingual and gastric lipases perform their catalytic action under acidic conditions and have a pH optimum between pH 4.0 and 6.0 (224). Preduodenal lipases are inhibited only by 20% in the presence of bile salts above their critical micellar concentration, which is in contrast to pancreatic lipase that has 100% inhibition by bile salts (220). Gastric lipase is still active at pH 6.5-7.0, therefore it can continue to hydrolyze TGs in the

duodenum, where pH is between 6 and 7 (201, 225). Preduodenal lipases preferentially cleave fatty acids at the *sn*-3 position of TGs, which occurs two times faster than the cleavage at the *sn*-1 position (201, 221, 226), and these lipases possess 5-8-fold higher activity towards MCTG than towards LCTG (227). The gastric lipolysis results in the digestion of 10-30% of dietary TGs and leads to the formation of diacylglycerols and fatty acids as major lipolytic products and monoacylglycerols as minor products, which together with dietary phospholipids facilitate the emulsification of lipids in the stomach (192, 201, 221, 228, 229). The protonated free long-chain fatty acids generated in the course of gastric lipolysis provide a feedback inhibition of gastric lipase, as the lipase becomes entrapped in free fatty acid-rich particles that are formed on the droplets surface during lipolysis (230). This phenomenon explains the relatively limited degree of gastric lipolysis (10-30%). For the same amount of TGs smaller initial lipid droplet size facilitates gastric lipolysis and increases the extent of TG digestion in the stomach, since under physiological conditions lipases are released in excess relative to its substrate, and larger lipid-water interface allows the binding of the higher number of lipase molecules to the TG substrate (219, 231). At the same time, the larger interface area delays inhibition of gastric lipase by free fatty acids, since high surface concentrations of fatty acids inhibiting the lipolysis are reached at later time points for larger surface areas (231). Taken together, the TG lipolysis in the stomach has an important contribution to the total TG digestion, since it hydrolyzes 10-30% of TGs and promotes fat emulsification by generated lipolytic products, therefore it facilitates the final digestion of lipids by pancreatic lipase (219). Moreover, in conditions of physiological (infants) and pathological (pancreatitis, cystic fibrosis) pancreatic deficiency gastric lipase plays a crucial role in the TG digestion (219, 221).

### 3.2.2 Intestinal lipid digestion

Following gastric digestion, partially hydrolyzed lipid emulsion enters the duodenum, where lipolysis is completed by the action of pancreatic enzymes. The duodenal entry of the gastric chyme containing free fatty acids triggers the release of a peptide hormone cholecystokinin (CCK) into the circulation, which stimulates the pancreatic secretion of digestive enzymes, activates gallbladder contraction with release of bile into the duodenum and slows gastric emptying (220, 232). Pancreas produces several enzymes with lipolytic activity: colipase-dependent lipase or pancreatic lipase (PL), carboxyl ester lipase (also named cholesterol ester hydrolase, cholesterol esterase, carboxylic ester hydrolase or bile salt-stimulated lipase) and phospholipase A<sub>2</sub> (195, 221). Pancreatic secretions also contain two pancreatic lipase-related proteins (PLRP1 and PLRP2), which have structural homology with pancreatic lipase, with only PLRP2 possessing TG lipase activity (197). The role of PLRP1 and PLRP2 in lipid digestion remains unclear. Among various lipolytic enzymes PL plays a major role in the digestion of TGs (193, 196, 201, 220, 221). Human PL is a serine hydrolase with a single-chain

glycoprotein containing 449 amino acids and has a molecular weight 49,558 (200, 233). The catalytic triad of PL consists of serine (Ser152), histidine (His263) and aspartate (Asp176) (233, 234). The mechanism of TG lipolysis by pancreatic lipase is illustrated in **Figure 3.3**.

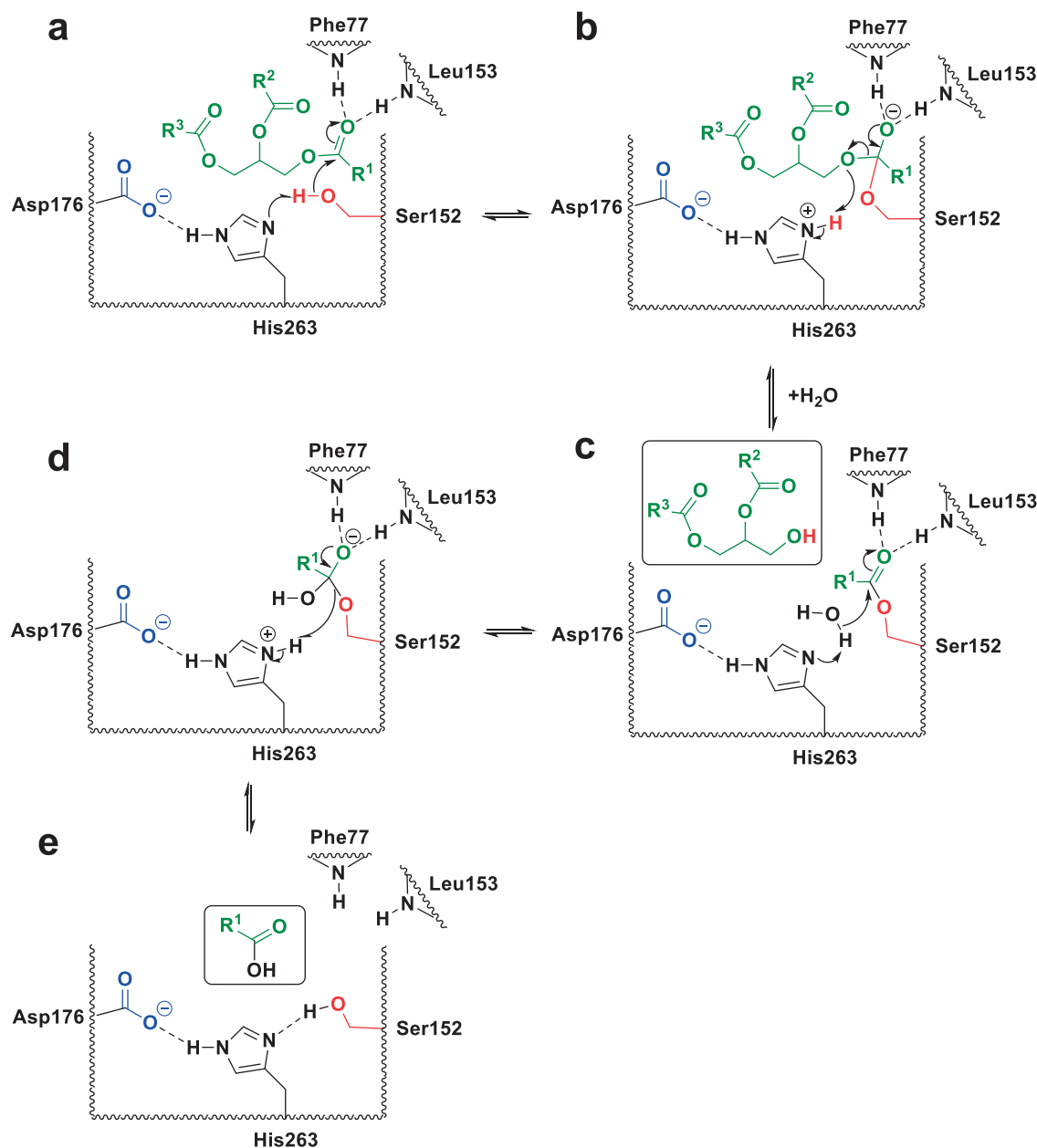


**Figure 3.3** Mechanism of pancreatic lipase catalysis.

During the first step, the hydroxyl group of Ser152 is deprotonated by His263, as the basicity of the latter is increased by hydrogen bonding to Asp176 (**Figure 3.3a**). This results in an increase of nucleophilicity of the hydroxyl residue of Ser152 that attacks the carbonyl group of one of the terminal fatty acyl chains of triglyceride producing the first tetrahedral intermediate (**Figure 3.3b**). The oxyanion hole formed by Phe77 and Leu153 stabilizes the negatively charged tetrahedral intermediate and



decreases the activation energy for its formation; therefore, it promotes the catalysis (234, 235). Then, the tetrahedral intermediate anion undergoes transformation with the restoration of the carbonyl group to form the acyl-enzyme intermediate, accompanied by the release of diglyceride as a leaving group (**Figure 3.3c**). During the following step, the acyl-enzyme intermediate undergoes a nucleophilic attack by a hydroxyl ion generated from a water molecule after donating its proton to His263 base. This attack produces the second tetrahedral intermediate, which is stabilized by the oxyanion hole (**Figure 3.3d**). Transformation of the tetrahedral intermediate anion restores the carbonyl group with the liberation of free fatty acid and release of the catalytic hydroxyl residue of Ser152 (**Figure 3.3e**) (234, 236). This catalytic triad is common to a large superfamily of lipases, esterases and thioesterases (237).

PL reaches the maximum of its catalytic activity in the range of pH 6.5-9.0 (238). The enzyme possesses much higher hydrolytic activity towards water-insoluble substrates such as TGs, than towards water-soluble substrates. It has been suggested that PL undergoes a conformational change, triggered by lipid-water interface, which is necessary for the catalytic site to become accessible for a substrate (200). For the lipolysis PL requires an additional protein, colipase, that enables efficient binding of lipase to the surface of lipid droplets (196).

In the small intestine the products of lipolysis are mixed with bile salts, phospholipids and cholesterol present in the bile with the formation of colloidal structures (multi- and unilamellar vesicles and mixed micelles), which provide solubilization of the lipolytic products in the intestinal lumen and their subsequent delivery to the brush border membrane of enterocytes for the cellular uptake. Incorporation of released fatty acids and monoglycerides into colloidal structures significantly facilitates the transport of these molecules across the unstirred water layer that acts as a barrier between the fluid phase in the intestine and the membrane of enterocytes (201, 239, 240). Interestingly, *sn*-2-monoglycerides can decrease the lipolysis of triglycerides as a result of their accumulation and absorption on the water-lipid interface, which prevents the access of lipase to the substrate. Therefore, *sn*-2-monoglycerides can have regulatory effect on lipolysis. Due to the action of bile salts *sn*-2-monoglycerides are solubilized and removed from the interface, which restores lipid digestion *in vivo* (211).

### 3.3 Methods for *in vivo* measurement of intestinal triglyceride absorption

Considering essential role of TGs in health and nutrition and their implication in a number of pathologies, methods and tools that allow measurement and quantification of intestinal triglyceride absorption *in vivo* are important for fundamental research as well as for clinical diagnostics. Existing



methods for *in vivo* measurement of intestinal triglyceride absorption are based on non-invasive and invasive protocols, and some of them require animal euthanasia.

A direct non-invasive method for the measurement of dietary fat absorption is a fat-balance assay, where the difference between fat intake and faecal fat excretion is calculated (241). However, this method is difficult in practice and has many limitations due to errors, as it requires accurate measurement of fat in the diet as well as complete collection of feces (242, 243). Another semiquantitative assay is based on fecal microscopy using stains for fat (244). Alternative method utilizing sucrose polybehenate as a non-absorbable marker was proposed by Tso and co-authors, where the marker that is non-hydrolyzable by gastrointestinal lipases was mixed with dietary fat and fed to rats and mice (242). Sucrose polybehenate is a component of a fat substituent olestra that is used commercially and has physical properties identical to that of TGs, but has no interference with absorption of dietary TGs. After animal feeding with the test food containing the marker a small fecal sample was assayed and fat absorption was determined from the ratios of behenic acid to other fatty acids in the diet and in feces, which was analyzed by gas chromatography of fatty acid methyl esters (242). An invasive approach that utilizes TG with odd-chain fatty acids was proposed as a fat absorption test, where simultaneous oral administration of odd-chain pentadecanoic acid and triheptadecanoin was followed by using gas-liquid chromatographic analysis of blood samples (245). This approach is based on the fact that odd-chain lipids are present in small quantities only in dairy food and their serum levels are very low (245).

Another group of methods for the assessment of intestinal TG absorption employs radiolabeled or stable isotope labeled TGs. Radiolabeled medium- and long-chain TGs as well as mixed TGs such as [ $^{14}\text{C}$ ]-trioctanoin, [ $^{14}\text{C}$ ]-tripalmitin, [ $^{14}\text{C}$ ]-triolein and 1,3-dioleoyl-2- $^{14}\text{C}$ -decanoyl glycerol have been proposed for non-invasive lipid absorption measurements in patients with pancreatic insufficiency, where the breath excretion of a fatty acid oxidation product  $^{14}\text{CO}_2$  was measured after oral administration of  $^{14}\text{C}$ -labeled TGs with a test meal (246-248). In a study performed by Greenberger et al. [ $^{14}\text{C}$ ]-tripalmitin and [ $^{14}\text{C}$ ]-trioctanoin were employed for the comparison of the intestinal hydrolysis and absorption of medium-chain TGs versus those of long-chain TGs in isolated intestinal loops of rats (249). In this study radiolabeled TGs were injected into the loops followed by radioactivity measurements of the excised intestine and collected blood samples.

Another radiolabeled TG tracer [9,10- $^3\text{H}$ ]-triolein is also utilized for dietary lipid absorption studies by analyzing feces, blood samples or excised intestine from animals fed with the probe (209, 250-252). Huggins et al. used [9,10- $^3\text{H}$ ]-triolein to measure the rate of lipid absorption in pancreatic lipase-knockout mice by measuring radioactivity in plasma after time point blood sampling (251). A study using [9,10- $^3\text{H}$ ]-triolein was performed by Hellgren et al. to investigate the influence of the emulsifier type on the intestinal TG absorption in mice by *ex vivo* analysis of the excised gastrointestinal

tract (209). In a study performed by Meier et al. radiolabeled TGs [9,10-<sup>3</sup>H]-triolein, [<sup>14</sup>C]-tripalmitin, [<sup>14</sup>C]-triolein and [<sup>14</sup>C]-tri-γ-linolenin were used to investigate the influence of the lipase inhibitor orlistat on the intestinal absorption of TGs in mice by measuring the residual radioactivity in feces excreted after oral administration of test meals mixed with the TG tracers (252).

TG probes containing radioactive iodine isotopes such as [<sup>125</sup>I]-triolein and [<sup>131</sup>I]-triolein were developed for the assessment of intestinal lipid absorption and were tested in humans and rats respectively (253, 254). These molecules were administered orally in a combination with a non-absorbable marker glycerol [<sup>75</sup>Se]-triether (1-butylselenyl-[<sup>75</sup>Se]-2,3-di(octadecyloxy)propane), followed by radioactivity measurements in feces using isotope balance method (oral ingestion minus fecal excretion) or isotope ratio method (comparison of isotope ratios in a test meal and in a stool sample).

TG tracers based on the stable isotope <sup>13</sup>C were applied for non-invasive assessment of intestinal lipid absorption by measuring <sup>13</sup>CO<sub>2</sub> to <sup>12</sup>CO<sub>2</sub> isotope ratio in exhaled air using continuous flow isotope ratio mass spectrometry (255-257). Mixed TG 1,3-distearoyl-2-[1-<sup>13</sup>C]octanoyl glycerol containing a <sup>13</sup>C-labeled medium-chain fatty acid at the *sn*-2 position and a long-chain stearic acid at the *sn*-1 and *sn*-3 positions was introduced by Ghoo et al. for the assessment of pancreatic function using the breath test (256). Kalivianakis et al. utilized this probe to study TG absorption in a rat model of lipid malabsorption generated by orlistat administration and demonstrated the relationship between the orlistat dose and a measured <sup>13</sup>CO<sub>2</sub> response (255).

A dual-modal optical/PET TG probe with oleic acid at *sn*-1 and *sn*-3 positions and a fluorescent fatty acid BODIPY-FL-C<sub>16</sub> (BODIPY-palmitic acid) at *sn*-2 position has been recently reported by Paulus et al. as a TG imaging agent for *in vitro* and *in vivo* applications (258). The probe contains a BODIPY fluorescent dye that was labeled with <sup>18</sup>F after performing <sup>18</sup>F/<sup>19</sup>F exchange reaction. Since BODIPY fluorophore does not possess suitable optical properties for *in vivo* imaging, *in vivo* utilization of this probe is limited only to PET modality. In the report only probe development but no *in vivo* applications were demonstrated (258).

In summary, the methods for *in vivo* measurement of TG absorption described to date require *ex vivo* processing and analysis of collected biological samples, which contain ingested radioactive or non-radioactive TG tracers or their metabolites, using weight measurements, chromatography, mass spectrometry or radioactivity counting. Many of them require invasive procedures and animal euthanasia. These methods do not give spatiotemporal information about the intestinal TG absorption; they enable measurements of the amount of absorbed TGs but do not allow for real-time *in vivo* imaging of lipid absorption dynamics. Up-to-date, no optical probes have been reported for *in vivo* imaging of TG absorption. Bioluminescence imaging is an attractive alternative to be used for preclinical studies, since it allows obtaining important biological information in a non-invasive way, is

rapid and relatively easy for implementation, affords high sensitivity and has relatively low cost, provided that an animal model being used is expressing luciferase (5, 13, 259).

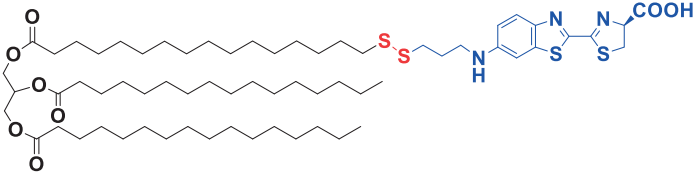
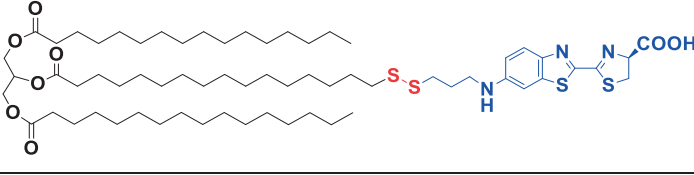
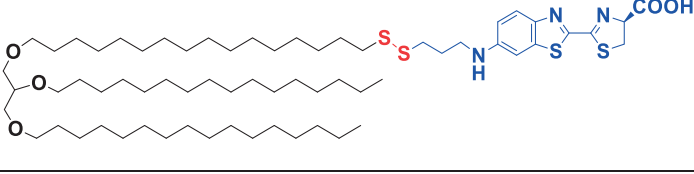
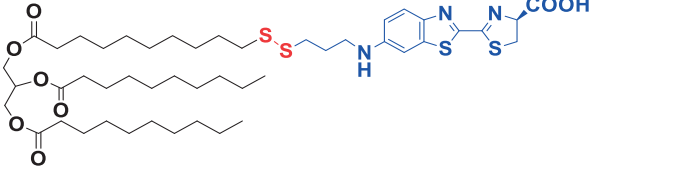
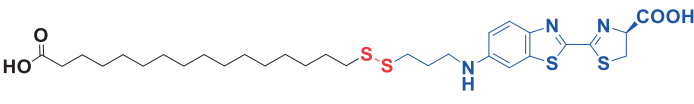
## 3.4 Results

### 3.4.1 Probe design

The approach used for the design of the probes for *in vivo* bioluminescence imaging of TG uptake is based on a bioluminescent reporter-biomolecule conjugate strategy, where a biomolecule is labeled with a bioluminescent reporter that generates the signal upon cellular uptake. The conjugation is performed in a way that it does not perturb the natural behavior of a biomolecule and at the same time, it enables the signal production only upon the cellular uptake of the conjugate or its metabolite. A previously described approach for generating luciferin-biomolecule conjugates for cellular uptake studies utilizes D-luciferin as a bioluminescent reporter, the latter one being connected to a biomolecule of interest through the disulfide-carbonate linker. The main disadvantage of this approach is the limited hydrolytic stability of the disulfide-carbonate linker, which leads to an increase of the background signal (71, 72, 74-77, 260). Moreover, the attempts to synthesize triglyceride-luciferin probes using the disulfide-carbonate linker turned out to be ineffective. In order to overcome these problems, for the design of TG probes a 6-N-alkylated analog of D-aminoluciferin 6-N-(3-mercaptopropyl)-aminoluciferin (MPr-AL) was employed as a bioluminescent reporter. This MPr-AL contains a non-hydrolyzable N-propyl linkage and a terminal thiol group for the conjugation to a biomolecule via a disulfide bond. 6-N-alkylated aminoluciferins are known to act as substrates for firefly luciferase (43, 44, 261-264). The applicability of MPr-AL scaffold for labeling biomolecules was first demonstrated by Manuel Drefahl, who generated the conjugates with nucleic acids (unpublished results). Based on the MPr-AL scaffold, bioluminescent analogs of a long-chain triglyceride tripalmitin, a medium-chain triglyceride tridecanoin and a long-chain free fatty acid palmitic acid (entries I-V, **Table 3.1**) were developed, where MPr-AL was attached to the lipid molecules at the end of their aliphatic chains via a disulfide bond. The choice of this site of the lipid molecules for the attachment of the bioluminescent reporter MPr-AL was based on the previous reports, which demonstrated that the modifications of fatty acids at the omega-carbon atom did not change their uptake mechanism by cells (72, 115, 116). Long-chain triglyceride probes LCTG-Luc1 and LCTG-Luc2 contain MPr-AL linked to the terminal acyl chain and to the *sn*-2-acyl chain respectively (entries I and II, **Table 3.1**). The medium-chain triglyceride probe MCTG-Luc1 (entry IV, **Table 3.1**) contains MPr-AL linked to the terminal acyl chain. As a control compound, which lacks hydrolyzable ester groups, a glycerol triether LCGE-Luc1, labeled with MPr-AL at the terminal acyl chain, was developed (entry III, **Table 3.1**). LCTG-Luc1, LCGE-Luc1 and MCTG-Luc1 were produced from racemic (*RS*)-3-benzyloxy-1,2-

propanediol. As a bioluminescent probe for long-chain free fatty acids, FA-Luc was generated, where MPr-AL was attached to palmitic acid (entry **V**, **Table 3.1**). FA-Luc is an improved bioluminescent fatty acid probe with stability to hydrolysis, compared to a previously reported fatty acid probe FFA-SS-Luc containing the disulfide-carbonate linker (72).

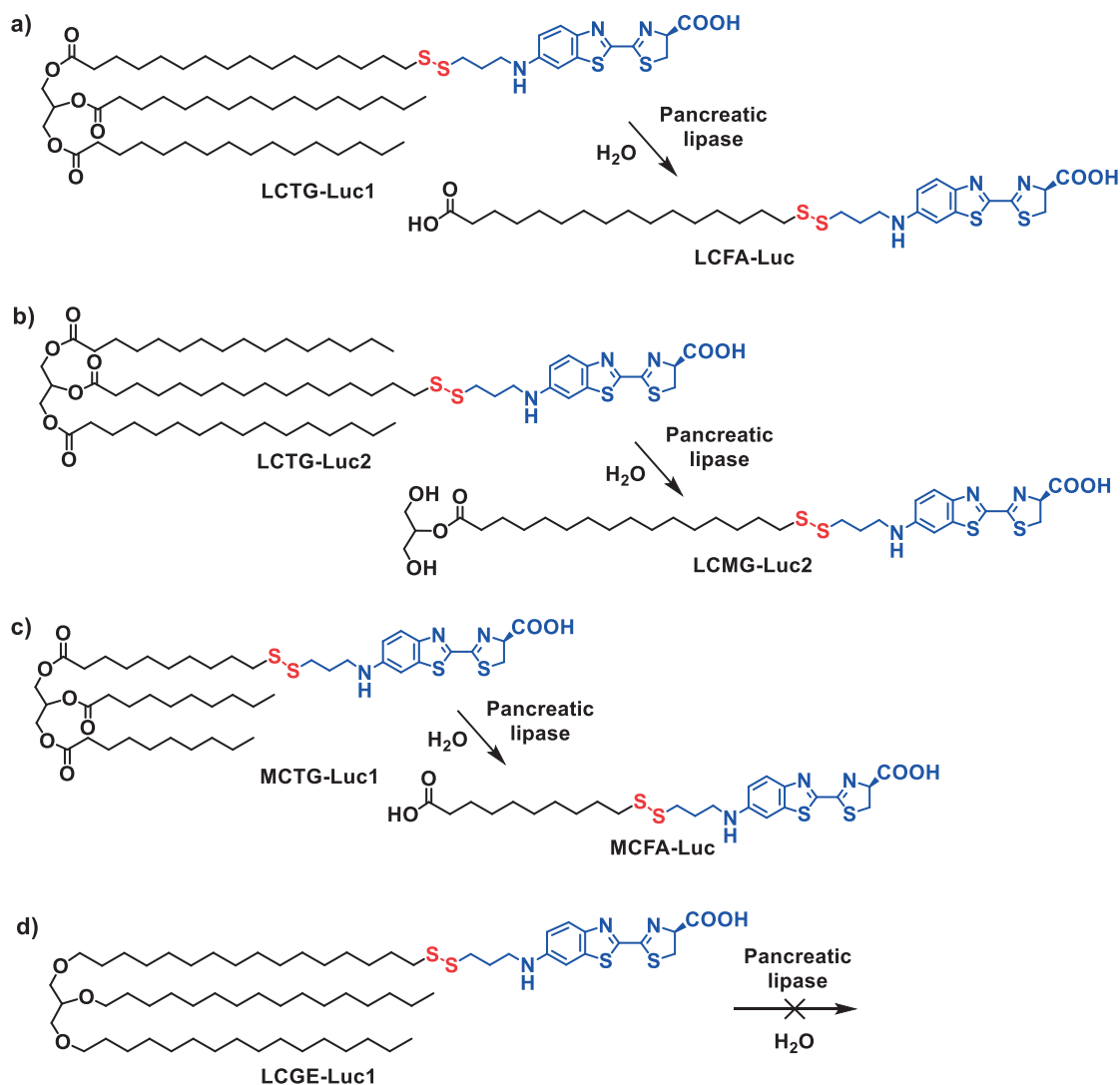
**Table 3.1** Structures of triglyceride-luciferin and fatty acid-luciferin probes

N	Probe structure	Abbreviation	Lipid precursor
I		LCTG-Luc1	glyceryl tripalmitate (tripalmitin)
II		LCTG-Luc2	glyceryl tripalmitate (tripalmitin)
III		LCGE-Luc1	1,2,3-tri-O-palmityl-glycerol
IV		MCTG-Luc1	glyceryl tridecanoate (tridecanoin)
V		FA-Luc	palmitic acid

### 3.4.2 Mechanism of the probe activation

The cellular absorption of triglycerides requires first their hydrolysis by lipases (195-198, 265, 266), with pancreatic lipase (PL) playing the main role in the gastrointestinal tract. PL hydrolyzes triglycerides acting at *sn*-1 and *sn*-3 positions, which leads to the release of free fatty acids and *sn*-2-monoacylglycerol (196, 238, 267). Upon the action of PL, triglyceride probes LCTG-Luc1, LCTG-Luc2 and MCTG-Luc1 would produce bioluminescent metabolites: long-chain fatty acid-luciferin

(LCFA-Luc = FA-Luc), *sn*-2-monoacylglycerol-luciferin (LCMG-Luc2) and medium-chain fatty acid-luciferin (MCFA-Luc) respectively (**Scheme 3.1a-c**).



**Scheme 3.1** Lipolysis of TG probes by pancreatic lipase. Only bioluminescent metabolites are shown as the products.

These metabolites would be taken up by cells, followed by intracellular release of MPr-AL, as the disulfide bond is stable extracellularly but undergoes rapid cleavage upon cellular uptake due to the high concentration of glutathione in the cytosol (71, 72, 74, 75, 268), as shown in **Figure 3.4** for LCTG-Luc1 probe. The released bioluminescent reporter MPr-AL would be converted by firefly luciferase to the corresponding oxyluciferin derivative producing a photon. Thus, the photon flux would represent the amount of triglyceride, which is hydrolyzed by lipases and absorbed by cells. Emitted light is detected with a charge-coupled device (CCD) camera allowing the quantification of the triglyceride absorption in luciferase expressing cells and mice (**Figure 3.4**). For the control compound

LCGE-Luc1, no lipolysis is possible as all the ester groups are replaced with the ether groups, therefore the probe cannot be hydrolysed by lipase and no specific signal would be generated (**Scheme 3.1d**).

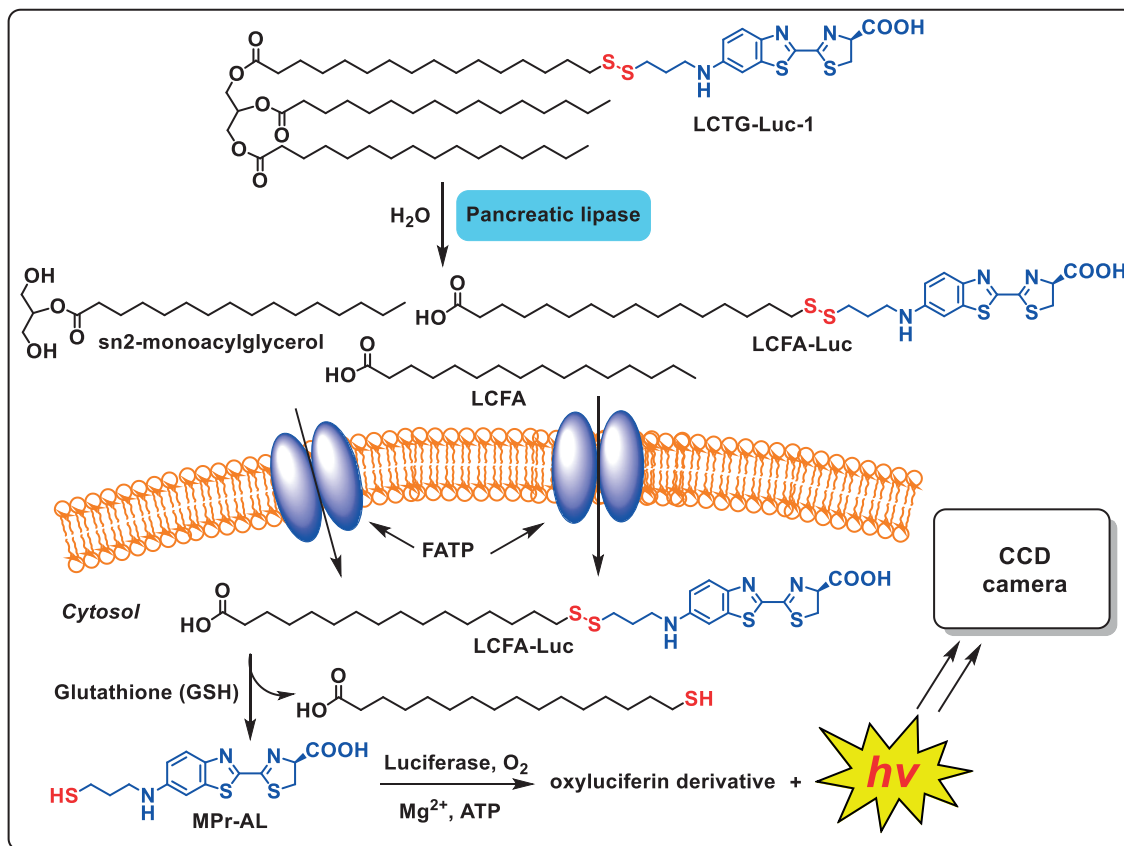
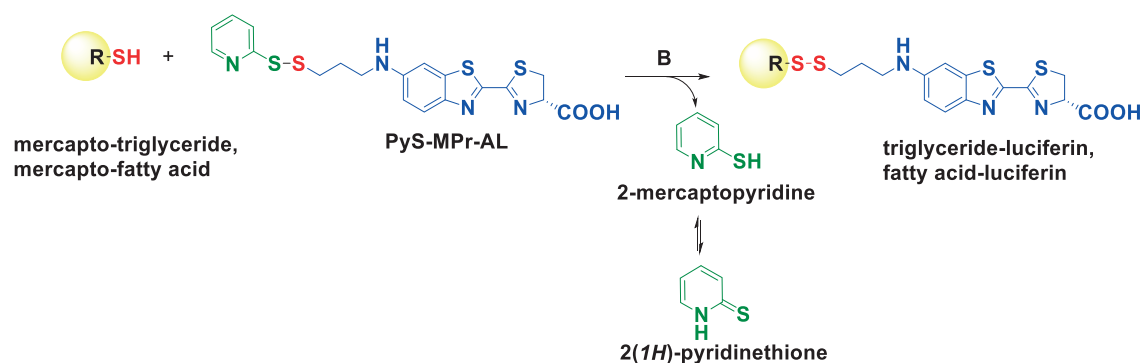


**Figure 3.4** The mechanism of the BL signal generation by LCTG-Luc1 in luciferase expressing cells.

### 3.4.3 Synthesis of probes

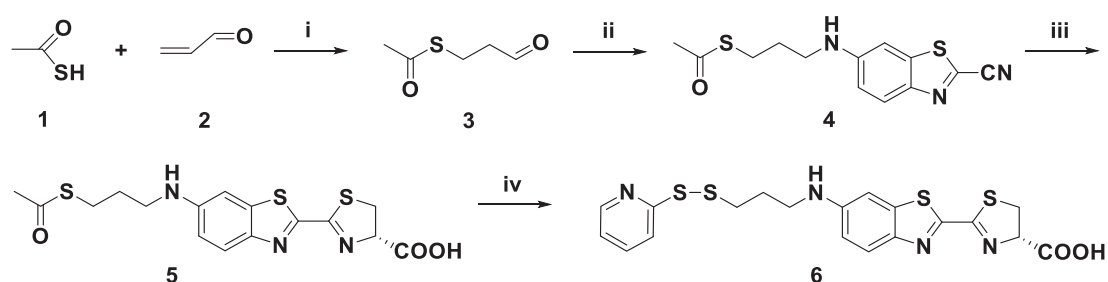
All developed probes LCTG-Luc1, LCTG-Luc2, MCTG-Luc1, LCGE-Luc1 and FA-Luc were synthesized using the general conjugation strategy with the bioluminescent reporter MPr-AL, as depicted in **Scheme 3.2**.



**Scheme 3.2** General approach for the synthesis of lipid-luciferin conjugates.

Specifically, a mercapto-triglyceride or a mercapto-fatty acid is reacted with MPr-AL derivative PyS-MPr-AL in the presence of a base (B) in a mixture of tetrahydrofuran-dimethylformamide. PyS-MPr-AL contains an activated disulfide bond due to the presence of the 2-mercaptopyridyl moiety and reacts with thiols via thiol-disulfide exchange with the liberation of 2-mercaptopyridine, which undergoes tautomerization in 2(1*H*)-pyridinethione as a main form existing in polar solvents (269, 270). The formation of 2(1*H*)-pyridinethione is a driving force of this thiol-disulfide exchange reaction (269, 271). As a result, this process allows the transfer of the luciferin reporter MPr-AL to thiol-containing molecules with the formation of the disulfide bond (**Scheme 3.2**).

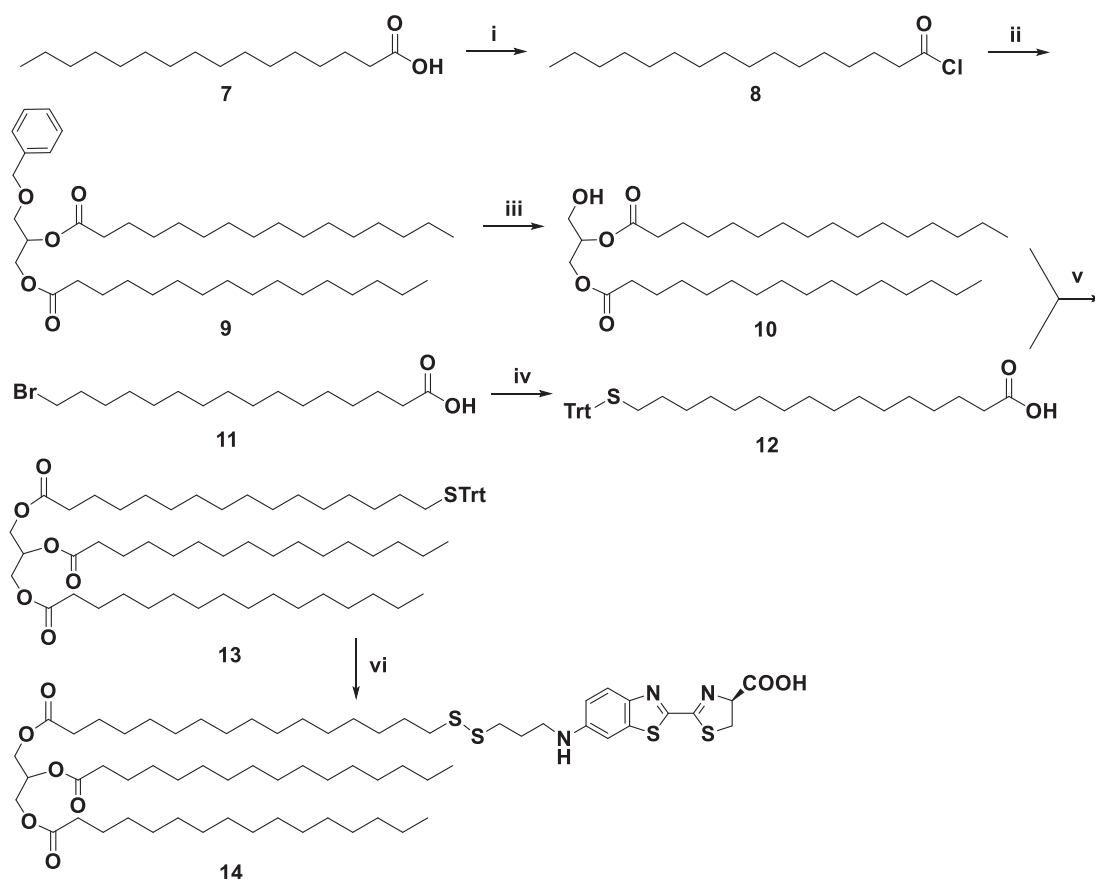
PyS-MPr-AL (**6**) was synthesized in 4 steps (41% overall yield), as outlined in **Scheme 3.3**. First, thioacetic acid (**1**) was reacted with acrolein (**2**) in the presence of DIPEA via the Michael addition to produce aldehyde (**3**), which was subsequently introduced into the reductive amination reaction with the 6-aminobenzothiazole-2-carbonitrile in the presence of NaBH(OAc)<sub>3</sub> to afford nitrile (**4**). The condensation reaction of D-cysteine with nitrile (**4**) under inert conditions in a mixture of acetonitrile-PBS gave rise to S-acetylated luciferin (**5**). In order to produce the final compound (**6**) a free thiol group formed after deacetylation of the precursor (**5**) should be reacted with 2,2'-dipyridyl disulfide. Isolation of the air-sensitive free thiol derivative of (**5**) would take extra steps and might be complicated by possible oxidation to form the dimer. The reaction was performed directly from the S-acetylated luciferin (**5**) to the final product (**6**) by combining in one step *in situ* deacetylation reaction and mixed disulfide formation, therefore the necessity to isolate the thiol-containing intermediate was avoided. This transformation was performed by treating compound (**5**) with excess of 1.2 M NH<sub>3</sub> in MeOH in the presence of 2,2'-dipyridyl disulfide under inert conditions. This step proceeded smoothly at RT to give PyS-MPr-AL (**6**) in 91% yield.



**Scheme 3.3** Synthesis of PyS-MPr-AL (**6**). Reagents and conditions: (i) DIPEA, DCM, 0 °C to RT, 12 h; (ii) 6-aminobenzothiazole-2-carbonitrile, NaBH(OAc)<sub>3</sub>, AcOH, THF, RT, 12 h; (iii) D-cysteine, acetonitrile-PBS (2:1), RT, 1 h; (iv) 2,2'-Dipyridyl disulfide, 1.2 M NH<sub>3</sub> in MeOH, RT, 12 h.

For the synthesis of LCTG-Luc1 (**14**) (*RS*)-3-benzyloxy-1,2-propanediol was utilized as a glycerol scaffold, as it allows constructing the triglyceride, which contains two identical acyl chains at vicinal oxygen atoms of the glycerol backbone and a different acyl chain at the third oxygen atom. The

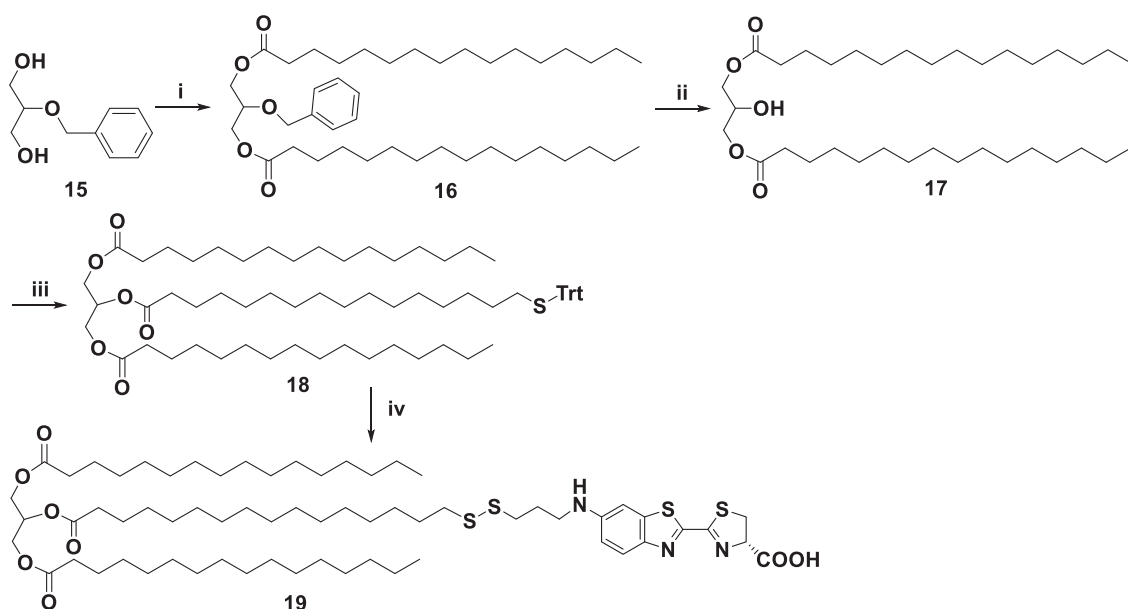
synthesis of LCTG-Luc1 proceeded in 6 steps with 45% overall yield (**Scheme 3.4**). First, activation of palmitic acid (**7**) using oxalyl chloride in the presence of catalytic amount of DMF gave palmitoyl chloride (**8**), which was reacted with (*RS*)-3-benzyloxy-1,2-propanediol in the presence of DMAP to afford diester (**9**) in 85% yield over two steps. Then, diester (**9**) was subjected to Pd-catalyzed hydrogenation to remove O-benzyl protecting group, which afforded diglyceride (**10**) in quantitative yield. In a separate route, 16-(tritylthio)hexadecanoic acid (**12**) was synthesized via reaction of 16-bromohexadecanoic acid (**11**) with triphenylmethanethiol in the presence of sodium methoxide. Acid (**12**), which contains masked thiol for further conjugation to the bioluminescent reporter MPr-AL, was attached to diglyceride (**10**) through Steglich esterification (272, 273) using EDCI and DMAP to afford triglyceride (**13**) in 65% yield after chromatographic purification. In the last step, the thiol group of (**13**) was *in situ* deprotected by TFA in the presence of  $\text{Et}_3\text{SiH}$ , followed by removal of volatiles. The final reaction was performed in the same flask without isolation of free thiol by adding PyS-MPr-AL (**6**) in the presence of DIPEA in a mixture of THF-DMF to give the probe LCTG-Luc1 (**14**) in 82% yield.



**Scheme 3.4** Synthesis of LCTG-Luc1 (**14**). Reagents and conditions: (i)  $(\text{COCl})_2$ , DMF, DCM, RT, 3 h; (ii) (*RS*)-3-Benzyloxy-1,2-propanediol, DMAP, Py, DCM, 0 °C to RT, 16 h; (iii)  $\text{H}_2$ , 5% Pd/C, AcOEt, RT, 21 h; (iv) triphenylmethanethiol, MeONa-MeOH, toluene, 5 to 50 °C, 2.5 h; (v) EDCI, DMAP, DCM, 0 °C to RT, 4 h; (vi) 1. TFA,  $\text{Et}_3\text{SiH}$ , DCM, 0 °C to RT, 4 h; 2. PyS-MPr-AL (**6**), DIPEA, THF-DMF, RT, 18 h.



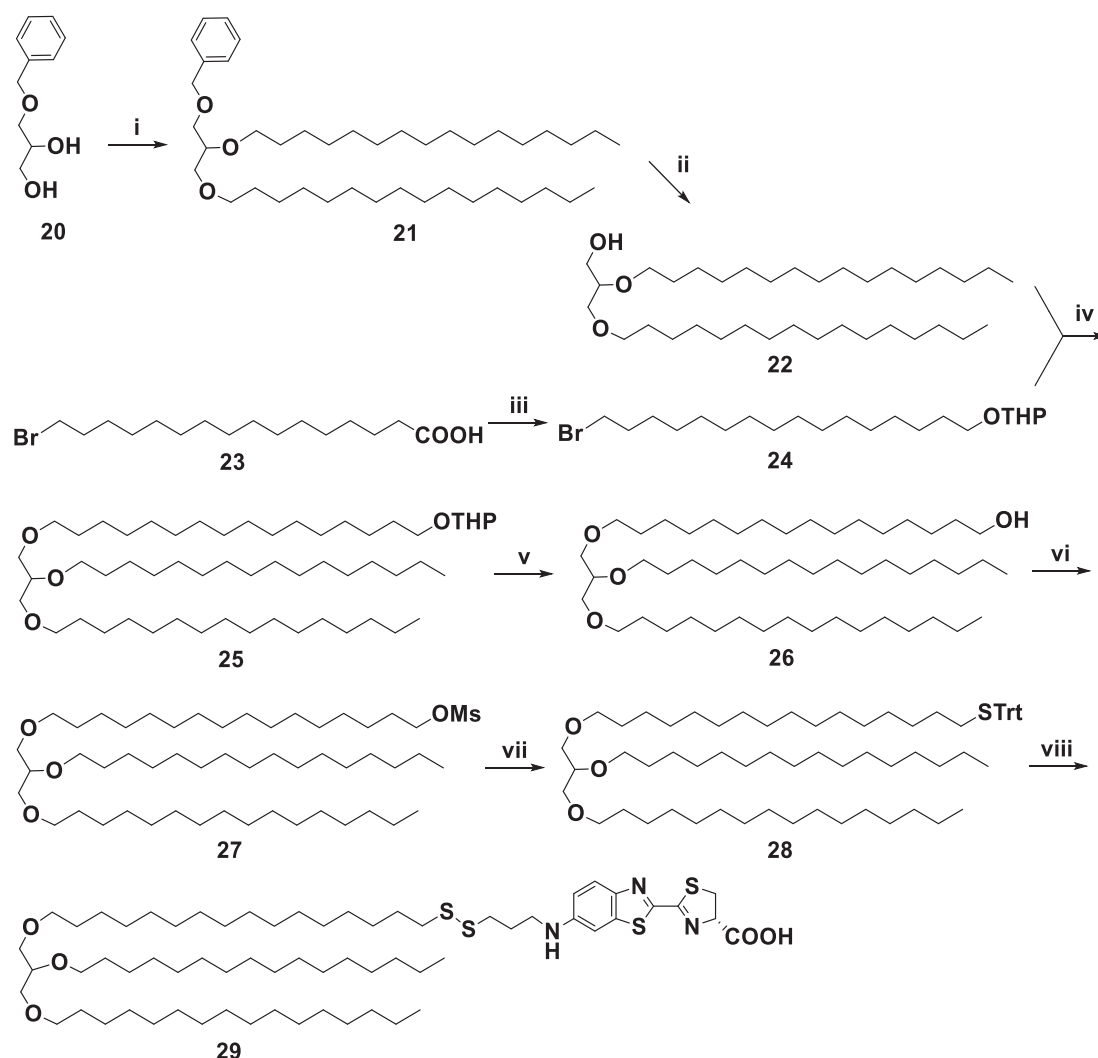
LCTG-Luc2 probe (**19**) was synthesized in 4 steps (32% overall yield) following a synthetic route similar to that of LCTG-Luc1, but 2-benzyloxy-1,3-propanediol (**15**) was utilized as a glycerol scaffold (**Scheme 3.5**), which allows introduction of identical acyl groups to *sn*-1 and *sn*-3 positions and a different acyl moiety to *sn*-2 position (**Scheme 3.5**). Acylation of diol (**15**) with palmitoyl chloride catalyzed by DMAP afforded diester (**16**) in 57% yield, which gave diglyceride (**17**) after Pd-catalyzed hydrogenation (92% yield). Next, attachment of 16-(tritylthio)hexadecanoic acid (**12**) to diglyceride (**17**) via Steglich esterification led to triglyceride (**18**) bearing a protected thiol group (72% yield). In the last step, thiol deprotection for compound (**18**) using TFA and Et<sub>3</sub>SiH, followed by reaction with PyS-MPr-AL (**6**) produced LCTG-Luc2 probe (**19**) in 86% yield.



**Scheme 3.5** Synthesis of LCTG-Luc2 (**19**). Reagents and conditions: (i) palmitoyl chloride, DMAP, Py, DCM, 0 °C to RT, 16 h; (ii) H<sub>2</sub>, 5% Pd/C, AcOEt, RT, 21 h; (iii) 16-(tritylthio)hexadecanoic acid (**12**), EDCI, DMAP, DCM, 0 °C to RT, overnight; (iv) 1. TFA, Et<sub>3</sub>SiH, DCM, 0 °C to RT, 4 h; 2. PyS-MPr-AL (**6**), DIPEA, THF-DMF, RT, 18 h.

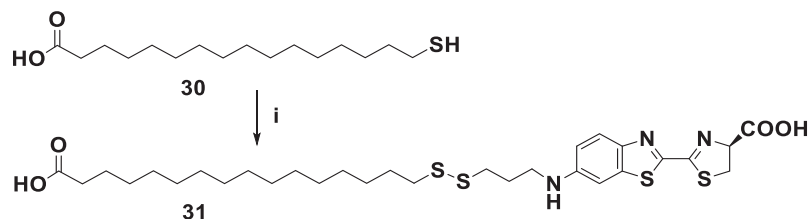
LCGE-Luc1 (control probe) (**29**) was prepared in 9 steps (10% overall yield) employing (*RS*)-3-benzyloxy-1,2-propanediol (**20**) as a glycerol scaffold (**Scheme 3.6**). First, two hexadecyl groups were introduced to (**20**) via ether bond, which was achieved using Williamson reaction between diol (**20**) and 1-bromohexadecane in the presence of NaH to afford ether (**21**) in 71% yield. Next, Pd-catalysed debenzoylation of (**21**) by hydrogen gave alcohol (**22**) in 99% yield. In a separate route, bromoalkane (**24**) containing terminal protected hydroxyl-group was synthesized by reducing 16-bromohexadecanoic acid (**23**) with borane-THF complex to produce 16-bromohexadecanol, which was converted to tetrahydropyranyl ether (**24**) via reaction with 3,4-dihydro-2*H*-pyran catalyzed by

pyridinium *p*-toluenesulfonate (PPTS) (94% yield). Then, alcohol (**22**) was treated with NaH and was alkylated with bromide (**24**) via the Williamson reaction, which resulted in triether (**25**). Removal of the tetrahydropyranyl protecting group upon treatment of (**25**) with PPTS in a mixture of THF and MeOH, led to alcohol (**26**), which was activated by reaction with mesyl chloride (MsCl) in the presence of Me<sub>3</sub>N·HCl and DIPEA following the protocol described by Yoshida et al. (274), to give mesylate (**27**) in 20% yield over 3 steps. In order to introduce thiol group, mesylate (**27**) was reacted with triphenylmethanethiol to afford triether (**28**) in 87% yield. Next, treatment of (**28**) with TFA and Et<sub>3</sub>SiH for *in situ* deprotection of the thiol group, followed by reaction with PyS-MPr-AL (**6**) gave LCGE-Luc1 probe (**29**) in 78% yield.



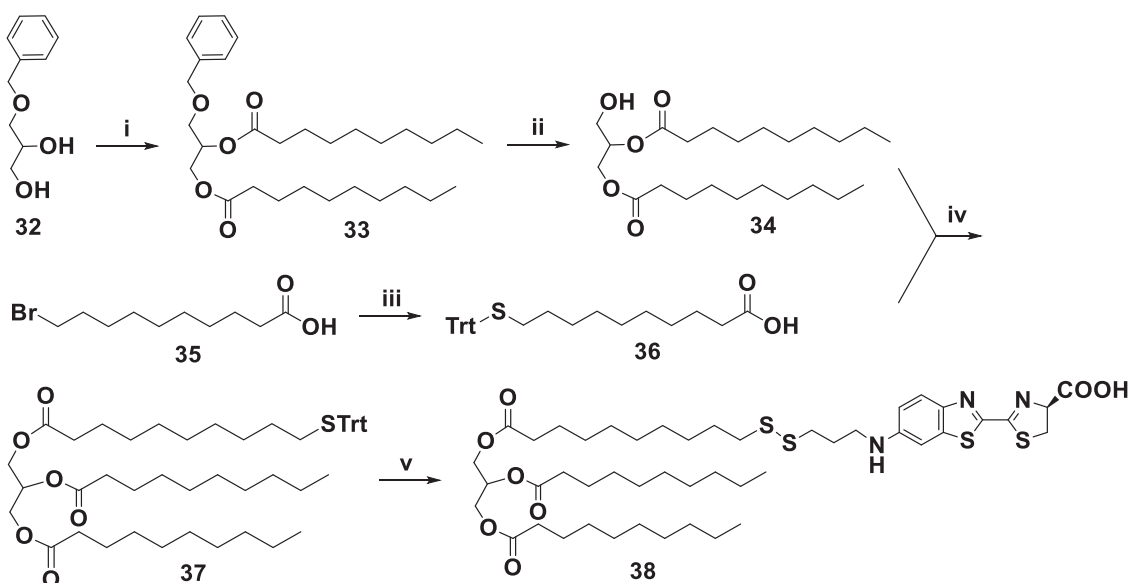
**Scheme 3.6** Synthesis of LCGE-Luc (**29**). Reagents and conditions: (i) 1. NaH, DMF-THF, RT, 30 min; 2. 1-bromohexadecane, THF, RT, 28 h; (ii) H<sub>2</sub>, 10% Pd/C, AcOEt, RT, 21 h; (iii) 1. BH<sub>3</sub>·THF, THF, 0 °C to RT, 24 h; 2. 3,4-dihydro-2H-pyran, PPTS, DCM, RT, 3 h; (iv) NaH, DMF-THF, RT, 72 h; (v) MeOH-THF, PPTS, 50 °C, 6 h; (vi) MsCl, Me<sub>3</sub>N·HCl, DIPEA, DCM, 0 °C to RT, 4.5 h; (vii) triphenylmethanethiol, DIPEA, THF-DMF, RT; (viii) 1. TFA, Et<sub>3</sub>SiH, DCM, 0 °C to RT, 2 h; 2. PyS-MPr-AL (**6**), DIPEA, THF-DMF, RT, 12 h.

FA-Luc probe (**31**) was synthesized in one step (63% yield) via reaction of 16-mercaptohexadecanoic acid (**30**) with PyS-MPr-AL (**6**) (**Scheme 3.7**).



**Scheme 3.7** Synthesis of FA-Luc (**31**). Reagents and conditions: (i) PyS-MPr-AL (**6**), DIPEA, THF-DMF, RT, 12 h.

The synthesis of the medium-chain triglyceride probe MCTG-Luc1 (**38**) was performed following the similar route, applied for LCTG-Luc1, but decanoyl chloride and 10-bromodecanoic acid were used for introducing fatty acid chains (**Scheme 3.8**). MCTG-Luc1 (**38**) was obtained in 5 steps (27% overall yield).



**Scheme 3.8** Synthesis of MCTG-Luc (**38**). Reagents and conditions: (i) decanoyl chloride, DMAP, Py, DCM, 15 °C to 40 °C, 12 h; (ii) H<sub>2</sub>, 5% Pd/C, AcOEt, RT, 24 h; (iii) triphenylmethanethiol, MeONa-MeOH, toluene, 5 to 50 °C, 2 h; (iv) EDCI, DMAP, DCM, 0 °C to RT, 12 h; (v) 1. TFA, Et<sub>3</sub>SiH, DCM, 0 °C to RT, 4 h; 2. PyS-MPr-AL (**6**), DIPEA, THF-DMF, RT, 12 h.

#### 3.4.4 Validation of triglyceride probes in luciferase expressing cells.

First, the ability of the TG probes to produce bioluminescence in live cells in the presence of pancreatic lipase (PL) was evaluated. If the probes are substrates for lipase, then they would be recognized and hydrolyzed by the enzyme and the products of hydrolysis containing the luciferin label (MPPr-AL) would be taken up by cells leading to the bioluminescent signal production. The experiments were performed in Caco2-luc cells that are a luciferase-expressing human colon adenocarcinoma cell line. Caco2 cells are widely used in research as a model of the intestinal barrier (275). For the uptake experiments the cells were loaded with the emulsions of long-chain TG probes LCTG-Luc1, LCTG-Luc2 and the medium-chain TG probe MCTG-Luc1. The emulsions were mixed with increasing concentrations of PL supplemented with colipase to assess the dose-response relationship between the amount of PL and emitted bioluminescence, which was continuously monitored by a CCD camera after addition of the reagents to the cells. Incubations of all TG probes (LCTG-Luc1, LCTG-Luc2 and MCTG-Luc1) with increasing concentrations of PL demonstrated an increase in bioluminescent response in cells. The higher the concentration of PL, the greater the light production from the probes in Caco2-luc cells, which can be seen from the kinetic data representing the real-time cellular bioluminescent response (**Figure 3.5a,c; Figure 3.6a**), as well as from the data representing the total photon fluxes from the cells (calculated as the area under the kinetic curves) (**Figure 3.5b,d; Figure 3.6b**). The maximal concentration of PL used in the assay (200 ng/mL) resulted in 20.9-fold signal increase for LCTG-Luc1, 16.4-fold signal increase for LCTG-Luc2 and 25.4-fold signal increase for MCTG-Luc2 over the corresponding background levels for each probe (signal from a probe in cells without addition of PL). Importantly, all TG probes demonstrate a linear response to PL ( $R^2$  values 0.9970, 0.9995 and 0.9862 for LCTG-Luc1, LCTG-Luc2 and MCTG-Luc1 respectively) in the range of used PL concentrations 0-200 ng/mL (**Figure 3.5e,f; Figure 3.6c**).

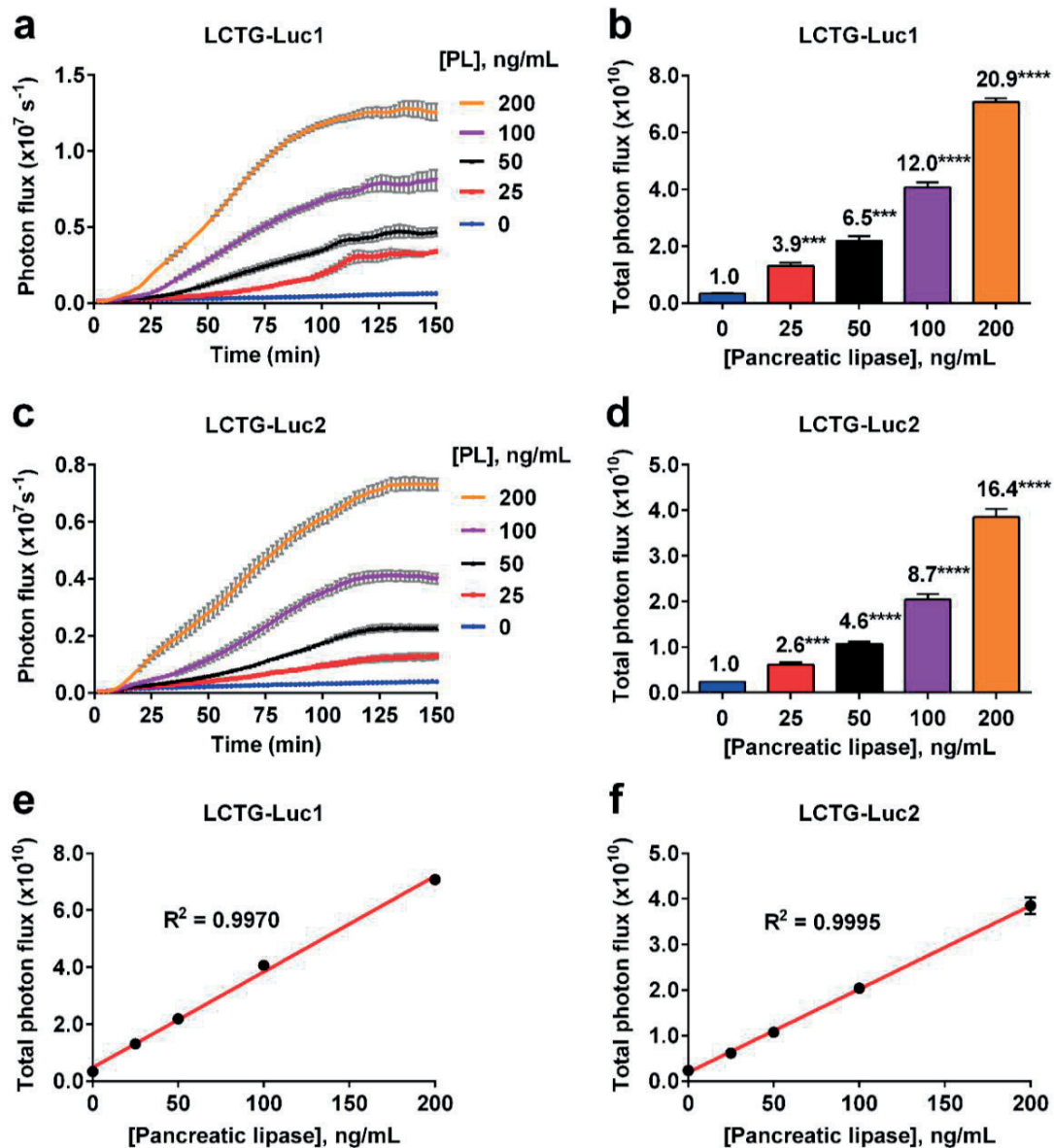


**Figure 3.5** Bioluminescence imaging of LCTG-Luc1 and LCTG-Luc2 uptake by Caco2-luc cells. Cells were incubated with an emulsion containing LCTG-Luc1 or LCTG-Luc2 (15  $\mu\text{M}$  for each probe in 1 mM NaTDC in PBS) in the presence of pancreatic lipase (0-200 ng/mL) supplemented with colipase (lipase to colipase ratio 5:1 (w/w)) at 37°C and imaged with a CCD camera. (a) Kinetics of a bioluminescent signal produced by LCTG-Luc1 in Caco2-luc cells in the presence of indicated concentrations of pancreatic lipase. (b) Total photon flux over 150 min produced in the cells incubated with LCTG-Luc1. (c) Kinetics of a bioluminescent signal produced by LCTG-Luc2 in Caco2-luc cells in the presence of indicated concentrations of pancreatic lipase. (d) Total photon flux over 150 min produced in the cells incubated with LCTG-Luc2. (e) Line graph representation of the total photon flux from LCTG-Luc1 (b), which shows a linear increase ( $R^2 = 0.9970$ ) in the bioluminescent response to pancreatic lipase. (f) Line graph representation of the total photon flux from LCTG-Luc2 (d), which indicates a linear increase ( $R^2 = 0.9995$ ) in the bioluminescent response to pancreatic lipase. The values above the bars in (b,d) indicate the fold-difference compared to background (probe without lipase). Error bars are  $\pm\text{SEM}$ ,  $n = 6$ . Statistical analyses were performed with a two-tailed Student's t-test (\*\* $P < 0.001$ , \*\*\*\* $P < 0.0001$ ).

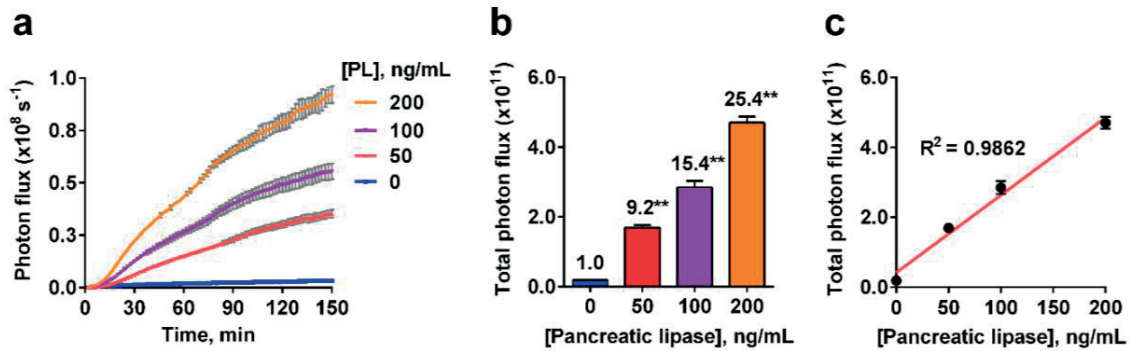


**Figure 3.6** Bioluminescence imaging of MCTG-Luc1 uptake by Caco2-luc cells. Cells were loaded with an emulsion containing MCTG-Luc1 (15  $\mu\text{M}$  in 1 mM NaTDC in PBS) followed by the addition of pancreatic lipase (0-200 ng/mL) supplemented with colipase (lipase to colipase ratio 5:1 (w/w)) and imaged with a CCD camera at 37°C. (a) Kinetics of a bioluminescent signal produced by MCTG-Luc1 in Caco2-luc cells in the presence of indicated concentrations of pancreatic lipase. (b) Total photon flux over 150 min generated in the cells incubated with MCTG-Luc1, which corresponds to the kinetics curves (a). (c) Line graph representation of the total photon flux from MCTG-Luc1 (b), which shows a linear increase ( $R^2 = 0.9862$ ) in the bioluminescent response to pancreatic lipase. Error bars are  $\pm\text{SEM}$ ,  $n = 3$ . Statistical analyses were performed with a two-tailed Student's t-test (\*\* $P < 0.01$ ).

Next, the bioluminescent response from LCTG-Luc1, LCTG-Luc2 and MCTG-Luc1 in Caco2-luc cells was compared for the same concentration of PL (200 ng/mL). The linear regression analysis of the cellular BL signal from the probes was performed over the period 0-3600 s to assess the slopes of the corresponding kinetics curves (Figure 3.7a).

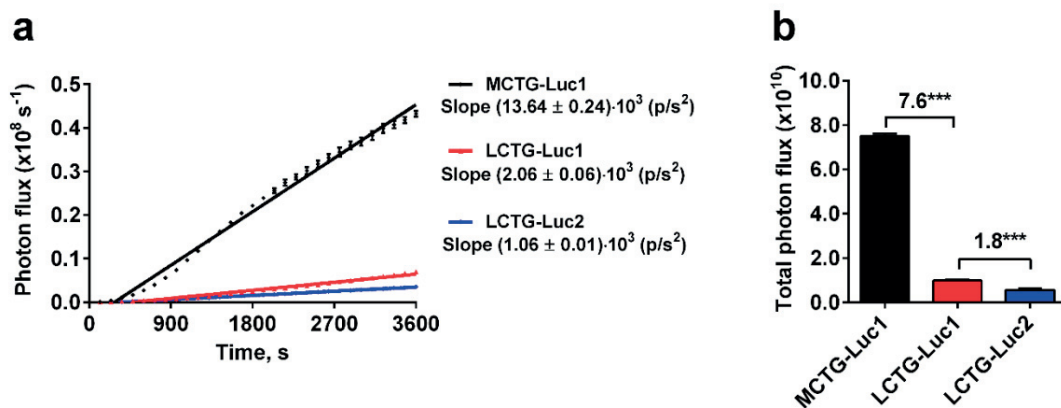


**Figure 3.7** Comparison of the bioluminescent signals produced from MCTG-Luc1, LCTG-Luc1 and LCTG-Luc2 (15  $\mu\text{M}$  for each probe in emulsion in 1 mM NaTDC in PBS) in Caco2-luc cells in the presence of pancreatic lipase (200 ng/mL) supplemented with colipase (40 ng/mL). (a) Linear regression analysis for the bioluminescent response produced by the probes in cells over 0-3600 s to determine the slopes of the kinetic curves. The graph shows a linear increase in bioluminescent signal for MCTG-Luc1 ( $R^2 = 0.9912$ ), LCTG-Luc1 ( $R^2 = 0.9778$ ) and LCTG-Luc2 ( $R^2 = 0.9995$ ) over the period 0-3600 s. The difference between the slopes is significant ( $P < 0.0001$ ). (b) Total bioluminescent signal produced by the probes in cells over 60 min. Error bars are  $\pm\text{SEM}$  ( $n = 3$  for MCTG-Luc1,  $n = 6$  for LCTG-Luc1 and LCTG-Luc2). Statistical analyses were performed with a two-tailed Student's t-test (\*\*\*) ( $P < 0.001$ ).

The obtained values of the slopes of the kinetic curves indicate that the medium-chain TG probe MCTG-Luc1 has 6.6-fold faster kinetics of light production compared to its long-chain analog LCTG-Luc1 (slopes  $13.64 \text{ p/s}^2$  versus  $2.06 \text{ p/s}^2$  respectively,  $P < 0.0001$ ) (**Figure 3.7a**). The comparison of the slopes for the long-chain TG probes LCTG-Luc1 and LCTG-Luc2 shows that the former produces bioluminescent signal 1.9 times faster than the latter (slopes  $2.06 \text{ p/s}^2$  vs  $1.06 \text{ p/s}^2$  respectively,  $P < 0.0001$ ). As expected, similar results were obtained, when the total photon fluxes over 1 h from the probes in cells were calculated and compared (**Figure 3.7b**), with 7.6-fold difference in the total photon flux from MCTG-Luc1 compared to that from LCTG-Luc1 ( $P < 0.001$ ) and 1.8-fold difference in total bioluminescence from LCTG-Luc1 versus total bioluminescence from LCTG-Luc2 ( $P < 0.001$ ). The faster kinetics of cellular BL signal production from MCTG-Luc1 compared to that of LCTG-Luc1 reflects the higher rate of lipolysis of MCTG-Luc1 compared to LCTG-Luc1 under the same experimental conditions. This result is qualitatively and quantitatively in agreement with the previous reports, which demonstrated that the lipolysis of medium-chain TGs proceeds faster than that of long-chain TGs (208, 249, 276). The difference in the BL response from LCTG-Luc1 and LCTG-Luc2 in cells indicates the differences in the rates of their lipolysis (**Scheme 3.1a,b**). Indeed, for luciferin-labeled *sn*-2-monoacylglycerol (LCMG-Luc2) formation two acyl groups have to be removed stepwise from *sn*-1 and *sn*-3 positions of LCTG-Luc2 by the action of PL (**Scheme 3.1b**), whereas the release of luciferin-labeled free fatty acid (LCFA-Luc) from LCTG-Luc1 probe requires only one reaction of lipolysis (**Scheme 3.1a**). These differences in cellular bioluminescence from LCTG-Luc1 and LCTG-Luc2 probes may also reflect different cellular absorption rates of their bioluminescent lipolysis products LCFA-Luc and MCTG-Luc2 respectively, since *sn*-2-monoacylglycerol was shown to have slower uptake rate in Caco2 cells compared to the corresponding free fatty acid, which was demonstrated in the previous reports using radiolabeled monoolein and oleic acid (153, 277).

To further demonstrate that PL is required for TG probes to produce bioluminescent response, the influence of orlistat, a covalent inhibitor of PL (278, 279), on the cellular bioluminescent signal from LCTG-Luc1 and LCTG-Luc2 was examined. Caco2-luc cells were treated with emulsions of TG probes supplemented with PL (200 ng/mL) in the presence of increasing concentrations of orlistat. Addition of orlistat resulted in a dose-dependent decrease of cellular bioluminescent response from both LCTG-Luc1 and LCTG-Luc2 (**Figure 3.8**).



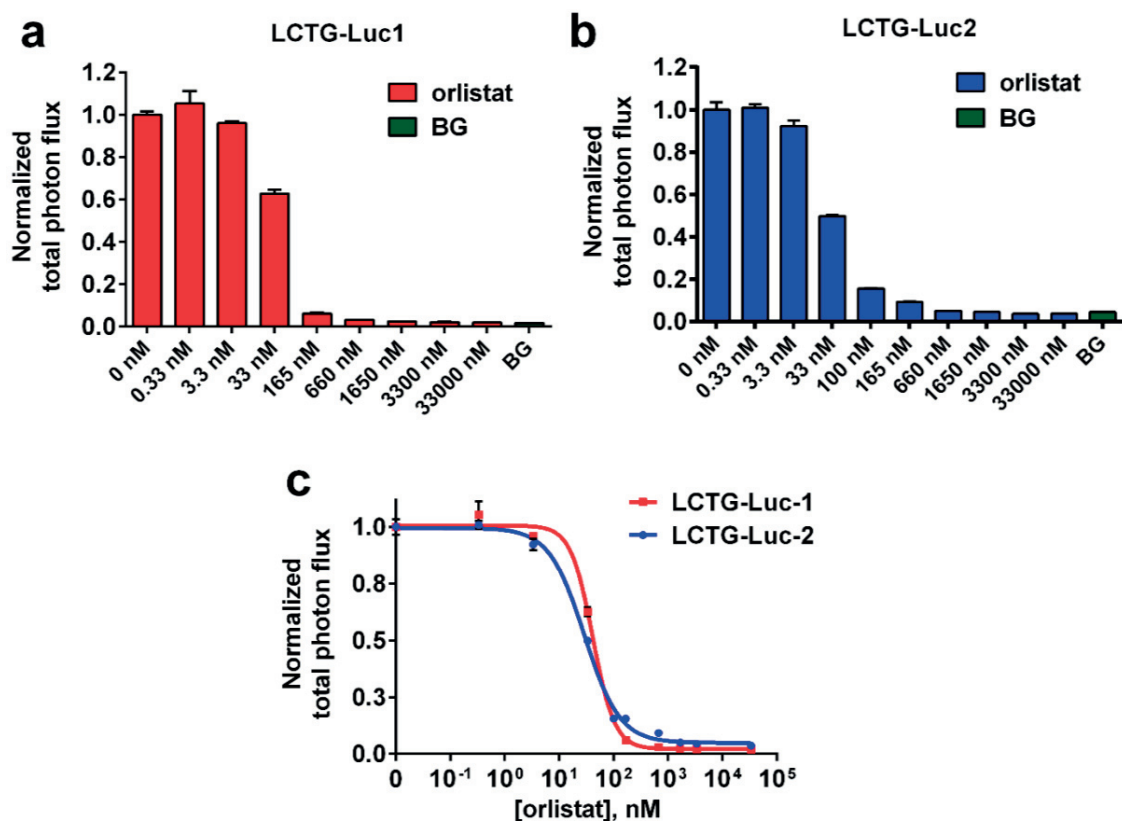


**Figure 3.8** Bioluminescence imaging of LCTG-Luc1 and LCTG-Luc2 uptake by Caco2-luc cells in the presence of orlistat. Cells were incubated with an emulsion of LCTG-Luc1 or LCTG-Luc2 (7.5  $\mu$ M for each probe in 1 mM NaTDC in PBS) supplemented with pancreatic lipase (200 ng/mL) and colipase (40 ng/mL) in the presence of orlistat. Background luminescent signal (BG) was acquired from cells incubated with the probes, but without addition of lipase and orlistat. (a) Total photon flux (normalized to 0-1) over 150 min produced by LCTG-Luc1 in the presence of orlistat (0-33000 nM). (b) Total photon flux (normalized to 0-1) over 150 min produced by LCTG-Luc2 in the presence of orlistat (0-33000 nM). (c) Sigmoidal graph representation of the total photon fluxes (a) and (b) obtained in the presence of orlistat, which gives  $IC_{50}$  values 41 nM and 29 nM for LCTG-Luc1 and LCTG-Luc2 respectively. The difference between the curves for the interval 0.33-660 nM is not significant ( $P = 0.2823$ ). Statistical analysis was performed with a paired t-test. Error bars are  $\pm$ SEM ( $n = 3$  for LCTG-Luc1,  $n = 6$  for LCTG-Luc2).

For the high concentrations of orlistat the cellular bioluminescent response from the probes was dramatically reduced to the levels close to the background (detected from the probes without addition of PL) (Figure 3.8a,b), comprising only 1.9% and 3.6% respectively of the total photon flux from the probes obtained after addition of PL in the absence of orlistat. These imaging data for both probes were plotted as normalized to 0-1 total photon flux versus log[orlistat] (Figure 3.8c) to calculate  $IC_{50}$ . As expected, for both LCTG-Luc1 and LCTG-Luc2 similar  $IC_{50}$  values were obtained 41 nM and 29 nM respectively, and statistical analysis for the curves (Figure 3.8c) for the interval of orlistat concentrations from 0.33 to 660 nM, which includes the calculated  $IC_{50}$  values, did not reveal significant difference between the curves ( $P = 0.2823$ ).



Since TGs must first be hydrolysed before their cellular uptake, the use of ether analogs of TGs is an appropriate negative control for TG uptake studies. Being resistant to hydrolysis, trialkyl glycerol ethers are isosteric to triglycerides and they have been characterized as non-absorbable TG analogs (198, 280). The performance of LCTG-Luc1 versus its triether analog LCGE-Luc1 (Table 3.1, entry III) was compared in Caco2-luc cells. The cells were incubated with emulsions containing equal concentrations of LCTG-Luc1 and LCGE-Luc1 in the presence of PL and the resultant bioluminescent response was measured over 150 min. Whereas LCTG-Luc1 generated robust bioluminescent signal in cells in the presence of PL, LCGE-Luc1 did not produce the same response to the addition of PL (Figure 3.9a).

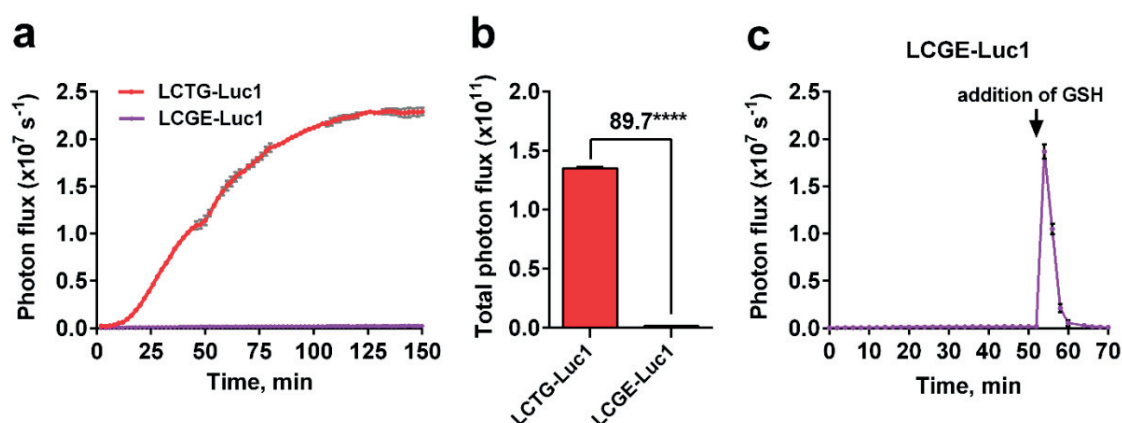


**Figure 3.9** Comparison of the bioluminescent signal produced from LCTG-Luc1 and LCGE-Luc1 in Caco2-luc cells. (a) Kinetics of bioluminescence from the cells incubated with an emulsion containing LCTG-Luc1 or LCGE-Luc1 (15  $\mu$ M for each probe in 1 mM NaTDC in PBS) in the presence of pancreatic lipase (200 ng/mL) and colipase (40 ng/mL). (b) Total bioluminescent signal produced by the probes in cells over 150 min, which corresponds to kinetics curves (a). (c) Bioluminescent response from the cells incubated with the emulsion of LCGE-Luc1 (15  $\mu$ M) in the presence of pancreatic lipase (200 ng/mL) and colipase (40 ng/mL) upon addition of GSH (5 mM final concentration) after 52 min. Error bars are  $\pm$ SEM ( $n = 3$  for LCTG-Luc1 and LCGE-Luc1). Statistical analysis was performed with a two-tailed Student's  $t$ -test (\*\*\*\* $P < 0.0001$ ).

The total bioluminescent signal generated from LCTG-Luc1 mixed with PL over 150 min in cells was 89.7-fold greater than the signal produced from the same amount of the control probe LCGE-Luc1 mixed with PL over the same period of time (Figure 3.9b). This result is in excellent agreement with the known properties of trialkyl glycerol ethers, which are not absorbed by cells, as it was shown in the studies using radiolabeled glycerol triethers (198, 280).

In another experiment, the effect of GSH addition to the control probe emulsion was examined in order to establish whether it would induce the BL signal production in Caco2-luc cells. First, the cells were loaded with the emulsified LCGE-Luc1 in the presence of PL and imaged. Then GSH was added to the probe after 52 min of imaging to provide 5 mM GSH in the mixture with the probe emulsion, which

corresponds to the physiological range of intracellular GSH concentrations (0.1-15 mM) (281), and then the cells were immediately imaged. While the presence of PL did not result in the signal generation from the control probe, the addition of GSH to the probe triggered the immediate cellular BL response (Figure 3.9c). The generation of light after addition of GSH indicates that the disulfide bond in the non-cell-permeable control probe LCGE-Luc1 was reduced by added GSH outside the cells with the release of luciferin (MPr-AL). Once released, luciferin MPr-AL was taken up by cells and generated light upon reaction with intracellular luciferase (Figure 3.10).

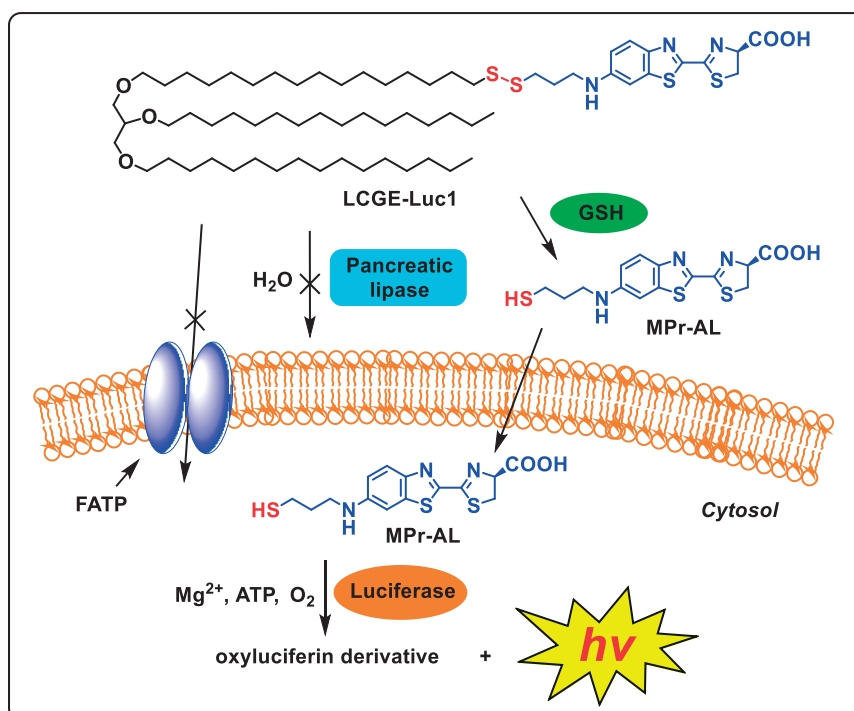


**Figure 3.10** Extracellular release of luciferin MPr-AL from the control probe LCGE-Luc1 induced by added GSH, which resulted in bioluminescent signal production in Caco2-luc cells. The amount of GSH added to the probe emulsion provided 5 mM GSH in the final mixture, which is similar to physiological intracellular concentration of GSH.

The immediate bioluminescent signal production in cells after addition of 5 mM GSH to LCGE-Luc1 demonstrates very fast kinetics of disulfide bond cleavage resulting in release of luciferin MPr-AL, which is consistent with the previous reports utilizing conjugates that undergo disulfide bond cleavage in the cytosol (71, 72, 74, 75, 268, 282). It confirms that the process of intracellular luciferin (MPr-AL) release from the corresponding products of lipolysis of TG probes is also very rapid that is triggered by the action of cytosolic GSH (Figure 3.4).

The studies in Caco2-luc cells demonstrate the essential role of the probe lipolysis for the cellular BL signal generation from LCTG-Luc1, LCTG-Luc2 and MCTG-Luc1. The lack of BL response from the non-hydrolyzable control probe LCGE-Luc1 in the presence of PL provides additional evidence for

the importance of lipolysis for activation of TG probes. These results are consistent with the known mechanism of intestinal triglyceride absorption, where triglycerides cannot cross the intestinal barrier without undergoing the hydrolysis by gastrointestinal lipases (195-198, 283). The data obtained for LCGE-Luc1 also indicate the stability of the linker between the TG moiety and the luciferin part of the developed probes in the aqueous extracellular environment containing PL. These experiments show that the luciferin scaffold (MPr-AL) utilized for TG probe development provides significant advantage over previously described approach for the synthesis of biomolecule-luciferin conjugates, which were developed using D-luciferin with disulfide-carbonate linker that has limited hydrolytic stability resulting in an increase of a background signal (71, 72, 74-77, 260). Taken together, the data in Caco2-luc cells demonstrate that developed TG probes produce cellular bioluminescent response only after the reaction with PL and subsequent cellular uptake of the products of their lipolysis, which suggests that these probes represent the absorption of natural triglycerides.

### 3.4.5 Validation of triglyceride probes in luciferase expressing mice.

Following the validation experiments in the luciferase expressing Caco2-luc cells, the uptake of TG probes was studied in living animals in order to establish whether this approach would allow for real-time imaging and quantification of intestinal TG absorption *in vivo* (Figure 3.11). FVB-luc+ mice that ubiquitously express luciferase under control of the beta-actin promoter (284) were used for the experiments.

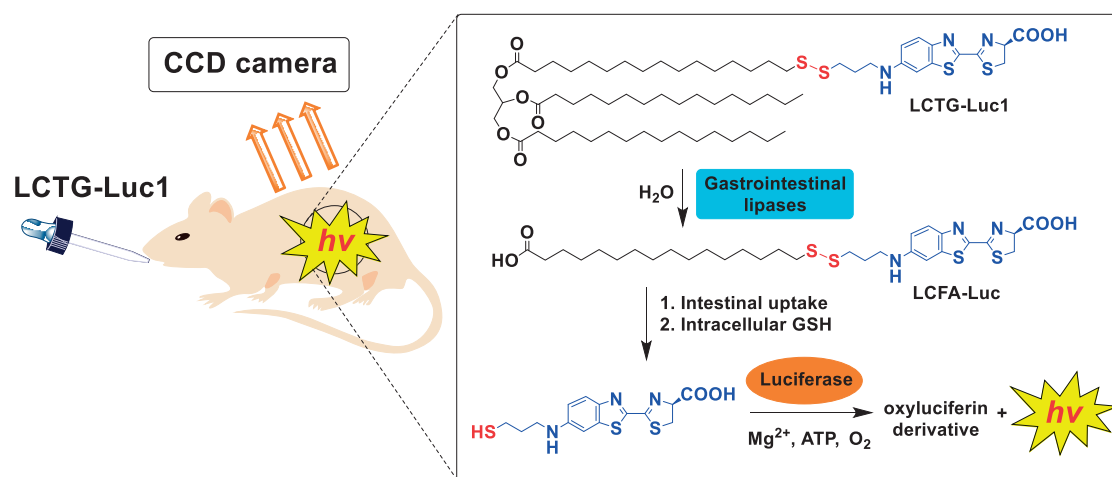


**Figure 3.11** Real-time bioluminescence imaging of intestinal triglyceride absorption in living mice using LCTG-Luc1.

For *in vivo* studies the focus was put on the absorption of long-chain TG probes, since long-chain TGs are the predominant type of fat in the diet (267). All *in vivo* imaging experiments were performed after mice starvation and without applying anesthesia by placing unrestricted mice in

ventilated transparent non-luminescent plastic boxes installed inside the IVIS imaging system, as the anesthesia was reported to influence gastrointestinal motility in animals (285), which would have the impact on the kinetics of digestion and absorption of lipids, making the experimental conditions non-physiological.

In the initial experiments, the BL response in mice from various doses (0, 10, 40, 100 nmol per mouse) of LCTG-Luc1 was examined. The probe dissolved in corn oil was administered by oral gavage after 10 h of fasting period, and the BL signal was acquired with the CCD camera (IVIS Spectrum). The same mice were used for gavage of different doses of LCTG-Luc1 with the interval of 5 days between the imaging sessions. The experiment revealed an increase in BL signal production in mice as a function of the amount of the gavaged probe (Figure 3.12).

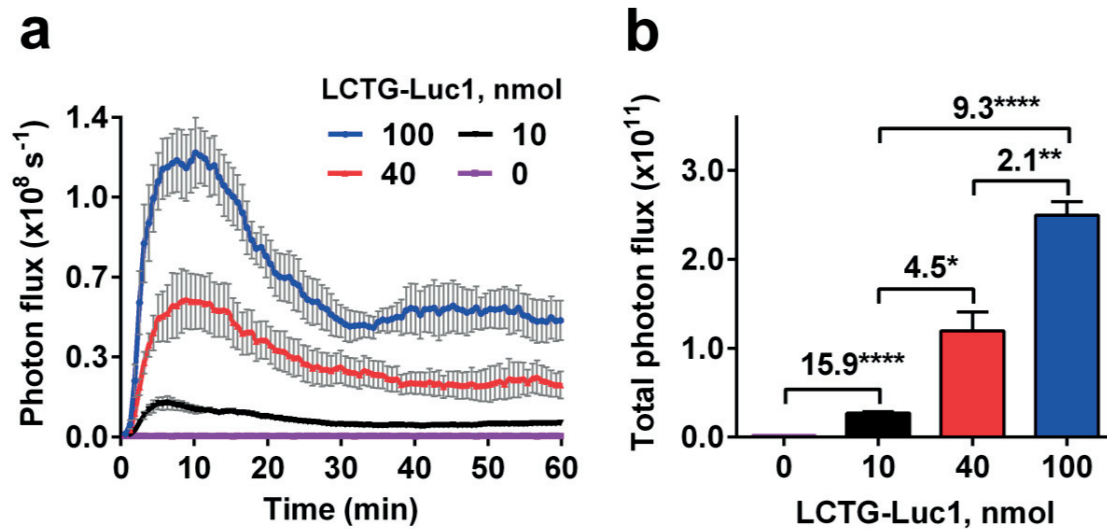


**Figure 3.12** Bioluminescence imaging of intestinal absorption of LCTG-Luc1 in FVB-luc<sup>+</sup> mice. (a) Kinetics of bioluminescent signal from non-anesthetized unrestricted mice after receiving various doses of LCTG-Luc1 (0-100 nmol per mouse in 150  $\mu\text{L}$  corn oil) by oral gavage. Imaging was performed immediately after gavage. (b) Total photon flux over 0-60 min corresponding to the kinetic curves shown in (a). Error bars are  $\pm\text{SEM}$  ( $n = 4-7$ ). Statistical analyses were performed with a two-tailed Student's t-test (\* $P < 0.05$ , \*\* $P < 0.01$ , \*\*\*\* $P < 0.0001$ ).

The signal from the lowest amount of the probe (10 nmol or 11.9  $\mu\text{g}$  per mouse) used in the experiment was robustly detected in mice with 15.9-fold increase ( $P < 0.0001$ ) in total photon flux, collected over 0-60 min, compared to the background level (0 nmol) (Figure 3.12b). This suggests that even lower gavaged doses ( $< 10$  nmol per mouse) of the probe would produce detectable BL response *in vivo*, demonstrating very high sensitivity of the method. A four- and ten-times increase of the dose of LCTG-Luc1 (from 10 to 40 nmol and from 10 to 100 nmol) resulted in a statistically significant 4.5-fold and 9.3-fold growth of the total bioluminescence in mice respectively, which indicates linear

dose-response relationship for the applied range of LCTG-Luc1 doses. These results suggest that the method allows for quantification of LCTG-Luc1 absorption in mice.

Considering much more complex environment in the gastrointestinal tract compared to the assay conditions used for Caco2-luc cells, the specificity of LCTG-Luc1 bioluminescent response to the probe lipolysis and absorption needed to be confirmed *in vivo*. As LCTG-Luc1 contains the disulfide bond between the luciferin part and the TG part, the disulfide might undergo unspecific cleavage prior to the probe lipolysis and absorption, once the probe is introduced into the intestinal lumen. This would liberate luciferin MPr-AL in the intestinal lumen, but not in the enterocytes. In this case, the BL signal generated after MPr-AL absorption into enterocytes would not represent the TG absorption. To verify that the BL signal in mice after oral gavage of LCTG-Luc1 results from the lipolysis of the probe and subsequent intestinal uptake of the resulting LCFA-Luc (Figure 3.11), the BL response from LCTG-Luc1 *in vivo* was compared to that from the same dose of the control compound LCGE-Luc1, that is stable to lipolysis. After oral gavage of the probes, the mice were immediately imaged over one hour without anesthesia. LCTG-Luc1 generated a robust BL signal in mice (Figure 3.13a), which was 24.2-fold higher ( $P = 0.0084$ ) when integrated over 1 h than the signal produced by the control probe LCGE-Luc1, and at the same time total signal from LCTG-Luc1 was 59.5-fold higher ( $P = 0.0079$ ) than the total background luminescence from mice received no probe (Figure 3.13b).

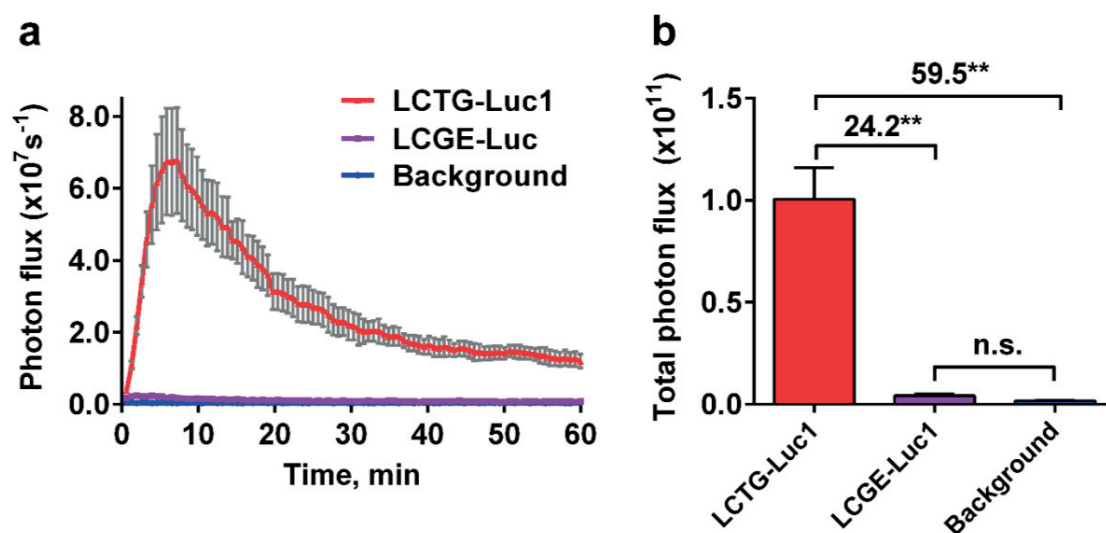


**Figure 3.13** Comparison of bioluminescent responses from LCTG-Luc1 and control probe LCGE-Luc1 administered by oral gavage in FVB-luc+ mice. (a) Kinetics of bioluminescent signal from non-anesthetized mice after receiving oral gavage of LCTG-Luc1 or LCGE-Luc1 or no probe (45 nmol for each probe in 250  $\mu\text{L}$  emulsion with 10 mM NaTDC in PBS). Imaging was performed immediately after gavage. (b) Total photon flux over 0-60 min corresponding to the kinetic curves shown in (a). Error bars are  $\pm$ SEM ( $n = 4$ ). Statistical analyses were performed with a two-tailed Student's *t*-test (\*\* $P < 0.01$ , n.s. – non-significant).

In contrast, the control probe LCGE-Luc1 produced a very low BL response *in vivo*, which was close to the background luminescence. The comparison of the total light emission integrated over 1 h for these two groups of mice (LCGE-Luc1 versus background) revealed small (2.4-fold) and non-significant difference ( $P = 0.0542$ ) (**Figure 3.13b**). These data demonstrate that the resistant to lipolysis trialkyl glycerol-luciferin probe LCGE-Luc1 did not undergo significant intestinal absorption in mice, since it did not produce significant BL response. These results are in excellent agreement with LCGE-Luc1 uptake experiments in Caco2-luc cells (**Figure 3.9**) as well as with the previous studies, in which the uptake of radiolabeled trialkyl glycerol ethers was measured in rats (198, 280). Importantly, the lack of luminescent signal from the non-absorbable control probe LCGE-Luc1 in mice indicates that the disulfide bond is stable in the intestinal environment, which confirms that BL response of LCTG-Luc1 is specific to its lipolysis and *in vivo* intestinal uptake of the released fatty acid labeled with luciferin.

To prove that the hydrolysis of LCTG-Luc1 by gastrointestinal lipases is required for the production of a bioluminescent signal from the probe in mice, the influence of the lipase inhibitor orlistat (278, 279) on the BL response from LCTG-Luc-1 in FVB-Luc<sup>+</sup> mice was examined. In this experiment a group of mice treated with orlistat consisted of the same animals as the control group (no orlistat), so that each animal served as its own control. First, the control group was pretreated with vehicle only by oral gavage and 10 min later was gavaged with LCTG-Luc1 probe and imaged with the CCD camera over 1 h (**Figure 3.14**). After 5 days of mice resting period the imaging with orlistat treatment was performed. First, the mice were pre-gavaged with orlistat in order to efficiently suppress the intestinal lipase activity, as the inhibition of pancreatic lipase by orlistat was reported to be non-immediate with half-inhibition time 5-6 min (286). After 10 min the mice were gavaged with LCTG-Luc1 mixed with orlistat and imaged over 1 h. As expected, orlistat suppressed the bioluminescent signal from LCTG-Luc1 in mice, with a significant 6.8-fold decrease ( $P = 0.0062$ ) in the total photon flux (**Figure 3.14b**), collected over 1 h, compared to the signal from LCTG-Luc1 alone, indicating the inhibition of intestinal absorption of the probe by orlistat. The **Figure 3.14c** shows the real-time BL images of mice 10 min post gavage with LCTG-Luc1 probe in the absence (left image) and in the presence of orlistat (right image) respectively, demonstrating the suppression of LCTG-Luc1 absorption in mice by orlistat.

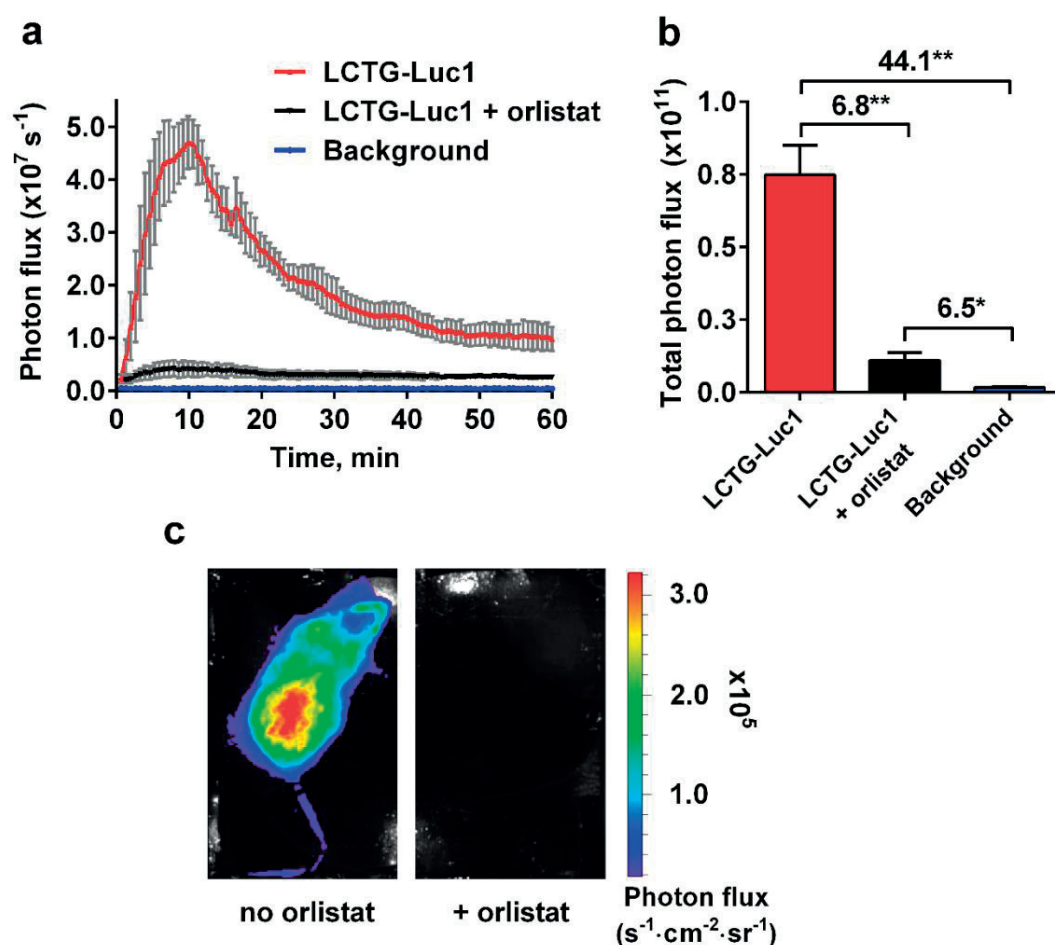


**Figure 3.14** Influence of orlistat on the bioluminescent response from LCTG-Luc1 administered by oral gavage in FVB-luc+ mice. (a) Kinetics of bioluminescent signal from non-anesthetized mice pretreated with orlistat (5 mg per mouse in 200  $\mu\text{L}$  emulsion) or vehicle alone (200  $\mu\text{L}$  emulsion) by oral gavage and 10 min later received LCTG-Luc1 (45 nmol in 250  $\mu\text{L}$  emulsion) mixed with orlistat (5 mg) or LCTG-Luc1 (45 nmol in 250  $\mu\text{L}$  emulsion) alone respectively by oral gavage. (b) Total photon flux over 1 h corresponding to the kinetic curves shown in (a). (c) Representative images acquired 10 min after start of luminescent signal acquisition for mice gavaged with LCTG-Luc1 only or LCTG-Luc1 mixed with orlistat as described in (a). Error bars are  $\pm\text{SEM}$  ( $n = 4$ ). Statistical analyses were performed with a two-tailed Student's t-test (\* $P < 0.05$ , \*\* $P < 0.01$ ).

These *in vivo* data are consistent with the uptake studies of LCTG-Luc1 in the presence of orlistat in Caco2-luc cells (Figure 3.8) and they are also in excellent agreement with the known mode of action of orlistat, which is used as an anti-obesity drug by inhibiting gastrointestinal lipases and suppressing the intestinal absorption of triglycerides (278, 279, 287).

To compare *in vivo* BL response from LCTG-Luc1 and LCTG-Luc2 that are different in the position of the luciferin label MPr-AL (attached to *sn*-1/*sn*-3 acyl chain versus *sn*-2 acyl chain respectively), the mice received oral gavage of LCTG-Luc1 followed by imaging over 1 h, and on another day the imaging experiment was performed for LCTG-Luc2 using the same animals. Since pancreatic lipase cleaves fatty acyl chains at *sn*-1 and *sn*-3 positions of triglycerides, the gastrointestinal lipolysis



of LCTG-Luc1 and LCTG-Luc2 would produce different bioluminescent metabolites, free fatty acid-luciferin (LCFA-Luc) and *sn*-2-monoacylglycerol-luciferin (LCMG-Luc2) respectively (Scheme 3.1a,b). Following oral gavage, the probes demonstrated different kinetics of light emission in mice (Figure 3.15a). The bioluminescence production *in vivo* from LCTG-Luc1 was significantly faster than that from LCTG-Luc2, with 8.2-fold difference ( $P < 0.0001$ ) between the initial slopes of the kinetic curves (Figure 3.15c).

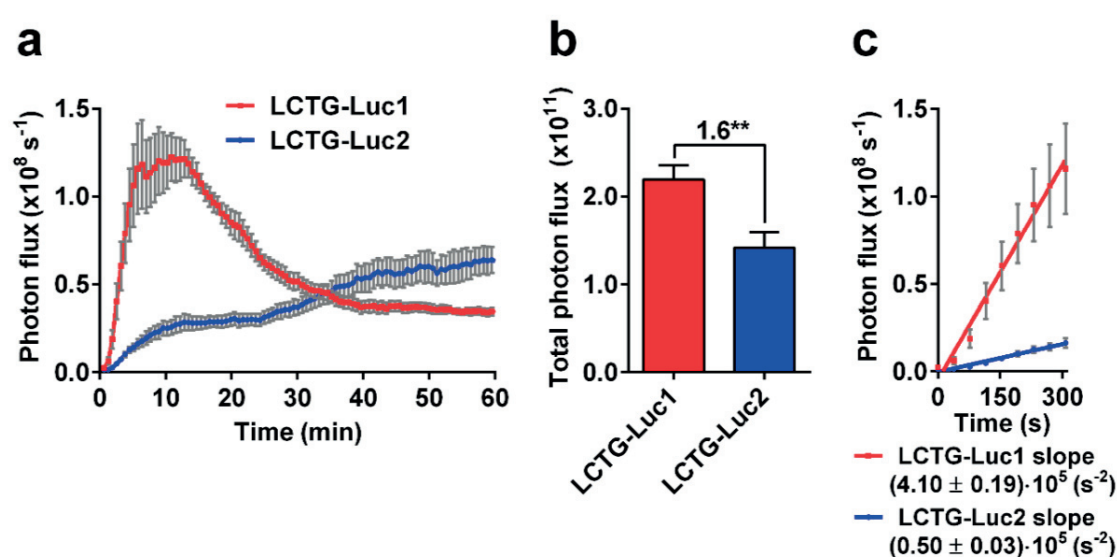


**Figure 3.15** Comparison of bioluminescent responses from LCTG-Luc1 and LCTG-Luc2 administered by oral gavage in FVB-luc+ mice. (a) Kinetics of bioluminescent signal from non-anesthetized mice after oral gavage of LCTG-Luc1 or LCTG-Luc2 (40 nmol of each probe in 150  $\mu\text{L}$  corn oil) followed by imaging. (b) Total photon flux over 1 h corresponding to the kinetic curves shown in (a). (c) Linear regression through initial time points to determine the initial slopes of the kinetic curves shown in (a). The difference between the slopes is significant ( $P < 0.0001$ ). Error bars are  $\pm \text{SEM}$  ( $n = 7-8$ ). Statistical analyses were performed with a two-tailed Student's t-test (\*\* $P < 0.01$ ).

These results suggest that during the initial period of LCTG-Luc2 digestion *in vivo* the process of release and intestinal absorption of *sn*-2-monoacylglycerol-luciferin is slower than that of free fatty acid-luciferin liberated from LCTG-Luc1. This finding is consistent with a previous study in rats based on using a radiolabeled triglyceride probe, which demonstrated that during the first hour after oral gavage of triglyceride the released *sn*-2-monoacylglycerol had slower intestinal absorption compared to the intestinal uptake of liberated free fatty acids (288).

To identify which part of the gastrointestinal tract is involved in the absorption of LCTG-Luc1 probe, the mice received oral gavage of LCTG-Luc1 and then were euthanized 10 min post gavage that corresponded to the maximal signal production *in vivo*, and the digestive tract was immediately excised from the stomach to the colon followed by bioluminescence imaging (Figure 3.16). *Ex vivo* imaging demonstrated that the strongest bioluminescent signal from LCTG-Luc1 was generated by the



proximal jejunum. This result is in excellent agreement with the previous studies, which showed that proximal jejunum is a major site of intestinal triglyceride absorption (196, 289).

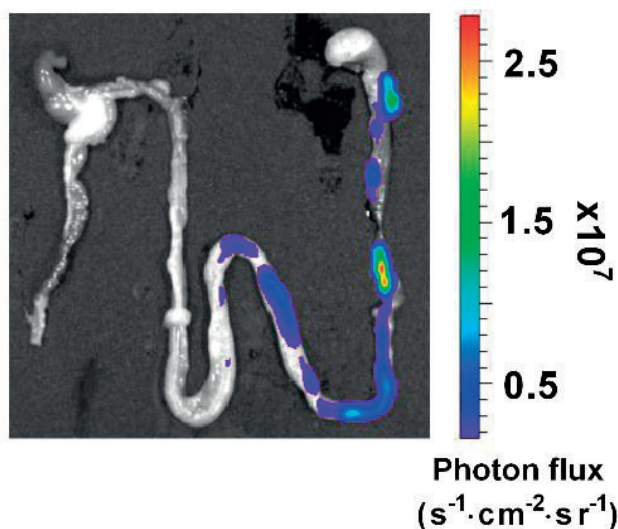


**Figure 3.16** Representative luminescent image of the excised gastro-intestinal tract from FVB-luc+ mouse 10 min after oral gavage of LCTG-Luc-1 (40 nmol in 150  $\mu$ L corn oil).

#### 3.4.6 Influence of the gut microbiota on triglyceride absorption *in vivo*

Bioluminescent triglyceride probes were employed to study the effects of the gut microbiota on the triglyceride absorption in living mice. First, the effects of the gut microbiota depletion were investigated. The suppression of the intestinal microbiota was achieved by treatment of mice with a mixture of broad-spectrum antibiotics, which consisted of ampicillin, vancomycin, neomycin and metronidazole (AVNM) in drinking water for 7-9 days (290). The mice received oral gavage of LCTG-Luc1 before the AVNM treatment, at the end of the AVNM treatment and a week after finishing the AVNM treatment, and the bioluminescent signal was acquired over 1 h. Suppression of the gut microbiota in mice resulted in substantial changes in the kinetics of LCTG-Luc1 absorption in the intestine (**Figure 3.17**). LCTG-Luc1 demonstrated much slower bioluminescence kinetics following the AVNM treatment with the 6-fold decrease ( $P < 0.0001$ ) in the initial slope of the kinetic curve (**Figure 3.17c**). Interestingly, 7 days after discontinuation of the antibiotics treatment the bioluminescence kinetics for LCTG-Luc1 was significantly restored and was close to the kinetics pattern observed in mice before the AVNM treatment with only 1.6-fold difference ( $P < 0.05$ ) in the slopes of the corresponding kinetic curves (**Figure 3.17c**).

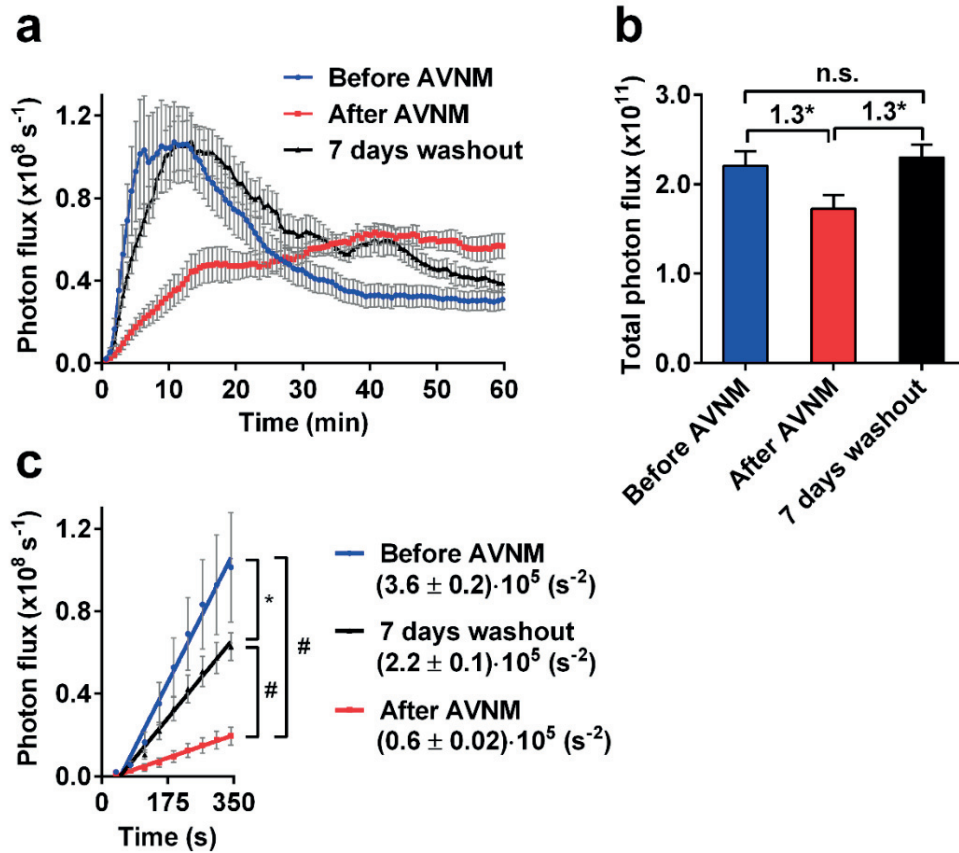


**Figure 3.17** Influence of antibiotics treatment on the intestinal absorption of LCTG-Luc1 in FVB-luc+ mice. (a) Kinetics of bioluminescent signal from LCTG-Luc1 (40 nmol in 150  $\mu\text{L}$  corn oil by oral gavage) in mice before treatment (before AVNM), at the end of treatment (after AVNM) with a mixture of antibiotics AVNM (A - ampicillin 1g/L, V - vancomycin 0.5 g/L, N - neomycin sulfate 1 g/L, M - metronidazole 1 g/L in drinking water) and 7 days AVNM post treatment (washout). (b) Total photon flux over 60 min corresponding to kinetic curves shown in (a). (c) Linear regression through initial time points to determine the initial slopes of the kinetic curves shown in (a). The slopes are indicated in the legend. Error bars are  $\pm\text{SEM}$  ( $n = 8$ ). Statistical analyses were performed with a two-tailed Student's t-test (\* $P < 0.05$ , # $P < 0.0001$ ).

The cessation of antibiotics treatment is known to result in the recovery of the gut microbial community (291-293). This suggests that the revealed restoration of the absorption kinetics for LCTG-Luc1 in mice after 7 days of the washout period is caused by the recovery of the gut microbiota. This result clearly demonstrates the influence of the gut microbiota on the intestinal absorption of triglycerides.

The AVNM treatment of mice also influenced the bioluminescence kinetics from LCTG-Luc2 (Figure 3.18). The suppression of LCTG-Luc2 signal was more substantial than that of LCTG-Luc1. The depletion of the gut microbiota resulted in 11-fold decrease in the initial slope of the kinetic curve for LCTG-Luc2 (Figure 3.18c). Interestingly, the mice treated with AVNM demonstrated the progressive reduction of the body weight.

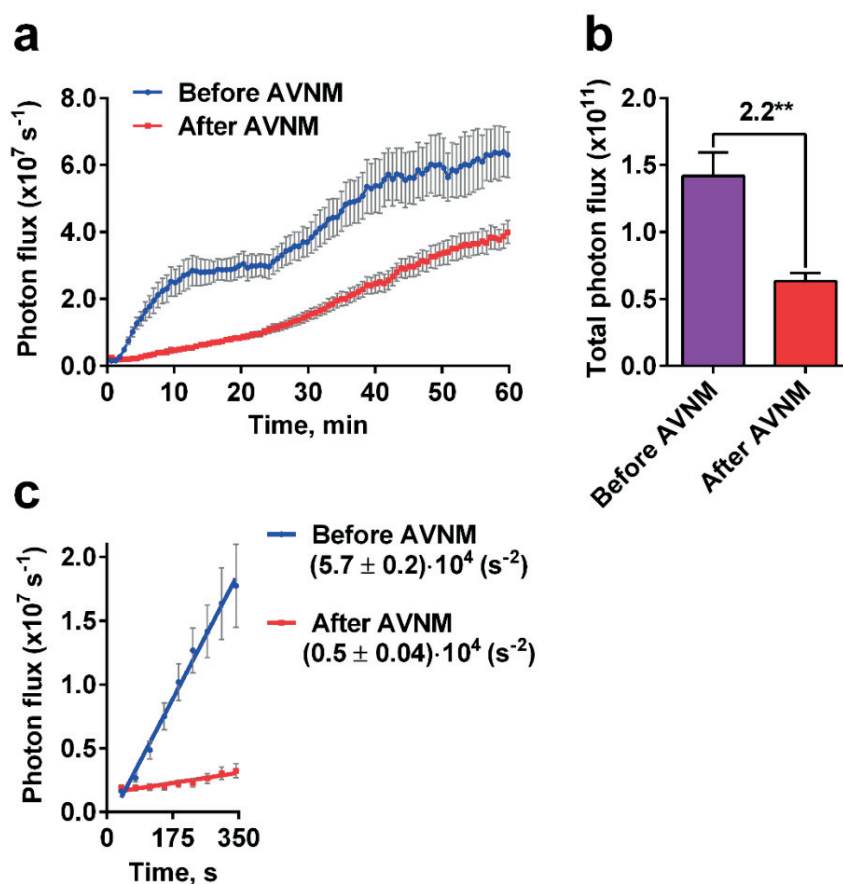


**Figure 3.18** Influence of antibiotics treatment on the intestinal absorption of LCTG-Luc2 in FVB-luc+ mice. (a) Kinetics of bioluminescent signal from LCTG-Luc2 (40 nmol in 150  $\mu\text{L}$  corn oil by oral gavage) in mice before treatment (before AVNM) and at the end of treatment (after AVNM) with a mixture of antibiotics AVNM (A - ampicillin 1g/L, V - vancomycin 0.5 g/L, N - neomycin sulfate 1 g/L, M - metronidazole 1 g/L in drinking water). (b) Total photon flux over 60 min corresponding to kinetic curves shown in (a). (c) Linear regression through initial time points to determine the initial slopes of the kinetic curves shown in (a). The slopes are indicated in the legend. The difference between the slopes is significant ( $P < 0.0001$ ). Error bars are  $\pm\text{SEM}$  ( $n = 8$ ). Statistical analyses were performed with a two-tailed Student's t-test (\*\* $P < 0.01$ ).

These results are consistent with the previous report that demonstrated the reduced lipid uptake in rats with the depleted gut microbiota following the antibiotics treatment (294).

Next, the influence of bile salt hydrolase (BSH) activity of probiotics on the triglyceride absorption in mice was investigated. Bile acids play important role in lipid digestion, since they aid in the solubilization of the lipolytic products to form colloidal structures that provide delivery of fatty acids and monoglycerides to the membrane of enterocytes (196, 201, 240, 295). Bile acids present in bile exist in the form of conjugates with taurine or glycine that make them soluble in aqueous solutions. Upon the action of bile salt hydrolase (BSH), an enzyme that is secreted by various microorganisms, conjugated bile acids undergo hydrolysis to form less soluble deconjugated bile acids that are less

efficient in solubilization of lipolytic products (296, 297). To test the effects of bile salt hydrolase producing probiotics on triglyceride absorption, the mice were first imaged following LCTG-Luc1 gavage. Then the mice were divided in 2 groups. One group was treated by oral gavage with *Lactobacillus plantarum* WCFS (wt) with high level of BSH activity. The second group received oral gavage of *L. Plantarum* NZS332 ( $\Delta bsh1-bsh4$ ) without BSH activity (297). The presence and the absence of BSH activity in these strains was confirmed *in vitro* by the ability of the bacteria to deconjugate glycodeoxycholate, which was monitored by HPLC-MS analysis. After 5 days of treatment with *L. Plantarum* strains no difference in bioluminescent signal from LCTG-Luc1 was observed between all the experimental groups (Figure 3.19a,b).

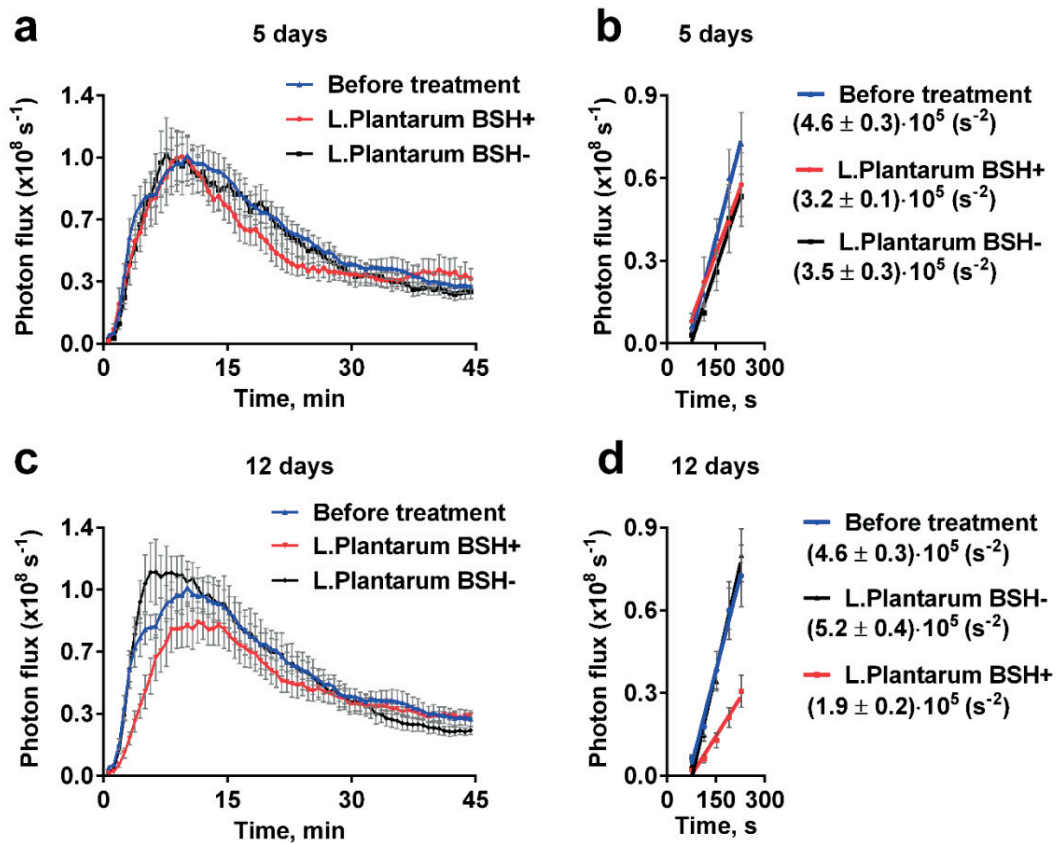


**Figure 3.19** Influence of *Lactobacillus plantarum* treatment with or without bile salt hydrolase activity on the bioluminescence from LCTG-Luc1 (40 nmol in 150  $\mu$ L corn oil by oral gavage) in FVB-luc+ mice. (a) Kinetics of bioluminescent signal from LCTG-Luc1 in mice before ( $n = 12$ ) and after oral treatment with *L. Plantarum* WCFS (wt) (*L. Plantarum* BSH+) or *L. Plantarum* NZS332 ( $\Delta bsh1-bsh4$ ) (*L. Plantarum* BSH-) ( $n = 6$  for each treated group) for 5 days ( $5 \cdot 10^9$  CFU for each strain in 200  $\mu$ L PBS per mouse). (b) Linear regression through initial time points to determine the initial slopes of the kinetic curves shown in (a). The difference between all slopes is not significant ( $P > 0.05$ ). (c) Kinetics of bioluminescent signal from LCTG-Luc1 in mice before ( $n = 12$ ) and after oral treatment with *L. Plantarum* BSH+ ( $n = 6$ ) and *L. Plantarum* BSH- ( $n = 6$ ) for 12 days (the same doses of bacteria as described in (a)). (d) Linear regression through initial time points to determine the initial slopes of the kinetic curves shown in (c). The differences between the red and the blue slopes (BSH+ vs before treatment), the red and the black slopes (BSH+ vs BSH-) are significant ( $P$  values are 0.0037 and  $< 0.0001$  respectively). The difference between the black and the blue slopes (BSH- vs before treatment) is not significant ( $P = 0.52$ ). In (b) and (d) the slopes are indicated in the legend.

The treatment with probiotics was continued for additional seven days (12 days in total) and the imaging was repeated again. As shown in **Figure 3.19c,d**, the group of mice that received wild-type *L.Plantarum* BSH+ (high BSH activity) demonstrated the decrease in the initial slope of the kinetic curve with 2.7-fold difference ( $P < 0.0001$ ) in comparison with the group received *L.Plantarum* BSH- (no BSH activity) for the same period of treatment. However, no difference in total photon flux over 45 min was found between all the groups. This result suggests that BSH activity of probiotics may have influence on the initial rate of lipid absorption *in vivo* as a result of the changes in the bile acid profile in the intestine induced by BSH-producing microorganisms.

## 3.5 Experimental Section

### 3.5.1 Materials and methods. Chemical part

**General information.** All reactions were performed under inert atmosphere of nitrogen or argon unless otherwise noted. The reagents and solvents were ordered from Sigma-Aldrich, Acros, TCI, Fluorochem and were used as received. Analytical thin-layer chromatography was carried out using SiO<sub>2</sub>-coated glass plates (DC Kieselgel 60G F<sub>254</sub>, Merck). The compounds on TLC plates were visualized by UV-light at 254 nm or by applying the iodine vapors or immersing the plates in cerium molybdate solution followed by heating. LCMS analysis was performed with Waters Acquity UPLC system with Acquity UPLC® BEH C8 or C18 column (2.1 × 50 mm, 1.7 μm) connected to Waters Acquity LC/MS system or with Agilent Infinity 1260 HPLC system (Agilent, Santa Clara, CA) using SunFire® C18 column (2.1 × 20 mm, 3.5 μm) connected to Quadrupole LC/MS system (Agilent). Degassed HPLC grade solvents from Fisher Chemicals and Millipore water were used for LCMS analysis. Flash chromatography was performed using silica gel P60, 40-63 μm, 60 Å (SiliCycle Inc.). Preparative HPLC purification was carried out with Waters preparative HPLC system connected to XTerra® Prep MS C18 OBD™ column (5 μm, 19 × 50 mm) using HPLC grade solvents from Fisher Chemicals and Millipore water. Nuclear magnetic resonance spectra were acquired on Bruker AV-400 MHz spectrometer. NMR chemical shifts are reported in parts per million  $\delta$  (ppm) using the central line of the solvent residual proton and carbon signal as an internal reference. Splitting patterns are defined as s (singlet), d (doublet), dd (doublet of doublets), t (triplet), q (quartet), m (multiplet), br (broad). HRMS measurements (ESI-HRMS) were performed at the EPFL Mass Spectrometry Service using Micro Mass QTOF Ultima (Waters).

**S-(3-oxopropyl) ethanethioate (3).** Thioacetic acid (7.1 mL, 100 mmol) dissolved in DCM (25 mL) was added dropwise under N<sub>2</sub> to an ice-cooled mixture of acrolein (7.0 mL, 100 mmol) and DIPEA (1.7 mL, 10 mmol) in DCM (50 mL) under stirring. Upon addition of thioacetic acid the cooling bath was removed and stirring was continued at RT. After 12 h volatile materials were removed *in*

*vacuo* and the oily residue was distilled under reduced pressure (bp. 78-82°C/7 mbar), yielding the product **3** as a colorless liquid (10.6 g, 80% yield). <sup>1</sup>H NMR (400 MHz, CDCl<sub>3</sub>) δ 9.74 (s, 1H), 3.11 (t, *J* = 6.7 Hz, 2H), 2.79 (t, *J* = 6.7 Hz, 2H), 2.32 (s, 3H).

**S-(3-((2-cyanobenzo[d]thiazol-6-yl)amino)propyl) ethanethioate (4).**

6-aminobenzo[d]thiazole-2-carbonitrile (131 mg, 0.75 mmol) was dissolved in THF (5 mL) under N<sub>2</sub> followed by addition of aldehyde **3** (159 μL, 1.43 mmol) and glacial acetic acid (100 μL, 1.74 mmol). After addition of NaBH(OAc)<sub>3</sub> (318 mg, 1.5 mmol) the reaction mixture was stirred at RT with protection from light until full disappearance of the starting amine, which was monitored by LCMS analysis. Then, the reaction mixture was diluted with AcOEt (15 mL) and washed with sat. NaHCO<sub>3</sub> (1 × 5 mL), water (2 × 10 mL) and brine (1 × 10 mL), then dried over Na<sub>2</sub>SO<sub>4</sub>. The solvent was evaporated *in vacuo* to give a crude material, which was purified by silica gel column chromatography (hexane-AcOEt 3:1) yielding the product **4** as a yellow solid (131 mg, 60% yield).

**(S)-2-(6-((3-(acetylthio)propyl)amino)benzo[d]thiazol-2-yl)-4,5-dihydrothiazole-4-carboxylic acid (5).** A solution of D-cysteine (89 mg, 0.73 mmol) in degassed PBS with pH 7.2 (5 mL) was added dropwise under N<sub>2</sub> to a stirred solution of compound **4** (71 mg, 0.24 mmol) in acetonitrile (8 mL). After completion of the reaction (monitored by LCMS analysis), the solvents were evaporated *in vacuo*. The crude mixture was purified by silica gel column chromatography (DCM-MeOH 30:1 + 2% (v/v) acetic acid) to give the product **5** as a yellow-orange solid (91 mg, 95% yield).

**(S)-2-(6-((3-(pyridin-2-yl)disulfaneyl)propyl)amino)benzo[d]thiazol-2-yl)-4,5-dihydrothiazole-4-carboxylic acid (6).** The compound **5** (24 mg, 0.06 mmol) was dissolved in 1 mL of dry MeOH followed by addition of 2,2'-dipyridyl disulfide (65 mg, 0.30 mmol) under nitrogen. 7 N NH<sub>3</sub> in MeOH solution (200 μL, 1.4 mmol) was added to the reaction mixture, followed by stirring at RT with protection from light until full conversion of the starting compound **5**, which was monitored by LCMS analysis. The reaction mixture was concentrated *in vacuo* and the residue was purified by silica gel column chromatography using DCM-MeOH (20:1) + 2% (v/v) acetic acid to give the product **6** (PyS-MPr-AL) as an orange-yellow solid (46 mg, 91% yield). **HRMS**: calculated for C<sub>19</sub>H<sub>19</sub>N<sub>4</sub>O<sub>2</sub>S<sub>4</sub> [M+H]<sup>+</sup> 463.0391, found 463.0393.

**Palmitoyl chloride (8).** Oxalyl chloride (1.5 mL, 17.8 mmol) was added slowly at RT under stirring to a solution containing palmitic acid (2.3 g, 8.9 mmol) and DMF (3 μL, 0.04 mmol) in dichloromethane (15 mL). Slow release of gas was observed. The reaction mixture was stirred at RT for 3 h and then evaporated *in vacuo* to give an oil, which was mixed with dry toluene (5 mL) and



evaporated *in vacuo* to provide the crude product **8**. The obtained palmitoyl chloride was directly used in the next step.

**RS-3-(benzyloxy)propane-1,2-diyl dipalmitate (9).** RS-3-Benzyloxy-1,2-propanediol (600 mg, 3.29 mmol) in dichloromethane (6 mL) was mixed with pyridine (1.1 mL, 13.2 mmol) and DMAP (10.1 mg, 0.08 mmol) under N<sub>2</sub>. The reaction mixture was cooled down to 0°C. The whole amount of palmitoyl chloride **8** obtained in the previous step was dissolved in DCM (6 mL) in a separate flask and added dropwise to the reaction mixture under stirring at 0°C. The formation of the precipitate was observed. After 10 min cooling bath was removed and stirring was continued at RT for 16 h. Then, the reaction mixture was diluted with DCM (20 mL) and washed with 0.1 M HCl (3 × 10 mL) and with brine (1 × 10 mL). Organic phase was dried with Na<sub>2</sub>SO<sub>4</sub>, the solvent was evaporated *in vacuo* to give a crude material, which was purified by silica gel column chromatography (hexane-AcOEt 10:1) yielding the product **9** as a white solid (1.85 g, 85% yield).

**RS-3-hydroxypropane-1,2-diyl dipalmitate (10).** RS-3-(benzyloxy)propane-1,2-diyl dipalmitate **9** (1.52 mg, 2.31 mmol) was dissolved in ethyl acetate (20 mL) followed by three vacuum-N<sub>2</sub> cycles. Then, 5% Pd/C (200 mg) was added to the reaction mixture under N<sub>2</sub>. The reaction flask was filled with H<sub>2</sub>, and the compound **9** was hydrogenated under normal pressure at RT for 21 h. The catalyst was removed by filtration through a pad of Celite and the filtrate was concentrated *in vacuo* to provide the product **10** as a white powder (1.32 g, quantitative yield) which was used in the next step without purification.

**16-(tritylthio)hexadecanoic acid (12).** Triphenylmethanethiol (829 mg, 3.0 mmol) was dissolved in toluene (6 mL) under N<sub>2</sub>, followed by the addition of 5.4 M MeONa (1.2 mL, 6.5 mmol) under stirring at RT, which led to the formation of white precipitate. Then, a solution of 16-bromohexadecanoic acid **11** (1.1 g, 3.3 mmol) in a mixture of MeOH (5 mL) and THF (5 mL) was added dropwise to the reaction mixture at 0°C under vigorous stirring. The mixture was heated to 50°C and stirring was continued for 2.5 h. After cooling the reaction mixture was quenched with aqueous 0.1% HCl (30 mL) and extracted with DCM (100 mL). Aqueous phase was separated and extracted again with DCM (2 × 40 mL). Combined organic phases were dried over Na<sub>2</sub>SO<sub>4</sub> and the solvent was evaporated *in vacuo*. The crude material was purified by silica gel column chromatography yielding the product **12** as a white solid (1.2 g, 75% yield).

**RS-3-((16-(tritylthio)hexadecanoyl)oxy)propane-1,2-diyl dipalmitate (13).** To a solution of acid **12** (700 mg, 1.32 mmol) in dichloromethane (2 mL) were added DMAP (27 mg, 0.22 mmol) and EDCI (253 mg, 1.32 mmol). The mixture was added to a vigorously stirred solution of compound **10**

(625 mg, 1.10 mmol) in dichloromethane (3 mL) at 0°C. The reaction mixture was warmed and stirred at RT for 4 h. The mixture was diluted with dichloromethane (50 mL), washed with 0.1 M HCl (2 × 40 mL) and then with brine (1 × 30 mL). Organic phase was dried over Na<sub>2</sub>SO<sub>4</sub> and evaporated *in vacuo*. The crude material was purified by silica gel column chromatography (hexane-AcOEt 10:1) yielding the product **13** as a white solid (774 mg, 65% yield).

**(5)-2-(6-((3-((16-(*RS*-2,3-bis(palmitoyloxy)propoxy)-16-oxohexadecyl)disulfaneyl)propyl)-amino)-benzo[d]thiazol-2-yl)-4,5-dihydrothiazole-4-carboxylic acid (**14**).** To a solution of the compound **13** (26 mg, 0.024 mmol) in dichloromethane (1.5 mL) cooled to 0°C were added TFA (111 µL, 1.44 mmol) and Et<sub>3</sub>SiH (46 µL, 0.29 mmol) under N<sub>2</sub>. The mixture was warmed and stirred at RT for 4 h and then the volatile materials were evaporated *in vacuo*. The residue was dissolved in THF (1 mL) under N<sub>2</sub>, followed by addition of the compound **6** (9 mg, 0.019 mmol) dissolved in DMF (1 mL) and DIPEA (11.4 µL, 0.065 mmol). The mixture was stirred at RT for 18 h with protection from light and then concentrated *in vacuo* to dryness. The residue was purified by silica gel column chromatography (DCM-MeOH 40:1 + 2% (v/v) acetic acid) to give the product **14** as an orange solid (19 mg, 82% yield). **HRMS:** calculated for C<sub>65</sub>H<sub>112</sub>N<sub>3</sub>O<sub>8</sub>S<sub>4</sub> [M+H]<sup>+</sup> 1190.7327, found 1190.7329.

**2-(benzyloxy)propane-1,3-diyl dipalmitate (**16**).** 2-Benzyloxy-1,3-propanediol (300 mg, 1.65 mmol) in dichloromethane (6 mL) was mixed with pyridine (532 µL, 6.59 mmol) and DMAP (5 mg, 0.04 mmol) under N<sub>2</sub>. The reaction mixture was cooled down to 0°C. A solution of palmitoyl chloride (1.33 mL, 4.4 mmol) in DCM (6 mL) was added dropwise to the reaction mixture under stirring at 0°C. After 10 min cooling bath was removed and stirring was continued at RT for 16 h. Then, the reaction mixture was diluted with DCM (10 mL) and washed with 0.1 M HCl (3 × 5 mL) and with brine (1 × 10 mL). Organic phase was dried with Na<sub>2</sub>SO<sub>4</sub>, the solvent was evaporated *in vacuo* to give a crude material, which was purified by silica gel column chromatography (hexane-AcOEt 10:1) yielding the product **16** as a white solid (618 mg, 57% yield).

**2-hydroxypropane-1,3-diyl dipalmitate (**17**).** Compound **16** (542 mg, 0.82 mmol) was dissolved in ethyl acetate (10 mL) followed by three vacuum-N<sub>2</sub> cycles. Then, 5% Pd/C (200 mg) was added to the reaction mixture under N<sub>2</sub>. The reaction flask was filled with H<sub>2</sub>, and the compound **16** was hydrogenated under normal pressure at RT for 21 h. The catalyst was removed by filtration through a pad of Celite and the filtrate was concentrated *in vacuo* to provide the product **17** as a white powder (430 mg, 92% yield) which was used in the next step without purification.

**2-((16-(tritylthio)hexadecanoyl)oxy)propane-1,3-diyl dipalmitate (**18**).** To a solution of acid **12** (370 mg, 0.70 mmol) in dichloromethane (5 mL) were added DMAP (14.2 mg, 0.12 mmol) and EDCI



(134 mg, 0.70 mmol). Then, this mixture was added to a vigorously stirred solution of compound **17** (331 mg, 0.58 mmol) in dichloromethane (5 mL) at 0°C under N<sub>2</sub>. The reaction mixture was warmed and stirred at RT overnight. The mixture was diluted with dichloromethane (20 mL), washed with 0.1 M HCl (2 × 20 mL) and then with brine (1 × 20 mL). Organic phase was dried over Na<sub>2</sub>SO<sub>4</sub> and evaporated *in vacuo*. The crude material was purified by silica gel column chromatography (hexane-AcOEt 10:1) yielding the product **18** as a white solid (452 mg, 72% yield).

**(S)-2-(6-((3-((16-((1,3-bis(palmitoyloxy)-propan-2-yl)oxy)-16-oxohexadecyl)disulfaneyl)-propyl)amino)benzo[d]thiazol-2-yl)-4,5-dihydrothiazole-4-carboxylic acid (19).** To a solution of the compound **18** (26 mg, 0.024 mmol) in dichloromethane (1.5 mL) cooled to 0°C were added TFA (111 µL, 1.44 mmol) and Et<sub>3</sub>SiH (46 µL, 0.29 mmol) under N<sub>2</sub>. The mixture was warmed and stirred at RT for 4 h and then the volatile materials were evaporated *in vacuo*. The residue was dissolved in THF (1 mL) under N<sub>2</sub>, followed by addition of the compound **6** (9 mg, 0.019 mmol) dissolved in DMF (1 mL) and DIPEA (11.4 µL, 0.065 mmol). The mixture was stirred at RT for 18 h with protection from light, then the solvents were evaporated *in vacuo* and the residue was purified by silica gel column chromatography (DCM-MeOH 40:1 + 2% (v/v) acetic acid) to give the product **19** as an orange solid (20 mg, 86% yield). **HRMS:** calculated for C<sub>65</sub>H<sub>112</sub>N<sub>3</sub>O<sub>8</sub>S<sub>4</sub> [M+H]<sup>+</sup> 1190.7327, found 1190.7333.

**RS-((2,3-bis(hexadecyloxy)propoxy)methyl)benzene (21).** A powder of 95% NaH (1.42 g, 56.3 mmol) was added to a solution of *RS*-3-benzyloxy-1,2-propanediol (3.42 g, 18.8 mmol) in DMF (257 mL) under N<sub>2</sub>. The mixture was stirred for 30 min at RT followed by dropwise addition of 1-bromohexadecane (16 mL, 52.6 mmol). After 28 h the reaction mixture was quenched with 200 mL of ice-cold water under stirring followed by extraction with Et<sub>2</sub>O (4 × 100 mL). Combined organic phase was washed with H<sub>2</sub>O (3 × 30 mL), dried over Na<sub>2</sub>SO<sub>4</sub> and concentrated *in vacuo*. The crude material was purified by silica gel column chromatography (gradient elution with hexane-AcOEt 50:1 → 10:1) yielding the product **21** as a transparent oil (8.45 g, 71% yield).

**RS-2,3-bis(hexadecyloxy)propan-1-ol (22).** Compound **21** (8.2 g, 12.99 mmol) was dissolved in ethyl acetate (70 mL) followed by three vacuum-N<sub>2</sub> cycles. Then, 10% Pd/C (200 mg) was added to the reaction mixture under N<sub>2</sub>. The reaction flask was filled with H<sub>2</sub>, and the compound **21** was hydrogenated under normal pressure at RT for 21 h. The catalyst was removed by filtration through a pad of Celite and the filtrate was concentrated *in vacuo* to provide the product **22** as a white powder (6.98 g, 99% yield) which was used in the next step without purification.

**2-((16-bromohexadecyl)oxy)tetrahydro-2H-pyran (24).**

Step 1. To a solution of 16-bromohexadecanoic acid (3.0 g, 8.95 mmol) in THF (18 mL)  $\text{BH}_3\cdot\text{THF}$  (10.8 mL, 10.74 mmol) was added dropwise at 0°C under  $\text{N}_2$ . The mixture was stirred at RT for 24 h and then quenched with  $\text{H}_2\text{O}$  (3 mL) and extracted with DCM (100 mL). Aqueous phase was separated and extracted with DCM (2 × 50 mL). Combined organic phase was washed with  $\text{H}_2\text{O}$ , then dried over  $\text{Na}_2\text{SO}_4$  and concentrated *in vacuo* to give 16-bromohexadecanol as a white solid (2.72 g, 95% yield), which was used in the next step without purification.

Step 2. 16-bromohexadecanol (2.5 g, 7.78 mmol) obtained in the previous step was dissolved in DCM (50 mL), followed by the addition of 3,4-dihydro-2H-pyran (1.07 mL, 11.67 mmol) and pyridinium p-toluenesulfonate (196 mg, 0.78 mmol). The mixture was stirred at RT under  $\text{N}_2$  for 3 h and then diluted with DCM and washed with aqueous half-saturated  $\text{NaHCO}_3$  (2 × 50 mL). Organic phase was separated, dried over  $\text{Na}_2\text{SO}_4$  and concentrated *in vacuo*. The crude product was purified by flash-filtration through a short pad of  $\text{SiO}_2$  using hexane-AcOEt 10:1 as an eluent, to provide the product **24** (2.95 g, 94% yield).

**RS-2-((16-(2,3-bis(hexadecyloxy)propoxy)hexadecyl)oxy)tetrahydro-2H-pyran (25).** The compound **22** (2.81 g, 5.20 mmol) was dissolved in the mixture of DMF (70 mL) and THF (35 mL) upon mild warming, followed by the addition of a powder of 95% NaH (208 mg, 8.68 mmol) under  $\text{N}_2$ . The mixture was stirred at RT for 30 min. Then, a solution of the compound **24** (2.95 g, 7.28 mmol) in THF (18 mL) was added dropwise to the reaction mixture, followed by stirring at RT for 72 h. The mixture was quenched by ice-cold water and then concentrated *in vacuo* to lower volume and extracted with  $\text{Et}_2\text{O}$  (1 × 100 mL). Aqueous phase was separated and extracted with  $\text{Et}_2\text{O}$  (2 × 30 mL). Combined organic extracts were dried over  $\text{Na}_2\text{SO}_4$  and concentrated *in vacuo* to give the crude product **25** as a yellow oil (5.05 g), which was used in the next step without purification.

**RS-16-(2,3-bis(hexadecyloxy)propoxy)hexadecan-1-ol (26).** To a solution of the compound **25** (3.53 g, 4.08 mmol) in a mixture of THF (50 mL) and MeOH (20 mL) PPTS (503 mg, 2.00 mmol) was added. A reflux condenser was connected to the reaction flask and the mixture was stirred at 50°C for 6 h. Then, the solvents were evaporated *in vacuo* and the residue was dissolved in AcOEt (100 mL) followed by washing with  $\text{H}_2\text{O}$  (3 × 50 mL) and brine (1 × 50 mL). Organic phase was dried over  $\text{Na}_2\text{SO}_4$  and the solvent was evaporated *in vacuo* to produce a white solid of **26** (2.66 g, 83% yield), which was used in the next step without purification.

**RS-16-(2,3-bis(hexadecyloxy)propoxy)hexadecyl methanesulfonate (27).** To a solution of the compound **26** (2.15 g, 2.75 mmol) in DCM (9 mL)  $\text{Me}_3\text{N}\cdot\text{HCl}$  (262 mg, 2.75 mmol) and DIPEA (956  $\mu\text{L}$ , 5.49 mmol) were added under  $\text{N}_2$ . The mixture was cooled to 0°C and then a solution of MsCl (472 mg,

4.12 mmol) in DCM (5 mL) was added dropwise under stirring. After 1 h the ice bath was removed and the stirring was continued at RT for 4.5 h. Then, N,N-dimethylethylenediamine (316  $\mu$ L, 2.89 mmol) was added to the mixture to quench the reaction. After stirring for 15 min the reaction mixture was diluted with AcOEt (150 mL) and washed with 0.1 M HCl (3  $\times$  30 mL), H<sub>2</sub>O (1  $\times$  50 mL) and brine (1  $\times$  30 mL). Organic phase was dried over Na<sub>2</sub>SO<sub>4</sub> and the solvent was evaporated *in vacuo*. The crude material was purified by silica gel column chromatography (gradient elution with CHCl<sub>3</sub>-toluene-Et<sub>2</sub>O 100:33:1  $\rightarrow$  100:33:5) yielding the product **27** as a white solid (491 mg, 21% yield).

**RS-(16-(2,3-bis(hexadecyloxy)propoxy)hexadecyl)(trityl)sulfane (28).** To a solution of the compound **27** (164 mg, 0.19 mmol) in THF (1 mL) were added a solution of triphenylmethanethiol (65 mg, 0.23 mmol) in DMF (1 mL) and DIPEA (40  $\mu$ L, 0.23 mmol) under N<sub>2</sub>. The mixture was stirred at RT until full conversion of the starting mesylate (monitored by TLC). Then, the solvents were evaporated *in vacuo* and the crude material was dissolved in DCM and mixed with SiO<sub>2</sub> (400 mg) followed by evaporation of DCM to dryness. The deposited on SiO<sub>2</sub> crude mixture was loaded on the SiO<sub>2</sub> column for chromatographic purification (elution with hexane-AcOEt 20:1), which gave the product **28** as a white solid (174 mg, 87% yield).

**(S)-2-(6-((3-(RS-(16-(2,3-bis(hexadecyloxy)propoxy)hexadecyl)disulfaneyl)propyl)amino)-benzo[d]-thiazol-2-yl)-4,5-dihydrothiazole-4-carboxylic acid (29).** To a solution of the compound **28** (25 mg, 0.024 mmol) in dichloromethane (1.5 mL) cooled to 0°C were added TFA (110  $\mu$ L, 1.44 mmol) and Et<sub>3</sub>SiH (46  $\mu$ L, 0.29 mmol) under N<sub>2</sub>. The mixture was warmed and stirred at RT for 2 h and then the volatile materials were evaporated *in vacuo*. The residue was dissolved in THF (1 mL) under N<sub>2</sub>, followed by addition of the compound **6** (9 mg, 0.019 mmol) dissolved in DMF (1 mL) and DIPEA (11.4  $\mu$ L, 0.065 mmol). The mixture was stirred at RT for 12 h with protection from light and then was concentrated *in vacuo* to dryness. The residue was purified by silica gel column chromatography (DCM-MeOH 40:1 + 2% (v/v) acetic acid) to give the product **29** as an orange solid (17 mg, 78% yield). **HRMS:** calculated for C<sub>65</sub>H<sub>118</sub>N<sub>3</sub>O<sub>5</sub>S<sub>4</sub> [M+H]<sup>+</sup> 1148.7949, found 1148.7959.

**(S)-2-(6-((3-((15-carboxypentadecyl)disulfaneyl)propyl)amino)benzo[d]thiazol-2-yl)-4,5-dihydro-thiazole-4-carboxylic acid (31).** To a solution of 16-mercaptohexadecanoic acid (3.5 mg, 0.012 mmol) in THF (1 mL) was added a solution of the compound **6** (4.7 mg, 0.01 mmol) in DMF (1 mL) and DIPEA (12  $\mu$ L, 0.07 mmol). The mixture was stirred at RT for 12 h with protection from light and then was concentrated *in vacuo* to dryness. The residue was purified by silica gel column chromatography (DCM-AcOEt 1:1 + 2% (v/v) acetic acid) to give the product **31** as an orange solid (4 mg, 63% yield). **HRMS:** calculated for C<sub>30</sub>H<sub>46</sub>N<sub>3</sub>O<sub>4</sub>S<sub>4</sub> [M+H]<sup>+</sup> 640.2371, found 640.2369.

**RS-3-(benzyloxy)propane-1,2-diyl bis(decanoate) (33).** (±)-3-Benzyloxy-1,2-propanediol (2.50 g, 13.7 mmol) in dichloromethane (16 mL) was mixed with pyridine (2.49 mL, 30.9 mmol) and DMAP (25 mg, 0.2 mmol) under N<sub>2</sub>. The reaction mixture was cooled down to 15°C. A solution of decanoyl chloride (5.7 mL, 27.4 mmol) in DCM (6 mL) was added dropwise to the reaction mixture under stirring at 15°C. The cooling bath was removed and stirring was continued at RT for 2.5 h and then at 40°C for 8.5 h. Then glacial acetic acid was added (0.7 mL). The mixture was diluted with DCM (20 mL) and washed with H<sub>2</sub>O (3 × 10 mL) and with brine (1 × 10 mL). Organic phase was dried over Na<sub>2</sub>SO<sub>4</sub>, the solvent was evaporated *in vacuo* to give a crude material, which was purified by silica gel column chromatography (hexane-AcOEt 10:1) to give the product **33** (4.79 g, 71% yield).

**RS-3-hydroxypropane-1,2-diyl bis(decanoate) (34).** The compound **33** (200 mg, 0.41 mmol) was dissolved in ethyl acetate (2 mL) followed by three vacuum-N<sub>2</sub> cycles. Then, 5% Pd/C (20 mg) was added to the reaction mixture under N<sub>2</sub>. The reaction flask was filled with H<sub>2</sub>, and the compound **33** was hydrogenated under normal pressure at RT for 24 h. The catalyst was removed by filtration through a pad of Celite and the filtrate was concentrated *in vacuo* to provide the product **34** as a white powder (139 mg, 85% yield) which was used in the next step without purification.

**10-(tritylthio)decanoic acid (36).** Triphenylmethanethiol (301 mg, 1.09 mmol) was dissolved in toluene (1 mL) under N<sub>2</sub>, followed by the addition of 5.4 M MeONa (0.43 mL, 2.38 mmol) under stirring at RT. Then, a solution of 10-bromodecanoic acid **35** (298 mg, 1.19 mmol) in MeOH (2 mL) was added dropwise to the reaction mixture at 5°C under vigorous stirring. The mixture was heated to 50°C and stirring was continued for 2 h. Then, the reaction mixture was cooled to RT, quenched with aqueous 0.1% HCl (10 mL) and extracted with DCM (30 mL). Aqueous phase was separated and extracted again with DCM (2 × 20 mL). Combined organic phases were dried over Na<sub>2</sub>SO<sub>4</sub> and the solvent was evaporated *in vacuo*. The crude material was purified by silica gel column chromatography (hexane-AcOEt 2:1) to provide the product **36** as a white solid (407 mg, 84% yield). <sup>1</sup>H NMR (400 MHz, CDCl<sub>3</sub>) δ 7.43-7.37 (m, 6H), 7.30-7.22 (m, 6H), 7.22-7.15 (m, 3H) 2.32 (t, *J* = 7.5 Hz, 2H), 2.12 (t, *J* = 7.3 Hz, 2H), 1.67-1.60 (m, 2H), 1.54-1.06 (m, 14H).

**RS-3-((10-(tritylthio)decanoyl)oxy)propane-1,2-diyl bis(decanoate) (37).** To a solution of acid **36** (150 mg, 0.34 mmol) in dichloromethane (2 mL) were added DMAP (7 mg, 0.06 mmol) and EDCI (64 mg, 0.34 mmol). The mixture was added to a vigorously stirred solution of compound **34** (112 mg, 0.28 mmol) in dichloromethane (1 mL) at 0°C. The reaction mixture was warmed and stirred at RT for 12 h. The mixture was diluted with dichloromethane (20 mL), washed with 0.1 M HCl (2 × 20 mL) and then with brine (1 × 20 mL). Organic phase was dried over Na<sub>2</sub>SO<sub>4</sub> and evaporated *in vacuo*. The crude material was purified by silica gel column chromatography (hexane-AcOEt 10:1) yielding the product

**37** as a white solid (178 mg, 64% yield). <sup>1</sup>H NMR (400 MHz, CDCl<sub>3</sub>) δ 7.44-7.37 (m, 6H), 7.30-7.23 (m, 6H), 7.23-7.17 (m, 3H), 5.30-5.22 (m, 1H), 4.33-4.24 (m, 2H), 4.14 (dd, *J* = 11.9, 6.0 Hz, 2H), 2.35-2.25 (m, 6H), 2.12 (t, *J* = 7.3 Hz, 2H), 1.66-1.53 (m, 6H), 1.45-1.08 (m, 36H), 0.88 (t, *J* = 6.7 Hz, 6H).

**(4*S*)-2-(6-((3-((10-(*RS*-2,3-bis(decanoyloxy)propoxy)-10-oxodecyl)disulfaneyl)propyl)amino)-benzo[d]thiazol-2-yl)-4,5-dihydrothiazole-4-carboxylic acid (38).** To a solution of the compound **37** (12.5 mg, 0.015 mmol) in dichloromethane (1.5 mL) cooled to 0°C were added TFA (69 µL, 0.9 mmol) and Et<sub>3</sub>SiH (29 µL, 0.18 mmol) under N<sub>2</sub>. The mixture was warmed and stirred at RT for 4 h and then the volatile materials were evaporated *in vacuo*. The residue was dissolved in THF (1 mL) under N<sub>2</sub>, followed by addition of the compound **6** (5.6 mg, 0.012 mmol) dissolved in DMF (1 mL) and DIPEA (7.1 µL, 0.04 mmol). The mixture was stirred at RT for 12 h with protection from light and then concentrated *in vacuo* to dryness. The residue was purified by silica gel column chromatography (DCM-MeOH 40:1 + 2% (v/v) acetic acid) to give the product **38** as an orange solid (8 mg, 71% yield). **HRMS**: calculated for C<sub>47</sub>H<sub>76</sub>N<sub>3</sub>O<sub>8</sub>S<sub>4</sub> [M+H]<sup>+</sup> 938.4510, found 938.4473.

### 3.5.2 Materials and methods. Biological part

**General information.** Lipase from porcine pancreas (Cat. # L3126, Sigma-Aldrich), Colipase from porcine pancreas (Cat. # C3028, Sigma-Aldrich), Bovine Serum Albumin (BSA, essentially fatty acid free, Cat. # A3803, Sigma-Aldrich), Sodium taurodeoxycholate hydrate (Cat. # T0875, Sigma-Aldrich), Sodium glycodeoxycholate (Cat. # G9910, Sigma-Aldrich), Orlistat (Cat. # O0381, TCI), Metronidazole (Cat. # M1547, Sigma-Aldrich), Vancomycin hydrochloride (Cat. # AB349704, ABCR), Neomycin sulfate (Cat. # 4801, Merck), Ampicillin sodium salt (Cat. # K029.1, Roth), MRS Broth (Cat. # X925.1, Roth), FBS (Cat. # 10270106, Gibco), Penicillin-Streptomycin (Cat. # 1540122, Gibco), TrypLE™ Express Enzyme (1 X) (Cat. # 12605010, Gibco), Minimum Essential Medium (Cat. # 10370047, Gibco), GlutaMAX™ Supplement (100 X) (Cat. # 35050038, Gibco), Sodium Pyruvate (100 X) (Cat. # 11360039), Phosphate-buffered saline (PBS), pH 7.2 (1 X) (Cat. # 20012019), HBSS (1 X) (Cat. # 14025050), D-luciferin potassium salt (Beetle Luciferin, Potassium Salt, Cat. # E160C, Promega), Corn oil (Cat. # 405435000, Acros), Tetrahydrofuran (Cat. # 34845-5000, Acros), D-(+)-Glucose (Cat. # G7528, Sigma-Aldrich) were used as received from suppliers without additional purification. Oxoid™ AnaeroGen™ 2.5L Sachet (Cat. # AN0025A, ThermoFisher Scientific), Oxoid™ AnaeroJar™ 2.5L (Cat. # AG0025A, ThermoFisher Scientific) were used for bacterial culture. Millipore water was used for solutions preparations. Cell-based assays were performed using Falcon® 96-well microplates (black, with clear flat bottom, tissue culture treated) (Product # 353219, Corning). LCMS analysis was performed with Agilent Infinity 1260 HPLC system (Agilent, Santa Clara, CA) using SunFire® C18 column (2.1 × 20 mm, 3.5 µm) connected to Quadrupole LC/MS system (Agilent). IVIS 100 imaging system (Xenogen) or IVIS Spectrum imaging

system (Xenogen) were used for bioluminescence imaging in cell and animal experiments. Analysis and quantification of the bioluminescent signal were performed using Living Image software (PerkinElmer). Statistical analysis of the data obtained in the experiments was carried out using GraphPad Prism software.

**Cell lines and cell culture.** Caco2-luc cells were cultured in EMEM (Minimal Essential Medium containing non-essential amino acids supplemented with 1% GlutaMAX™, 1% Sodium Pyruvate, 10% FBS and 1% Penicillin-Streptomycin) and subcultured when reached 60-70% confluency. For the assays, the cells were seeded in 96-well plates with flat transparent bottom at density  $5 \cdot 10^4$  cells per well and used 24 h after seeding.

**Bacterial lines and bacterial culture.** For the bacterial (probiotics) experiments *Lactobacillus Plantarum* WCFS1 (BSH-positive, wt) and *Lactobacillus Plantarum* NZS332 (BSH-negative,  $\Delta bsh1-bsh4$ ) were used. *Lactobacillus Plantarum* strains were obtained from Dr. James Collins. The bacterial culture was initiated by inoculating MRS broth (15 mL) with thawed glycerol stock suspensions of bacteria (30  $\mu$ L) and incubating them in a static anaerobic chamber Oxoid™ AnaeroJar™ 2.5L in the presence of Oxoid™ AnaeroGen™ 2.5L Sachet at 37°C for 24 h. The bacteria were isolated by centrifugation ( $4000 \times g$  for 10 min) and washed by resuspending in PBS ( $3 \times 10$  mL) and centrifugation. Then, the bacteria were resuspended in PBS to get a required bacterial concentration and were directly used in the experiments. The concentrations of bacterial suspensions were calculated by inoculating MRS-agar plates with serial dilutions (from  $10^{-1}$  to  $10^{-10}$ , in triplicates) of the suspensions followed by the incubation for 24 h in the anaerobic chamber (as described above for preparing bacterial cultures in MRS broth) and counting the numbers of colony-forming units.

**Bile salt hydrolase activity assay in bacterial lines.** The bile salt hydrolase activity assay in bacterial lines was performed by LCMS analysis of the glycodeoxycholate deconjugation reaction in the presence of the bacterial suspension with formation of the deoxycholate. For the assay *Lactobacillus Plantarum* WCFS1 and *Lactobacillus Plantarum* NZS332 were cultured as described above. The bacterial suspensions were prepared in PBS ( $1 \cdot 10^9$  CFU/mL). For each bacterial line an aliquot of sodium glycodeoxycholate solution (225  $\mu$ L, 6.67 mM) in PBS (without  $\text{Ca}^{2+}$  and  $\text{Mg}^{2+}$ ) was mixed with a bacterial suspension (75  $\mu$ L,  $1 \cdot 10^9$  CFU/mL). The control samples were prepared by using PBS (75  $\mu$ L) instead of bacterial suspensions. Next, the mixtures (in triplicates for each sample) were incubated at 37°C for 35 min and then centrifuged. Supernatants were separated and analyzed by LCMS (mobile phase - 5 mM ammonium formate in  $\text{H}_2\text{O}$  – acetonitrile; gradient – from 5% to 95% (v/v) acetonitrile over 3 min; flow rate – 1.0 mL/min; injection volume – 3  $\mu$ L). Quantification was performed by analyzing the areas under the chromatographic peaks.



**Animals.** FVB-luc<sup>+</sup> transgenic mice [FVB-Tg(CAG-luc,-GFP)L2G85Chco/J] (284) were purchased from The Jackson Laboratory and bred at the EPFL SPF animal facility. The mice were housed at the EPFL UDP animal facility under pathogen free conditions in individually ventilated cages in groups of 4-5 mice according to their gender and age with 12h/12h light-dark cycle at 22°C and free access to regular chow diet and water unless otherwise specified. All experiments were performed in strict accordance to the Swiss regulation on animal experimentation and the experimental protocol (VD 2849) was approved by the authority of the Canton Vaud, Switzerland (EXPANIM (Expérience sur animaux)–SCAV, Département de la sécurité et de l'environnement, Service de la consommation et des affaires vétérinaires).

**Real time bioluminescence imaging of LCTG-Luc1, LCTG-Luc2, MCTG-Luc and LCGE-Luc uptake by Caco2-luc cells.** Caco2-luc cells were grown and plated in 96-well plates as described above. For the cellular uptake experiments the probes were formulated as emulsions in an uptake buffer (HBSS with Ca<sup>2+</sup> and Mg<sup>2+</sup> containing 0.01% fatty acid free BSA and 1 mM sodium taurodeoxycholate). For the emulsion preparation each probe (0.3 mg) was dissolved in THF (20 µL) and mixed with a calculated volume of corn oil in order to obtain 6 mM stock solution, followed by THF evaporation *in vacuo*. An aliquot of the stock solution was added to 200× volume of the uptake buffer and the mixture was sonicated for 5 min at room temperature with stirring to produce emulsion, which was loaded into a 96 well plate. Porcine pancreatic lipase solutions (0-400 ng/mL) were prepared in the uptake buffer and were supplemented with porcine pancreatic colipase to provide lipase-colipase ratio 5:1 (w/w) and then were loaded into a separate 96 well plate. Before adding the probes the culture medium was removed and the cells were washed with PBS. Next, the emulsified probes were added to the cells using a multichannel micropipette (50 µL/well, 30 µM probe in emulsion) followed by the addition of pancreatic lipase solutions (50 µL/well, 0-400 ng/mL), which provided the final probes concentration in the wells 15 µM and the final lipase concentrations 0-200 ng/mL. Then, the plate was immediately placed in the IVIS 100 imaging system and the bioluminescent signal was acquired for 150 min at 37°C every 2 min for 150 min with autoexposure setting. The BLI quantification was performed using Living Image software by selecting the region-of-interest (ROI) around each well.

**Real time bioluminescence imaging of LCTG-Luc1 and LCTG-Luc2 uptake by Caco2-luc cells in the presence of orlistat.** Caco2-luc cells were plated in 96-well plates as described above. Solutions of orlistat in corn oil (1.5 µL, 0-13.2 mM) were mixed with the stock solutions of LCTG-Luc1 and LCTG-Luc2 probes in corn oil (1.5 µL, 6 mM) and these mixtures were added to 200× volume (600 µL) of the uptake buffer (described above) followed by sonication for 5 min at room temperature with stirring to produce emulsions. Then, the cells were cleared from the culture medium, washed with PBS and loaded first with the prepared emulsions (50 µL/well) and then with the pancreatic lipase solution in the uptake

buffer (50  $\mu$ L, 400 ng/mL) supplemented with pancreatic colipase (lipase-colipase ratio 5:1 (w/w)), providing the final lipase concentration 200 ng/mL, the probes final concentration 7.5  $\mu$ M and final orlistat concentrations 0-25  $\mu$ M. After additions the plate with cells was immediately placed in the IVIS 100 imaging system and the bioluminescent signal was acquired at 37°C every 2 min for 150 min with autoexposure setting.

**Real time bioluminescence imaging of LCGE-Luc activation by glutathione in the presence of Caco2-luc cells.** Caco2-luc cells were plated in the 96-well plate as described above. The emulsion of LCGE-Luc probe (30  $\mu$ M) and a pancreatic lipase solution (400 ng/mL) were prepared in the uptake buffer (HBSS with  $\text{Ca}^{2+}$  and  $\text{Mg}^{2+}$  containing 0.01% fatty acid free BSA and 1 mM sodium taurodeoxycholate) as described above. Glutathione solution (15 mM) was prepared in the degassed uptake buffer. Next, the cell culture medium was removed, cells were washed with PBS and loaded first with LCGE-Luc emulsion (50  $\mu$ L) and then with the pancreatic lipase solution (50  $\mu$ L), followed by immediate light acquisition using IVIS 100 imaging system at 37°C every 2 min. After 52 min of imaging the glutathione solution (50  $\mu$ L, 15 mM) was added directly to the wells with Caco2-Luc cells containing the mixture of LCGE-Luc emulsion and the pancreatic lipase, which were imaged up to 52 min. The final concentration of glutathione in each well after addition was 5 mM. The plate was immediately imaged again for 18 min with the same imaging settings.

**Real time bioluminescence imaging of LCTG-Luc1, LCTG-Luc2, LCGE-Luc and FA-Luc uptake in FVB-luc+ mice. General procedure.** For administration by oral gavage the probes were formulated as solutions in corn oil or as emulsions. The emulsions were prepared by adding one volume of the probe stock solution (6 mM) in corn oil to 32 volumes of the sodium taurodeoxycholate solution (10 mM) in PBS (pH 7.2, with  $\text{Ca}^{2+}$  and  $\text{Mg}^{2+}$ ), supplemented with 0.4% (v/v) glycerol and followed by sonication. Male FVB-luc+ mice (15-20 week old, 4-8 mice per group) were starved for 10 h (from 10 a.m. to 8 p.m.) and then received oral gavage of the probes solutions in corn oil (150  $\mu$ L, 40 nmol/mouse) or the probes in emulsions (250  $\mu$ L, 40-45 nmol/mouse). After the gavage the mice were immediately placed in the transparent ventilated plastic boxes, installed inside the IVIS Spectrum imaging system allowing free movement of animals during the experiment, and were imaged without anesthesia for 1 h at room temperature with supply of oxygen (1.5 L/min) inside the IVIS chamber. Bioluminescent signal was acquired every 30 s for 1 h with exposure time 30 s.

For LCTG-Luc1 probe a dose-response study was carried out where the same mice ( $n = 4$ ) received various doses of LCTG-Luc1 (10, 40 and 100 nmol/mouse in 150  $\mu$ L of corn oil) by oral gavage and imaged as described above. For the study, administration of various doses of the probe in mice was performed with the time interval of 5 days.



**Real time bioluminescence imaging of LCTG-Luc1 uptake in the presence of orlistat in FVB-luc+ mice.** For this study four types of emulsions were prepared: 1) the pre-gavage emulsion with orlistat, 2) the pre-gavage emulsion with the vehicle only (corn oil), 3) the gavage emulsion containing both the LCTG-Luc1 probe and orlistat, 4) gavage emulsion containing LCTG-Luc1 only. A stock solution of orlistat (300 mg/mL) in corn oil was prepared by mixing orlistat (100 mg) with corn oil (200  $\mu$ L) followed by warming the mixture to 42°C and sonication. Pre-gavage emulsions (containing 25 mg/mL orlistat or vehicle only) were obtained by mixing one volume of the warmed orlistat solution (300 mg/mL) in corn oil or 0.6 volumes of corn oil only (vehicle) with 11 volumes of the sodium taurodeoxycholate solution (10 mM) in PBS (pH 7.2, with  $\text{Ca}^{2+}$  and  $\text{Mg}^{2+}$ ), supplemented with 0.4% (v/v) glycerol and followed by sonication. The gavage emulsions (containing 180  $\mu$ M LCTG-Luc1 with or without 20 mg/mL orlistat) were prepared by mixing one volume of LCTG-Luc1 solution (9.25 mM) in corn oil with 3.4 volumes of the warmed orlistat solution (300 mg/mL) in corn oil or with 2 volumes of corn oil only and then added to 47 volumes of the sodium taurodeoxycholate solution (10 mM) in PBS (pH 7.2, with  $\text{Ca}^{2+}$  and  $\text{Mg}^{2+}$ ), supplemented with 0.4% (v/v) glycerol and followed by sonication.

In this experiment, the treatment group consisted of the same mice as the control group, so that each mouse served as its own control. In each experiment male FVB-luc+ mice (15-20 week old, 4 mice per group) were starved for 10 h (from 10 a.m. to 8 p.m.) before administration of the probes. First, in the control experiment, the mice received the pre-gavage emulsion containing the vehicle only (200  $\mu$ L by oral gavage) and 10 min later they were administered with the gavage emulsion containing the probe only (250  $\mu$ L by oral gavage, LCTG-Luc1 dose 45 nmol/mouse). After receiving the gavage emulsion the mice were immediately imaged as described in the general procedure. After imaging the mice were placed back in the cages with the chow. One week later, the same mice were starved for 10 h (from 10 a.m. to 8 p.m.) before the experiment and then received the pre-gavage emulsion containing orlistat (200  $\mu$ L by oral gavage, orlistat dose 5 mg/mouse). 10 min later the mice were administered with the emulsion containing orlistat and the probe (250  $\mu$ L by oral gavage, orlistat dose 5 mg/mouse and LCTG-Luc1 dose 45 nmol/mouse), followed by immediate bioluminescent signal acquisition using the same instrumental set-up and imaging setting as described in the general procedure. After the experiment the mice were returned to the cages with the chow.

**Real time bioluminescence imaging of LCTG-Luc1 and LCTG-Luc2 uptake in FVB-luc+ mice with normal, depleted and restored gut microbiota.** In this experiment, the treatment group consisted of the same mice as the control group, so that each mouse served as its own control. Male FVB-luc+ mice (control group, 15-20 week old, 7-8 mice per group) were starved for 10 h (from 10 a.m. to 8 p.m.) and then received oral gavage of the probes solutions in corn oil (150  $\mu$ L, 40 nmol/mouse) and immediately imaged using the same instrumental set-up and imaging setting as described in the

general procedure. After 24 h the bottles with drinking water were replaced with the bottles containing antibiotics mixture (AVNM) (ampicillin sodium salt 1 g/L, vancomycin hydrochloride 0.5 g/L, neomycin sulfate 1 g/L, metronidazole 1 g/L and d-glucose 50 g/L in drinking water) and this mixture was given to mice for 7-9 days. During the AVNM treatment the mice weight was monitored daily and the cages were changed every other day. After ending the AVNM treatment, the mice were given drinking water for the rest of the study. At the day of finishing the AVNM treatment and 7 days after antibiotics withdrawal the mice were imaged again using the same preparations, doses of the probes and imaging settings as for the control experiment.

**Real time bioluminescence imaging of LCTG-Luc1 uptake in FVB-luc<sup>+</sup> mice after treatment with probiotics.** Twelve male FVB-luc<sup>+</sup> mice (15-20 week old, control group) were starved for 10 h and then were gavaged with LCTG-Luc1 in corn oil (150  $\mu$ L, 40 nmol/mouse) followed by immediate imaging as described in the general procedure. The next day, the mice were divided in two groups (6 mice per group). The first group was receiving once daily oral gavage of *Lactobacillus Plantarum* WCFS1 (BSH<sup>+</sup>, 200  $\mu$ L,  $5 \cdot 10^9$  CFU) for 12 days in total. The second group was receiving once daily oral gavage of *Lactobacillus Plantarum* NZS332 (BSH<sup>-</sup>, 200  $\mu$ L,  $5 \cdot 10^9$  CFU) for 12 days in total. At day 5 and day 12 of probiotics treatment both groups of mice were starved for 10 h (from 10 a.m. to 8 p.m.) and then were imaged after oral gavage of LCTG-Luc1 in corn oil (150  $\mu$ L, 40 nmol/mouse) as described in the general procedure and then were returned to the cages with the chow.

**Ex vivo bioluminescence imaging of excised gastrointestinal tract after oral gavage of LCTG-Luc1 in FVB-luc<sup>+</sup> mice.** Male FVB-luc<sup>+</sup> mice (15-20 week old) were starved for 10 h and then were gavaged with LCTG-Luc1 in corn oil (150  $\mu$ L, 40 nmol/mouse). 10 min post-gavage the mice were sacrificed by cervical dislocation, the gastrointestinal tract (stomach, small and large intestine) was excised and bioluminescent signal was immediately acquired using IVIS Spectrum imaging system.

## Chapter 4 Conclusion

Molecular imaging provides valuable information about cellular and molecular events within intact living organisms. It advances our understanding of fundamental biological processes and can aid in earlier disease diagnostics. Visualization of biological processes of interest at the cellular and subcellular levels requires development of imaging agents that are capable to interact with specific molecular targets providing a detectable signal. Among various imaging techniques, optical imaging that includes bioluminescence and fluorescence plays a key role for preclinical studies. Moreover, fluorescent imaging agents have a potential for clinical translation. In this thesis, I described my work on the development of lipid-based optical imaging probes for *in vivo* applications.

In the first project, I developed a near-infrared fluorescent fatty acid probe as a tool for *in vivo* tumor imaging. Fatty acids are important molecules for tumor growth and progression. Apart from intracellular fatty acid synthesis, certain tumors such as glioma may rely on the uptake of fatty acids from circulation. Therefore, fatty acids can be envisioned as ligands for tumor targeting. Based on this idea, I designed a fluorescent fatty acid probe ICG-FA that consists of a long-chain fatty acid, palmitic acid, and a near-infrared fluorescent dye indocyanine green (ICG) attached to the end of the aliphatic chain. The choice of the  $\omega$ -carbon atom of the fatty acid for fluorophore attachment was based on the previous studies, which demonstrated that modifications of long-chain fatty acids at the end of the aliphatic chain do not change their uptake mechanism by cells. ICG was chosen as a fluorescent reporter for the probe design, since it has suitable optical properties for *in vivo* imaging and furthermore it was approved by the FDA as an imaging agent for clinical applications. Importantly, free ICG lacks the ability to interact specifically with tumors. Starting from the construction of a conjugatable ICG-analog, I developed and optimized the ICG-FA probe synthesis and then studied the probe uptake in cells. The experiments with ICG-FA in 3T3-L1 cell line, which is a classical model for fatty acid uptake studies, proved that the probe is cell-permeable and that its uptake by cells is comparable to that of natural fatty acids. Furthermore, they showed that ICG-FA can compete for the cellular uptake with natural substrates. Uptake studies in the glioma cell line U87MG-luc revealed that ICG-FA accumulates inside the cells with significantly higher uptake compared to free ICG dye, which indicates that the fluorophore conjugation to palmitic acid improves its cellular accumulation and enables better fluorescence detection of glioma cells compared to free ICG dye. In a next step, I studied the performance of ICG-FA as an imaging probe in living mice. As expected, biodistribution of ICG-FA

in mice demonstrated increased probe uptake and retention in various tissues upon intravenous injection as compared to free ICG, suggesting that the cellular fatty acid uptake mechanism contributes to the tissue retention of ICG-FA *in vivo*. Validation of ICG-FA in the murine glioma xenograph model demonstrated the ability of the probe to target efficiently glioma tumors *in vivo* providing prolonged tumor fluorescence compared to free ICG dye and showed consistency with the probe uptake studies in U87MG-luc glioma cells *in vitro*. Importantly, ICG-FA demonstrated 4.5-fold increase of fluorescence in the tumor xenographs compared to the healthy brain tissue, which is considered substantial probe accumulation in the tumor (165). Moreover, ICG-FA was tested as an imaging agent for intraoperative fluorescence image-guided surgery of mastocytoma in real clinical settings. In this proof-of-concept study, the probe showed the ability to accumulate in the tumor of a canine patient providing distinction between the tumor and healthy tissue that enables visual guidance for a surgeon in real time for efficient tumor resection. Although the mechanism of ICG-FA accumulation in mastocytoma is not clear, the demonstrated applicability of the probe for intraoperative tumor imaging suggests that ICG-FA has a potential as a tumor-imaging agent for fluorescence-guided surgery of cancers that have enhanced ICG-FA uptake, such as gliomas. It is promising to test the ability of ICG-FA to target various tumors, since upregulated fatty acid uptake may be implicated in the metabolism of other types of cancer.

In the second project, I developed bioluminescent probes for *in vivo* imaging of triglyceride uptake and validated them in luciferase-expressing cells and mice, since no methods had existed for non-invasive real-time assessment of triglyceride absorption in living animals. I used 6-N-(3-mercaptopropyl)-aminoluciferin (MPr-AL) as a scaffold for designing bioluminescent triglyceride probes because the traditional approach based on the disulfide-carbonate linker for labeling biomolecules with luciferin has disadvantages such as limited hydrolytic stability and cumbersome synthesis of the corresponding conjugates. I optimized the synthesis of the luciferin-labeling reagent PyS-MPr-AL, which allowed using mild synthetic conditions, providing high yield of this compound. The MPr-AL scaffold enabled successful synthesis of bioluminescent medium- and long-chain triglyceride probes from corresponding mercapto-triglycerides. Validation of the developed probes in cells and living mice demonstrated that these imaging tools represent the absorption of natural triglycerides, since they only produce bioluminescence upon hydrolysis by lipases and subsequent cellular uptake of the generated lipolytic products. In particular, the requirement of the probes' lipolysis for the signal generation as well as *in vivo* stability of the disulfide linker between the triglyceride part and luciferin moiety of the probes in the intestinal lumen were confirmed by using a lipolysis-stable trialkyl glycerol-luciferin LCGE-Luc1 that did not produce bioluminescent signal after oral administration in mice. The developed TG probes enabled sensitive *in vivo* imaging, where only 10 nmol of LCTG-Luc1

produced a 16-fold stronger luminescent signal *in vivo* compared to background, suggesting that even lower doses can be applied. The developed triglyceride probes enable non-invasive *in vivo* imaging, providing real-time kinetics of intestinal triglyceride absorption in awake living animals, while previously developed methods afford only end-point information and require *ex vivo* analysis or invasive procedures. For example, I used the bioluminescent triglyceride probe LCTG-Luc1 to demonstrate the suppressive effects of the anti-obesity drug orlistat on the triglyceride absorption in living mice in real time, whereas previously the orlistat action in mice was studied using methods such as *ex vivo* analysis of radiolabeled triglycerides in feces (252). Importantly, the imaging probes were efficiently employed to study the effects of the gut microbiota on triglyceride absorption in mice and demonstrated substantial influence of gut bacteria on the intestinal triglyceride uptake. The developed probes could potentially be applied for *in vivo* studies of certain types of drugs or microorganisms that may help to treat obesity by decreasing lipid absorption (298). The probes could also be useful for the development of functional foods using food structure design with the aim to decrease or enhance the bioavailability of triglycerides that is important for the obesity management, neonatal nutrition and pathologies with nutrient malabsorption, such as cystic fibrosis (208, 299). These triglyceride probes offer a unique possibility to investigate quantitatively and non-invasively the effects of various agents on the intestinal absorption of triglycerides in luciferase expressing animals, which could be of great importance for the studies in the field of nutrition, obesity and metabolic diseases.



## Chapter 5      References

1. R. Weissleder, U. Mahmood, Molecular Imaging. *Radiology* **219**, 316-333 (2001).
2. X. Chen, *Molecular Imaging Probes for Cancer Research*. (WORLD SCIENTIFIC, 2012), pp. i-xviii.
3. S. A. Hilderbrand, R. Weissleder, Near-infrared fluorescence: application to in vivo molecular imaging. *Current opinion in chemical biology* **14**, 71-79 (2010).
4. C. S. Levin, *Molecular Imaging Probes for Cancer Research*. (WORLD SCIENTIFIC, 2012), pp. 29-96.
5. T. F. Massoud, S. S. Gambhir, Molecular imaging in living subjects: seeing fundamental biological processes in a new light. *Genes & development* **17**, 545-580 (2003).
6. M. Rudin, R. Weissleder, Molecular imaging in drug discovery and development. *Nature reviews. Drug discovery* **2**, 123-131 (2003).
7. M. L. James, S. S. Gambhir, A molecular imaging primer: modalities, imaging agents, and applications. *Physiol Rev* **92**, 897-965 (2012).
8. R. Alford, M. Ogawa, P. L. Choyke, H. Kobayashi, Molecular probes for the in vivo imaging of cancer. *Mol Biosyst* **5**, 1279-1291 (2009).
9. F. McCapra, Chemical mechanisms in bioluminescence. *Accounts Chem Res* **9**, 201-208 (1976).
10. P. J. Herring, Luminous fungi. *Mycologist* **8**, 181-183 (1994).
11. E. A. Widder, Bioluminescence in the Ocean: Origins of Biological, Chemical, and Ecological Diversity. *Science* **328**, 704-708 (2010).
12. T. O. Baldwin, Firefly luciferase: the structure is known, but the mystery remains. *Structure* **4**, 223-228 (1996).
13. J. A. Prescher, C. H. Contag, Guided by the light: visualizing biomolecular processes in living animals with bioluminescence. *Current opinion in chemical biology* **14**, 80-89 (2010).
14. C. E. Badr, B. A. Tannous, Bioluminescence imaging: progress and applications. *Trends in Biotechnology* **29**, 624-633 (2011).
15. M. P. Hall *et al.*, Engineered luciferase reporter from a deep sea shrimp utilizing a novel imidazopyrazinone substrate. *ACS chemical biology* **7**, 1848-1857 (2012).
16. A. C. Stacer *et al.*, NanoLuc Reporter for Dual Luciferase Imaging in Living Animals. *Molecular imaging* **12**, 1-13 (2013).
17. E. M. Thompson, S. Nagata, F. I. Tsuji, Vargula hilgendorffii luciferase: a secreted reporter enzyme for monitoring gene expression in mammalian cells. *Gene* **96**, 257-262 (1990).

18. C. A. Maguire *et al.*, Triple bioluminescence imaging for in vivo monitoring of cellular processes. *Molecular therapy. Nucleic acids* **2**, e99 (2013).
19. D. Scott, E. Dikici, M. Ensor, S. Daunert, Bioluminescence and its impact on bioanalysis. *Annual review of analytical chemistry* **4**, 297-319 (2011).
20. R. Tinikul, P. Chaiyen, Structure, Mechanism, and Mutation of Bacterial Luciferase. *Advances in biochemical engineering/biotechnology* **154**, 47-74 (2016).
21. L. Mezzanotte, M. van 't Root, H. Karatas, E. A. Goun, C. Lowik, In Vivo Molecular Bioluminescence Imaging: New Tools and Applications. *Trends Biotechnol* **35**, 640-652 (2017).
22. H. Zhao *et al.*, Emission spectra of bioluminescent reporters and interaction with mammalian tissue determine the sensitivity of detection in vivo. *J Biomed Opt* **10**, 41210 (2005).
23. B. R. Branchini *et al.*, Red-emitting luciferases for bioluminescence reporter and imaging applications. *Analytical biochemistry* **396**, 290-297 (2010).
24. T. Miloud, C. Henrich, G. J. Hammerling, Quantitative comparison of click beetle and firefly luciferases for in vivo bioluminescence imaging. *J Biomed Opt* **12**, 054018 (2007).
25. C. A. Maguire, J. C. van der Mijn, M. H. Degeling, D. Morse, B. A. Tannous, Codon-optimized *Luciola italica* luciferase variants for mammalian gene expression in culture and in vivo. *Molecular imaging* **11**, 13-21 (2012).
26. E. B. Santos *et al.*, Sensitive in vivo imaging of T cells using a membrane-bound *Gaussia princeps* luciferase. *Nature medicine* **15**, 338-344 (2009).
27. B. A. Tannous, D. E. Kim, J. L. Fernandez, R. Weissleder, X. O. Breakefield, Codon-optimized *Gaussia* luciferase cDNA for mammalian gene expression in culture and in vivo. *Molecular therapy : the journal of the American Society of Gene Therapy* **11**, 435-443 (2005).
28. S. Bhaumik, S. S. Gambhir, Optical imaging of Renilla luciferase reporter gene expression in living mice. *Proceedings of the National Academy of Sciences of the United States of America* **99**, 377-382 (2002).
29. A. M. Loening, A. M. Wu, S. S. Gambhir, Red-shifted Renilla reniformis luciferase variants for imaging in living subjects. *Nature methods* **4**, 641-643 (2007).
30. C. H. Contag *et al.*, Photonic detection of bacterial pathogens in living hosts. *Molecular microbiology* **18**, 593-603 (1995).
31. M. Matsumoto, Advanced chemistry of dioxetane-based chemiluminescent substrates originating from bioluminescence. *Journal of Photochemistry and Photobiology C: Photochemistry Reviews* **5**, 27-53 (2004).
32. H. H. Seliger, J. B. Buck, W. G. Fastie, W. D. McElroy, The Spectral Distribution of Firefly Light. *The Journal of General Physiology* **48**, 95-104 (1964).
33. S. M. Marques, J. C. Esteves da Silva, Firefly bioluminescence: a mechanistic approach of luciferase catalyzed reactions. *IUBMB life* **61**, 6-17 (2009).
34. M. DeLuca, W. D. McElroy, Kinetics of the firefly luciferase catalyzed reactions. *Biochemistry* **13**, 921-925 (1974).
35. Y. Ando *et al.*, Firefly bioluminescence quantum yield and colour change by pH-sensitive green emission. *Nature Photonics* **2**, 44 (2007).



36. T. Nakatsu *et al.*, Structural basis for the spectral difference in luciferase bioluminescence. *Nature* **440**, 372 (2006).
37. N. Lemberg, Firefly luciferase can use L-luciferin to produce light. *Biochemical Journal* **317**, 273-277 (1996).
38. K. Niwa, M. Nakamura, Y. Ohmiya, Stereoisomeric bio-inversion key to biosynthesis of firefly D-luciferin. *Febs Lett* **580**, 5283-5287 (2006).
39. E. H. White, H. Wörther, H. H. Seliger, W. D. McElroy, Amino Analogs of Firefly Luciferin and Biological Activity Thereof. *Journal of the American Chemical Society* **88**, 2015-2019 (1966).
40. R. Shinde, J. Perkins, C. H. Contag, Luciferin Derivatives for Enhanced in Vitro and in Vivo Bioluminescence Assays. *Biochemistry* **45**, 11103-11112 (2006).
41. W. Miska, R. Geiger, Synthesis and characterization of luciferin derivatives for use in bioluminescence enhanced enzyme immunoassays. New ultrasensitive detection systems for enzyme immunoassays, I. *Journal of clinical chemistry and clinical biochemistry. Zeitschrift für klinische Chemie und klinische Biochemie* **25**, 23-30 (1987).
42. T. Monsees, R. Geiger, W. Miska, A novel bioluminogenic assay for alpha-chymotrypsin. *Journal of bioluminescence and chemiluminescence* **10**, 213-218 (1995).
43. C. C. Woodrooffe *et al.*, N-Alkylated 6'-Aminoluciferins Are Bioluminescent Substrates for Ultra-Glo and QuantiLum Luciferase: New Potential Scaffolds for Bioluminescent Assays. *Biochemistry* **47**, 10383-10393 (2008).
44. H. Takakura *et al.*, Aminoluciferins as functional bioluminogenic substrates of firefly luciferase. *Chemistry, an Asian journal* **6**, 1800-1810 (2011).
45. W. Miska, R. Geiger, A new type of ultrasensitive bioluminogenic enzyme substrates. I. Enzyme substrates with D-luciferin as leaving group. *Biological chemistry Hoppe-Seyler* **369**, 407-411 (1988).
46. J. Hickson *et al.*, Noninvasive molecular imaging of apoptosis in vivo using a modified firefly luciferase substrate, Z-DEVD-aminoluciferin. *Cell Death Differ* **17**, 1003-1010 (2010).
47. A. G. Vorobyeva *et al.*, Development of a Bioluminescent Nitroreductase Probe for Preclinical Imaging. *PloS one* **10**, e0131037 (2015).
48. D. M. Mofford, S. T. Adams, G. S. K. K. Reddy, G. R. Reddy, S. C. Miller, Luciferin Amides Enable in Vivo Bioluminescence Detection of Endogenous Fatty Acid Amide Hydrolase Activity. *Journal of the American Chemical Society* **137**, 8684-8687 (2015).
49. G. C. Van de Bittner, E. A. Dubikovskaya, C. R. Bertozzi, C. J. Chang, In vivo imaging of hydrogen peroxide production in a murine tumor model with a chemoselective bioluminescent reporter. *Proceedings of the National Academy of Sciences of the United States of America* **107**, 21316-21321 (2010).
50. A. T. Aron *et al.*, In vivo bioluminescence imaging of labile iron accumulation in a murine model of *Acinetobacter baumannii* infection. *Proceedings of the National Academy of Sciences of the United States of America* **114**, 12669-12674 (2017).
51. A. S. Cohen, E. A. Dubikovskaya, J. S. Rush, C. R. Bertozzi, Real-time bioluminescence imaging of glycans on live cells. *Journal of the American Chemical Society* **132**, 8563-8565 (2010).
52. W. Zhou *et al.*, Self-cleavable bioluminogenic luciferin phosphates as alkaline phosphatase reporters. *Chembiochem* **9**, 714-718 (2008).

- 
53. J. S. Rush, K. E. Beatty, C. R. Bertozzi, Bioluminescent Probes of Sulfatase Activity. *Chembiochem : a European journal of chemical biology* **11**, 2096-2099 (2010).
54. H. Yao, M. K. So, J. Rao, A bioluminogenic substrate for in vivo imaging of beta-lactamase activity. *Angewandte Chemie* **46**, 7031-7034 (2007).
55. R. Geiger, E. Schneider, K. Wallenfels, W. Miska, A new ultrasensitive bioluminogenic enzyme substrate for beta-galactosidase. *Biological chemistry Hoppe-Seyler* **373**, 1187-1191 (1992).
56. T. S. Wehrman, G. von Degenfeld, P. O. Krutzik, G. P. Nolan, H. M. Blau, Luminescent imaging of beta-galactosidase activity in living subjects using sequential reporter-enzyme luminescence. *Nature methods* **3**, 295-301 (2006).
57. Y. Lin *et al.*, Bioluminescence probe for gamma-glutamyl transpeptidase detection in vivo. *Bioorg Med Chem* **26**, 134-140 (2018).
58. J. J. Liu, W. Wang, D. T. Dicker, W. S. El-Deiry, Bioluminescent imaging of TRAIL-induced apoptosis through detection of caspase activation following cleavage of DEVD-aminoluciferin. *Cancer Biol Ther* **4**, 885-892 (2005).
59. A. Dragulescu-Andrasi, G. Liang, J. Rao, In Vivo Bioluminescence Imaging of Furin Activity in Breast Cancer Cells Using Bioluminogenic Substrates. *Bioconjugate chemistry* **20**, 1660-1666 (2009).
60. P. L. Meisenheimer *et al.*, Proluciferin acetals as bioluminogenic substrates for cytochrome P450 activity and probes for CYP3A inhibition. *Drug Metab Dispos* **39**, 2403-2410 (2011).
61. C. Roncoroni *et al.*, Molecular imaging of cytochrome P450 activity in mice. *Pharmacological research* **65**, 531-536 (2012).
62. Y. C. Chang, P. W. Chao, C. H. Tung, Sensitive luciferin derived probes for selective carboxypeptidase activity. *Bioorganic & medicinal chemistry letters* **21**, 3931-3934 (2011).
63. B. Ke *et al.*, Cell and in Vivo Imaging of Fluoride Ion with Highly Selective Bioluminescent Probes. *Anal Chem* **87**, 9110-9113 (2015).
64. C. Tang *et al.*, Bioluminescent probe for detecting endogenous hypochlorite in living mice. *Organic & biomolecular chemistry* **16**, 645-651 (2018).
65. J.-B. Li *et al.*, A Bioluminescent Probe for Imaging Endogenous Peroxynitrite in Living Cells and Mice. *Anal Chem* **90**, 4167-4173 (2018).
66. X. Tian, Z. Li, C. Lau, J. Lu, Visualization of in Vivo Hydrogen Sulfide Production by a Bioluminescence Probe in Cancer Cells and Nude Mice. *Anal Chem* **87**, 11325-11331 (2015).
67. B. Ke *et al.*, Bioluminescence Probe for Detecting Hydrogen Sulfide in Vivo. *Anal Chem* **88**, 592-595 (2016).
68. M. Hemmi *et al.*, Highly Sensitive Bioluminescent Probe for Thiol Detection in Living Cells. *Chemistry, an Asian journal* **13**, 648-655 (2018).
69. M. C. Heffern *et al.*, In vivo bioluminescence imaging reveals copper deficiency in a murine model of nonalcoholic fatty liver disease. *Proceedings of the National Academy of Sciences of the United States of America* **113**, 14219-14224 (2016).
70. Z. Zheng *et al.*, Hydrazide d-luciferin for in vitro selective detection and intratumoral imaging of Cu(2+). *Biosens Bioelectron* **83**, 200-204 (2016).

71. L. R. Jones *et al.*, Releasable luciferin-transporter conjugates: tools for the real-time analysis of cellular uptake and release. *Journal of the American Chemical Society* **128**, 6526-6527 (2006).
72. A. H. Henkin *et al.*, Real-Time Noninvasive Imaging of Fatty Acid Uptake in Vivo. *ACS chemical biology* **7**, 1884-1891 (2012).
73. M. D. Lynes *et al.*, The cold-induced lipokine 12,13-diHOME promotes fatty acid transport into brown adipose tissue. *Nature medicine* **23**, 631-637 (2017).
74. P. A. Wender *et al.*, Real-time analysis of uptake and bioactivatable cleavage of luciferin-transporter conjugates in transgenic reporter mice. *Proceedings of the National Academy of Sciences* **104**, 10340-10345 (2007).
75. E. A. Dubikovskaya, S. H. Thorne, T. H. Pillow, C. H. Contag, P. A. Wender, Overcoming multidrug resistance of small-molecule therapeutics through conjugation with releasable octaarginine transporters. *Proceedings of the National Academy of Sciences* **105**, 12128-12133 (2008).
76. E. Eiríksdóttir, I. Mäger, T. Lehto, S. El Andaloussi, Ü. Langel, Cellular Internalization Kinetics of (Luciferin-)Cell-Penetrating Peptide Conjugates. *Bioconjugate chemistry* **21**, 1662-1672 (2010).
77. I. Mäger, K. Langel, T. Lehto, E. Eiríksdóttir, Ü. Langel, The role of endocytosis on the uptake kinetics of luciferin-conjugated cell-penetrating peptides. *Biochimica et Biophysica Acta (BBA) - Biomembranes* **1818**, 502-511 (2012).
78. K. Sakamoto *et al.*, Novel DOCK2-selective inhibitory peptide that suppresses B-cell line migration. *Biochem Biophys Res Commun* **483**, 183-190 (2017).
79. J. W. Lichtman, J. A. Conchello, Fluorescence microscopy. *Nature methods* **2**, 910-919 (2005).
80. M. Quaranta, S. M. Borisov, I. Klimant, Indicators for optical oxygen sensors. *Bioanalytical reviews* **4**, 115-157 (2012).
81. E. A. Owens, S. Lee, J. Choi, M. Henary, H. S. Choi, NIR Fluorescent Small Molecules for Intraoperative Imaging. *Wiley interdisciplinary reviews. Nanomedicine and nanobiotechnology* **7**, 828-838 (2015).
82. R. Weissleder, V. Ntziachristos, Shedding light onto live molecular targets. *Nature medicine* **9**, 123-128 (2003).
83. R. Weissleder, A clearer vision for in vivo imaging. *Nature biotechnology* **19**, 316-317 (2001).
84. S. Gioux, H. S. Choi, J. V. Frangioni, Image-Guided Surgery Using Invisible Near-Infrared Light: Fundamentals of Clinical Translation. *Molecular imaging* **9**, 237-255 (2010).
85. P. P. Ghoroghchian, M. J. Therien, D. A. Hammer, In vivo fluorescence imaging: a personal perspective. *Wiley Interdiscip Rev Nanomed Nanobiotechnol* **1**, 156-167 (2009).
86. P. J. Cassidy, G. K. Radda, Molecular imaging perspectives. *Journal of the Royal Society, Interface* **2**, 133-144 (2005).
87. S. Chapman *et al.*, Nanoparticles for cancer imaging: The good, the bad, and the promise. *Nano today* **8**, 454-460 (2013).
88. J. A. Schwartzbaum, J. L. Fisher, K. D. Aldape, M. Wrensch, Epidemiology and molecular pathology of glioma. *Nature clinical practice. Neurology* **2**, 494-503 (2006).
89. E. A. Maher *et al.*, Malignant glioma: genetics and biology of a grave matter. *Genes & development* **15**, 1311-1333 (2001).

90. J. T. C. Liu, D. Meza, N. Sanai, Trends in Fluorescence Image-guided Surgery for Gliomas. *Neurosurgery* **75**, 61-71 (2014).
91. E. Belykh *et al.*, Intraoperative Fluorescence Imaging for Personalized Brain Tumor Resection: Current State and Future Directions. *Frontiers in surgery* **3**, 55 (2016).
92. Q. T. Nguyen, R. Y. Tsien, Fluorescence-guided surgery with live molecular navigation--a new cutting edge. *Nature reviews. Cancer* **13**, 653-662 (2013).
93. M. Garland, J. J. Yim, M. Bogyo, A bright future for precision medicine: advances in fluorescent chemical probe design and their clinical application. *Cell chemical biology* **23**, 122-136 (2016).
94. J. Fang, H. Nakamura, H. Maeda, The EPR effect: Unique features of tumor blood vessels for drug delivery, factors involved, and limitations and augmentation of the effect. *Advanced drug delivery reviews* **63**, 136-151 (2011).
95. V. Torchilin, Tumor delivery of macromolecular drugs based on the EPR effect. *Advanced drug delivery reviews* **63**, 131-135 (2011).
96. H. Maeda, J. Wu, T. Sawa, Y. Matsumura, K. Hori, Tumor vascular permeability and the EPR effect in macromolecular therapeutics: a review. *J Control Release* **65**, 271-284 (2000).
97. M. M. Haglund, M. S. Berger, D. W. Hochman, Enhanced optical imaging of human gliomas and tumor margins. *Neurosurgery* **38**, 308-317 (1996).
98. F. Acerbi *et al.*, Is fluorescein-guided technique able to help in resection of high-grade gliomas? *Neurosurg Focus* **36**, E5 (2014).
99. Y. Li, R. Rey-Dios, D. W. Roberts, P. A. Valdes, A. A. Cohen-Gadol, Intraoperative fluorescence-guided resection of high-grade gliomas: a comparison of the present techniques and evolution of future strategies. *World Neurosurg* **82**, 175-185 (2014).
100. B. E. Schaafsma *et al.*, The clinical use of indocyanine green as a near-infrared fluorescent contrast agent for image-guided oncologic surgery. *Journal of surgical oncology* **104**, 323-332 (2011).
101. R. J. Diaz *et al.*, Study of the biodistribution of fluorescein in glioma-infiltrated mouse brain and histopathological correlation of intraoperative findings in high-grade gliomas resected under fluorescein fluorescence guidance. *J Neurosurg* **122**, 1360-1369 (2015).
102. S. E. L. Craig, J. Wright, A. E. Sloan, S. M. Brady-Kalnay, Fluorescent-Guided Surgical Resection of Glioma with Targeted Molecular Imaging Agents: A Literature Review. *World Neurosurg* **90**, 154-163 (2016).
103. W. Stummer *et al.*, Fluorescence-guided surgery with 5-aminolevulinic acid for resection of malignant glioma: a randomised controlled multicentre phase III trial. *Lancet Oncol* **7**, 392-401 (2006).
104. S. L. Gibbs *et al.*, Protoporphyrin IX level correlates with number of mitochondria, but increase in production correlates with tumor cell size. *Photochem Photobiol* **82**, 1334-1341 (2006).
105. P. A. Valdés *et al.*, Gadolinium and 5-Aminolevulinic Acid-induced Protoporphyrin IX Levels in Human Gliomas: An Ex Vivo Quantitative Study to Correlate Protoporphyrin IX Levels and Blood-Brain Barrier Breakdown. *Journal of neuropathology and experimental neurology* **71**, 806-813 (2012).
106. G. Blum, G. von Degenfeld, M. J. Merchant, H. M. Blau, M. Bogyo, Noninvasive optical imaging of cysteine protease activity using fluorescently quenched activity-based probes. *Nat Chem Biol* **3**, 668-677 (2007).

107. J. L. Cutter *et al.*, Topical application of activity-based probes for visualization of brain tumor tissue. *PloS one* **7**, e33060 (2012).
108. J. P. Weichert *et al.*, Alkylphosphocholine Analogs for Broad-Spectrum Cancer Imaging and Therapy. *Sci Transl Med* **6**, 240ra75 (2014).
109. K. I. Swanson *et al.*, Fluorescent Cancer-Selective Alkylphosphocholine Analogs For Intraoperative Glioma Detection. *Neurosurgery* **76**, 115-124 (2015).
110. J. M. Warram *et al.*, Fluorescence-guided Resection of Experimental Malignant Glioma Using Cetuximab-IRDye 800CW. *Brit J Neurosurg* **29**, 850-858 (2015).
111. F. P. Kuhajda, Fatty-acid synthase and human cancer: new perspectives on its role in tumor biology. *Nutrition* **16**, 202-208 (2000).
112. L. Yang, C. Lin, L. Wang, H. Guo, X. Wang, Hypoxia and hypoxia-inducible factors in glioblastoma multiforme progression and therapeutic implications. *Exp Cell Res* **318**, 2417-2426 (2012).
113. K. Bensaad *et al.*, Fatty acid uptake and lipid storage induced by HIF-1 $\alpha$  contribute to cell growth and survival after hypoxia-reoxygenation. *Cell Rep* **9**, 349-365 (2014).
114. H. Lin *et al.*, Fatty acid oxidation is required for the respiration and proliferation of malignant glioma cells. *Neuro Oncol* **19**, 43-54 (2017).
115. A. Stahl *et al.*, Identification of the major intestinal fatty acid transport protein. *Mol Cell* **4**, 299-308 (1999).
116. J. E. Schaffer, H. F. Lodish, Expression cloning and characterization of a novel adipocyte long chain fatty acid transport protein. *Cell* **79**, 427-436 (1994).
117. J. Liao, R. Sportsman, J. Harris, A. Stahl, Real-time quantification of fatty acid uptake using a novel fluorescence assay. *Journal of lipid research* **46**, 597-602 (2005).
118. G. Müller, H. Jordan, S. Petry, E.-M. Wetekam, P. Schindler, Analysis of lipid metabolism in adipocytes using a fluorescent fatty acid derivative. I. Insulin stimulation of lipogenesis. *Biochimica et Biophysica Acta (BBA) - Lipids and Lipid Metabolism* **1347**, 23-39 (1997).
119. E. Dubikovskaya, R. Chudnovskiy, G. Karateev, H. M. Park, A. Stahl, Measurement of long-chain fatty acid uptake into adipocytes. *Methods in enzymology* **538**, 107-134 (2014).
120. A. Stahl, J. G. Evans, S. Pattel, D. Hirsch, H. F. Lodish, Insulin causes fatty acid transport protein translocation and enhanced fatty acid uptake in adipocytes. *Developmental cell* **2**, 477-488 (2002).
121. M. L. Landsman, G. Kwant, G. A. Mook, W. G. Zijlstra, Light-absorbing properties, stability, and spectral stabilization of indocyanine green. *J Appl Physiol* **40**, 575-583 (1976).
122. J. V. Frangioni, In vivo near-infrared fluorescence imaging. *Current opinion in chemical biology* **7**, 626-634 (2003).
123. D. D. Nolting, J. C. Gore, W. Pham, NEAR-INFRARED DYES: Probe Development and Applications in Optical Molecular Imaging. *Curr Org Synth* **8**, 521-534 (2011).
124. N. Onda, M. Kimura, T. Yoshida, M. Shibutani, Preferential tumor cellular uptake and retention of indocyanine green for in vivo tumor imaging. *Int J Cancer* **139**, 673-682 (2016).
125. M. V. Marshall *et al.*, Near-Infrared Fluorescence Imaging in Humans with Indocyanine Green: A Review and Update. *Open surgical oncology journal* **2**, 12-25 (2010).

126. J. T. Alander *et al.*, A review of indocyanine green fluorescent imaging in surgery. *International journal of biomedical imaging* **2012**, 940585 (2012).
127. M. Xu, L. V. Wang, Photoacoustic imaging in biomedicine. *Review of Scientific Instruments* **77**, 041101 (2006).
128. P. Beard, Biomedical photoacoustic imaging. *Interface Focus* **1**, 602-631 (2011).
129. V. Ntziachristos, D. Razansky, Molecular Imaging by Means of Multispectral Optoacoustic Tomography (MSOT). *Chemical reviews* **110**, 2783-2794 (2010).
130. I.-H. An, S. Hye-Ran, K. H. Ahn, Reductive Dimerization of Azides to Secondary Amines under Hydrogenation Conditions. *Bull. Korean Chem. Soc.* **25**, 420-422 (2004).
131. M. Lange, A. L. Pettersen, K. Undheim, Synthesis of secondary amines by reductive dimerization of azides. *Tetrahedron* **54**, 5745-5752 (1998).
132. T. Desmettre, J. M. Devoisselle, S. Mordon, Fluorescence properties and metabolic features of indocyanine green (ICG) as related to angiography. *Survey of ophthalmology* **45**, 15-27 (2000).
133. J. Gathje, R. R. Steuer, K. R. Nicholes, Stability studies on indocyanine green dye. *J Appl Physiol* **29**, 181-185 (1970).
134. F. Brouns, G. J. van der Vusse, Utilization of lipids during exercise in human subjects: metabolic and dietary constraints. *Br J Nutr* **79**, 117-128 (1998).
135. A. A. Spector, Fatty acid binding to plasma albumin. *Journal of lipid research* **16**, 165-179 (1975).
136. M. Fasano *et al.*, The extraordinary ligand binding properties of human serum albumin. *IUBMB life* **57**, 787-796 (2005).
137. H. Green, M. Meuth, An established pre-adipose cell line and its differentiation in culture. *Cell* **3**, 127-133 (1974).
138. H. Green, O. Kehinde, An established preadipose cell line and its differentiation in culture II. Factors affecting the adipose conversion. *Cell* **5**, 19-27 (1975).
139. S. Lobo, B. M. Wiczer, A. J. Smith, A. M. Hall, D. A. Bernlohr, Fatty acid metabolism in adipocytes: functional analysis of fatty acid transport proteins 1 and 4. *Journal of lipid research* **48**, 609-620 (2007).
140. J. Pohl, A. Ring, U. Korkmaz, R. Ehehalt, W. Stremmel, FAT/CD36-mediated long-chain fatty acid uptake in adipocytes requires plasma membrane rafts. *Molecular Biology of the Cell* **16**, 24-31 (2005).
141. J. E. Schaffer, Fatty acid transport: the roads taken. *American journal of physiology. Endocrinology and metabolism* **282**, E239-246 (2002).
142. T. Y. Hui, D. A. Bernlohr, Fatty acid transporters in animal cells. *Frontiers in bioscience : a journal and virtual library* **2**, d222-231 (1997).
143. M. Y. Berezin, H. Lee, W. Akers, S. Achilefu, Near Infrared Dyes as Lifetime Solvatochromic Probes for Micropolarity Measurements of Biological Systems. *Biophys J* **93**, 2892-2899 (2007).
144. S. Boddington *et al.*, Improved fluorescence of indocyanine green in vitro and in vivo after simple cooling procedures. *Contrast Media Mol I* **3**, 191-197 (2008).
145. A. R. Thiam, R. V. Farese Jr, T. C. Walther, The biophysics and cell biology of lipid droplets. *Nature Reviews Molecular Cell Biology* **14**, 775 (2013).

146. I. A. Boldyrev *et al.*, New BODIPY lipid probes for fluorescence studies of membranes. *Journal of lipid research* **48**, 1518-1532 (2007).
147. A.-K. Kirchherr, A. Briel, K. Mäder, Stabilization of Indocyanine Green by Encapsulation within Micellar Systems. *Mol Pharmaceut* **6**, 480-491 (2009).
148. P. R. van den Biesen, F. H. Jongsma, G. J. Tangelder, D. W. Slaaf, Yield of fluorescence from indocyanine green in plasma and flowing blood. *Ann Biomed Eng* **23**, 475-481 (1995).
149. R. Philip, A. Penzkofer, W. Bäuml, R. M. Szeimies, C. Abels, Absorption and fluorescence spectroscopic investigation of indocyanine green. *Journal of Photochemistry and Photobiology A: Chemistry* **96**, 137-148 (1996).
150. N. A. Abumrad, R. C. Perkins, J. H. Park, C. R. Park, Mechanism of long chain fatty acid permeation in the isolated adipocyte. *The Journal of biological chemistry* **256**, 9183-9191 (1981).
151. N. A. Abumrad, J. H. Park, C. R. Park, Permeation of long-chain fatty acid into adipocytes. Kinetics, specificity, and evidence for involvement of a membrane protein. *Journal of Biological Chemistry* **259**, 8945-8953 (1984).
152. J. J. Luiken, L. P. Turcotte, A. Bonen, Protein-mediated palmitate uptake and expression of fatty acid transport proteins in heart giant vesicles. *Journal of lipid research* **40**, 1007-1016 (1999).
153. K. Murota, J. Storch, Uptake of Micellar Long-Chain Fatty Acid and sn-2-Monoacylglycerol into Human Intestinal Caco-2 Cells Exhibits Characteristics of Protein-Mediated Transport. *The Journal of Nutrition* **135**, 1626-1630 (2005).
154. M. J. Clark *et al.*, U87MG Decoded: The Genomic Sequence of a Cytogenetically Aberrant Human Cancer Cell Line. *PLOS Genetics* **6**, e1000832 (2010).
155. M. Allen, M. Bjerke, H. Edlund, S. Nelander, B. Westermarck, Origin of the U87MG glioma cell line: Good news and bad news. *Sci Transl Med* **8**, 354re353-354re353 (2016).
156. O. Szentirmai *et al.*, Noninvasive bioluminescence imaging of luciferase expressing intracranial U87 xenografts: correlation with magnetic resonance imaging determined tumor volume and longitudinal use in assessing tumor growth and antiangiogenic treatment effect. *Neurosurgery* **58**, 365-372; discussion 365-372 (2006).
157. C. Abels *et al.*, Indocyanine green (ICG) and laser irradiation induce photooxidation. *Arch Dermatol Res* **292**, 404-411 (2000).
158. T. Ishizawa *et al.*, Mechanistic background and clinical applications of indocyanine green fluorescence imaging of hepatocellular carcinoma. *Annals of surgical oncology* **21**, 440-448 (2014).
159. Z. Pei *et al.*, Acyl-CoA synthetase VL3 knockdown inhibits human glioma cell proliferation and tumorigenicity. *Cancer Res* **69**, 9175-9182 (2009).
160. C. M. Anderson, A. Stahl, SLC27 fatty acid transport proteins. *Molecular aspects of medicine* **34**, 516-528 (2013).
161. D. G. Mashek, R. A. Coleman, Cellular fatty acid uptake: the contribution of metabolism. *Curr Opin Lipidol* **17**, 274-278 (2006).
162. M. E. Elsherbiny, M. Emara, R. Godbout, Interaction of brain fatty acid-binding protein with the polyunsaturated fatty acid environment as a potential determinant of poor prognosis in malignant glioma. *Progress in lipid research* **52**, 562-570 (2013).



163. J. Gao, G. Serrero, Adipose differentiation related protein (ADRP) expressed in transfected COS-7 cells selectively stimulates long chain fatty acid uptake. *The Journal of biological chemistry* **274**, 16825-16830 (1999).
164. H. Doege, A. Stahl, Protein-mediated fatty acid uptake: novel insights from in vivo models. *Physiology* **21**, 259-268 (2006).
165. O. A. Andreev *et al.*, Mechanism and uses of a membrane peptide that targets tumors and other acidic tissues in vivo. *Proceedings of the National Academy of Sciences* **104**, 7893-7898 (2007).
166. K. Shchors, A. Massaras, D. Hanahan, Dual Targeting of the Autophagic Regulatory Circuitry in Gliomas with Repurposed Drugs Elicits Cell-Lethal Autophagy and Therapeutic Benefit. *Cancer cell* **28**, 456-471 (2015).
167. A. L. Vahrmeijer, M. Hutteman, J. R. van der Vorst, C. J. H. van de Velde, J. V. Frangioni, Image-guided cancer surgery using near-infrared fluorescence. *Nature reviews. Clinical oncology* **10**, 507-518 (2013).
168. M. M. Welle, C. R. Bley, J. Howard, S. Rufenacht, Canine mast cell tumours: a review of the pathogenesis, clinical features, pathology and treatment. *Veterinary dermatology* **19**, 321-339 (2008).
169. D. D. Metcalfe, D. Baram, Y. A. Mekori, Mast cells. *Physiol Rev* **77**, 1033-1079 (1997).
170. A. Behrooz *et al.*, Multispectral open-air intraoperative fluorescence imaging. *Opt Lett* **42**, 2964-2967 (2017).
171. S. Yoshioka, S. Nakashima, Y. Okano, Y. Nozawa, Arachidonic acid mobilization among phospholipids in murine mastocytoma P-815 cells: role of ether-linked phospholipids. *Journal of lipid research* **27**, 939-944 (1986).
172. I. Mellman, G. Coukos, G. Dranoff, Cancer immunotherapy comes of age. *Nature* **480**, 480-489 (2011).
173. J. N. Blattman, P. D. Greenberg, Cancer immunotherapy: a treatment for the masses. *Science* **305**, 200-205 (2004).
174. Z. Liu, Z. Li, Molecular imaging in tracking tumor-specific cytotoxic T lymphocytes (CTLs). *Theranostics* **4**, 990-1001 (2014).
175. C. Gonzales *et al.*, In-Vivo Detection and Tracking of T Cells in Various Organs in a Melanoma Tumor Model by 19F-Fluorine MRS/MRI. *PloS one* **11**, e0164557 (2016).
176. A. Li *et al.*, Surface biotinylation of cytotoxic T lymphocytes for in vivo tracking of tumor immunotherapy in murine models. *Cancer immunology, immunotherapy* **65**, 1545-1554 (2016).
177. H. W. Lee, P. Gangadaran, S. Kalimuthu, B. C. Ahn, Advances in Molecular Imaging Strategies for In Vivo Tracking of Immune Cells. *Biomed Res Int* **2016**, 1946585 (2016).
178. H. M. Shehata *et al.*, Sugar or Fat?-Metabolic Requirements for Immunity to Viral Infections. *Frontiers in immunology* **8**, 1311 (2017).
179. M. Angela *et al.*, Fatty acid metabolic reprogramming via mTOR-mediated inductions of PPAR $\gamma$  directs early activation of T cells. *Nature communications* **7**, 13683 (2016).
180. M. E. Muroski *et al.*, Fatty Acid Uptake in T Cell Subsets Using a Quantum Dot Fatty Acid Conjugate. *Scientific reports* **7**, 5790 (2017).
181. D. O'Sullivan *et al.*, Memory CD8(+) T cells use cell-intrinsic lipolysis to support the metabolic programming necessary for development. *Immunity* **41**, 75-88 (2014).



182. T. Carmenate *et al.*, Human IL-2 mutein with higher antitumor efficacy than wild type IL-2. *J Immunol* **190**, 6230-6238 (2013).
183. R. Meir, M. Motiei, R. Popovtzer, Gold nanoparticles for in vivo cell tracking. *Nanomedicine* **9**, 2059-2069 (2014).
184. R. Meir *et al.*, Nanomedicine for Cancer Immunotherapy: Tracking Cancer-Specific T-Cells in Vivo with Gold Nanoparticles and CT Imaging. *Acs Nano* **9**, 6363-6372 (2015).
185. R. A. Juergens *et al.*, Imaging Biomarkers in Immunotherapy. *Biomarkers in cancer* **8**, 1-13 (2016).
186. R. Tavaré *et al.*, Immuno-PET of Murine T Cell Reconstitution Postadoptive Stem Cell Transplantation Using Anti-CD4 and Anti-CD8 Cys-Diabodies. *Journal of Nuclear Medicine* **56**, 1258-1264 (2015).
187. A. E. Foster *et al.*, In vivo fluorescent optical imaging of cytotoxic T lymphocyte migration using IRDye800CW near-infrared dye. *Applied optics* **47**, 5944-5952 (2008).
188. A. A. Lugade *et al.*, Local radiation therapy of B16 melanoma tumors increases the generation of tumor antigen-specific effector cells that traffic to the tumor. *J Immunol* **174**, 7516-7523 (2005).
189. V. Čaplar, L. Frkanec, N. Š. Vujičić, M. Žinić, Positionally Isomeric Organic Gelators: Structure–Gelation Study, Racemic versus Enantiomeric Gelators, and Solvation Effects. *Chemistry – A European Journal* **16**, 3066-3082 (2010).
190. R. Jetty *et al.*, Protein triggered fluorescence switching of near-infrared emitting nanoparticles for contrast-enhanced imaging. *Journal of Materials Chemistry B* **1**, 4542-4554 (2013).
191. D. M. Mizrahi, O. Ziv-Polat, B. Perlstein, E. Gluz, S. Margel, Synthesis, fluorescence and biodistribution of a bone-targeted near-infrared conjugate. *European journal of medicinal chemistry* **46**, 5175-5183 (2011).
192. T. Y. Wang, M. Liu, P. Portincasa, D. Q. Wang, New insights into the molecular mechanism of intestinal fatty acid absorption. *European journal of clinical investigation* **43**, 1203-1223 (2013).
193. H. Mu, C.-K. Høy, The digestion of dietary triacylglycerols. *Prog in Lipid Res* **43**, (2004).
194. J. Hall, A. Guyton, *Textbook of medical physiology*. (Elsevier Saunders, ed. 11th, 2006), pp. 840 - 851.
195. P. Reis, K. Holmberg, H. Watzke, M. E. Leser, R. Miller, Lipases at interfaces: A review. *Advances in Colloid and Interface Science* **147–148**, 237-250 (2009).
196. J. Iqbal, M. M. Hussain, Intestinal lipid absorption. *American journal of physiology. Endocrinology and metabolism* **296**, E1183-1194 (2009).
197. M. E. Lowe, The triglyceride lipases of the pancreas. *Journal of lipid research* **43**, 2007-2016 (2002).
198. F. Spener, F. Paltauf, A. Holasek, The intestinal absorption of glycerol trioctadecenyl ether. *Biochimica et Biophysica Acta (BBA) - Lipids and Lipid Metabolism* **152**, 368-371 (1968).
199. E. P. DiMagno, V. L. W. Go, W. H. J. Summerskill, Relations between Pancreatic Enzyme Outputs and Malabsorption in Severe Pancreatic Insufficiency. *New Engl J Med* **288**, 813-815 (1973).
200. M. E. Lowe, STRUCTURE AND FUNCTION OF PANCREATIC LIPASE AND COLIPASE. *Annual review of nutrition* **17**, 141-158 (1997).
201. C. T. Phan, P. Tso, Intestinal lipid absorption and transport. *Frontiers in bioscience : a journal and virtual library* **6**, D299-319 (2001).

202. J. Hall, A. Guyton, *Textbook of medical physiology*. (Elsevier Saunders, ed. 11th, 2006), pp. 808 - 818.
203. G. A. Bray, B. M. Popkin, Dietary fat intake does affect obesity! *The American Journal of Clinical Nutrition* **68**, 1157-1173 (1998).
204. R. H. Eckel, S. M. Grundy, P. Z. Zimmet, The metabolic syndrome. *The Lancet* **365**, 1415-1428 (2005).
205. G. De Pergola, F. Silvestris, Obesity as a Major Risk Factor for Cancer. *Journal of Obesity* **2013**, 11 (2013).
206. M. Miller *et al.*, Triglycerides and Cardiovascular Disease. *A Scientific Statement From the American Heart Association* **123**, 2292-2333 (2011).
207. Y. Kawano, D. E. Cohen, Mechanisms of hepatic triglyceride accumulation in non-alcoholic fatty liver disease. *J Gastroenterol* **48**, 434-441 (2013).
208. Q. Guo, A. Ye, N. Bellissimo, H. Singh, D. Rousseau, Modulating fat digestion through food structure design. *Progress in lipid research* **68**, 109-118 (2017).
209. J. H. Mathiassen *et al.*, Emulsifying triglycerides with dairy phospholipids instead of soy lecithin modulates gut lipase activity. *Eur J Lipid Sci Tech* **117**, 1522-1539 (2015).
210. P. J. Wilde, B. S. Chu, Interfacial & colloidal aspects of lipid digestion. *Advances in Colloid and Interface Science* **165**, 14-22 (2011).
211. P. M. Reis *et al.*, Influence of Surfactants on Lipase Fat Digestion in a Model Gastro-intestinal System. *Food Biophysics* **3**, 370 (2008).
212. L. Sjöström *et al.*, Randomised placebo-controlled trial of orlistat for weight loss and prevention of weight regain in obese patients. *The Lancet* **352**, 167-172 (1998).
213. D. M. Small, The effects of glyceride structure on fat absorption and metabolism. *Ann Rev Nutr* **11**, (1991).
214. The nomenclature of lipids. *Chem Phys Lipids* **2**, 156-167 (1968).
215. N. Shah, B. Limketkai, The Use of Medium-Chain Triglycerides in Gastrointestinal Disorders. *Practical gastroenterology*, 20-28 (2017).
216. V. K. Babayan, Medium chain triglycerides and structured lipids. *Lipids* **22**, 417-420 (1987).
217. J. P. Flatt, E. Ravussin, K. J. Acheson, E. Jéquier, Effects of dietary fat on postprandial substrate oxidation and on carbohydrate and fat balances. *The Journal of clinical investigation* **76**, 1019-1024 (1985).
218. M. Koushki, M. Nahidi, F. Cheraghali, Physico-chemical properties, fatty acid profile and nutrition in palm oil. *Journal of Paramedical Sciences* **6**, 117-134 (2015).
219. G. Fave, T. C. Coste, M. Armand, Physicochemical properties of lipids: New strategies to manage fatty acid bioavailability. *Cell Mol Biol* **50**, 815-831 (2004).
220. M. C. Carey, D. M. Small, C. M. Bliss, Lipid Digestion and Absorption. *Annu Rev Physiol* **45**, 651-677 (1983).
221. E. Bauer, S. Jakob, R. Mosenthin, Principles of physiology of lipid digestion. *Asian Austral J Anim* **18**, 282-295 (2005).
222. H. Moreau, R. Laugier, Y. Gargouri, F. Ferrato, R. Verger, Human preduodenal lipase is entirely of gastric fundic origin. *Gastroenterology* **95**, 1221-1226 (1988).

- 
223. M. W. Bodmer *et al.*, Molecular-Cloning of a Human Gastric Lipase and Expression of the Enzyme in Yeast. *Biochimica et biophysica acta* **909**, 237-244 (1987).
224. H. Moreau, Y. Gargouri, D. Lecat, J. L. Junien, R. Verger, Screening of Preduodenal Lipases in Several Mammals. *Biochimica et biophysica acta* **959**, 247-252 (1988).
225. E. Ville, F. Carriere, C. Renou, R. Laugier, Physiological study of pH stability and sensitivity to pepsin of human gastric lipase. *Digestion* **65**, 73-81 (2002).
226. F. Paltauf, F. Esfandi, A. Holasek, Stereospecificity of Lipases-Enzymic Hydrolysis of Enantiomeric Alkyl Diacylglycerols by Lipoprotein-Lipase, Lingual Lipase and Pancreatic Lipase. *Febs Lett* **40**, 119-123 (1974).
227. T. H. Liao, P. Hamosh, M. Hamosh, Fat Digestion by Lingual Lipase - Mechanism of Lipolysis in the Stomach and Upper Small-Intestine. *Pediatr Res* **18**, 402-409 (1984).
228. M. Hamosh, R. O. Scow, Lingual Lipase and Its Role in Digestion of Dietary Lipid. *Journal of Clinical Investigation* **52**, 88-95 (1973).
229. M. Armand *et al.*, Characterization of emulsions and lipolysis of dietary lipids in the human stomach. *Am J Physiol-Gastr L* **266**, G372-G381 (1994).
230. Y. Pafumi *et al.*, Mechanisms of Inhibition of Triacylglycerol Hydrolysis by Human Gastric Lipase. *Journal of Biological Chemistry* **277**, 28070-28079 (2002).
231. M. Armand *et al.*, Digestion and absorption of 2 fat emulsions with different droplet sizes in the human digestive tract. *The American Journal of Clinical Nutrition* **70**, 1096-1106 (1999).
232. J. N. Crawley, R. L. Corwin, Biological actions of cholecystokinin. *Peptides* **15**, 731-755 (1994).
233. F. K. Winkler, A. D'Arcy, W. Hunziker, Structure of human pancreatic lipase. *Nature* **343**, 771 (1990).
234. M.-P. Egloff *et al.*, The 2.46 Å Resolution Structure of the Pancreatic Lipase-Colipase Complex Inhibited by a C11 Alkyl Phosphonate. *Biochemistry* **34**, 2751-2762 (1995).
235. J. Kraut, Serine Proteases: Structure and Mechanism of Catalysis. *Annual Review of Biochemistry* **46**, 331-358 (1977).
236. G. Dodson, A. Wlodawer, Catalytic triads and their relatives. *Trends in biochemical sciences* **23**, 347-352 (1998).
237. H. Wong, M. C. Schotz, The lipase gene family. *Journal of lipid research* **43**, 993-999 (2002).
238. J. K. Embleton, C. W. Pouton, Structure and function of gastro-intestinal lipases. *Advanced drug delivery reviews* **25**, 15-32 (1997).
239. F. A. Wilson, V. L. Sallee, J. M. Dietschy, Unstirred water layers in intestine: rate determinant of fatty acid absorption from micellar solutions. *Science* **174**, 1031-1033 (1971).
240. C. J. Porter, N. L. Trevaskis, W. N. Charman, Lipids and lipid-based formulations: optimizing the oral delivery of lipophilic drugs. *Nature reviews. Drug discovery* **6**, 231-248 (2007).
241. J. H. van de Kamer, H. t. B. Huinink, H. A. Weyers, RAPID METHOD FOR THE DETERMINATION OF FAT IN FECES. *Journal of Biological Chemistry* **177**, 347-355 (1949).
242. R. J. Jandacek, J. E. Heubi, P. Tso, A novel, noninvasive method for the measurement of intestinal fat absorption. *Gastroenterology* **127**, 139-144 (2004).

243. G. H. Peter, Faecal fat: time to give it up. *Ann Clin Biochem* **38**, 164-167 (2001).
244. I. H. Rosenberg, M. D. Sitrin, Screening for fat malabsorption. *Ann Intern Med* **95**, 776-777 (1981).
245. V. A. Stallings *et al.*, Diagnosing malabsorption with systemic lipid profiling: pharmacokinetics of pentadecanoic acid and triheptadecanoic acid following oral administration in healthy subjects and subjects with cystic fibrosis. *International Journal of Clinical Pharmacology and Therapeutics* **51**, 263-273 (2013).
246. A. D. Newcomer, A. F. Hofmann, E. P. DiMagno, P. J. Thomas, G. L. Carlson, Triolein breath test: a sensitive and specific test for fat malabsorption. *Gastroenterology* **76**, 6-13 (1979).
247. S. Kaihara, H. N. Wagner, Jr., Measurement of intestinal fat absorption with carbon-14 labeled tracers. *J Lab Clin Med* **71**, 400-411 (1968).
248. Y. F. Ghoo, G. R. Vantrappen, P. J. Rutgeerts, P. C. Schurmans, A mixed-triglyceride breath test for intraluminal fat digestive activity. *Digestion* **22**, 239-247 (1981).
249. N. J. Greenberger, J. B. Rodgers, K. J. Isselbacher, Absorption of medium and long chain triglycerides: factors influencing their hydrolysis and transport. *The Journal of clinical investigation* **45**, 217-227 (1966).
250. F. Bietrix *et al.*, Accelerated Lipid Absorption in Mice Overexpressing Intestinal SR-BI. *Journal of Biological Chemistry* **281**, 7214-7219 (2006).
251. K. W. Huggins, L. M. Camarota, P. N. Howles, D. Y. Hui, Pancreatic Triglyceride Lipase Deficiency Minimally Affects Dietary Fat Absorption but Dramatically Decreases Dietary Cholesterol Absorption in Mice. *Journal of Biological Chemistry* **278**, 42899-42905 (2003).
252. D. Isler, C. Moeglen, N. Gains, M. K. Meier, Effect of the lipase inhibitor orlistat and of dietary lipid on the absorption of radiolabelled triolein, tri- $\gamma$ -linolenin and tripalmitin in mice. *Brit J Nutr* **73**, 851-862 (1995).
253. J. Hoving, A. J. Valkema, J. H. P. Wilson, M. G. Woldring, Properties of glycerol- $^{75}\text{Se}$ -triether: a lipid-soluble marker for the estimation of intestinal fat absorption. *The Journal of Laboratory and Clinical Medicine* **86**, 286-294.
254. B. Lembcke *et al.*, Clinical value of dual-isotope fat absorption test system (FATS) using glycerol [ $^{125}\text{I}$ ]trioleate and glycerol [ $^{75}\text{Se}$ ]triether. *Digestive diseases and sciences* **31**, 822-828 (1986).
255. M. Kalivianakis *et al.*, Validation in an animal model of the carbon 13-labeled mixed triglyceride breath test for the detection of intestinal fat malabsorption. *The Journal of pediatrics* **135**, 444-450 (1999).
256. G. R. Vantrappen, P. J. Rutgeerts, Y. F. Ghoo, M. I. Hiele, Mixed triglyceride breath test: a noninvasive test of pancreatic lipase activity in the duodenum. *Gastroenterology* **96**, 1126-1134 (1989).
257. B. Braden, B. Lembcke, W. Kuker, W. F. Caspary,  $^{13}\text{C}$ -breath tests: Current state of the art and future directions. *Digestive and Liver Disease* **39**, 795-805 (2007).
258. A. Paulus *et al.*, Synthesis, radiosynthesis and in vitro evaluation of  $^{18}\text{F}$ -Bodipy-C16/triglyceride as a dual modal imaging agent for brown adipose tissue. *PloS one* **12**, e0182297 (2017).
259. A. McCaffrey, M. A. Kay, C. H. Contag, Advancing Molecular Therapies through In Vivo Bioluminescent Imaging. *Molecular imaging* **2**, 75-86 (2003).
260. E. Eiríksdóttir, Ü. Langel, K. Rosenthal-Aizman, An improved synthesis of releasable luciferin-CPP conjugates. *Tetrahedron Lett.* **50**, 4731 (2009).

261. R. Kojima *et al.*, Rational Design and Development of Near-Infrared-Emitting Firefly Luciferins Available In Vivo. *Angewandte Chemie International Edition* **52**, 1175-1179 (2013).
262. M. S. Evans *et al.*, A synthetic luciferin improves bioluminescence imaging in live mice. *Nat Meth* **11**, 393-395 (2014).
263. H. Takakura *et al.*, New Class of Bioluminogenic Probe Based on Bioluminescent Enzyme-Induced Electron Transfer: BioLeT. *Journal of the American Chemical Society* **137**, 4010-4013 (2015).
264. R. Kojima *et al.*, Development of a Sensitive Bioluminogenic Probe for Imaging Highly Reactive Oxygen Species in Living Rats. *Angewandte Chemie* **127**, 14981-14984 (2015).
265. B. P. C. Chow, E. A. Shaffer, H. G. Parsons, Absorption of triglycerides in the absence of lipase. *Can J Physiol Pharm* **68**, 519-523 (1990).
266. I. J. Goldberg, R. H. Eckel, N. A. Abumrad, Regulation of fatty acid uptake into tissues: lipoprotein lipase- and CD36-mediated pathways. *Journal of lipid research* **50**, S86-S90 (2009).
267. H. Mu, C.-E. Høy, The digestion of dietary triacylglycerols. *Progress in lipid research* **43**, 105-133 (2004).
268. G. Saito, J. A. Swanson, K.-D. Lee, Drug delivery strategy utilizing conjugation via reversible disulfide linkages: role and site of cellular reducing activities. *Advanced drug delivery reviews* **55**, 199-215 (2003).
269. E. J. Stoner, G. Negrón, R. Gaviño, 2,2'-Dipyridyl Disulfide. *Encyclopedia of Reagents for Organic Synthesis*. (John Wiley & Sons, Ltd, 2008).
270. S. Eckert *et al.*, Molecular structures and protonation state of 2-Mercaptopyridine in aqueous solution. *Chem Phys Lett* **647**, 103-106 (2016).
271. F. Batista-Viera, L. Rydén, J. Carlsson, *Protein Purification : Principles, High Resolution Methods, and Applications*. (John Wiley & Sons, Inc., 2011), pp. 203-219.
272. B. Neises, W. Steglich, Simple Method for the Esterification of Carboxylic Acids. *Angewandte Chemie International Edition in English* **17**, 522-524 (1978).
273. J.-L. Gras, J.-F. Bonfanti, Efficient Syntheses of Pure Mixed Triglycerides. *Synthetic Communications* **30**, 4213-4219 (2000).
274. Y. Yoshida, Y. Sakakura, N. Aso, S. Okada, Y. Tanabe, Practical and efficient methods for sulfonylation of alcohols using Ts(Ms)Cl/Et<sub>3</sub>N and catalytic Me<sub>3</sub>H-HCl as combined base: Promising alternative to traditional pyridine. *Tetrahedron* **55**, 2183-2192 (1999).
275. Y. Sambuy *et al.*, The Caco-2 cell line as a model of the intestinal barrier: influence of cell and culture-related factors on Caco-2 cell functional characteristics. *Cell Biology and Toxicology* **21**, 1-26 (2005).
276. L. Sek, C. J. H. Porter, A. M. Kaukonen, W. N. Charman, Evaluation of the in-vitro digestion profiles of long and medium chain glycerides and the phase behaviour of their lipolytic products. *J Pharm Pharmacol* **54**, 29-41 (2002).
277. S.-Y. Ho, J. Storch, Common mechanisms of monoacylglycerol and fatty acid uptake by human intestinal Caco-2 cells. *Am J Physiol-Cell Ph* **281**, C1106-C1117 (2001).
278. P. Hadváry, H. Lengsfeld, H. Wolfer, Inhibition of pancreatic lipase *in vitro* by the covalent inhibitor tetrahydrolipstatin. *Biochemical Journal* **256**, 357-361 (1988).

279. E. Fernandez, B. Borgström, Effects of tetrahydrolipstatin, a lipase inhibitor, on absorption of fat from the intestine of the rat. *Biochimica et Biophysica Acta (BBA) - Lipids and Lipid Metabolism* **1001**, 249-255 (1989).
280. R. G. H. Morgan, A. F. Hofmann, Synthesis and metabolism of glycerol-<sup>3</sup>H triether, a nonabsorbable oil-phase marker for lipid absorption studies. *Journal of lipid research* **11**, 223-230 (1970).
281. M. Deponte, Glutathione catalysis and the reaction mechanisms of glutathione-dependent enzymes. *Biochimica et Biophysica Acta (BBA) - General Subjects* **1830**, 3217-3266 (2013).
282. M. H. Lee *et al.*, Disulfide-Cleavage-Triggered Chemosensors and Their Biological Applications. *Chemical reviews* **113**, 5071-5109 (2013).
283. B. P. Chow, E. A. Shaffer, H. G. Parsons, Absorption of triglycerides in the absence of lipase. *Can J Physiol Pharmacol* **68**, 519-523 (1990).
284. Y.-A. Cao *et al.*, Shifting foci of hematopoiesis during reconstitution from single stem cells. *Proceedings of the National Academy of Sciences* **101**, 221-226 (2004).
285. M. C. Torjman, J. I. Joseph, C. Munsick, M. Morishita, Z. Grunwald, Effects of Isoflurane on gastrointestinal motility after brief exposure in rats. *Int J Pharmaceut* **294**, 65-71 (2005).
286. F. Carrière *et al.*, Inhibition of gastrointestinal lipolysis by Orlistat during digestion of test meals in healthy volunteers. *American Journal of Physiology - Gastrointestinal and Liver Physiology* **281**, G16-G28 (2001).
287. A. Ballinger, S. R. Peikin, Orlistat: its current status as an anti-obesity drug. *Eur J Pharmacol* **440**, 109-117 (2002).
288. R. G. Morgan, B. Borgstrom, The mechanism of fat absorption in the bile fistula rat. *Quarterly journal of experimental physiology and cognate medical sciences* **54**, 228-243 (1969).
289. B. Borgström, A. Dahlqvist, G. Lundh, J. Sjövall, Studies of Intestinal Digestion and Absorption in the Human. *Journal of Clinical Investigation* **36**, 1521-1536 (1957).
290. J. S. Ayres, N. J. Trinidad, R. E. Vance, Lethal inflammasome activation by a multidrug-resistant pathobiont upon antibiotic disruption of the microbiota. *Nature medicine* **18**, 799-806 (2012).
291. D. A. Antonopoulos *et al.*, Reproducible community dynamics of the gastrointestinal microbiota following antibiotic perturbation. *Infect Immun* **77**, 2367-2375 (2009).
292. L. Dethlefsen, D. A. Relman, Incomplete recovery and individualized responses of the human distal gut microbiota to repeated antibiotic perturbation. *Proceedings of the National Academy of Sciences of the United States of America* **108** Suppl 1, 4554-4561 (2011).
293. S. R. Modi, J. J. Collins, D. A. Relman, Antibiotics and the gut microbiota. *The Journal of clinical investigation* **124**, 4212-4218 (2014).
294. H. Sato *et al.*, Antibiotics Suppress Activation of Intestinal Mucosal Mast Cells and Reduce Dietary Lipid Absorption in Sprague-Dawley Rats. *Gastroenterology* **151**, 923-932 (2016).
295. A. F. Hofmann, Bile Acids: The Good, the Bad, and the Ugly. *News in physiological sciences* **14**, 24-29 (1999).
296. M. Begley, C. Hill, C. G. M. Gahan, Bile Salt Hydrolase Activity in Probiotics. *Appl Environ Microb* **72**, 1729-1738 (2006).

- 297. J. M. Lambert, R. S. Bongers, W. M. de Vos, M. Kleerebezem, Functional analysis of four bile salt hydrolase and penicillin acylase family members in *Lactobacillus plantarum* WCFS1. *Appl Environ Microbiol* **74**, 4719-4726 (2008).
- 298. H. J. Chung *et al.*, Intestinal removal of free fatty acids from hosts by *Lactobacilli* for the treatment of obesity. *FEBS open bio* **6**, 64-76 (2016).
- 299. D. J. McClements, Y. Li, Structured emulsion-based delivery systems: controlling the digestion and release of lipophilic food components. *Adv Colloid Interface Sci* **159**, 213-228 (2010).





# Chapter 6 Annexes

## 6.1 Curriculum Vitae

### Grigory Karateev

Route Cantonale 37

CH 1025, St-Sulpice VD

Tel.: +41766158876

e-mail: [grigory.karateev@gmail.com](mailto:grigory.karateev@gmail.com), [grigory.karateev@epfl.ch](mailto:grigory.karateev@epfl.ch)

Nationality: Russian

Date of birth: 20.06.1985

### EDUCATION

---

- |                        |   |
|------------------------|---|
| <b>09.2012-05.2018</b> | <b>PhD studies in Chemical Biology, Swiss Federal Institute of Technology Lausanne (EPFL), Switzerland</b>                        |
| <b>09.2005-06.2009</b> | <b>Master degree (M.Sc.) in Chemistry, Lomonosov Moscow State University, Russia</b><br>Organic Chemistry. Graduated with Honors. |
| <b>09.2004-08.2005</b> | <b>Peoples' Friendship University of Russia (RUDN), Russia</b><br>Chemistry.  |

### CERTIFICATE

---

**RESAL Module 1.** Introductory course in Laboratory Animal Science (theoretical and practical). February 2014. Lausanne, Switzerland.

### LANGUAGES

---

English (fluent spoken and written), Russian (native), German (basic, A2 level).

### PUBLICATIONS

---

- Park, H. M.; Russo, K. A.; **Karateev, G.**; Park, M.; Dubikovskaya, E.; Kriegsfeld, L. J.; Stahl, A., A System for In Vivo Imaging of Hepatic Free Fatty Acid Uptake. *Gastroenterology* **2017**, 152 (1), 78-81.e2.
- Tharp, K. M.; Jha, A. K.; Kraiczy, J.; Yesian, A.; **Karateev, G.**; Sinisi, R.; Dubikovskaya, E. A.; Healy, K. E.; Stahl, A., Matrix-Assisted Transplantation of Functional Beige Adipose Tissue. *Diabetes* **2015**, 64 (11), 3713-3724.
- Vorobyeva, A. G.; Stanton, M.; Godinat, A.; Lund, K. B.; **Karateev, G. G.**; Francis, K. P.; Allen, E.; Gelovani, J. G.; McCormack, E.; Tangney, M.; Dubikovskaya, E. A. *PlosOne* **2015**, 10, e0131037.

- Dubikovskaya, E.; Chudnovskiy, R.; **Karateev, G.**; Park, H. M.; Stahl, A., Measurement of long-chain fatty acid uptake into adipocytes. *Methods in enzymology* **2014**, 538, 107-34.
- Matveeva, E. D.; Podrugina, T. A.; Kolesnikova, I. N.; Prisyazhnoi, M. V.; **Karateev, G. G.**; Zefirov, N. S., Catalytic hydrophosphorylation of alkyl- and acylhydrazones. *Russ Chem B+* **2010**, 59 (2), 418-424.

#### **PATENTS**

---

- Goun E.A.; Khodakivskiy P.; **Karateev G.** Substances and methods for the controlled intracellular release of molecules of interest. Patent application N°: US 62/553,172.
- Sinisi, R.; Dubikovskaya, E.; Budin, G.; **Karateev, G.**; Frigell, J.; Konovalova, A.; Godinat, A. Bioluminescence imaging of small biomolecules, PCT Int. Appl. **2014**. Patent number WO2014111906 A1.

#### **PROFESSIONAL MEMBERSHIPS**

---

- Member of the Swiss Chemical Society (SCS)
- Member of the European Society for Molecular Imaging (ESMI)



